

Maximilian Josef Doppelbauer

**The AlF Molecule as a Candidate for
Laser Cooling and Trapping**

The AIF Molecule as a Candidate for Laser Cooling and Trapping
PhD Thesis, Radboud Universiteit, Nijmegen, the Netherlands

© 2022 Maximilian Josef Doppelbauer
ISBN: 978-94-6421-935-7
Printed by IPSKAMP Printing, Enschede

The cover design is based on a photograph by the author. It shows the cryogenic buffer gas cell, designed by Sebastian Kray, as it was used in parts of the thesis research.

The work described in this thesis has been performed in the Molecular Physics department at the Fritz-Haber-Institut der Max-Planck-Gesellschaft in Berlin, Germany.

FRITZ-HABER-INSTITUT
MAX-PLANCK-GESELLSCHAFT



The AlF Molecule as a Candidate for Laser Cooling and Trapping

Proefschrift ter verkrijging van de graad van doctor
aan de Radboud Universiteit Nijmegen
op gezag van de rector magnificus prof. dr. J.H.J.M. van Krieken,
volgens besluit van het college voor promoties
in het openbaar te verdedigen op
maandag 19 december 2022
om 10:30 uur precies

door

Maximilian Josef Doppelbauer

geboren op 11 juni 1992
te Wenen, Oostenrijk

Promotor: Prof. dr. G.J.M. Meijer

Copromotor: Dr. S. Truppe (*Imperial College London, Verenigd Koninkrijk*)

Manuscriptcommissie:

Prof. dr. S.Y.T. van de Meerakker

Prof. dr. W.E. Ernst (*Technische Universität Graz, Oostenrijk*)

Dr. B.R. Heazlewood (*University of Liverpool, Verenigd Koninkrijk*)

The AlF Molecule as a Candidate for Laser Cooling and Trapping

Dissertation to obtain the degree of doctor
from Radboud University Nijmegen
on the authority of the Rector Magnificus prof. dr. J.H.J.M. van Krieken,
according to the decision of the Doctorate Board
to be defended in public on
Monday, December 19, 2022
at 10:30 am

by

Maximilian Josef Doppelbauer

born on June 11, 1992
in Vienna, Austria

PhD supervisor: Prof. dr. G.J.M. Meijer

PhD co-supervisor: Dr. S. Truppe (*Imperial College London, United Kingdom*)

Manuscript Committee:

Prof. dr. S.Y.T. van de Meerakker

Prof. dr. W.E. Ernst (*Technische Universität Graz, Austria*)

Dr. B.R. Heazlewood (*University of Liverpool, United Kingdom*)

4'33"

I
TACET

II
TACET

III
TACET

John Cage, 1952

(Copyright ©1960 by Henmar Press Inc. All rights reserved. Used by permission.)

Contents

1	Introduction	1
1.1	The Beginnings of Laser Cooling	1
1.2	Ultracold Molecules	3
1.3	Ultracold AIF	6
1.4	Outline of this Thesis	9
2	Spectroscopic Characterisation of the $X^1\Sigma^+$, $A^1\Pi$ and $a^3\Pi$ States in AIF	11
2.1	Introduction	11
2.2	Experiment	11
2.3	Molecular Hamiltonian	16
2.4	Characterisation of the $a^3\Pi$ State	17
2.4.1	The $a^3\Pi, v' = 0 \leftarrow X^1\Sigma^+, v'' = 0$ Band	17
2.4.2	Hyperfine Measurements in the $a^3\Pi, v = 0$ State	21
2.5	Hyperfine Measurements in the $A^1\Pi$ State	26
2.6	The $A^1\Pi, v' = 0 \rightarrow a^3\Pi, v'' = 0$ Transition: A Possible Loss Channel?	28
2.6.1	Motivation	28
2.6.2	Spectra	28
2.6.3	Transition Strength	29
2.7	Conclusion	31
3	Spectroscopic Characterisation of the $b^3\Sigma^+$ State in AIF	33
3.1	Introduction	33
3.2	Previous Work	33
3.3	Rotational Structure of the $b^3\Sigma^+, v' = 0 \leftarrow a^3\Pi_1, v'' = 0$ Band and the Radiative Lifetime of the $b^3\Sigma^+, v = 0$ State	34
3.4	The Fine and Hyperfine Structure of the $b^3\Sigma^+$ State	36
3.5	The $b^3\Sigma^+, v' = 0 \leftarrow a^3\Pi, v'' = 0$ Transition	39
3.6	The $A^1\Pi \rightarrow a^3\Pi$ Bands	47
3.7	Spin-Orbit Interaction Between the $A^1\Pi$ and $b^3\Sigma^+$ States	48
3.7.1	Intensities of the Intersystem Bands	49
3.7.2	Effect on the Fine Structure in the $b^3\Sigma^+, v = 0$ State	52
3.8	Conclusion	54

4	Optical Cycling of AlF	55
4.1	Introduction	55
4.2	Modelling Optical Cycling	56
4.2.1	Rate Equations	56
4.2.2	Optical Bloch Equations	60
4.2.3	The Low Intensity Case	63
4.3	Application to Multilevel Systems	65
4.3.1	General	65
4.3.2	Dark States	66
4.3.3	Simple Cases	68
4.3.4	The $A^1\Pi \leftarrow X^1\Sigma^+$ Transition of AlF	70
4.4	Application to the Experiment	73
4.4.1	Scattered Photons in the Laser Profile	73
4.4.2	Experimental Observables	74
4.4.3	Monte Carlo Simulation of Transverse Deflection	75
4.5	Narrow-Line Laser Cooling of AlF	79
4.5.1	Introduction	79
4.5.2	The Lifetime of the Metastable $a^3\Pi$ State	80
4.5.3	Cooling Scheme	84
4.6	Conclusion	84
5	Experimental Characterisation of Diatomic Monofluoride Molecule Formation in a Cryogenic Buffer Gas Cell	87
5.1	Introduction	87
5.2	Molecule Sources	88
5.2.1	Supersonic Expansion	89
5.2.2	Cryogenic Buffer Gas Cell	89
5.3	Historical Overview	90
5.4	Experimental Setup	93
5.4.1	Cryogenic Buffer Gas Cell	93
5.4.2	Source Characterisation Experiments	96
5.4.3	Laser Systems	99
5.5	Results: Atomic Beams	100
5.5.1	Aluminium	100
5.5.2	Calcium	106
5.5.3	Ytterbium	108
5.5.4	Influence of a Fluorine Donor Gas	110
5.6	Results: Molecular Beams	111
5.6.1	Standard Candle Transitions	111
5.6.2	Comparison of Molecular Beams	111
5.6.3	Collision Cross Section of AlF and Helium	112
5.6.4	Influence of the Ablation Laser Fluence	115
5.6.5	Influence of the Fluorine Donor Gas	117
5.6.6	Influence of the Helium Buffer Gas Flow Rate	121
5.6.7	Velocity Distribution of the Molecular Beam	121

5.6.8	Studying the Phase Space Distribution Using a Stark Decelerator	122
5.6.9	Further Observations	123
5.7	Conclusion and Outlook	125
6	Hyperfine Resolved Optical Spectroscopy of the $A^2\Pi \leftarrow X^2\Sigma^+$ Transition in MgF	127
6.1	Introduction	127
6.2	Motivation	127
6.3	Hamiltonian	129
6.4	Experimental Setup and Absolute Frequency Calibration	131
6.5	Isotope Shifts, Spectroscopic Constants, Hyperfine Structure, and Λ -Doubling	132
6.5.1	Isotope Shifts	133
6.5.2	Spectroscopic Constants of the $A^2\Pi$ State	137
6.5.3	Hyperfine Structure	139
6.5.4	Λ -Doubling	140
6.6	Radiative Lifetime of the $A^2\Pi$, $v' = 0$ Level	142
6.7	Electric Dipole Moment Measurements	144
6.8	Electric Field Induced Rotational Branching	146
6.9	Conclusion	149
	Summary	151
	Samenvatting	153
	A Transition Frequencies in the $a^3\Pi, v = 0$ State	155
	B Sanity Check for OBEs	159
	C Closed-Cycle He Cryocooler	161
	D Hamiltonian of $A^2\Pi$ States of MgF	163
	E MgF Linelist	165
	Bibliography	166
	Research Data Management	201
	Curriculum Vitae	203
	List of Publications	205
	Acknowledgements	207

Chapter 1

Introduction

Over the last decades, enormous progress has been made in the development of laser cooling techniques for atoms and molecules. This has opened up entirely new fields of research and has made it possible to address many fundamental questions of physics and chemistry. In this introductory chapter, I give an overview of developments from the first laser-cooled atoms to current endeavours working on ever-larger molecules, and I explain why aluminium monofluoride (AlF) is an exciting candidate molecule for many ultracold physics experiments.

1.1 The Beginnings of Laser Cooling

Only a little less than 50 years ago, gas-phase atoms were cooled down for the first time to temperatures of a few Kelvin and lower by exploiting the radiation pressure force from a laser [1–5]. This was made possible by progress in vacuum technology and narrow-linewidth tunable laser sources. Upon absorption of a photon, its momentum is transferred to the atom, which slows it down. Excitation with a laser from a certain direction on a closed transition, i.e. where the excited atom decays back to the initial ground state, with a short excited-state lifetime, results in multiple photon momentum transfers, always in the same direction. The absorbed photons are re-emitted in a random direction and therefore, the momentum transfer in emission averages out. This spontaneous emission is the dissipative process that removes thermal energy from the system. The entropy of the system decreases because the incoming laser beam with very low entropy is converted into isotropic fluorescence with very high entropy [6].* Cooling increases the phase space density of the atoms, which is advantageous in atomic physics and beyond [7].

About ten years after the first reports of laser slowing with a single beam, researchers presented advanced techniques including several counter-propagating laser beams — the optical molasses [8] — that allow for cooling and confinement

*Since the system is not at thermal equilibrium with its surroundings, temperature and entropy are not rigorously defined. Here, temperature is a measure of the average kinetic energy of the system.

of the atoms with optical forces. With additional magnetic fields, this becomes a magneto-optical trap (MOT) [9] that strongly confines the atoms. Strong off-resonant lasers can similarly be used to trap atoms, either in single tweezers,[†] tweezer arrays, optical dipole traps or in two- and three-dimensional optical lattices [10–14].

At a temperature close to absolute zero, a gas at atmospheric pressure condenses. The investigation of a liquid or solid only yields limited information on single atoms and their interactions; furthermore, single atoms cannot be manipulated independently. At low densities in vacuum, however, cold and ultracold[‡] atoms exist as a gas of isolated particles. These can, in principle, be investigated independently and gas-phase spectra yield high-resolution information on the energy structure of single atoms. Therefore, laser cooling of atoms in the gas phase opens up a plethora of research directions and enables many new technological applications.

One immediate application of confined samples of ultracold atoms is high-precision measurements. Thermal atoms at room temperature move with speeds on the order of the speed of sound. Therefore, spectral lines are broadened by the Doppler effect and can be displaced because of relativistic time dilation [16]. Observation times are limited by the short presence of the fast atoms in the interaction zone of light and matter. Transition frequencies of ultracold atoms in traps or in fountains can be determined at mHz precision [7, 17, 18]. Possible applications of these measurements are frequency standards like in atomic clocks, atom interferometers as precision force sensors, and the investigation of physics beyond the Standard Model of particle physics [18, 19].

Another important focus of the cold atom community is the study of atomic interactions and quantum collective behaviour [16]. When the interatomic spacing is smaller than the thermal de Broglie wavelength of an atom with mass M at the temperature T (where h and k_B are the Planck and Boltzmann constants, respectively) [20],

$$\lambda_{\text{dB}} = \frac{h}{\sqrt{2\pi M k_B T}},$$

the matter waves of bosonic atoms overlap and interfere constructively [21].

In the classical picture of chemical reactivity as described by the Arrhenius equation, the reaction rate decreases with temperature and approaches zero at ultralow temperatures. At these low temperatures, the de Broglie wavelength of the reactants approaches the order of magnitude of bond lengths. A classical description is then not suitable anymore and reactions must be viewed from a quantum perspective, where coherent phenomena, quantum fluctuations, and entanglement influence the reaction [15, 22–24]. This holds for both atoms and molecules.

The most famous collective effect is the Bose-Einstein condensate (BEC). For a long time, experiments on achieving Bose-Einstein condensation of spin-polarised

[†]The use of optical tweezers is not limited to atoms: they can be used equally well for molecules, nanoparticles and even biological cells — this earned Arthur Ashkin one half of the 2018 Physics Nobel Prize.

[‡]Most commonly, cold temperatures are defined as being below 1 K, ultracold temperatures are below 1 μK [15].

hydrogen in a magnetic or microwave trap were leading the field [25–28]. The first experimental BECs, however, were made with alkali atoms by two independent groups in 1995 [29, 30]. They evaporatively cooled Na or Rb atoms that were initially laser-cooled and trapped using magnetic fields. In a BEC, the ground state of the atoms is populated macroscopically. The study of these condensates and other collective effects promises a better understanding of superconductivity, superfluidity, and supersolidity [29, 31].

Nowadays, the temperatures achieved with laser cooling are in the pK range [32–34] and MOTs and BECs have become common tools of atomic physics that are already available in almost-turnkey commercial systems.

The fast progress in all areas of quantum science over the last five decades has also become relevant for industry and society as a whole — terms like “quantum computing” or “quantum cryptography” are known far beyond the physics community. Laser cooled atoms will play an essential role as qubits — quantum memory units — and therefore become an integral part of the quantum internet.

1.2 Ultracold Molecules

Studies on molecules at room temperature suffer from the same problems concerning interaction times and line broadening as their atomic siblings. Additionally, hot molecules are distributed over many quantum states and the signal from detecting one quantum state is low. The use of ultracold molecules reduces the line broadening and allows to increase interaction times and the detectable population in low quantum states. It also opens up new avenues because their internal degrees of freedom can be precisely controlled and samples prepared in defined quantum states [15, 35].

The vibrational and rotational energy structure of molecules complicates direct laser cooling of molecules. Therefore, other methods to cool down molecules were pursued first. These are buffer gas cooling [36] and cooling in supersonic expansions with subsequent Stark [37] or Zeeman deceleration [38–40]. These methods can be applied relatively universally to various molecules; the latter methods only require permanent electric (Stark deceleration) or magnetic (Zeeman deceleration) dipole moments of the molecules. The molecules can subsequently be trapped to achieve long interrogation times [41].

Ultracold diatomic molecules can be assembled from two ultracold atoms by photo- [42–45] or magnetoassociation [46]. The molecules are formed in a weakly-bound highly excited vibrational state and are then transferred to the ground state. Among the species that have been produced by these methods, one finds RbCs [47], KRb [48–50], LiCs [51], Cs₂ [52], NaCs [53], LiK [54], NaK [55], NaLi [56] and NaRb [57].

Around the same time that these associated molecules were first produced in experiments, some types of diatomic molecules were suggested for direct laser cooling [58, 59]. The molecules must have a strong rotationally closed cycling transition with a high scattering rate, a diagonal Franck-Condon matrix and no electronic states intervening in the cycling transition to which the upper state

can decay [58]. At first, hydrides, carbides and oxides were proposed as possible candidates with the right level structure for laser cooling; metal halides were presented less prominently. Rather unexpectedly, the first demonstration of direct laser cooling of molecules was made with SrF [60,61]. This molecule was the harbinger of many other laser-cooled molecules that were presented in the following years. To date, the diatomic molecules YO [62], CaF [63], YbF [64], the triatomic molecules SrOH [65], and YbOH [66] as well as the polyatomic molecule calcium-monomethoxide (CaOCH_3) [67] have been laser cooled. Magneto-optical trapping has been demonstrated for SrF [68], CaF [69,70], YO [71] and CaOH [72]. Other molecules that show promise for laser cooling and that are being investigated in experiments are MgF [73], BaF [74], BaH [75], TlF [76], AlCl [77], and YbOCH₃ [78]. RaF is currently under investigation at CERN, where this radioactive element is being produced [79,80]. Candidate molecules that have been proposed for future experiments are TiO [59], BeF [81] and HgOH [82]. The complexity of proposed polyatomics with a metal cycling centre is increasing [83,84]. Larger organic molecules with several aromatic rings can be functionalised with a CaO moiety and show potential for laser cooling [85–87]. A common criterion for the structure of laser-coolable molecules can be formulated considering that the Franck-Condon matrix has to be very diagonal. The electron that is being promoted to an excited state during optical cycling should not be part of the metal-ligand bond so that the bond length changes only minimally [88]. It is important to note that samples of ultracold molecules from direct cooling are still several orders of magnitude less dense than the ones obtained from association methods [89].

There are several reasons why it is worth going the extra mile to produce ultracold molecules: They are a unique tool to gain new insights into chemical reactivity, test fundamental physics, study quantum many-body phenomena and can be used for quantum simulation and computing [35,90].

Studies on reactions of ultracold molecules allow us to understand quantum influences on reactivity and the chemistry in our universe [24]. Furthermore, external fields can be used to precisely steer chemical encounters and to study the intermolecular forces at play [91,92]. Reactions at ultralow temperatures have been experimentally realised with a trapped gas of KRb, demonstrating that quantum-state controlled and -resolved dynamics can be studied [93–95]. CaF molecules in optical or magnetic traps have recently been used to study collisions between two molecules or with a Rb atom in a quantum-state resolved manner [96–98]. Also without laser cooling, collision and reaction dynamics are studied in a quantum regime. Collisions between cold oxygen molecules have been observed in a superconducting magnetic trap [99]. In experiments based on Stark decelerators, with precisely tuned velocities, collisions and scattering resonances of molecules were investigated [100–103]. Reactive collisions of velocity-selected polar molecules and laser-cooled ions were studied in a “Coulomb crystal” of laser-cooled ions in a Paul ion trap [104–106].

Some questions of fundamental physics that arise from cosmological observations cannot be explained by the Standard Model of particle physics. These effects are the existence of dark matter, the amount of dark energy and the imbalance of matter over antimatter in the universe. Normally, the particles and forces that

can provide explanations for these effects can only be detected at large-scale particle physics facilities, at enormous financial cost [107, 108]. Tabletop experiments with molecules are a more accessible alternative to explore fundamental physics questions in individual laboratories.

Permanent electric dipole moments of particles with spin angular momentum — such as electrons and protons — violate time-reversal symmetry. This violation is highly suppressed in the Standard Model of particle physics but is necessary to support a theory beyond the Standard Model that explains the matter-antimatter asymmetry [19, 109]. According to these theories beyond the Standard Model, the electric dipole moment of the electron (eEDM) should be up to ten orders of magnitude larger than predicted by the Standard Model [109–113]. The large intramolecular electric fields present in heavy molecules — such as YbF, ThO and BaF — aid to achieve sufficient sensitivity to detect an eEDM. The majority of molecules for eEDM experiments are currently being investigated in beams that are only cooled in a buffer gas cell or supersonic expansion. Laser-cooling and trapping will significantly increase the coherence time and therefore reduce the linewidth of the measurement [64, 114]. Laser-cooled polyatomic molecules are suggested to show increased sensitivity because of internal comagnetometer states — these serve as reference for minute shifts of lines [114–116].

Other experiments to investigate time-reversal symmetry and parity violation have been proposed using molecules containing radium, such as RaF [117], RaOH [118] and RaOCH_3^+ [119].

The high resolution of spectroscopic measurements on slow and cold molecules can also be exploited to study changes of fundamental constants like the fine structure constant α or the proton-to-electron mass ratio μ over time or position [120–123]. Frequencies of Λ -doublet transitions in small radicals that lie in the microwave range are measured to Hz precision and values obtained at different times or in different laboratories are compared. A big increase in the observation timescales is obtained by comparing laboratory data to astrophysical measurements.

The progress in obtaining new phases of matter like a BEC with cold molecules has not yet kept up with atoms. Degenerate gases of polar Fermions (a *degenerate Fermi gas*) have been reported for KRb [89] and NaK [124]. Both were formed by association of degenerate atom gases. This progress will allow the investigation of chemistry in the quantum regime and many-body interactions. It is also a step towards the production of a heteroatomic molecular BEC.

Because of their dipole moments, polar molecules show long-range dipole-dipole interactions.[§] These can be exploited to understand quantum many-body physics phenomena such as high-temperature superconductivity and quantum magnetism. The molecules are trapped in the wells of an optical lattice and form an ideal model system for solid state physics — a so-called quantum simulator [14, 128–135]. Quantum computation using molecules has been studied theoretically in several publications [136–139].

[§]Magnetic atoms, e.g. Cr and Dy, have a relatively strong magnetic dipole-dipole interaction. However, the electric dipole-dipole interaction is much stronger [125–127].

At ultralow temperatures, a naive mind would only expect nothingness but, in fact, this regime allows us to observe many fascinating effects that are otherwise inaccessible. In some ways, this is reminiscent of John Cage’s famous 1952 composition *4'33''* that is quoted on page i of this thesis. The composer lets the performer present 273 seconds of silence.[¶] He challenges the idea of nothingness — even in an attempt of absolute silence, the sounds produced by the audience open up a whole new musical experience.

1.3 Ultracold AlF

AlF was one of the molecules proposed for direct laser cooling to low temperatures and with a high density by Di Rosa in 2004 [58]. It is a strongly-bound molecule with a $^1\Sigma^+$ ground state that can be produced efficiently in supersonic, buffer gas, and oven sources [140]. The strong $A^1\Pi, v = 0 \leftarrow X^1\Sigma^+, v'' = 0$ band near 227.5 nm can be used for laser cooling and magneto-optical trapping because of the high photon scattering rate that was calculated to be $\Gamma = 1/\tau = 2\pi \times 84$ MHz, where the radiative lifetime of the $A^1\Pi, v = 0$ state is $\tau = 1.89$ ns. Any Q-line of the $A^1\Pi, v = 0 \leftarrow X^1\Sigma^+, v'' = 0$ transition is closed and the Franck-Condon matrix is very diagonal [141, 142].^{||} After cooling and trapping on this strong transition, any Q-line of the spin-forbidden $a^3\Pi_1, v' = 0 \leftarrow X^1\Sigma^+, v'' = 0$ band can be used for narrow-line cooling of the molecules down to a few μ K. Losses to the $a^3\Pi$ state are predicted to be too weak to intervene in optical cycling. The potential energy curves of the three lowest electronic states of AlF are shown in figure 1.1, together with a scheme of the calculated Franck-Condon factors based on experimental data.

The cycling transition deep in the ultraviolet region of the electromagnetic spectrum is a difficulty and an advantage at the same time. High intensity sources of continuous wave (cw) light at 227.5 nm have only become available recently. This wavelength is produced by frequency-doubling the fundamental of a titanium sapphire laser twice, which is technically challenging. However, the momentum of a high-energy photon slows molecules more upon scattering than the longer-wavelength photons used to cool other molecules. Therefore, and together with the high spontaneous decay rate, the distance needed to slow the molecules from a buffer gas beam to standstill is only a few cm and the capture velocity of a magneto-optical trap will be large.

All the diatomic molecules that have been directly laser cooled so far are radicals with a doublet ground state and a $^2\Pi_{1/2} \leftarrow ^2\Sigma^+$ transition is used for optical cycling. Only a single rotational transition can be used for cycling. Molecules in $^1\Sigma$ states are chemically more stable than these radicals. Even in a dense, cold sample, AlF molecules will not rearrange to form a F_2 molecule and an Al dimer.

[¶]To the best of my knowledge, John Cage did not choose the length based on the absolute zero of temperature at -273.15°C . It seems to just be a very fitting coincidence.

^{||}If the Franck-Condon matrix is very diagonal, the probabilities of transitions with $\Delta v = 0$ are near unity while the probabilities in cases with $\Delta v \neq 0$ are very low. This can be seen in the inset of figure 1.1 for the case of AlF.

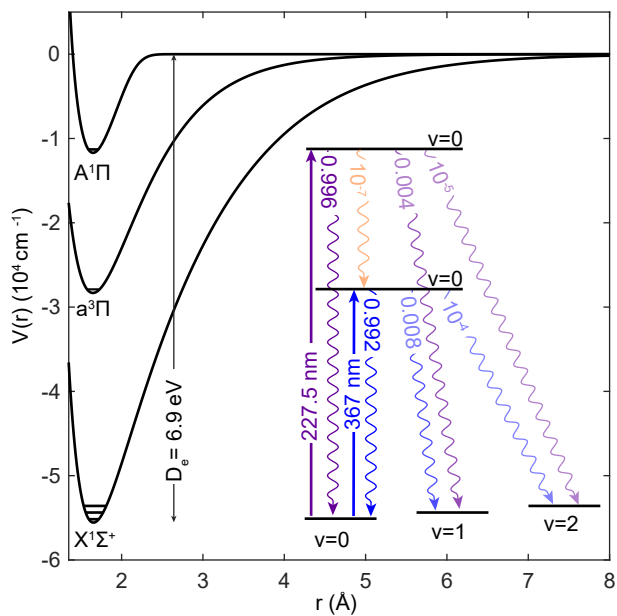


Figure 1.1: Potential energy curves of the three lowest electronic states of AlF. RKR potentials were derived using Le Roy's program [143] to fit both Morse and expanded Morse oscillator (EMO) functions to precise spectroscopic data [144,145]. In the inset, the Franck-Condon factors of relevant transitions are shown. They were calculated from the potentials.

Furthermore, all Q-lines of the $A^1\Pi \leftarrow X^1\Sigma^+$ transition are closed and can be used for optical cycling because no population is lost to non-resonant rotational states.

The first goal to be achieved with laser-cooled AlF molecules is a magneto-optical trap at high densities unprecedented for directly-cooled molecules. Sub-Doppler cooling in a gray molasses [146–148], followed by evaporative cooling, can then be used to attain quantum degeneracy. These cold molecules can subsequently be loaded into an optical lattice formed from interfering laser beams. In this highly controlled state, AlF has great potential for precision measurements as well as quantum information and simulation. Possible goals of precision measurements are time variations of the proton-to-electron mass ratio or the permanent electric dipole moment of the proton [123, 149].

AlF is also a promising candidate for a molecular optical clock. Transitions to the long-lived metastable $a^3\Pi$ state (with a predicted lifetime of tens of milliseconds for the $J = 1$ level in the $\Omega = 0$ state) are well-suited for this, although the best optical clocks have excited state lifetimes of 10 s [123]. The electronic structure of AlF with two valence electrons is analogous to the structure of current clock atoms Sr [18], Yb [150], and Cd [151]; their clock transitions are $^1S_0 - ^3P_0$ or $^1S_0 - ^3P_1$, similar to the $a^3\Pi - X^1\Sigma^+$ transition of AlF. An optical lattice clock of AlF can achieve high accuracy and frequency stability and has applications for precision measurements [152, 153].

AlF is not just a promising candidate for ultracold physics experiments. The molecule has nuclear spins of $I_{Al} = 5/2$ for ^{27}Al and $I_F = 1/2$ for ^{19}F , leading to a rich hyperfine structure. This makes the spectroscopic investigation of AlF interesting on its own. Precise spectroscopic parameters for AlF are useful for the astrophysics community: AlF has been detected in sunspots, stellar atmospheres, circumstellar envelopes and proto-planetary nebulae [154, 155]; the isotopologue ^{26}AlF was the first radioactive molecule to be discovered in space [156]. In theoretical studies of AlF using *ab initio* quantum chemistry, radiative lifetimes, dipole moments and potential energy curves for its electronic states were determined [141, 142, 157, 158]. High-resolution spectroscopic information can serve as a benchmark for these studies.

The first band spectrum of AlF without rotational resolution was observed over 80 years ago [159]. The first estimate of the rotational constant in the electronic and vibrational ground state was obtained from emission spectra of the $A^1\Pi \rightarrow X^1\Sigma^+$ band by Rowlinson and Barrow in 1953 [160]. Further emission spectroscopy studies that were performed around the same time improved the vibrational constants and the rotational constant in the $A^1\Pi, v = 0$ state was determined for the first time [161–163]. The $a^3\Pi - X^1\Sigma^+$ transition was first observed in emission [164] and absorption [165] in 1976. The hyperfine structure in the triplet states was first analysed from the lineshapes of unblended rotational lines by Barrow *et al.* [144] in 1974 and Brown *et al.* [166] in 1978. Before the work presented in this thesis, spectroscopic information on AlF has been restricted to data from absorption and emission measurements on molecules at temperatures of several hundred K.

Any experiment on laser cooling and magneto-optical trapping of molecules is based on more precise information on the internal energy structure of the molecule.

The strongest cooling transitions of AlF need to be identified and the lifetimes of the excited states determined. The fine and hyperfine structures are of particular interest: the working principle of a magneto-optical trap (MOT) is based on exploiting the hyperfine structure and magnetic g -factors of a molecule. Rotational state mixing because of hyperfine interactions induces losses from the cooling cycle. Other loss channels involve higher vibrational levels in the $X^1\Sigma^+$ electronic ground state and decay on the spin-forbidden $A^1\Pi \rightarrow a^3\Pi$ transition. These need to be carefully investigated so that mitigation strategies can be devised. The $b^3\Sigma^+$ state is valuable for high-resolution spectroscopy in the triplet manifold and its interaction with the $A^1\Pi$ can open up doorways between the singlet and triplet manifolds.

1.4 Outline of this Thesis

In this thesis, I follow the chronological path of our experiments that study AlF as a promising candidate for laser cooling and trapping experiments. In the beginning, we used a pulsed supersonic expansion source to produce AlF molecules and applied various spectroscopic methods to characterise the energy levels in the molecule. In **chapter 2**, I present the first spectroscopic work that we performed on the $A^1\Pi \leftarrow X^1\Sigma^+$ and $a^3\Pi \leftarrow X^1\Sigma^+$ transitions in AlF. Because of its long lifetime, the hyperfine structure of the $a^3\Pi$ state was resolved at high precision. Additionally, losses from the spin-forbidden $A^1\Pi \rightarrow a^3\Pi$ transition were characterised. These experiments allowed us to determine the laser cooling scheme and set the stage for our future work on AlF. **Chapter 3** presents the continuation of the work on the triplet manifold, where the $b^3\Sigma^+$ state and its interactions with the $A^1\Pi$ state are investigated. These results give an insight into the coupling between the singlet and triplet manifolds of states.

During this time, optical cycling experiments were started in a newly-built cryogenic buffer gas beam machine. In **chapter 4**, I present the theoretical foundations of modelling of optical cycling on the $A^1\Pi \leftarrow X^1\Sigma^+$ transition and the results of calculations on the optical cycling experiments. I explain how dark states can hinder efficient optical cycling and why the hyperfine structure in the $X^1\Sigma^+$ state is crucial for laser cooling of AlF. Additionally, I present a supersonic beam excitation-delayed detection measurement of the lifetime of the $a^3\Pi$ state and the implications these results have for narrow-line cooling of aluminium monofluoride to sub-Doppler temperatures.

The chemistry of the formation of AlF in a cryogenic buffer gas source must be well understood to optimise molecule production. An extensive study on characterising and comparing the formation of the monofluorides AlF, CaF, MgF and YbF in a cryogenic buffer gas source is presented in **chapter 5**. This chapter demonstrates some of the advantages that AlF has compared to other molecules on the way to creating a high-density sample of ultracold molecules.

Finally, I present our work on hyperfine-resolved spectroscopy of MgF in **chapter 6**. This study originated in the source chemistry experiments of the previous chapter and established essential information on laser cooling of this

molecule. The influence of Λ -doubling on the hyperfine structure in the $A^2\Pi$ state is observed and discussed for the first time.

Chapter 2

Spectroscopic Characterisation of the $X^1\Sigma^+$, $A^1\Pi$ and $a^3\Pi$ States in AlF

2.1 Introduction

In the experiments presented in this chapter, we produce cold AlF molecules by laser ablation of aluminium in a supersonic expansion of SF₆ seeded in neon. In combination with narrow-band pulsed or cw lasers as well as radio-frequency and microwave sources, this enabled us to resolve the fine and hyperfine structure of the $X^1\Sigma^+$, $A^1\Pi$ and $a^3\Pi$ states and to investigate relevant loss channels to the $A^1\Pi \leftrightarrow X^1\Sigma^+$ optical cycle. The electronic states that are investigated in the experiments of this chapter are presented in figure 2.1. This is an essential step towards establishing AlF as a candidate for laser cooling and trapping experiments.

2.2 Experiment

Figure 2.2 shows the experimental setup. We use a molecular beam machine consisting of a source chamber, a differentially pumped preparation chamber, and two differentially pumped detection chambers. AlF molecules are produced by laser ablation of Al in a supersonic expansion of 2% SF₆ in Ne or Ar carrier gas (3 bar backing pressure). The fundamental (1064 nm) of a diode-pumped pulsed Nd:YAG laser (3 mJ/pulse, 10 ns pulse duration) is focused to a spot size of about 0.5 mm on a rotating Al rod. The ablated atoms react with SF₆ to form

This chapter is based on reference [167] – S. Truppe, *et al.*, “Spectroscopic characterization of aluminum monofluoride with relevance to laser cooling and trapping.” In *Physical Review A* **100**(5), (2019). doi:10.1103/PhysRevA.100.052513.

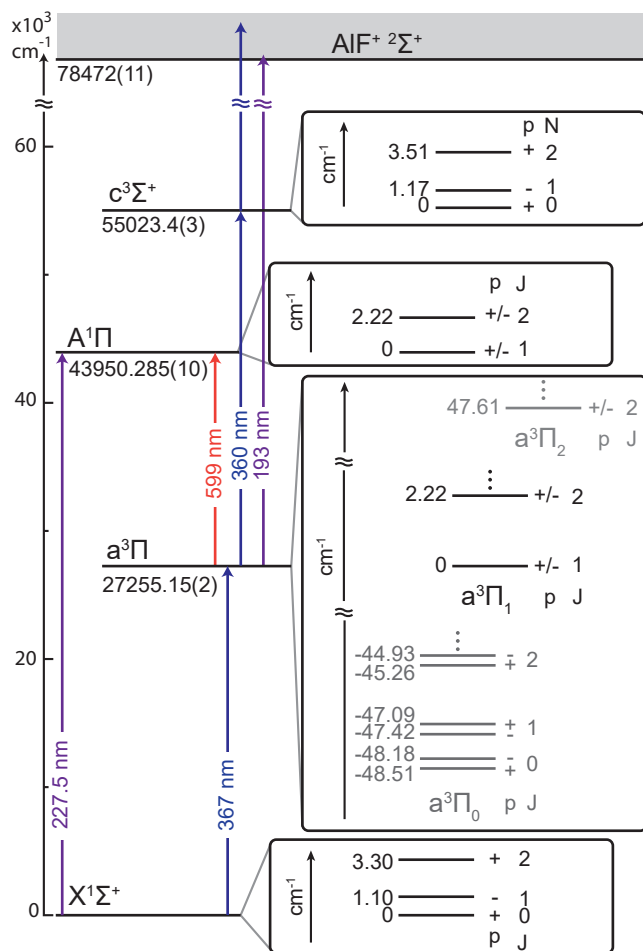


Figure 2.1: Energy-level diagram of the relevant electronic states of AlF using accurate spectroscopic data. The optical transitions used for excitation and ionisation are indicated. The lowest rotational levels in the electronic states are shown on an expanded scale. Λ -doubling is only resolved in the $a^3\Pi_0$ manifold.

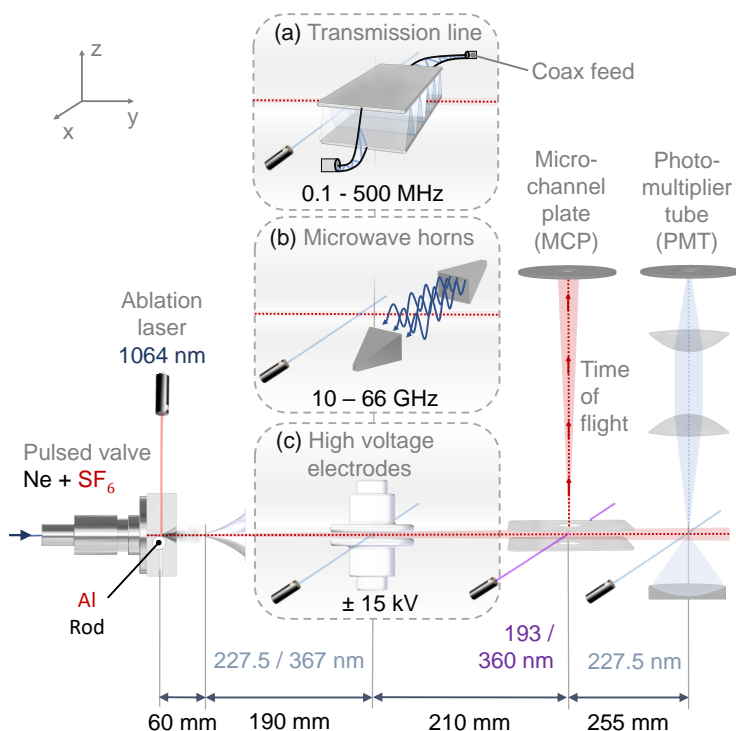


Figure 2.2: Schematic view of the experimental setup. A supersonic molecular beam passes through a skimmer into the preparation chamber, where the internal quantum state of the AIF molecules is prepared via optical pumping. The optical pumping can be done under field-free conditions or in a high electric field (c). Alternatively, radio-frequency or microwave transitions can be driven using a transmission line (a) or microwave horn antennae (b). In the first detection chamber, resonant excitation and ionisation, followed by mass-selective detection of the parent ions, can be performed. In the second detection chamber, laser-induced fluorescence of the molecules is imaged onto a photomultiplier tube.

vibrationally and rotationally excited AlF molecules in the $a^3\Pi$ state [164] that are efficiently quenched by collisions in the expansion. The broad thermal velocity distribution of the room-temperature gas is converted into a narrow distribution around a high forward velocity by the adiabatic expansion. The molecules then have a rotational temperature of about 10 K and a mean velocity of 780 m s^{-1} (in Ne carrier gas). We operate the experiment at a 10 Hz repetition rate.

About 60 mm after the laser ablation point, the molecular beam passes through a 5 mm skimmer to the preparation chamber that is centred at 190 mm after the skimmer; this serves to collimate the molecular beam and reduces the gas load to the science chambers. In the preparation chamber, the internal state of the molecules can be prepared by optical pumping or resonant excitation, driving transitions in either the $A^1\Pi \leftarrow X^1\Sigma^+$ or the $a^3\Pi \leftarrow X^1\Sigma^+$ band. For optical pumping on the $A^1\Pi \leftarrow X^1\Sigma^+$ band near 227.5 nm, we use a cw Ti:Sa laser that is frequency-doubled twice using resonant bow-tie cavities, to produce up to 200 mW of deep UV radiation (Solstis and ECD, manufactured by MSquared). For resonant excitation to selected rotational levels in the metastable $a^3\Pi$ state on the $a^3\Pi \leftarrow X^1\Sigma^+$ band near 367 nm, we either use a frequency-doubled pulsed dye laser (PDL, $\approx 10 \text{ mJ}$ per pulse, 5 ns pulse duration, about 0.1 cm^{-1} bandwidth), a frequency-doubled pulsed dye amplifier (PDA) seeded by a cw Ti:Sa laser ($\approx 10 \text{ mJ}$ per pulse, 5 ns pulse duration, about 250 MHz linewidth), or a frequency-doubled cw Ti:Sa laser (up to 1 W, sub-MHz linewidth). In both cases, the Ti:Sa is also an MSquared system. PDL and PDA (both by Sirah) are pumped by an injection seeded Nd:YAG laser (Spectra Physics Quanta Ray, 350 mJ, 5 ns). The molecules can be excited under field-free conditions or in static electric fields up to 150 kV cm^{-1} ; during operation, the pressure in this region is below 10^{-6} mbar.

Directly after optical pumping or resonant excitation with (near-) UV radiation, the molecules can be exposed to radio-frequency (rf) radiation to drive electric dipole allowed transitions between Λ -doublet or rotational levels. The rf and microwave (mw) radiation is generated by a synthesizer (Rohde & Schwarz SMR20) that is phase locked to a stable GPS frequency reference (Quartzlock). The output of the synthesizer is connected to a fast, high-isolation switch and coupled to free space. For frequencies in the range of 0.1-500 MHz, a transverse electromagnetic (TEM) transmission line is used, consisting of two square copper plates with a side length of 57 mm that are separated along z by 7.5 mm. The TEM mode propagates along x , orthogonal to the direction of the molecular beam. To produce radiation near 10 GHz, the output of the synthesizer is coupled to free space through a horn antenna. To produce radiation near 66 GHz, the output of the synthesizer is connected to a frequency quadrupler (Militech, AMC-15-RFH00) and a precision attenuator, and coupled to free space through a standard pyramidal gain horn. The quadrupler delivers microwave powers of up to 10 mW (10 dBm). The interaction time of the molecules with the radiation is set by the switch to values ranging from 40 to 80 μs . In the preparation chamber, the ambient magnetic field is compensated by three pairs of coils that are close to Helmholtz configuration. They reduce the magnetic field in the interaction region to 3 μT .

In the first detection chamber, centred 210 mm downstream from the centre of

the preparation chamber, molecules in the metastable $a^3\Pi$ state can be ionised with a single 193 nm photon from an ArF excimer laser (NEWEKS, ≈ 2 mJ, 10 ns pulse duration). The molecules in the $a^3\Pi$ state can also be state-selectively ionised via resonant excitation on the $c^3\Sigma^+ \leftarrow a^3\Pi$ transition, followed by single-photon ionisation from the $c^3\Sigma^+$ state using a frequency-doubled PDL near 360 nm. This is a (1+1)-resonance enhanced multi-photon ionisation (REMPI) process that enables parity selective detection of molecules in the $a^3\Pi$ state. A linear time-of-flight (TOF) setup extracts the ions perpendicular to the molecular beam and accelerates them to a microchannel plate (MCP) detector. The signal from the MCP detector is amplified and read into a computer on a fast (5 ns/channel) digitizer card. The TOF electrodes are grounded during ionisation and switched to high voltage to extract the ions. This ensures field-free excitation and ionisation in the detection region. The mass resolution $m/\Delta m$ of the TOF mass spectrometer is about 100, sufficient to unambiguously identify the AlF^+ parent cations at the mass of 46 amu. A grounded metal plate with a vertical slit is attached to the entrance of the TOF setup. This slit can be adjusted between 5 and 15 mm. This shields the ionisation region from stray electric fields and can reduce the residual Doppler broadening of the transitions in the $a^3\Pi \leftarrow X^1\Sigma^+$ band to about 30 MHz. The field-free REMPI ionisation is parity selective and permits detecting the transitions between Λ -doublet levels or rotational levels in the $a^3\Pi$ state against zero background. This optical-rf/mw-optical triple resonance ionisation detection scheme has large similarities to schemes that have been used in the past to characterise the metastable $a^3\Pi$ state of CO, for example by Freund and Klemperer [168].

In the second detection chamber, at $y = 715$ mm from the source, the AlF molecules can be detected via laser-induced fluorescence (LIF) on the $A^1\Pi, v = 0 - X^1\Sigma^+, v'' = 0$ band. The UV fluorescence is imaged onto a photomultiplier tube (Hamamatsu) and either the photoelectron pulses are counted (in the case of low fluorescence intensity) or the photocurrent is amplified and measured.

For the results presented in this chapter, the frequency of the PDL is measured with a wavelength meter (HighFinesse WS6-600) and recorded for each spectrum. It has an absolute accuracy of 600 MHz and is calibrated using a frequency-stabilised and calibrated HeNe laser. The resolution of the wavelength meter is 20 MHz. Long- and short-term drifts of the wavelength meter could be estimated by recording its reading over time. The frequency of the Ti:Sa fundamental used for direct spectroscopy or to seed the PDA was also determined by the same wavelength meter. Thermal drifts of the cw lasers can be removed by locking to the calibrated HeNe laser using a short scanning transfer cavity. This cavity can also be used to scan the laser in a reproducible way by changing the lock point. Finally, we linearise the frequency scan of the cw lasers by recording the transmission of a long, temperature stabilised confocal Fabry-Pérot cavity with a free spectral range of 149.9 MHz.

2.3 Molecular Hamiltonian

To describe the energy-level structure of any molecule, all relevant interactions need to be included in the molecular Hamiltonian [169–175]. Its general form can be written as the sum of the electronic and vibrational part H_{ev} , the rotational part H_{rot} , the fine-structure part H_{fs} , and the hyperfine structure part H_{hfs} :

$$H = H_{ev} + H_{rot} + H_{fs} + H_{hfs}. \quad (2.1)$$

The electronic and vibrational term of the Hamiltonian determines the vibrational energy levels E_v for a given electronic state and can be approximated by

$$E_v = T_e + \hbar\omega_e(v + 1/2) - \hbar\omega_e x_e(v + 1/2)^2 + \dots, \quad (2.2)$$

where T_e is the electronic term energy,* ω_e is the vibrational energy and $\omega_e x_e$ is its first-order correction term.

The rotational Hamiltonian is written as

$$H_{rot} = A_v(\mathbf{L} \cdot \mathbf{S}) + B_v(\mathbf{J} - \mathbf{L} - \mathbf{S})^2 - D_v(\mathbf{J} - \mathbf{L} - \mathbf{S})^4, \quad (2.3)$$

where the first term describes the electron spin-orbit coupling with its constant A_v . This interaction splits electronic states with nonzero values of L and S into Ω manifolds. Here, $\Omega = \Lambda + \Sigma$, where Λ and Σ are the projections of L and S on the internuclear axis. The second term describes the molecular rotation kinetic energy with the rotational constant $B_v = B_e + \alpha_e(v + 1/2)$, where B_e is the rotational constant at equilibrium and α_e is the rotation-vibration constant. The last term describes the centrifugal distortion with the constant D_v . The different angular momenta present in the molecule are the following: \mathbf{J} is the total angular momentum of the molecule excluding hyperfine interaction, \mathbf{S} is the total electron spin angular momentum and \mathbf{L} is the total orbital angular momentum of the electron motion. The difference between the angular momentum vector \mathbf{J} and $(\mathbf{L} + \mathbf{S})$ is the end-over-end rotation of the molecule, often expressed as $\mathbf{R} = \mathbf{J} - \mathbf{L} - \mathbf{S}$.

The fine-structure part of the Hamiltonian can be expressed as [170, 171]

$$H_{fs} = \gamma(\mathbf{N} \cdot \mathbf{S}) + 2\lambda(S_Z^2 - \frac{1}{3}\mathbf{S}^2) + H_\Lambda, \quad (2.4)$$

where the first term describes the interaction of the electron spin \mathbf{S} with the angular momentum $\mathbf{N} = \mathbf{J} - \mathbf{S}$, using the constant γ . We omit the subscript v for the vibrational level for the fine and hyperfine interaction parameters. The second term describes the electron spin-spin interaction (using the constant λ), resulting from the spin-orbit interaction between a given and other electronic states. S_Z is the Z -component of the electron spin in the molecule-fixed frame. It appears as a second-order perturbation to the spin-orbit interaction. Both of these terms affect the Ω sublevels but do not affect the Λ splitting of the energy levels. The term

*The minimum of the potential for this electronic state

H_Λ can be written as

$$H_\Lambda = \frac{1}{2} \left\{ -o(\Lambda_+^2 S_-^2 + \Lambda_-^2 S_+^2) + p(\Lambda_+^2 S_- N_- + \Lambda_-^2 S_+ N_+) - q(\Lambda_+^2 N_-^2 + \Lambda_-^2 N_+^2) \right\}. \quad (2.5)$$

This describes the second-order perturbation with respect to the spin-orbit interaction that causes the Λ splitting. The two different orientations (senses of rotation) of the orbital angular momentum for states with $\Lambda > 0$ make up two states with different parities that are non-degenerate. The + and - subscripts designate the appropriate axial components of the corresponding vector. The energy splitting originates from mixing with Σ electronic states of the same spin multiplicity via spin-orbit coupling and the rotational electronic Coriolis interaction [175]. The Λ -doubling splitting increases with J .

The hyperfine structure part of the Hamiltonian, H_{hfs} , describes the interaction of the nuclear spins with the electronic and rotational degrees of freedom. The strongest hyperfine interactions are magnetic interactions between nuclear spins and the degrees of freedom of the electron. They are discussed in detail by Frosch and Foley [169]. For each nucleus, there are four parameters, a, b, c, d that describe its interaction with the electrons. Here, instead of using the parameters b and c , the Fermi contact parameter $b_F = b + \frac{1}{3}c$ and c are used, as by Brown *et al.* [166].

$$H_{\text{hfs}} = aI_Z L_Z + b_F \mathbf{I} \cdot \mathbf{S} + \frac{1}{3}c(3I_Z S_Z - \mathbf{I} \cdot \mathbf{S}) - \frac{1}{2}d(S_+ I_+ + S_- I_-). \quad (2.6)$$

Here, $\mathbf{I} = \mathbf{I}_{\text{Al}} + \mathbf{I}_{\text{F}}$ is the vectorial sum of the nuclear spins of aluminium and fluorine, respectively. The interaction of the electric quadrupole moment Q of the Al nucleus with the electric field gradient at the nucleus is determined by the two parameters $eq_0 Q$ and $eq_2 Q$ [166], where q_0 is the electric field gradient in the direction of the internuclear axis and q_2 is the field gradient in the perpendicular direction.

The interaction of the nuclear magnetic moments with each other and the interaction between the pure rotational angular momentum of the molecule and the nuclear magnetic moments are a factor m_p/m_e smaller than the electronic contribution to the hyperfine structure, where m_p and m_e are the proton and electron masses. These interactions are therefore at least three orders of magnitude weaker than the electron hyperfine interactions. The parameters used to describe the nuclear spin-rotation interaction between $\Lambda' = \Lambda$ and $\Lambda' = -\Lambda$ basis wave functions are C_I and C_I^+ for each of the nuclei, respectively. The parameter D_1 is used to describe the spin-spin interaction between the nuclei [176, 177].

2.4 Characterisation of the $a^3\Pi$ State

2.4.1 The $a^3\Pi, v' = 0 \leftarrow X^1\Sigma^+, v'' = 0$ Band

The $a^3\Pi, v' = 0 \leftarrow X^1\Sigma^+, v'' = 0$ band is spin-forbidden and, therefore, weak. To determine the overall rotational structure of this band, we use pulsed excitation with 367 nm light. The molecules in the metastable state are then ionised with

a spatially overlapping beam of a 193 nm ArF excimer laser, whose pulse is delayed relative to the dye laser pulse by about 50 ns. Both laser beams have a diameter of approximately 3 mm. The ionisation potential (IP) of AlF was determined by Dearden *et al.* from extrapolation of a series of Rydberg states to be 9.729 ± 0.001 eV [178]. Thus, an AlF molecule in the $a^3\Pi$ state can be ionised with a single UV photon from the ArF excimer at 6.4–6.42 eV. The ions are then mass-selectively detected in our time of flight mass spectrometer (TOF-MS) setup. When the molecules are ionised with a single photon of the ArF excimer laser, all rotational levels in the $a^3\Pi$ state are detected with the same efficiency.

The transitions to the three Ω -manifolds in the $a^3\Pi$ state are labelled with an index $\mathcal{F} = 1, 2, 3$ for the transitions to $\Omega = 0, 1, 2$, respectively, e.g. “ R_1 ” for a transition to $\Omega = 0$ with $\Delta J = +1$.

Figure 2.3 shows overview spectra of the $a^3\Pi_0, v' = 0 \leftarrow X^1\Sigma^+, v'' = 0$ and $a^3\Pi_1, v' = 0 \leftarrow X^1\Sigma^+, v'' = 0$ bands. The spin-forbidden transitions obtain intensity from spin-orbit mixing with singlet states. The $a^3\Pi_0, v' = 0 \leftarrow X^1\Sigma^+, v'' = 0$ band is shown in figure 2.3a. The rotational spectrum misses a Q-branch, it therefore resembles a $^1\Sigma^+ \leftarrow ^1\Sigma^+$ band. For transitions to be allowed, the spin angular momentum of the incoming photon must be conserved in the transition. For a $^1\Sigma^+ \leftarrow ^1\Sigma^+$ transition, there are no electron spin or electron orbital angular momenta involved, therefore the photon spin must be absorbed into the total angular momentum J — a $J'' = J'$ transition is therefore impossible. The $a^3\Pi_0, v' = 0 \leftarrow X^1\Sigma^+, v'' = 0$ band becomes weakly allowed due to mixing of the $a^3\Pi$ state with $^1\Sigma^+$ states. The spectrum of the $a^3\Pi_1, v' = 0 \leftarrow X^1\Sigma^+, v'' = 0$ band is shown in figure 2.3b. This band is about a factor 20 stronger than the $a^3\Pi_0, v' = 0 \leftarrow X^1\Sigma^+, v'' = 0$ band and is shifted 50 cm^{-1} to higher energy. The relative intensities in the experimental spectrum are consistent with a rotational temperature of 10 K. The $a^3\Pi_1, v' = 0 \leftarrow X^1\Sigma^+, v'' = 0$ band gets intensity from a small admixture of $^1\Pi$ character to the $a^3\Pi_1$ state and the spectrum is equivalent to that of a $^1\Pi \leftarrow ^1\Sigma$ transition. This is similar to the Cameron band of CO. The $a^3\Pi_0 \leftarrow X^1\Sigma^+, v'' = 0$ band of CO, however, obtains its intensity via the $\Omega = 1$ character in the $\Omega = 0$ wave functions. This effect is much less pronounced in AlF because the ratio of spin-orbit coupling constant A to rotational constant B in the $a^3\Pi$ state is four times larger than in CO.

Using the excitation and detection scheme described above, the $a^3\Pi_2, v' = 0 \leftarrow X^1\Sigma^+, v'' = 0$ band was not found because it is almost three orders of magnitude weaker than the $a^3\Pi_1, v' = 0 \leftarrow X^1\Sigma^+, v'' = 0$ band. Moreover, there are also $a^3\Pi_1, v' = 2 \leftarrow X^1\Sigma^+, v'' = 2$ hot bands in the same spectral region.

The excitation spectra show a constant background signal due to the ionisation of metastable AlF molecules that are produced in the source and are still present when the molecular beam reaches the detector. These triplet molecules mainly reside in the $a^3\Pi_0$ manifold because the molecules are cooled in the expansion and as the radiative lifetime of the rotational levels in this manifold is longer. The $J = 1$ level in the $a^3\Pi_1, v = 0$ state has the shortest lifetime. A precise measurement of the radiative lifetimes is presented in section 4.5.2 of this thesis.

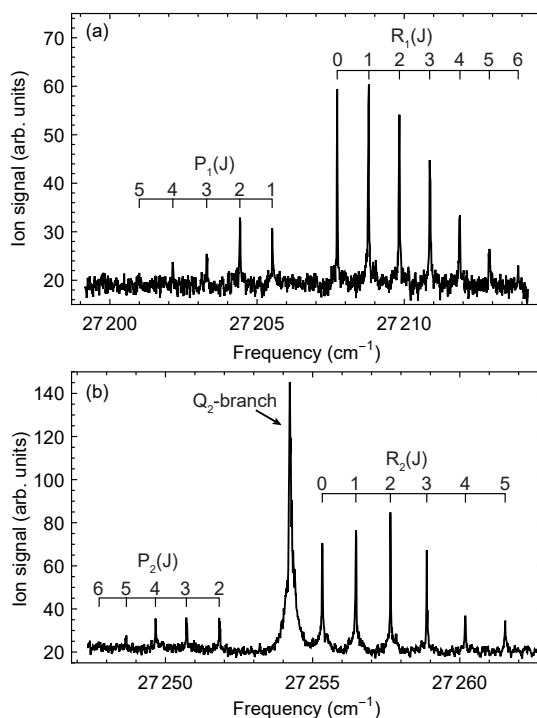


Figure 2.3: Excitation spectra of the $a^3\Pi_0, v' = 0 \leftarrow X^1\Sigma^+, v'' = 0$ (a) and $a^3\Pi_1, v' = 0 \leftarrow X^1\Sigma^+, v'' = 0$ (b) bands of AlF. After excitation with a pulsed dye laser, the molecules are ionised with a broadband ArF excimer laser. The pulse energy of the excitation laser used to record spectrum (a) is ten times higher than the energy used to record spectrum (b).

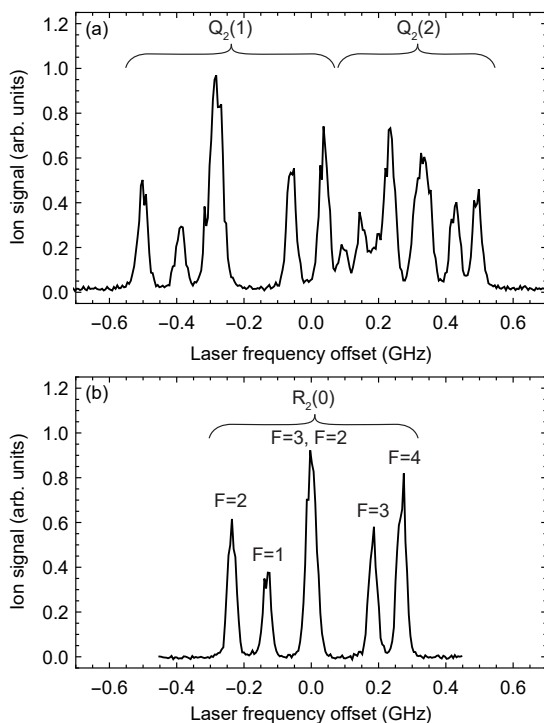


Figure 2.4: (a) High-resolution excitation spectrum of the $Q_2(1)$ and $Q_2(2)$ transitions of the $a^3\Pi_1, v' = 0 \leftarrow X^1\Sigma^+, v'' = 0$ band, using cw laser excitation and (1+1)-REMPI detection via the Q branch of the $c^3\Sigma^+, v = 0 \leftarrow a^3\Pi_1, v = 0$ band around 360 nm. (b) High-resolution excitation spectrum of the $R_2(0)$ line of the $a^3\Pi_1, v' = 0 \leftarrow X^1\Sigma^+, v'' = 0$ band.

Weak rotational lines of the $a^3\Pi_\Omega, v' = 0 \leftarrow X^1\Sigma^+, v'' = 0$ bands can be excited using the frequency-doubled PDA. The PDA linewidth is about a factor 10 smaller than the PDL linewidth, thus increasing the peak intensity by approximately the same factor. The excited molecules can then be state-selectively ionised from the $a^3\Pi$ state via the $c^3\Sigma^+$ state, using the frequency-doubled PDL. With this excitation and ionisation detection scheme, we can observe even the weak low- J transitions to the $\Omega = 2$ manifold.

The AIF molecules can also be excited on the spin-forbidden transition using a frequency-doubled cw TI:Sa laser. This laser is used to record the hyperfine resolved excitation spectra of the two lowest rotational transitions in the Q_2 branch as well as on the $R_2(0)$ line, shown in figure 2.4. We can saturate the rotational transitions of the $a^3\Pi_1, v' = 0 \leftarrow X^1\Sigma^+, v'' = 0$ band with about 300 mW of cw radiation at 367 nm with a laser beam diameter of 2.0 mm. With about 1 W of cw radiation, we can also detect molecules that have been excited on the weak $P_1(1)$ line.

2.4.2 Hyperfine Measurements in the $a^3\Pi, v = 0$ State

To determine the hyperfine structure in the metastable state with higher accuracy, we measure rf transitions between Λ -doublet components. The molecules are prepared in the $J = 1$ level of the $a^3\Pi_1, v = 0$ state using excitation with the PDA on the $R_2(0)$ line. The molecules are now distributed across the negative parity components of the $J = 1$ level, i.e. in the $J = 1, e$ levels [179].[†] We then pulse the rf radiation on for a short period of 40-80 μs at the time when the molecular pulse is inside the rf transmission line. If the rf is tuned to a resonance frequency, the population is transferred to a level with positive parity. Provided the electric fields inside the molecular beam machine are kept sufficiently low, parity remains well defined and we can use parity-selective detection to probe the transferred population. In the ionisation detection chamber, the AIF molecules are resonantly excited from the metastable $a^3\Pi$ to the $c^3\Sigma^+, v = 0$ state and are subsequently ionised by the same laser. We choose to address a rotational level with odd rotational quantum number N , i.e. with negative parity. Thus, only molecules in a positive parity level in the $a^3\Pi$ can be detected. In this case, we ionise the molecules via the $N = 3$ level to record the rf spectra background free. The TOF extraction plates are switched to high voltage only after ionisation to prevent parity mixing.

In the $J = 1$ level, there are 12 hyperfine components in total with 26 possible, electric-dipole allowed transitions between them. We determine the transition frequencies by recording the ion signal originating from the positive parity components as a function of the rf frequency. The strengths of these transitions vary by over four orders of magnitude, and the rf power coupled into the transmission line is adjusted accordingly. Transitions between levels with small differential g_F factors have the expected Rabi line shape (see equation (4.20)).[‡] A fit to the data determines the line centre with an accuracy of well below 1 kHz. This is shown in figure 2.5 for the transition around 21.8264 MHz. A residual magnetic field in the interaction region broadens the line, which can cause a systematic frequency shift. We model this effect, place an upper bound to the frequency shift, and add a magnetic field related uncertainty to the error budget. Transitions with a large differential g_F factor appear considerably broader, and with a Gaussian line shape. In this case, a systematic uncertainty associated with the unknown line shape is added to the statistical uncertainty obtained from the fit. For some of the weaker transitions, when high rf powers are needed, ac Stark shifts of several kHz are observed.[§] To find the transition frequency of these lines, we determine the line centre at different rf powers and extrapolate to zero power. The transition frequencies with their statistical and systematic uncertainties are given in appendix A.

[†]The e and f labelling is a very convenient alternative convention for parity labels. For molecules with integral J values, the convention states that levels with parity $+(-1)^J$ are called e levels and levels with parity $-(-1)^J$ are called f levels. The parity selection rules for electric dipole transitions, written in terms of e and f labels, are $e \leftrightarrow f$ if $\Delta J = 0$ and $e \leftrightarrow e$ and $f \leftrightarrow f$ for $\Delta J = \pm 1$ [179].

[‡]In cases where spontaneous decay is negligible, the spectroscopic lines have this Rabi line-shape and not a Lorentzian lineshape.

[§]Similarly to the dc Stark effect, an oscillating electric field shifts the energies of hyperfine levels — this is called ac Stark effect [20].

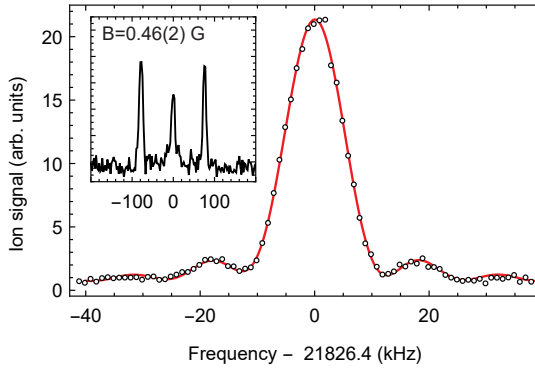


Figure 2.5: Observed $F = 4, + \leftarrow F = 4, -$ transition in the $J = 1$ level of the $a^3\Pi_1, v' = 0$ state. The line shows a fit to the data using the Rabi line shape, with the background, amplitude and central frequency as free parameters. The inset shows the Zeeman splitting of the line when the magnetic field compensation coils along x and z are turned off.

All 26 transitions are observed and we uniquely assign the F hyperfine quantum numbers using angular momentum selection rules. We verify this assignment by applying a static magnetic field in the preparation chamber along x and/or y to measure the Zeeman splitting of some of these transitions. The inset of figure 2.5 shows the Zeeman splitting of the $F = 4, + \leftarrow F = 4, -$ transition when the compensation coils along x and z are turned off. The splitting in three relatively narrow $\Delta M_F = 0, \pm 1$ (M_F designates the Zeeman sublevels of the hyperfine level F) components indicates that this transition connects two F levels with almost identical g_F factors. The ambient magnetic field has a strength of approximately $46 \pm 2 \mu\text{T}$ with an inclination of 67° between the lines of magnetic flux and the (x, y) plane. The $\Delta M_F = \pm 1$ lines are split by ± 77 kHz which gives a magnetic g_F factor of 0.115 ± 0.005 , consistent with the theoretically predicted value of 0.113 (see appendix A). The experimentally determined hyperfine energy-level diagram of the $J = 1$ level, together with all the observed transitions, is shown in figure 2.6. The level diagram shows six pairs of opposite parity F levels. To identify the hyperfine components, it is useful to introduce the intermediate quantum number F_1 that labels the vectorial coupling of the rotational angular momentum \mathbf{J} with the spin of the aluminium nucleus \mathbf{I}_{Al} ($5/2$): $\mathbf{F}_1 = \mathbf{I}_{\text{Al}} + \mathbf{J}$. The spin of the fluorine nucleus \mathbf{I}_{F} ($1/2$) is then vectorially added to \mathbf{F}_1 to obtain the final vector $\mathbf{F} = \mathbf{F}_1 + \mathbf{I}_{\text{F}}$. This procedure allows to differentiate between the influences of the two nuclear spins on the hyperfine structure. In figure 2.6, both F and F_1 quantum numbers are given, showing the triplet structure arising from the nuclear spin of ^{27}Al . The splitting caused by the ^{19}F nucleus is of the same order of magnitude.

We fit the eigenvalues of the Hamiltonian to the measured hyperfine energy levels of the $J = 1$ level to determine preliminary values for the spectroscopic parameters. We then use these parameters to predict the hyperfine levels, transition frequencies and transition dipole moments in the $J = 2$ and $J = 3$ level

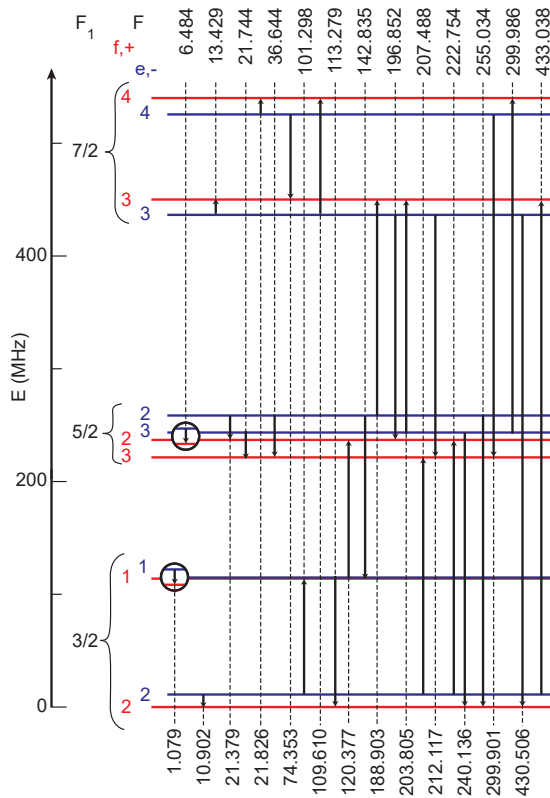


Figure 2.6: Hyperfine energy level diagram of the $J = 1$ level in the $a^3\Pi_1, v = 0$ state, All 26 allowed transitions are shown with their transition frequencies in MHz. To aid the identification of the levels, the intermediate quantum number F_1 is given as well.

of the $\Omega = 1$ manifold. The experimentally determined transition frequencies are typically within several MHz of the predicted frequencies. We use the measured values to improve the parameters in the fit or, if necessary, we include higher-order terms. This iterative procedure is followed for the $J = 7$ level in the $\Omega = 1$ manifold as well as for the $J = 4$ and $J = 7$ levels in the $\Omega = 2$ manifold. All relevant hyperfine parameters can be determined this way. To accurately determine the Λ -doubling parameters, we measure the hyperfine resolved Λ -doubling transitions in the $J = 0, 1$, and 2 levels of the $\Omega = 0$ manifold around 10 GHz. To accurately determine the rotational splitting in the $a^3\Pi, v = 0$ state, we measure several hyperfine resolved lines of the $J = 2 \leftarrow 1$ transitions in both the $\Omega = 1$ and $\Omega = 0$ manifolds around 66 GHz. Compared to the rf transmission line, the electric field distribution of the microwave radiation in free space is not very well defined which affects the observed line shape. All the measured frequencies of the rf and microwave transitions, together with their experimental uncertainties, as well as the calculated frequencies with their assignments and calculated intensities are given in appendix A.

The spin-orbit parameter A and its second-order correction λ cannot be determined accurately from the rf and microwave measurements. We therefore measure the centre frequencies of selected rotational transitions from the $X^1\Sigma^+, v = 0$ state to each of the Ω manifolds in the $a^3\Pi, v' = 0$ state with our wavelength meter. P and R lines reach e levels and Q lines reach f levels. In particular, we choose the $P_1(1)$, the $R_2(8)$, and the $Q_3(9)$ lines because they reach levels in the metastable state for which the total span of the hyperfine structure is smaller than 40 MHz. Therefore, they appear as single lines and the resolution is mainly limited by the bandwidth of the narrow-band PDA. The $P_1(1)$ transition appears 1 762 797 \pm 100 MHz lower and the $Q_3(9)$ transition appears 1 098 984 \pm 120 MHz higher in frequency than the $R_2(8)$ transition. The uncertainty in the relative frequencies is determined by tracking the wavelength of a temperature stabilised helium neon laser coupled to the same wavelength meter. Using the known rotational energies in the electronic ground state, this gives values of $A = 47.395 \pm 0.007 \text{ cm}^{-1}$ and $\lambda = 0.0887 \pm 0.0011 \text{ cm}^{-1}$. These values agree with a fit to the rotationally resolved absorption spectra for the $a^3\Pi, v' = 0 \leftarrow X^1\Sigma^+, v'' = 0$ band measured by Kopp, Lindgren, and Malmberg [165]. From their spectra, we could also determine the energy difference between the gravity centres of the $a^3\Pi_0, v = 0, J = 1$ level and the $X^1\Sigma^+, v = 0, J = 0$ level to 27255.14 \pm 0.01 cm^{-1} . A more precise measurement of A and λ is presented in section 3.5 of this thesis, where we use a narrow-band cw dye laser to drive $b^3\Sigma^+, v = 0 \leftarrow a^3\Pi_0, v = 0$ transitions to hyperfine-resolved levels in the $b^3\Sigma^+$ state to measure the spacing of the spin-orbit manifolds.

With a fit using the second-order gradient technique, we determine the hyperfine structure parameters, the parameters describing the Λ -doubling, the spin-rotation interaction parameter γ , and the rotational constant with high accuracy, and the results are summarised in table 2.1. For each of the parameters, the standard deviation (SD) as well as the product of the standard deviation with the square-root of the quality factor Q is given. The latter is a better measure for the accuracy with which each parameter is determined by a fit whose parameters are correlated [180]. In other words, it gives the range in which a change of one

parameter can be compensated by a change in another parameter without altering the outcome of the calculation.

Table 2.1: Spectroscopic parameters of the $a^3\Pi, v = 0$ state. Rotational constant B_0 , fine-structure constant γ , Λ -doubling parameters and hyperfine structure parameters for the $a^3\Pi, v=0$ state as obtained from the best fit to the experimental data together with their standard deviation (SD) and the product of SD and \sqrt{Q} (all values in MHz). For the Λ -doubling parameter o and for four hyperfine structure parameters, the centrifugal distortion term has been included. These terms are labelled with a superscript (R) and are given directly underneath the parameter in the Table. The term $eq_0Q_{LS}(Al)$ describes the spin-orbit correction to $eq_0Q(Al)$. In the fit, the parameters $A_0 = 47.395 \text{ cm}^{-1}$, $\lambda = 0.0887 \text{ cm}^{-1}$ and $D_0 = 0.0314 \text{ MHz}$ have been kept fixed to the best known experimental values. The centrifugal distortion term of the spin-orbit splitting, A_D , as well as the parameter for the spin-spin interaction between the nuclei, D_1 , are fixed to the calculated values of $A_D = 0.1 \text{ MHz}$ and $D_1 = 0.0066 \text{ MHz}$.

Parameter	Value (MHz)	SD	SD $\cdot\sqrt{Q}$
B_0	16634.7458	0.0010	0.0024
γ	-7.6089	0.0526	0.1369
o	4968.3175	0.0510	2.9243
$o^{(R)}$	-0.0061	0.0012	0.0097
p	-24.3462	0.0510	4.7224
q	-1.8176	0.0023	0.1798
$a(Al)$	199.1620	0.0353	0.4525
$b_F(Al)$	1247.9697	0.2783	9.2715
$b_F^{(R)}(Al)$	0.0222	0.0045	0.1638
$c(Al)$	-21.0093	0.4124	13.7410
$c^{(R)}(Al)$	-0.0568	0.0114	0.5826
$d(Al)$	121.9077	0.0155	0.0935
$eq_0Q(Al)$	-12.9921	0.0159	0.0286
$eq_0Q_{LS}(Al)$	-0.0392	0.0042	0.0097
$eq_2Q(Al)$	51.1137	0.0054	0.0062
$C_I(Al)$	-0.0569	0.0169	1.3288
$C'_I(Al)$	-0.0115	0.0007	0.0043
$a(F)$	207.1350	0.0109	0.0156
$a^{(R)}(F)$	-0.0688	0.0038	0.0338
$b_F(F)$	169.6289	0.1605	0.5853
$b_F^{(R)}(F)$	-0.0346	0.0019	0.0152
$c(F)$	122.8043	0.2596	1.3787
$d(F)$	119.2769	0.0868	0.4241
$C'_I(F)$	0.0346	0.0041	0.0202

To reach a standard deviation of the fit comparable with the accuracy of the rf and mw measurements of a few kHz, we first include centrifugal distortion terms to each Λ -doubling and hyperfine parameter. We must then find out which ones

are necessary and do improve the fit. We analyse the correlations between the parameters and exclude them one by one, testing whether the standard deviation of the fit increases significantly. This procedure results in five remaining centrifugal distortion terms that are listed in table 2.1, labelled with a superscript (R). If any one of these is set to zero, the standard deviation of the fit increases significantly. We also find that it is straightforward to achieve a good fit to all measured hyperfine levels within one Ω -manifold, but that the $e_{q0}Q(\text{Al})$ parameter needs a correction depending on the Ω -manifold, which we name $e_{q0}Q_{LS}(\text{Al})$.

With this precise knowledge of the hyperfine structure in the $a^3\Pi$ state, the hyperfine parameters in the $X^1\Sigma^+$ ground state were also determined by mw spectroscopy [167]. To maximise the signal-to-noise ratio, the population in the $J'' = 1$ level is depleted using optical pumping on the R(1) line of the $A^1\Pi, v = 0 \leftarrow X^1\Sigma^+, v'' = 0$ band. Transitions from hyperfine states in the $J'' = 2$ level to hyperfine states in the $J'' = 1$ level were driven with microwave radiation. The molecules in the $J'' = 1$ level were then excited to the $a^3\Pi$ state with a 367 nm cw laser and state-selectively ionised via the $c^3\Sigma^+$ state.

2.5 Hyperfine Measurements in the $A^1\Pi$ State

The accuracy with which the hyperfine structure in the $A^1\Pi$ state can be determined from $A^1\Pi \leftarrow X^1\Sigma^+$ spectra is limited by the short radiative lifetime of the excited state. The hyperfine structure can only be partly resolved for the lowest rotational levels in the $A^1\Pi$ state. This can be seen in the Q-branch spectrum shown in figure 2.7a. Only the hyperfine structure of the Q(1) line at 227.536 nm is resolved, it vanishes in the broadening for all higher Q lines.

The transverse spread of the molecular beam was reduced by using a 2 mm skimmer and a 3 mm vertical slit in front of the LIF detection zone. Additionally, the beam speed was reduced by using Ar as carrier gas. An upper limit to the Doppler contribution of 12 MHz was determined by recording several hyperfine resolved rotational lines of the $A^2\Sigma^+, v' = 0 \leftarrow X^2\Pi_{1/2}, v'' = 0$ band of NO. The lifetime of the $A^2\Sigma^+$ state of NO is about 100 times longer than of the $A^1\Pi$ state in AIF.

The R(0) line shown in figure 2.7b appears isolated and can be used for fitting. Hyperfine quantum numbers were assigned by comparison to the $R_2(0)$ line shown in figure 2.4b.

From the information obtained from the lifetime-broadened spectra, the rotational constant B_0 , the Λ -doubling parameter q and the two hyperfine parameters $a(\text{Al})$ and $a(\text{F})$ could be determined. The Lorentzian contribution to the Voigt profile has a full width at half maximum of 84 ± 1 MHz. The equivalent radiative lifetime of the $A^1\Pi, v = 0$ state is 1.90 ± 0.03 ns, in good agreement with the calculated value of 1.89 ns [141].

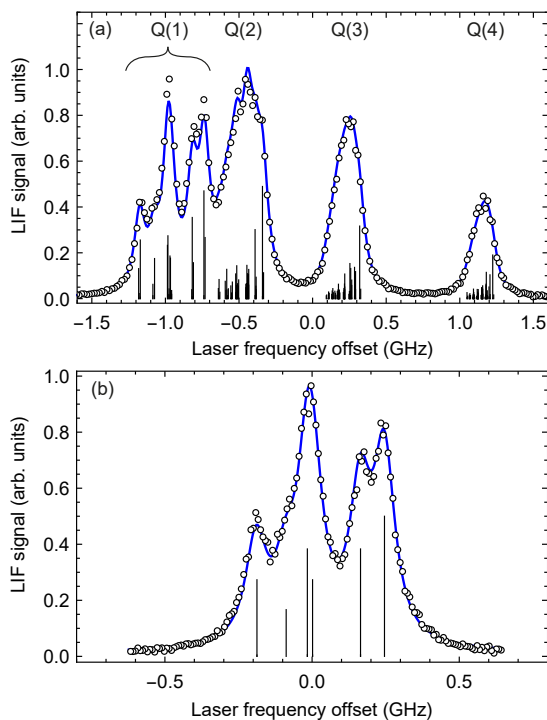


Figure 2.7: Observed laser-induced fluorescence excitation spectra of the Q(1), Q(2), Q(3), and Q(4) lines (a) and of the R(0) line (b) of the $A^1\Pi, v = 0 \leftarrow X^1\Sigma^+, v'' = 0$ band of AlF, together with the simulated spectra (solid curves). The frequency scale in panel (b) is a factor 2 smaller than in panel (a). The sticks underneath the spectrum show the position of the individual hyperfine components of the rotational lines and their intensities.

2.6 The $A^1\Pi, v' = 0 \rightarrow a^3\Pi, v'' = 0$ Transition: A Possible Loss Channel?

2.6.1 Motivation

Any Q-line of the $A^1\Pi \leftarrow X^1\Sigma^+$ transition is rotationally closed. Unfortunately, there are other loss channels that can be detrimental to optical cycling and therefore hinder efficient laser cooling. These need to be identified and quantified and strategies to overcome them need to be devised.

The hyperfine interaction mixes rotational states in the $A^1\Pi$ state, this could in theory lead to decay to dark rotational states in the ground state. The calculated branching ratios to higher rotational levels in the ground electronic state are in the 10^{-6} range.

One important loss channel is to higher vibrational states in the ground state because the Franck-Condon-Factor (FCF) of the cycling transition is not exactly 1. From a thorough investigation of fluorescence on the 0-1 band after excitation on the 0-0 band of the $A^1\Pi \leftarrow X^1\Sigma^+$ transition, the FCF of the 0-0 band was determined to be 0.996, using an expanded Morse oscillator fit.

On top of a filled σ -orbital, AlF has two π electrons, contrary to alkaline earth monofluorides (CaF, SrF, BaF) or YbF, that have only one π electron. The π^1 configuration results in spin-doublet terms, while the π^2 configuration can result in both spin-singlet and spin-triplet terms for AlF. Therefore, for AlF, a triplet manifold of states exists; furthermore, the $a^3\Pi$ state lies between the $X^1\Sigma^+$ and $A^1\Pi$ states. A significant part of the molecules could decay into the metastable $a^3\Pi$ state and thereby be lost for the cooling cycle. This loss channel is not present in the alkaline earth monofluorides and YbF.[¶] It is important to determine the strength of this transition which is a measure for the fraction of molecules that are lost from the cooling cycle.

2.6.2 Spectra

As a first step, we measure hyperfine-resolved spectra of two lines of the $A^1\Pi, v' = 0 \leftarrow a^3\Pi, v'' = 0$ transition. The theoretical positions of these lines are calculated from the spectroscopic information that was already obtained. We expect very weak transitions in this case, and aim at the strongest transitions in order to achieve meaningful signal at the laser powers available. The two candidate lines with the highest predicted strength both originate from the $\Omega = 0$ manifold of the $a^3\Pi$ state; they are the $A^1\Pi, v = 0, J = 1, - \leftarrow a^3\Pi_0, v' = 0, J' = 0, +$ ($R_1(0)$) and the $A^1\Pi, v = 0, J = 1, + \leftarrow a^3\Pi_0, v' = 0, J' = 1, -$ ($Q_1(1)$) lines. These transitions address different parity components in the same rotational level in the $A^1\Pi$ state. In order to be able to drive molecules from the $a^3\Pi$ state to the $A^1\Pi$ state, they first need to be excited from the ground electronic state to the metastable state.

[¶]For YbF, however, a recent theoretical study points out that inner-shell excitation of a 4f electron of Yb will result in an electronic state within the main cooling transition. This constitutes an important loss channel with a branching ratio of about 5×10^{-4} [181].

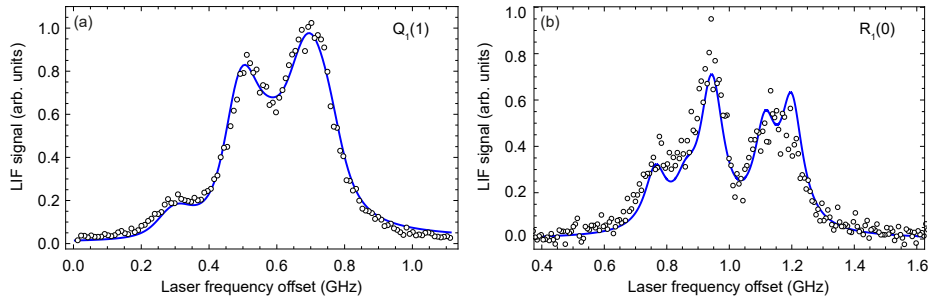


Figure 2.8: Measured LIF spectra of the $A^1\Pi, v = 0, J = 1, + \leftarrow a^3\Pi_0, v' = 0, J' = 1, -$ ($Q_1(1)$, a) and the $A^1\Pi, v = 0, J = 1, - \leftarrow a^3\Pi_0, v' = 0, J' = 0, +$ ($R_1(0)$, b) transitions near 597 nm. Black circles are the experimental data, the blue solid line is a simulated spectrum. The hyperfine structure of the $R_1(0)$ line is almost identical to the spectrum shown in figure 2.7b, since both transitions have the $A^1\Pi, v = 0, J = 1, -$ level as final state.

This is achieved via the $P_1(1)$ and $R_1(0)$ lines of the $a^3\Pi \leftarrow X^1\Sigma$ transition, respectively.

We first excite the molecules on the $a^3\Pi \leftarrow X^1\Sigma^+$ transition with 10 mJ of pulsed light from a Ti:Sa seeded pulsed dye amplifier. 5 mm downstream, we shine between 300 and 500 mW of 597 nm cw light from a ring dye laser (Coherent 899) in a 1.6-mm-diameter ($1/e^2$) beam into the chamber and thereby drive the transitions to the $A^1\Pi$ state. The resulting fluorescence at 227.5 nm is recorded as a function of the dye laser frequency. We detect the fluorescence with a photomultiplier tube that is only sensitive in the UV. This allows for background-free detection in presence of high intensity red cw light.

Both spectra are shown in figure 2.8. To the best of our knowledge, this is the first time that this very weak forbidden band has been observed. The transitions get weakly allowed because of spin-orbit mixing of the $a^3\Pi_0$ state with $^1\Sigma^+$ and $^1\Pi$ states as well as due to spin-orbit mixing of the $A^1\Pi$ state with $^3\Sigma^+$ states.

The hyperfine structure in both the $A^1\Pi$ and the $a^3\Pi$ state is known from previous measurements, therefore the hyperfine structure in the $a^3\Pi \leftarrow X^1\Sigma^+$ spectra can be simulated well, shown as blue curves in figure 2.8. The Doppler width and the population distribution across the hyperfine components in the $a^3\Pi_0$ state were left as fitting parameters. We use the 84 MHz natural linewidth. The best fit for both observed lines is obtained assuming equal population of the hyperfine levels and a Doppler broadening of 82 MHz.

2.6.3 Transition Strength

To determine the strength of the loss channel from the main cycling transition to the $a^3\Pi$ state, we measure the strength of the spin-forbidden $A^1\Pi, v = 0 \leftarrow a^3\Pi, v' = 0$ band relative to the $A^1\Pi, v = 0 \leftarrow X^1\Sigma^+, v'' = 0$ band. We can directly compare the 227.5 nm fluorescence after excitation on both bands. We first want to quantify

the losses on the $Q_1(1)$ line of the $a^3\Pi_0$ transition. The UV laser frequency of the $A^1\Pi \leftarrow X^1\Sigma^+$ transition is fixed at the $R(0)$ line, at an intensity set to a value where each molecule scatters two photons on average (≈ 2.7 mW in a 2.0 mm $1/e^2$ diameter beam). The number of photons emitted per molecule before being optically pumped to a dark state is determined by the Hönl-London factors of the driven (bright) transition $R(0)$ and of the transition to a dark rotational state, which is the $P(2)$ line. From these Hönl-London factors, we determine the probability that the molecule relaxes to the bright ground state to $p = 2/3$, and the maximum number of emitted photons is $n = 1/(1 - p) = 3$. Guided by an experimental saturation curve, we can adjust the intensity to scatter fewer photons than this number. The TOF profile, scattering 2 photons per molecule, is shown in figure 2.9a. Using optical pumping on the $R_1(0)$ line of the $a^3\Pi_0, v' = 0 \leftarrow X^1\Sigma^+, v'' = 0$ transition, we transfer population to the $a^3\Pi_0, v' = 0, J' = 1, -$ level. The dip in the TOF distribution shown in figure 2.9a is caused by this pumping and is a measure of the fraction of molecules that is transferred to the metastable triplet state. The depth of the dip depends on the number of accessible excited states relative to the number of ground hyperfine states. In the case of the $R_1(0)$ line, however, this does not introduce an additional factor in the calculation. By comparing the amplitude of the dip in figure 2.9a to the $Q_1(1)$ TOF profile shown in figure 2.9b, we can determine the relative transition strength. The ratio of the two TOF amplitudes is $5 \pm 0.5 \times 10^{-4}$.[†] The strong, narrow peaks present in the TOF profiles are scattered light from the PDA excitation. From the ratio of TOF amplitudes, and accounting for the different laser intensities and wavelengths, we measure a decay rate from the $A^1\Pi, v = 0, J = 1, +/ -$ level to the $a^3\Pi_0$ state of $29 \pm 3 \text{ s}^{-1}$, which corresponds to a relative loss from the cycling transition of $(0.56 \pm 0.1) \times 10^{-7}$.

We performed the same measurement, but exciting the molecules first to the $a^3\Pi_0, v = 0, J = 0$ level using the PDA to drive the $P_1(1)$ transition and then driving the $R_1(1)$ line of the $A^1\Pi, v = 0 \leftarrow a^3\Pi_0, v' = 0$ band with the cw ring dye laser light. The ratio of the TOF amplitudes is $9 \pm 0.6 \times 10^{-4}$ and the resulting decay rate of the $A^1\Pi, v = 0, J = 1, +/ -$ level is $38 \pm 4 \text{ s}^{-1}$.

There are six possible decay channels for the $A^1\Pi, v = 0, J = 1, +/ -$ level to the $a^3\Pi_0$ state that end up in six different rotational and parity levels. Decay to higher vibrational levels in the metastable state can be neglected. From the experimentally measured $Q_1(1)$ and $R_1(0)$ lines, we can calculate the other four decay channels and give a total decay rate from the $A^1\Pi, v = 0, J = 1, +/ -$ level to the $a^3\Pi$ state of $53 \pm 5 \text{ s}^{-1}$. This corresponds to a relative loss from the cycling transition of $(1.0 \pm 0.1) \times 10^{-7}$.

In a more recent study performed in our group [182], the actual ratio of the fluorescence on the A-X and A-a transitions was measured to be $(6 \pm 2) \times 10^{-7}$ (see also chapter 3.6).

[†]Please note that the signal in figure 2.9a corresponds to two photons, while the signal in figure 2.9b is only from one photon scattering event. Therefore, we need to include a factor 2 in this calculation.

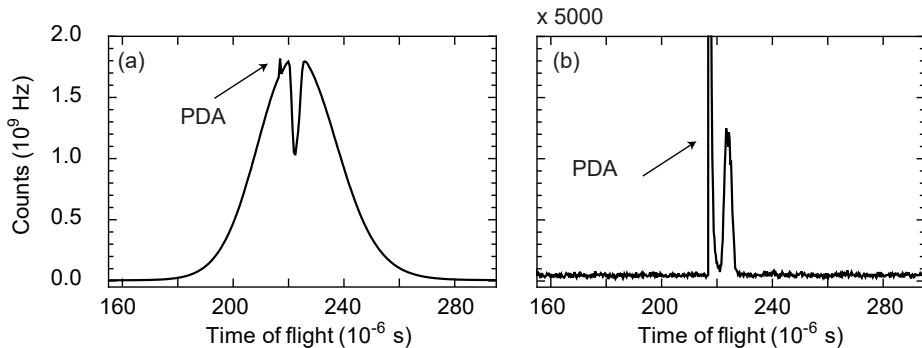


Figure 2.9: (a) LIF signal as a function of time when the frequency of the 227.5 nm laser is locked to the center of the R(0) line of the $A^1\Pi, v = 0 \leftarrow X^1\Sigma^+, v'' = 0$ band. The laser power is set such that each molecule scatters on average two UV photons. Optical pumping by the PDA on the $R_1(0)$ line of the $a^3\Pi_0, v' = 0 \leftarrow X^1\Sigma^+, v'' = 0$ band creates a dip in the center of the TOF profile. (b) LIF signal as a function of time when the cw dye laser is locked to the highest frequency component of the $Q_1(1)$ line of the $A^1\Pi, v = 0 \leftarrow a^3\Pi_0, v' = 0$ band. Each excited molecule emits only a single UV photon. The signal is about 2000 times weaker and the stray light from the PDA excitation can be seen as a sharp peak detected 10 μ s before the signal.

2.7 Conclusion

In this chapter, I have presented several experiments that we performed to spectroscopically characterise the AIF molecule and to determine the feasibility of laser cooling experiments.

Transitions to the metastable $a^3\Pi$ state get allowed because of spin-orbit mixing with $^1\Sigma^+$ and $^1\Pi$ states. Combining pulsed excitation to the $a^3\Pi$ state with radio frequency spectroscopy and pulsed ionisation in a triple-resonance scheme, we determined the hyperfine energy levels with kHz accuracy and could calculate precise hyperfine and rotational constants as well as the magnetic g_F factors.

From LIF excitation spectra of the $A^1\Pi, v = 0 \leftarrow X^1\Sigma^+, v'' = 0$ transition, we could determine hyperfine interaction and rotational constants as well as the radiative lifetime in the $A^1\Pi$ state. All Q lines of the $A^1\Pi, v = 0 \leftarrow X^1\Sigma^+, v'' = 0$ band are rotationally closed and can be used for optical cycling.

The spin-forbidden $A^1\Pi, v = 0 \leftarrow a^3\Pi, v' = 0$ band was observed for the first time and the relative losses from the optical cycle to the $a^3\Pi$ state were determined to be in the 10^{-7} range.

These results show that AIF indeed is a suitable candidate for laser cooling. With only one vibrational repump laser on the 0-1 band, it will be possible to scatter 10^4 photons on the $A^1\Pi \leftarrow X^1\Sigma^+$ band.

Chapter 3

Spectroscopic Characterisation of the $b^3\Sigma^+$ State in AlF

3.1 Introduction

In this chapter, I present rotationally-resolved optical spectra of the $b^3\Sigma^+, v' = 0 \leftarrow a^3\Pi, v'' = 0$ band and demonstrate state-selective ionisation of $a^3\Pi$ molecules via (1+2)-resonance-enhanced multi-photon ionisation (REMPI). Pulsed excitation followed by time-delayed ionisation with a KrF excimer laser is used to determine the radiative lifetime of the $b^3\Sigma^+, v = 0$ state. Next, high-resolution, cw laser-induced fluorescence (LIF) spectra of the $b^3\Sigma^+, v' = 0 \leftarrow X^1\Sigma^+, v'' = 1$ band are presented. The hyperfine structure in the $b^3\Sigma^+, v = 0$ state is resolved and precise spectroscopic constants for the $b^3\Sigma^+$ state are determined. Laser-induced fluorescence spectra, recorded using a cw laser to drive rotational lines of the $b^3\Sigma^+, v' = 0 \leftarrow a^3\Pi, v'' = 0$ band, allow us to reduce the uncertainty in the spin-orbit constant A and the spin-spin interaction constant λ of the $a^3\Pi$ state by nearly two orders of magnitude. A fraction of the excited state molecules decays on the $b^3\Sigma^+, v' = 0 \rightarrow X^1\Sigma^+, v''$ bands to the ground state. This is caused by spin-orbit coupling of the $b^3\Sigma^+, v = 0$ state with the nearby $A^1\Pi$ state. This perturbation of the $A^1\Pi$ state and the $b^3\Sigma^+$ state is analysed in detail as it induces also a small loss channel for the strong $A^1\Pi-X^1\Sigma^+$ cooling transition.

3.2 Previous Work

In 1953, Rowlinson and Barrow reported the first observation of transitions between triplet states in AlF by recording emission spectra from a hollow-cathode

This chapter is based on reference [182] – M. Doppelbauer, *et al.*, “Characterisation of the $b^3\Sigma^+, v = 0$ state and its interaction with the $A^1\Pi$ state in aluminium monofluoride.” In *Molecular Physics* **119**(1-2), (2021). doi:10.1080/00268976.2020.1810351.

discharge [160]. In the following decades, new triplet states were identified and characterised in more detail [161, 183–186]. Kopp and Barrow analysed the interaction of the $A^1\Pi$ state with the nearby $b^3\Sigma^+$ state and thereby determined the term energy of the triplet states relative to the singlet states [186]. A comprehensive study of the electronic states and the interaction between the singlet and triplet states followed [144]. In 1976, Rosenwaks *et al.* observed the $a^3\Pi \rightarrow X^1\Sigma^+$ transition directly in emission [164] at the same time as Kopp *et al.* did in absorption [165]. Both studies confirmed the singlet-triplet separation determined from the earlier perturbation analysis.

The hyperfine structure of the rotational states in $b^3\Sigma^+$ was partly resolved and analysed by Barrow *et al.* [144]. Their low-resolution spectra (typical linewidth of 0.05 cm^{-1}) showed a triplet structure, which they ascribed to magnetic hyperfine effects of the ^{27}Al nucleus, whose nuclear spin is $I_{\text{Al}} = 5/2$. A more detailed analysis of both the fine and hyperfine structure in the triplet states was presented by Brown *et al.* in 1978 [166]. The hyperfine structure was partially resolved and they determined values for the Fermi contact parameter $b_F(\text{Al})$, the electron spin-spin interaction parameter λ , and the spin-rotation parameter γ .

We have recently reported on the detailed energy level structure of the $X^1\Sigma^+$, $A^1\Pi$ and $a^3\Pi$ states in AlF [167]. That study resolves the complete hyperfine structure, including the contribution due to fluorine nuclear spin, in all three states. The energy levels in $X^1\Sigma^+$ and in the three Ω manifolds of the metastable $a^3\Pi$ state were measured with kHz resolution; this allowed us to determine the spectroscopic constants precisely and study subtle effects, such as a spin-orbit correction to the nuclear quadrupole interaction of the Al nucleus.

3.3 Rotational Structure of the $b^3\Sigma^+$, $v' = 0 \leftarrow a^3\Pi_1$, $v'' = 0$ Band and the Radiative Lifetime of the $b^3\Sigma^+$, $v = 0$ State

To study the $b^3\Sigma^+ \leftarrow a^3\Pi$ transition, the molecules must first be prepared in the $a^3\Pi$ state. Previously, we described this state and the $a^3\Pi \leftarrow X^1\Sigma^+$ transition in detail [167]. The hyperfine structure in $X^1\Sigma^+$ is small and for the purpose of this study, the ground state is comprised of single rotational levels with energies given by $BJ(J+1)$.

The angular momentum coupling in the $a^3\Pi$ state of AlF is well-described by Hund's case (a). The energy levels are labelled by the total angular momentum (excluding hyperfine interaction) $\mathbf{J} = \mathbf{R} + \mathbf{L} + \mathbf{S}$, with \mathbf{R} the rotational angular momentum of the rigid nuclear framework, and \mathbf{L} and \mathbf{S} the total orbital and spin angular momenta of the electrons, respectively. Both, \mathbf{L} and \mathbf{S} are not well defined. However, their projection onto the internuclear axis $\mathbf{\Lambda}$, $\mathbf{\Sigma}$ and the total electronic angular momentum along the internuclear axis $\mathbf{\Omega} = \mathbf{\Lambda} + \mathbf{\Sigma}$ are well defined. The spin-orbit interaction leads to three fine-structure states with $\Omega = |\Lambda + \Sigma|$, labelled with \mathcal{F}_1 , \mathcal{F}_2 and \mathcal{F}_3 , in order of increasing energy, corresponding to the states $a^3\Pi_0$, $a^3\Pi_1$ and $a^3\Pi_2$. The splitting between the Ω manifolds is determined by A , the electron spin-orbit coupling constant and the spin-spin interaction coupling

constant λ . Each Ω has its own rotational manifold with energies $BJ(J+1)$, where the rotational constant B is slightly different for each Ω manifold.

The $b^3\Sigma^+$ state is well-described by Hund's case (b), for which \mathbf{L} couples to the rotation \mathbf{R} to form $\mathbf{N} = \mathbf{R} + \mathbf{L}$. The rotational energy levels follow $BN(N+1)$. For Σ electronic states $\mathbf{N} = \mathbf{R}$ and the total angular momentum (without hyperfine interaction) is $\mathbf{J} = \mathbf{N} + \mathbf{S}$. The combined effect of the spin-rotation interaction $\gamma(\mathbf{N} \cdot \mathbf{S})$ and the spin-spin interaction $\frac{2}{3}\lambda(3S_z^2 - \mathbf{S}^2)$ splits each rotational level $N > 0$ of $b^3\Sigma^+$ into three J-levels; these components are labelled \mathcal{F}_1 , \mathcal{F}_2 and \mathcal{F}_3 with quantum numbers $J = N + 1$, $J = N$ and $J = N - 1$, respectively.

Following the convention of Brown *et al.* [179] the parity states can be labelled by e and f , where e levels have parity $+(-1)^J$ and f labels have parity $-(-1)^J$. All rotational levels of the $X^1\Sigma^+$ state are e -levels, while in the $b^3\Sigma^+$ state, all \mathcal{F}_2 levels are e -levels, while \mathcal{F}_1 and \mathcal{F}_3 are f -levels. In the $a^3\Pi$ state, each J-level has an e and an f component due to Λ -doubling.

Figure 3.1a shows the energy level diagram of the electronic states relevant to this study, together with a rotationally resolved spectrum of the $b^3\Sigma^+, v' = 0 \leftarrow a^3\Pi_1, v'' = 0$ band in 3.1b, and a sketch of the experimental setup in 3.1c, which is similar to the one reported previously [167]. The molecules are produced by laser-ablating an aluminium rod in a supersonic expansion of 2% SF_6 seeded in Ne. After passing through a skimmer, the ground-state molecules are optically pumped to the metastable $a^3\Pi_1, v = 0$ state by a frequency-doubled pulsed dye laser using the Q-branch of the $a^3\Pi_1, v' = 0 \leftarrow X^1\Sigma^+, v'' = 0$ band. For this, 367 nm radiation with a bandwidth of 0.1 cm^{-1} and a pulse energy of 6 mJ in a beam with a e^{-2} waist radius of about 2 mm is used. The Q-branch of this transition falls within this bandwidth. Therefore, many rotational levels in the metastable $a^3\Pi_1, v = 0$ state are populated simultaneously. Via the Q-branch, only the f -levels in $a^3\Pi_1$ are populated. Alternatively, if the molecules are optically pumped to the metastable state using spectrally isolated R or P lines, only the e -levels are populated. Further downstream, at $z = 55 \text{ cm}$ from the source, the molecular beam is intersected with light from a second pulsed dye laser tuned to the $b^3\Sigma^+, v' = 0 \leftarrow a^3\Pi_1, v'' = 0$ transition near 569 nm. For pulse energies exceeding 6 mJ (unfocused, with an e^{-2} waist radius of about 5 mm), this laser transfers population to the $b^3\Sigma^+, v = 0$ state and subsequently ionises the molecules by having them absorb two more photons from the same laser. Such a one-colour (1+2)-REMPI scheme using an unfocused laser beam is very uncommon. However, AlF has numerous electronically excited states that lie one photon-energy above the $b^3\Sigma^+$ state energy, strongly enhancing the non-resonant two-photon ionisation probability. The ions are mass-selected in a short time-of-flight mass spectrometer (TOF-MS) and detected using micro-channel plates. The TOF-MS voltages are switched on shortly after the ionisation laser fires; this way ionisation occurs under field-free conditions and parity mixing of closely spaced levels is avoided. The (1+2)-REMPI scheme uses low-energy photons and an unfocused laser beam, which has the benefit of producing a mass spectrum with only a single peak, corresponding to AlF. The spectrum, displayed in figure 3.1b, shows the ion signal as a function of the REMPI laser frequency. The spectral lines are labelled by $\Delta(NJ)_{\mathcal{F}''}(J'')$, where $\Delta(NJ) = N' - J''$, as the quantum number J is not

well-defined in the $b^3\Sigma^+$ state (*vide infra*). Since only the f -levels of the $a^3\Pi$ state are populated, the spectrum consists of $\Delta(NJ) = -2, 0, +2$, i.e., O, Q and S branches.

To determine the radiative lifetime of the $b^3\Sigma^+, v = 0$ state, we reduce the pulse energy of the $b^3\Sigma^+ \leftarrow a^3\Pi$ excitation laser to about 1 mJ. At pulse energies below 2 mJ, the $a^3\Pi_1$ molecules are excited to the $b^3\Sigma^+$ state, but are not ionised via (1+2)-REMPI. Instead, a KrF excimer laser is used to ionise the $b^3\Sigma^+$ state molecules with a single 248 nm photon and a pulse energy of about 3 mJ. The radiative lifetime of the $b^3\Sigma^+, v = 0$ state is measured by varying the time-delay between excitation and ionisation [187]. The determination of radiative lifetimes in the range of 20 ns to 1 μ s is relatively straightforward, because it is longer than the laser pulse duration, but short enough so that the molecules do not leave the detection region. Figure 3.2 shows the ion signal (black dots) as a function of the time delay with $1 - \sigma$ standard error bars. The blue line is a fit to the data using the model $S(t) = Ce^{-t/\tau_b} \text{erfc}[(t_0 - t)/(\sqrt{2}\sigma)]$, where erfc is the complementary error function, C and t_0 are fit parameters, τ_b is the lifetime of the $b^3\Sigma^+, v = 0$ state and σ is the measured, combined pulse-width of the excitation and ionisation laser. In this model the lifetime $\tau_b = 190(2)$ ns is fixed to the value determined from a linear fit to the semi-log plot shown in the inset. In 1988, Langhoff et al. calculated an approximate radiative lifetime of the $b^3\Sigma^+$ state of 135 ns [141], considerably shorter than the measured lifetime.

3.4 The Fine and Hyperfine Structure of the $b^3\Sigma^+$ State

Aluminium and fluorine have a nuclear spin of $I_{\text{Al}} = 5/2$ and $I_{\text{F}} = 1/2$, respectively. Following the description of Brown et al. [166] and including the magnetic interaction of the fluorine nuclear spin, the effective Hamiltonian reads

$$\begin{aligned}
 H_{\text{eff}} = & \frac{2}{3}\lambda(3S_z^2 - \mathbf{S}^2) + \gamma(\mathbf{N} \cdot \mathbf{S}) \\
 & + b_{\text{F}}(\text{Al})\mathbf{I}_{\text{Al}} \cdot \mathbf{S} + \frac{1}{3}c(\text{Al})(3I_{\text{Al},z}S_z - \mathbf{I}_{\text{Al}} \cdot \mathbf{S}) \\
 & + b_{\text{F}}(\text{F})\mathbf{I}_{\text{F}} \cdot \mathbf{S} + \frac{1}{3}c(\text{F})(3I_{\text{F},z}S_z - \mathbf{I}_{\text{F}} \cdot \mathbf{S}) \\
 & + \frac{eq_0Q}{4I_{\text{Al}}(2I_{\text{Al}} - 1)}(3I_{\text{Al},z}^2 - I_{\text{Al}}^2),
 \end{aligned} \tag{3.1}$$

where λ is the spin-spin interaction constant and γ the spin-rotation interaction constant. The parameters $b_{\text{F}}(\text{Al})$ and $b_{\text{F}}(\text{F})$ describe the Fermi contact interaction for the aluminium and fluorine nucleus, respectively, $c(\text{Al})$ and $c(\text{F})$ the dipolar interaction, and eq_0Q the electric quadrupole interaction of the Al nucleus.

In the $b^3\Sigma^+$ state of AlF, the Fermi contact interaction $b_{\text{F}}(\text{Al})(\mathbf{I}_{\text{Al}} \cdot \mathbf{S})$ between the nuclear spin of aluminium and the electronic spin angular momentum is

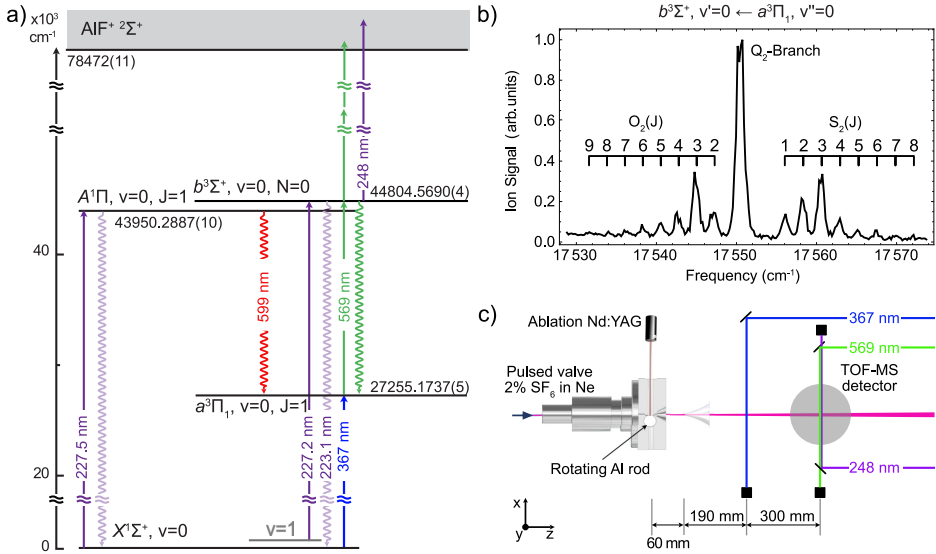


Figure 3.1: a) Electronic energy level scheme of the relevant states of AlF. The transitions used for laser excitation are shown as solid arrows. The laser-induced fluorescence used for detecting the molecules is indicated by downward wavy arrows. The indicated energies are the gravity centres of the respective states in absence of hyperfine structure. b) (1+2)-REMPI spectrum of the $b^3\Sigma^+, v' = 0 \leftarrow a^3\Pi_1, v'' = 0$ band. The $a^3\Pi_1, v = 0$ state is populated via the Q-branch of the $a^3\Pi_1, v' = 0 \leftarrow X^1\Sigma^+, v'' = 0$ band using a frequency-doubled pulsed dye laser. c) Scheme of the experimental setup used for the determination of the lifetime of the $b^3\Sigma^+, v = 0$ state.

strong compared to the spin-rotation interaction [166]. The coupling case approximates ($b_{\beta S}$). The $N = 0$ level has only one spin-component for which $J = N + S = 1$; this $J = 1$ level is split into three components due to the aluminium nuclear spin, each of which is again split by the nuclear spin of fluorine. This results in a total of six F levels. For $N > 0$, J is not well defined and it is useful to introduce an intermediate angular momentum $\mathbf{G} = \mathbf{I}_{Al} + \mathbf{S}$ (see figure 3.4). \mathbf{G} then couples to \mathbf{N} which results in three sets of sub-levels, with quantum numbers $G = 3/2, 5/2$ and $7/2$, each of which contains the closely spaced stacks of $N + 3/2, \dots, N - 3/2, N + 5/2, \dots, N - 5/2$ and $N + 7/2, N + 5/2, \dots, N - 7/2$ levels. Each of these levels is again split by the interaction with the fluorine nuclear spin to give the total angular momentum $\mathbf{F} = \mathbf{N} + \mathbf{G} + \mathbf{I}_F$. For $N = 1, 2$ and 3 this results in a total of 18, 28 and 34 F levels, respectively. For $N > 3$ the number of F levels reaches its limit of 36.

To determine the hyperfine energy levels of the $b^3\Sigma^+$ state, we drive the $b^3\Sigma^+, v' = 0 \leftarrow X^1\Sigma^+, v'' = 1$ band near 227.2 nm with a cw laser and detect the $b^3\Sigma^+ \rightarrow a^3\Pi$ fluorescence at 569 nm. The spectrum of this transition directly reflects the energy level structure in the $b^3\Sigma^+$ state, because the hyperfine structure

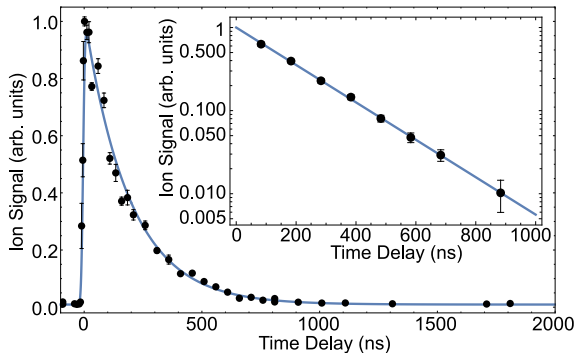


Figure 3.2: Measurement of the radiative lifetime of the $b^3\Sigma^+, v = 0$ state. First, the ground-state molecules are optically pumped to the $b^3\Sigma^+, v = 0$ state via the two-colour excitation scheme described in the text. The population in the $b^3\Sigma^+, v = 0$ state is probed by single-photon ionisation using a KrF excimer laser, followed by TOF-MS detection. The black dots show the AlF⁺ ion signal as a function of the time delay between excitation and ionisation. The blue line is a fit to the data using the model described in the text. The inset shows a semi-log plot of a second measurement for eight specific time delays. A linear fit to the data gives a $b^3\Sigma^+$ state lifetime of 190(2) ns.

of the $X^1\Sigma^+$ state is smaller than the residual Doppler broadening in the molecular beam. The wavelength required to drive this transition is close to that of the $A^1\Pi, v' = 0 \rightarrow X^1\Sigma^+, v'' = 0$ band near 227.5 nm, for which we have a powerful UV laser system installed.

The $b^3\Sigma^+, v' = 0 \leftarrow X^1\Sigma^+, v'' = 1$ transition is spin-forbidden and the overlap of the vibrational wave functions is poor, with a calculated Franck-Condon factor of 0.02. However, the transition becomes weakly allowed due to the spin-orbit interaction between the $b^3\Sigma^+$ and the nearby $A^1\Pi$ state. In section 3.7 this interaction will be discussed in more detail. To compensate for the weak transition dipole moment, we use a high excitation laser intensity of up to 75 mW in a laser beam with a e^{-2} waist radius of 0.6 mm. The resulting laser-induced fluorescence occurs mainly on the dipole-allowed $b^3\Sigma^+ \rightarrow a^3\Pi$ transition near 569 nm. The far off-resonant fluorescence allows us to block scattered laser light with a bandpass filter and to record background-free spectra. To increase the number of molecules in $X^1\Sigma^+, v = 1$, we use a cryogenic helium buffer gas source, instead of the supersonic molecular beam introduced in the previous section. Figure 3.3 shows a sketch of the experimental setup that is used for this measurement.

The design of this source is similar to the one described in [188–190]. A pulsed Nd:YAG laser ablates a solid aluminium target in the presence of a continuous flow of 0.01 sccm room-temperature SF₆ gas, which is mixed with 1 sccm of cryogenic helium gas (2.7 K) inside a buffer gas cell. The hot Al atoms react with the SF₆ and form hot AlF molecules, which are subsequently cooled through collisions with the cold helium atoms. More details on this setup can be found in chapter 5. Compared to the supersonic molecular beam, this source delivers over 100 times

more AlF molecules per pulse in the ro-vibronic ground-state to the detection region. The forward velocity of the molecules is four times lower. To increase the number of molecules in $X^1\Sigma^+, v = 1$, we increase the pulse energy and repetition rate of the ablation laser, increase the temperature of the SF_6 gas to 350 K and increase its mass flow rate to 0.1 sccm. At $z = 35$ cm the molecules interact with cw UV laser light to drive the $b^3\Sigma^+, v' = 0 \leftarrow X^1\Sigma^+, v'' = 1$ transition near 227.2 nm. The laser light is produced by frequency-doubling the output of a cw titanium sapphire laser twice. The laser-induced fluorescence passes through an optical filter to block scattered light from the excitation laser, and is imaged onto a photomultiplier tube (PMT). The photo-current is amplified and acquired by a computer. The wavelength of the excitation laser is recorded with an absolute accuracy of 120 MHz using a calibrated wavemeter (HighFinesse WS8-10).

Figure 3.5 shows the recorded spectra reaching the three lowest N levels in the $b^3\Sigma^+$ state. The panels demonstrate the increasing complexity of the hyperfine structure with increasing N . The three spectra allow us to measure the rotational constant of the $b^3\Sigma^+$ state. Gaussian lineshapes are fitted to the experimental spectra to determine the line-centres. We then fit the eigenvalues of the hyperfine Hamiltonian to the measured energy levels with the spectroscopic parameters as fit parameters. We assign a total of 48 lines and the standard deviation of the fit is 11 MHz. The best fit parameters together with their standard deviations are summarised in Table 3.1. E_0 is the pure vibronic energy of $b^3\Sigma^+, v = 0$, i.e. the energy of the $N = 0$ level in absence of spin, fine and hyperfine splitting. This is referenced to the $J = 0$ level of the $X^1\Sigma^+, v = 0$ state by using the precise infrared emission lines of [191] to determine the energy difference between the $v = 0$ and $v = 1$ level in the $X^1\Sigma^+$ state. The inverted spectra in figure 3.5 are simulated spectra using the spectroscopic parameters presented in Table 3.1 and reproduce the measured spectra well. The Fermi contact parameter $b_F(\text{F})$ for fluorine and the two hyperfine parameters $c(\text{Al})$ and $c(\text{F})$ for the aluminium and fluorine nucleus, respectively, are determined for the first time. In previous, low-resolution studies, the interaction of the fluorine nuclear spin has been neglected. However, we conclude that the magnitude of the interaction parameter for the two nuclei is comparable. This indicates that there is a significant electron density at both nuclei which is in stark contrast to the situation in the $a^3\Pi$ state. In the latter state, the Fermi contact term for the ^{19}F nucleus is about seven times smaller than for the ^{27}Al nucleus [167]. The Fermi contact parameter for the aluminium nucleus $b_F(\text{Al})$ and the spin-spin interaction parameter λ presented here are consistent with the previously determined values, but their uncertainty is reduced significantly.

3.5 The $b^3\Sigma^+, v' = 0 \leftarrow a^3\Pi, v'' = 0$ Transition

The $b^3\Sigma^+ - a^3\Pi$ bands have a diagonal Franck-Condon matrix and the $b^3\Sigma^+, v' = 0 \leftarrow a^3\Pi, v'' = 0$ band has a Franck-Condon factor of 0.994. Its natural linewidth is 100 times smaller than the natural linewidth of the strong $A^1\Pi, v' = 0 \leftarrow X^1\Sigma^+, v'' = 0$ transition near 227.5 nm. Laser cooling AlF molecules on the $b^3\Sigma^+ - a^3\Pi$ transition could therefore reach temperatures far below the Doppler limit of the

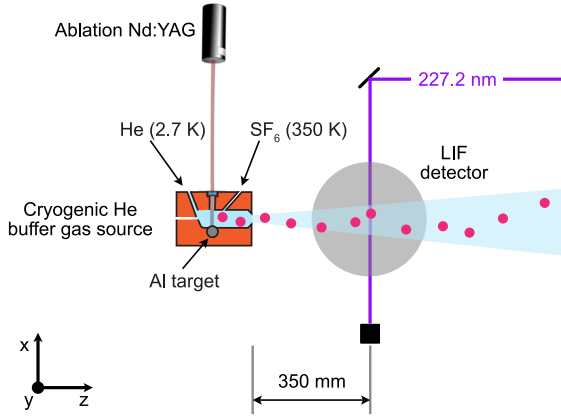


Figure 3.3: Schematic view of the experimental setup used to measure the fine and hyperfine structure of the $b^3\Sigma^+$, $v = 0$ state. AlF molecules are produced in a cryogenic helium buffer gas source. The molecular beam is intersected with UV laser light from a frequency-quadrupled cw titanium sapphire laser. The molecules are excited on the weak, spin-forbidden $b^3\Sigma^+$, $v' = 0 \leftarrow X^1\Sigma^+$, $v'' = 1$ transition. The laser-induced fluorescence occurs mainly on the $b^3\Sigma^+$, $v' = 0 \rightarrow a^3\Pi$, $v'' = 0$ transition near 569 nm and is imaged onto a PMT.

Table 3.1: Experimentally determined spectroscopic constants of $b^3\Sigma^+$, $v = 0$. E_0 and its uncertainty are given in cm^{-1} , all other parameters are given in MHz. SD gives the standard deviation in the absence of correlations and $\text{SD} \cdot \sqrt{Q}$ gives the standard deviation of the parameter including the correlations between the parameters [180]. The previous best values are taken from [144] and [166] and given with the reported standard error (SE).

Parameter	This Work	SD	SD $\cdot\sqrt{Q}$	Refs. [144] & [166]	SE
E_0	44804.5692	0.0004	0.0004		
B	16772	2	5	16774.6	0.2
λ	-919	15	18	-750	300
γ	-9	7	13	0	9
$b_F(\text{Al})$	1311	2	3	1469	90
$c(\text{Al})$	73	12	18		
$eq_0Q(\text{Al})$	-62	69	99		
$b_F(\text{F})$	870	10	11		
$c(\text{F})$	305	50	53		

strong $A^1\Pi-X^1\Sigma^+$ transition. The vibrational branching to $a^3\Pi$, $v = 1$ is small and, if addressed with a repump laser, a molecule could scatter about 1000 photons before being pumped into $a^3\Pi$, $v = 2$. However, the radiative decay from the $b^3\Sigma^+$ state to multiple J levels in all three spin-orbit manifolds of the $a^3\Pi$ state is allowed. This results in a large number of rotational branches that must be

Table 3.2: Measured energies, E , of the hyperfine levels in $b^3\Sigma^+, v = 0$, relative to the $X^1\Sigma^+, v = 0, J = 0$ level, magnetic g-factors g_F , rotational quantum number N , total angular momentum F and parity p . Since the assignment of the quantum numbers N, F, p , is not unique, we use n to index the levels that share the same set of quantum numbers F and p , with increasing energy. The final state of the transition used to investigate the singlet contribution to the $b^3\Sigma^+$ state wave function in section 3.5 is highlighted in red.

E (cm $^{-1}$)	g_F	N	F	p	n	E (cm $^{-1}$)	g_F	N	F	p	n
44804.4031	-0.661	0	2	+1	1	44807.7613	-0.298	2	4	+1	2
44804.4305	-1.000	0	1	+1	1	44807.7630	-0.517	2	1	+1	2
44804.5235	0.327	0	2	+1	2	44807.7685	0.000	2	0	+1	1
44804.5268	0.170	0	3	+1	1	44807.7838	-0.228	2	2	+1	4
44804.6622	0.663	0	3	+1	2	44807.7868	-0.291	2	3	+1	4
44804.6928	0.500	0	4	+1	1	44807.7883	0.261	2	1	+1	3
44805.5139	-0.617	1	2	-1	1	44807.8599	0.000	2	0	+1	2
44805.5217	-0.411	1	3	-1	1	44807.8657	0.517	2	1	+1	4
44805.5282	-0.991	1	1	-1	1	44807.8704	0.551	2	1	+1	5
44805.5454	-0.712	1	1	-1	2	44807.8731	0.140	2	4	+1	3
44805.5479	-0.461	1	2	-1	2	44807.8749	0.090	2	5	+1	1
44805.5540	0.000	1	0	-1	1	44807.8792	0.308	2	2	+1	5
44805.6297	0.703	1	1	-1	3	44807.8844	0.323	2	2	+1	6
44805.6344	0.292	1	2	-1	3	44807.8917	0.179	2	3	+1	5
44805.6373	0.196	1	3	-1	2	44807.8930	0.153	2	3	+1	6
44805.6396	0.117	1	4	-1	1	44807.8966	0.088	2	4	+1	4
44805.6548	0.341	1	2	-1	4	44808.0120	0.454	2	4	+1	5
44805.6615	0.172	1	3	-1	3	44808.0151	0.470	2	3	+1	7
44805.7708	0.632	1	3	-1	4	44808.0237	0.397	2	5	+1	2
44805.7845	0.497	1	4	-1	2	44808.0253	0.569	2	2	+1	7
44805.7958	0.779	1	2	-1	5	44808.0345	1.188	2	1	+1	6
44805.8053	0.486	1	4	-1	3	44808.0457	0.380	2	5	+1	3
44805.8142	0.400	1	5	-1	1	44808.0468	0.415	2	4	+1	6
44805.8216	0.578	1	3	-1	5	44808.0529	0.333	2	6	+1	1
44807.7541	-0.342	2	3	+1	3	44808.0530	0.499	2	3	+1	8
44807.7565	-0.416	2	2	+1	3	44808.0597	0.777	2	2	+1	8

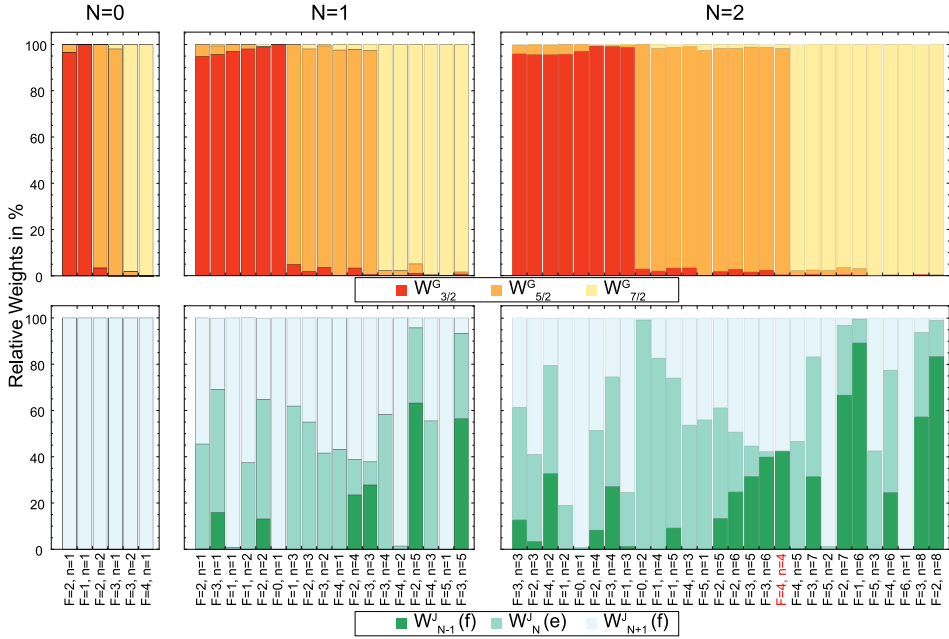


Figure 3.4: Relative weights W^G and W^J of the $|N, G, F\rangle$ and $|N, J, F\rangle$ basis wave functions in the eigenfunctions $|E\rangle$ of the energy levels in the three lowest rotational states of the $b^3\Sigma^+, v = 0$ state. The weights are obtained by projecting the eigenstate of the Hamiltonian onto the basis wave function $|N, G, F\rangle$ and $|N, J, F\rangle$, respectively. G can take the values $3/2, 5/2$ and $7/2$ and J can be $N - 1, N$ or $N + 1$. The energy levels are described uniquely by the quantum numbers F , p and the index n . This analysis shows that G is a good quantum number for the description of any rotational level of the $b^3\Sigma^+, v = 0$ state, while J only characterises the levels well for $N = 0$.

addressed to close the optical cycle [192]. In addition, the hyperfine structure in the $a^3\Pi$ state is large compared to the linewidth of the transition. Both effects make laser-cooling of AIF, using an optical transition in the triplet manifold very challenging. This is in stark contrast to the strong $A^1\Pi-X^1\Sigma^+$ transition, for which all Q-lines are rotationally closed and for which all hyperfine levels of a given rotational level in the $X^1\Sigma^+$ state lie within the natural linewidth.

Here, we show that laser-induced fluorescence spectroscopy of the $b^3\Sigma^+, v' = 0 \leftarrow a^3\Pi, v'' = 0$ transition can be used to efficiently detect $a^3\Pi$ molecules with hyperfine resolution. In this section, we show that this method works well to detect molecules in all three Ω manifolds to improve two important spectroscopic constants of the $a^3\Pi$ state: the spin-orbit (A) and spin-spin (λ) interaction parameter, which determine the relative spacing of the three Ω manifolds in $a^3\Pi$. The effective fine structure Hamiltonian is

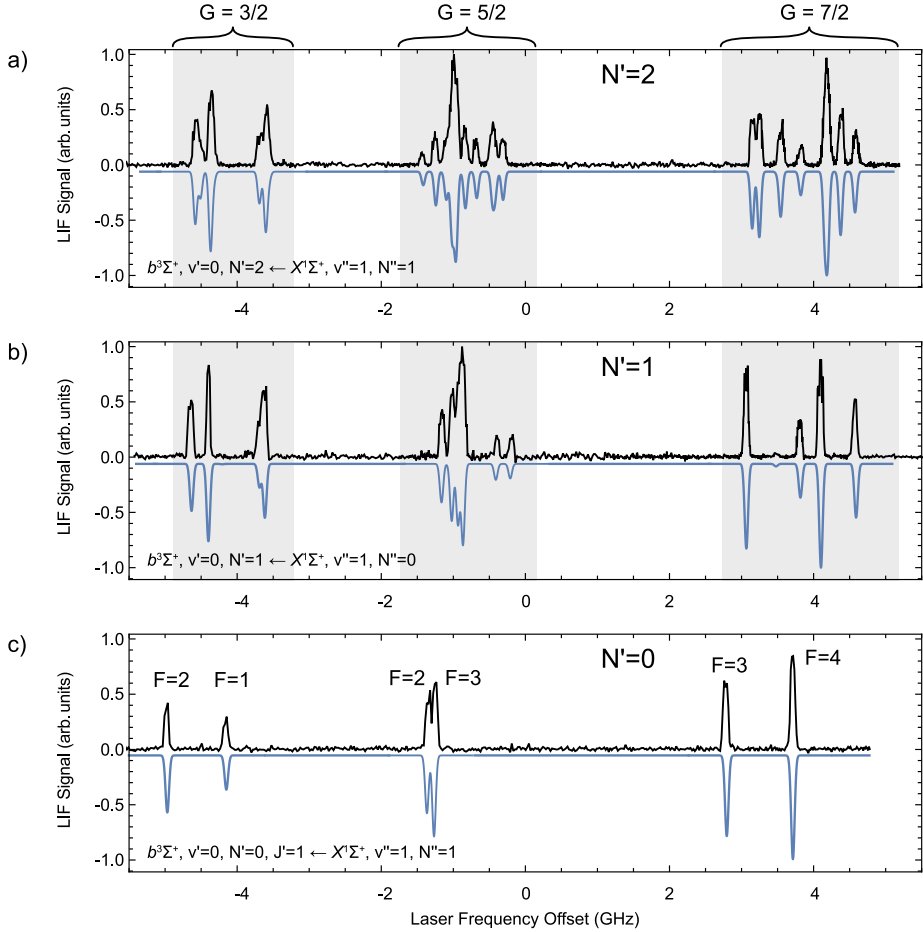


Figure 3.5: Direct measurement of the fine and hyperfine structure of the three lowest rotational levels in the $b^3\Sigma^+$ state, i.e. for $N' = 0$ in panel c), $N' = 1$, in panel b) and $N' = 2$ in panel a). The experimental data are shown in black, pointing up and the simulated spectra are shown in blue, pointing down. The spectra are centred at the gravity centre, i.e., the line position in absence of hyperfine, spin-spin and spin-rotation interaction.

$$H = AL_zS_z + \frac{2}{3}\lambda(3S_z^2 - \mathbf{S}^2). \quad (3.2)$$

The interval between the $\Omega = 0$ and $\Omega = 1$ manifolds is approximately $A - 2\lambda$, while the $\Omega = 1$ and $\Omega = 2$ manifolds are about $A + 2\lambda$ apart.

For this experiment we use the supersonic molecular beam setup introduced in section 3.3, with an additional LIF detector installed between the excitation region

and the TOF-MS. After passing through the skimmer, the molecules are excited on a specific rotational line of the $a^3\Pi, v' = 0 \leftarrow X^1\Sigma^+, v'' = 0$ band to one of the three spin-orbit manifolds, using a frequency-doubled pulsed dye amplifier (PDA), which is seeded by a cw titanium sapphire laser. About 30 cm further downstream, a cw ring dye laser intersects the molecular beam orthogonally and is scanned over a rotational line of the $b^3\Sigma^+, v' = 0 \leftarrow a^3\Pi, v'' = 0$ band. The laser frequency is stabilised and scanned with respect to a frequency-stabilised and calibrated HeNe reference laser (SIOS SL 03), using a scanning transfer cavity. The wavelength is recorded with an absolute accuracy of 10 MHz using the wavemeter, calibrated by the same HeNe laser.

Figure 3.6 shows hyperfine-resolved LIF excitation spectra of the $b^3\Sigma^+, v' = 0 \leftarrow a^3\Pi, v'' = 0$ band. Figure 3.6a shows the hyperfine spectrum of the $b^3\Sigma^+, v' = 0, N' = 1 \leftarrow a^3\Pi_0, v'' = 0, J'' = 0$ lines. The positive parity Λ -doublet level of $a^3\Pi_0, J = 0$ has only two hyperfine components with total angular momentum quantum numbers $F = 2$ and $F = 3$ that are only split by about 3 MHz, much smaller than the residual Doppler broadening in the molecular beam. Therefore, this $b^3\Sigma^+ \leftarrow a^3\Pi$ spectrum directly reflects the energy level structure in the $b^3\Sigma^+$ state and is identical to the one of the $b^3\Sigma^+ \leftarrow X^1\Sigma^+$ spectrum shown in figure 3.5b.

The spectrum of the $b^3\Sigma^+, v' = 0, N' = 2 \leftarrow a^3\Pi_1, v'' = 0, J'' = 1$ transition, presented in figure 3.6b, shows a richer structure, and no longer directly reflects the energy level structure in the $b^3\Sigma^+$ state. The total span of the hyperfine splitting in the $a^3\Pi_1, v = 0, J = 1$ level is about 500 MHz [167], and contributes to the complexity of this spectrum.

Optical pumping to the $a^3\Pi_2, v = 0$ state is challenging because the $R_3(1)$ transition of the $a^3\Pi_2, v' = 0 \leftarrow X^1\Sigma^+, v'' = 0$ band is about 1000 times weaker than the corresponding $R_2(1)$ line to the $a^3\Pi_1$ state. Only a small fraction of the ground-state molecules produced in the source is transferred to the $a^3\Pi_2, v = 0$ level, even with a PDA pulse energy of about 10 mJ in beam with a e^{-2} waist radius of 1.5 mm. Figure 3.6c shows the $R_3(1)$ line of the $a^3\Pi_2, v' = 0 \leftarrow X^1\Sigma^+, v'' = 0$ band, recorded by scanning the seed laser of the frequency-doubled PDA, followed by (1+2)-REMPI and TOF-MS detection. The hyperfine structure in $a^3\Pi_2, v = 0$ is very large and it is possible to resolve six of the ten hyperfine levels using a narrow-band pulsed laser. This enables us to populate a specific hyperfine component of the $a^3\Pi_2, v = 0, J = 2$ level, which is then followed by cw excitation to the $b^3\Sigma^+$ state and LIF detection. Figure 3.6d shows two LIF spectra that originate from two different hyperfine states in $a^3\Pi_2$, indicated by the two colours. The green spectrum originates from the $a^3\Pi_2, v = 0, J = 2, F = 4$ level and the grey spectrum from the $a^3\Pi_2, v = 0, J = 2, F = 5$ level. The line-centres are determined by fitting Gaussians to the spectral lines.

The hyperfine structure and Λ -doubling of the $a^3\Pi$ state has been investigated extensively in our previous study and is known to kHz precision [167]. However, the constants A and λ of the $a^3\Pi$ state could only be determined with an accuracy of about 200 MHz, due to the finite bandwidth of the pulsed laser and the lower accuracy of the wavemeter that was used in that study to measure the relative energy of the Ω manifolds. Here, we take advantage of the reduced linewidth in

the cw LIF spectra of the $b^3\Sigma^+a^3\Pi$ transition, in combination with the increased accuracy of our new wavemeter, to improve this measurement and therefore the spectroscopic constants A and λ . By using the hyperfine constants for the $a^3\Pi$ state from reference [167] in combination with the parameters for the $b^3\Sigma^+$ state, listed in Table 3.1, the $b^3\Sigma^+a^3\Pi$ spectra can be simulated, and new values for A and λ are derived. The simulated spectra, using the full Hamiltonian and including the hyperfine interactions in both states, are shown in figure 3.6 as blue, inverted curves. The uncertainty of the improved spectroscopic constants, listed in Table 3.3, is reduced by nearly two orders of magnitude compared to the ones presented previously [167]. E_0 is the term energy of the $a^3\Pi$ state in the absence of rotation, fine and hyperfine structure, calculated by using the term energy of the $b^3\Sigma^+$ state determined in the previous section. This means that the gravity centre, i.e. the position of the $a^3\Pi_1, v = 0, J = 1$ level in the absence of hyperfine structure, relative to the $X^1\Sigma^+, J = 0$ level is at $27255.1737(5)$ cm^{-1} .

It is also possible to record the LIF excitation spectra by detecting the weak UV fluorescence, on the $b^3\Sigma^+, v' = 0 \rightarrow X^1\Sigma^+, v''$ bands which occurs predominantly at 223.1 nm. Part of the spectrum displayed in figure 3.6b has also been recorded this way and is shown by the inset labelled ‘UV’. To measure the ratio of the emission occurring in the UV, relative to the emission occurring in the visible, we lock the excitation laser to the resonance indicated by the arrow in 3.6b and average the signal over 1000 shots. To distinguish the two wavelengths, we use two different PMTs: a UV sensitive one with a specified quantum efficiency of 0.35 ± 0.05 at 223.1 nm and negligible sensitivity for wavelengths > 350 nm and a second PMT with a specified quantum efficiency of 0.1 ± 0.015 at 569 nm that is sensitive in the range of 200 – 800 nm. The quantum efficiencies of the PMTs are taken from the data sheet and are not calibrated further. However, three identical UV PMTs give the same photon count rate to within 15% which we take as the systematic uncertainty. Both PMTs are operated in photon-counting mode, counting the number of UV and visible photons, n_{uv} and n_{vis} , respectively. The visible PMT is combined with a band-pass interference filter to block the UV fluorescence and a small amount of phosphorescence on the $a^3\Pi, v' = 0 \rightarrow X^1\Sigma^+, v'' = 0$ transition near 367 nm. The measured transmission of the filter at 569 nm is 0.57. We combine the slightly different transmission through the imaging optics, the different detector efficiencies and the filter transmission into the total detection efficiencies η_{uv} and η_{vis} . Including these values, we measure a ratio of

$$R_b = \frac{n_{\text{uv}} \eta_{\text{vis}}}{n_{\text{vis}} \eta_{\text{uv}}} = (4.3 \pm 1.3) \times 10^{-3}. \quad (3.3)$$

This is the result of multiple experimental runs with a statistical error that is significantly smaller than the uncertainty in the quantum efficiencies of the PMTs. An additional 20% systematic uncertainty is added to the total error budget because we do not correct for the spherical and chromatic aberration of the fluorescence detector. However, simulations using ray-tracing software show a typical difference in imaging efficiency for the two wavelengths of about 10%. The value for R_b is identical to the ratio of the Einstein A -coefficients for $b^3\Sigma^+ \rightarrow X^1\Sigma^+$ and $b^3\Sigma^+ \rightarrow a^3\Pi$ emission, i.e. $R_b = A_{b,X}/A_{b,a}$. The specific level in the $b^3\Sigma^+, v = 0$

state for which this ratio of Einstein A -coefficients is determined, is the positive parity level with $N = 2$, $F = 4$, $n = 4$ which is almost a pure f -level, with 42.3% \mathcal{F}_3 and 57.4% \mathcal{F}_1 character, and only 0.3% \mathcal{F}_2 character. The level is highlighted in red in table 3.2 and figure 3.4.

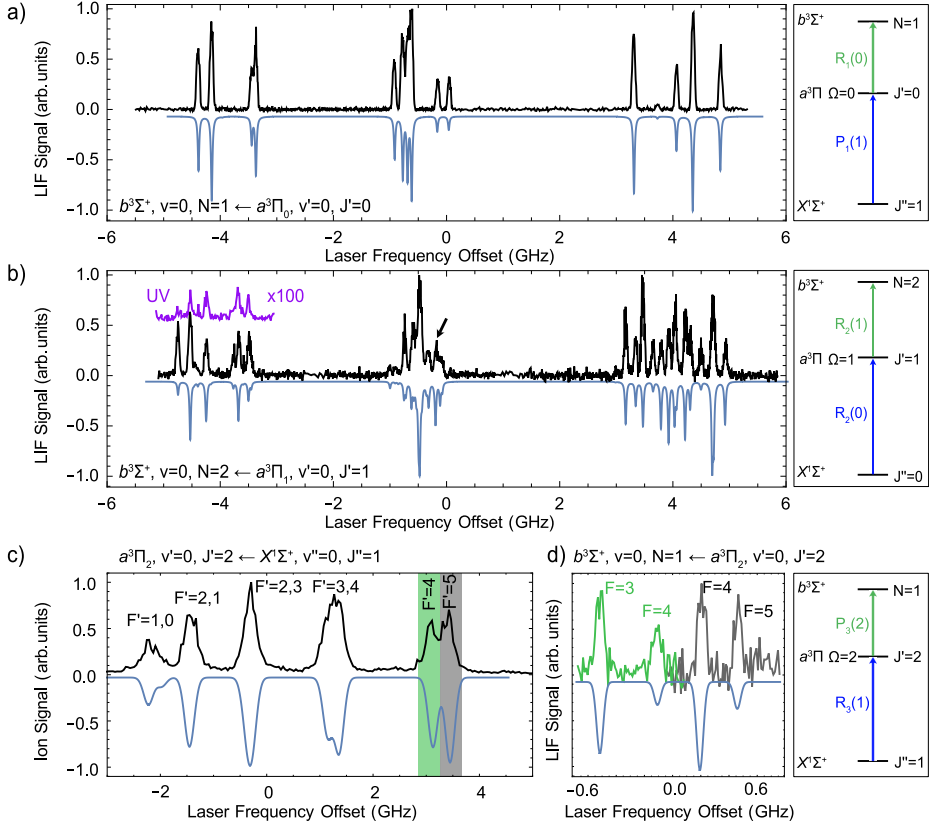


Figure 3.6: LIF excitation spectra of the $b^3\Sigma^+ - a^3\Pi$ transition. Panels a) and b) show spectra of the $b^3\Sigma^+, v' = 0, N' = 1 \leftarrow a^3\Pi_0, v'' = 0, J'' = 0$ and $b^3\Sigma^+, v' = 0, N' = 2 \leftarrow a^3\Pi_1, v'' = 0, J'' = 1$ transitions, respectively. The spectrum in the inset labelled UV is detected by recording the emission on the $b^3\Sigma^+, v = 0, N = 2 \rightarrow X^1\Sigma^+, v''$ bands as a function of the excitation frequency. c) Hyperfine resolved spectrum of the $R_3(1)$ line of the $a^3\Pi, v' = 0 \leftarrow X^1\Sigma^+, v'' = 0$ band, showing the large hyperfine splitting in $a^3\Pi_2$. d) Part of the hyperfine resolved spectrum of the $b^3\Sigma^+, v' = 0, N' = 1 \leftarrow a^3\Pi_2, v'' = 0, J'' = 2$ transition. The low (high) frequency part of this spectrum was recorded after excitation to the $F = 4$ ($F = 5$) component of the $R_3(1)$ line of the $a^3\Pi \leftarrow X^1\Sigma^+$ transition. a) - d): The relevant energy level scheme is displayed next to each spectrum. Since J is not well-defined in the $b^3\Sigma^+$ state, the $b^3\Sigma^+ \leftarrow a^3\Pi$ transitions are labelled with $\Delta(NJ)_{\mathcal{F}'(J')}$. The measured spectra are printed in black, while the simulated spectra are shown in blue and inverted.

Table 3.3: Spectroscopic constants for the $a^3\Pi, v = 0$ state of AlF, determined from a fit to the spectra. E_0 is the energy of the electronic state in the absence of rotation, fine- and hyperfine structure relative to the $X^1\Sigma^+, v = 0, J = 0$ level (in cm^{-1}). The spin-orbit coupling constant, A , and the spin-spin interaction constant, λ , are given in MHz. Their respective values from our earlier publication [167] are also reproduced for comparison.

Parameter	Value	SD	Value [167]	SD
E_0	27253.0507	0.0005	27253.04	0.01
A	1421089	5	1420870	210
λ	2766	4	2659	33

3.6 The $A^1\Pi \rightarrow a^3\Pi$ Bands

To probe the amount of triplet wave function that is mixed into the $A^1\Pi$ state directly, we measure the ratio R_A of the number of fluorescence photons emitted on the $A^1\Pi \rightarrow a^3\Pi$ and on the $A^1\Pi \rightarrow X^1\Sigma^+$ transition. The value for R_A is identical to the ratio of the Einstein A -coefficients for $A^1\Pi \rightarrow a^3\Pi$ and $A^1\Pi \rightarrow X^1\Sigma^+$ emission, i.e., $R_A = A_{A,a}/A_{A,X}$. The value for R_A gives the loss from the main laser cooling cycle due to electronic branching to the $a^3\Pi$ state. Previously, we measured this electronic branching ratio on the $A^1\Pi \rightarrow a^3\Pi$ bands indirectly to be at the 10^{-7} level, by comparing the absorption-strength of the $A^1\Pi, v = 0 \leftarrow a^3\Pi_0, v' = 0$ transition relative to the absorption-strength of the $A^1\Pi, v = 0 \leftarrow X^1\Sigma^+, v'' = 0$ transition (see chapter 2.6.3) [167]. In that analysis we only took into account the amount of singlet character in the wave function of the $a^3\Pi$ state to deduce the strength of the $A \leftarrow a$ transition. We did not account for the (then unknown) amount of triplet character in the wave function of the $A^1\Pi$ state due to the interaction of the $A^1\Pi$ and $b^3\Sigma^+$ states, which, as we will see here, turns out to be the dominant effect.

The ratio R_A is determined by directly recording the fluorescence at 227.5 nm as well as 599 nm in a well-characterised experimental setup with narrow wavelength selecting elements in front of the PMT detectors. The details of this experiment will be presented in the forthcoming Ph.D. thesis of Simon Hofsäss [193].

The ratio of Einstein coefficients is determined from a measurement using optical cycling on the Q(1) line of the $A^1\Pi-X^1\Sigma^+$ transition to be

$$R_A = \frac{n_{\text{vis}} \eta_{\text{uv}}}{n_{\text{uv}} \eta_{\text{vis}}} = (6 \pm 2) \times 10^{-7}, \quad (3.4)$$

where n_{vis} and n_{uv} are the number of photons detected in the visible and UV, respectively.

The measurement of R_A is significantly more challenging than the measurement of R_b . This is because n_{uv} is 10^7 times larger than n_{vis} and the phosphorescence of the optical elements typically occurs red-shifted, i.e., in the wavelength

range of the weak fluorescence in the visible. This is in contrast to the measurement of R_b , for which n_{uv} is about 200 times smaller than n_{vis} , and for which any background caused by phosphorescence of the optical elements is absent.

We also measure the ratio of the visible to the UV fluorescence following excitation on the Q(1) line of the 1 – 1 band of the $A^1\Pi-X^1\Sigma^+$ transition. Since the $A^1\Pi, v = 1$ level is energetically much closer to the $b^3\Sigma^+, v = 0$ level, one might expect a significantly larger fraction of visible fluorescence. However, we find that the two ratios R_A are equal to within the 15% uncertainty of the measurement.

3.7 Spin-Orbit Interaction Between the $A^1\Pi$ and $b^3\Sigma^+$ States

The observation of the $b^3\Sigma^+, v' = 0 \leftrightarrow X^1\Sigma^+, v''$ and of the $A^1\Pi, v' = 0 \rightarrow a^3\Pi, v''$ intersystem bands reported here indicates that the wave function of the $b^3\Sigma^+$ state of AlF contains a fraction of singlet character and that the $A^1\Pi$ state contains a fraction of triplet character. This is due to the spin-orbit interaction of the $b^3\Sigma^+$ state with the nearby $A^1\Pi$ state. Figure 3.7 shows the potential energy curves for the lowest singlet and triplet electronic states of AlF. The inset shows a more detailed view of the $A^1\Pi$ and $b^3\Sigma^+$ states with their vibrational levels indicated. For low vibrational quantum numbers, the vibrational level v_b in the $b^3\Sigma^+$ state lies slightly above the vibrational level $v_A = v_b + 1$ in the $A^1\Pi$ state. The energy difference between v_b and $v_A = v_b + 1$ decreases with increasing vibrational quantum numbers until the levels have just crossed and are nearly degenerate at $v_A = 6$ ($v_b = 5$), leading to a large perturbation of the rotational energy levels. This interaction has already been analysed by Barrow *et al.* in 1974, who introduced the parameter $H_0(v_A)$ to describe the effect of the spin-orbit interaction of specific pairs of vibrational levels, i.e., of $v_A = 4, 5$ and 6 with $v_b = 3, 4$ and 5 , respectively [144]. They used the observed perturbation to determine the energy of the triplet manifold relative to the singlet manifold with an accuracy of 0.05 cm^{-1} .

In this section we give a more general description of the spin-orbit interaction between the $A^1\Pi, v_A$ state and the $b^3\Sigma^+, v_b$ state. We deduce the expressions for R_b and R_A in terms of the spin-orbit coupling constant A_{so} between the $A^1\Pi$ and the $b^3\Sigma^+$ state, to experimentally determine the value for A_{so} . This is then compared to the value of A_{so} that can be deduced from the $H_0(v_A)$ parameters as given by Barrow and co-workers [144]. The effect of the interaction on the rotational energy levels in the $A^1\Pi, v = 0$ and $b^3\Sigma^+, v = 0$ states is also discussed.

For the spin-orbit interaction of a $^1\Pi$ state with a $^3\Sigma^+$ state, the interaction terms between the e - and f -levels belonging to a given J are given by [194]:

$$H(^1\Pi, f|^3\Sigma^+, \mathcal{F}_1) = \sqrt{\frac{J+1}{2J+1}} \frac{\xi}{\sqrt{2}} \quad (3.5)$$

$$H(^1\Pi, e|^3\Sigma^+, \mathcal{F}_2) = -\frac{\xi}{\sqrt{2}} \quad (3.6)$$

$$H(^1\Pi, f|^3\Sigma^+, \mathcal{F}_3) = \sqrt{\frac{J}{2J+1}} \frac{\xi}{\sqrt{2}}. \quad (3.7)$$

In the Born-Oppenheimer approximation, the parameter ξ only depends on the vibrational wave functions of the coupled states and can be written in terms of the spin-orbit operator H_{so} as

$$\xi(v_A, v_b) = \langle \Psi_{A,v_A} | H_{so} | \Psi_{b,v_b} \rangle = A_{so} \int \phi_{b,v_b}^*(\rho) \phi_{A,v_A}(\rho) d\rho = A_{so} \sqrt{q_{v_A v_b}}. \quad (3.8)$$

The expressions $\phi_{b,v_b}(\rho)$ and $\phi_{A,v_A}(\rho)$ are the vibrational wave functions for the $b^3\Sigma^+$ and $A^1\Pi$ state, respectively, and ρ is the inter-nuclear distance between the Al and F atoms. The square of the expression for the integral is the Franck-Condon factor $q_{v_A v_b}$ between the A, v_A and b, v_b levels. The Franck-Condon matrix between the $A^1\Pi$ and $b^3\Sigma^+$ states is very diagonal. The value of q_{00} is very close to one and even though the $v = 0$ levels of both states are about $(E_{b,0} - E_{A,0}) = 855 \text{ cm}^{-1}$ apart, the interaction between these levels dominates. The value of q_{10} is much smaller than one, but as the $v_b = 0$ and $v_A = 1$ levels are only $(E_{b,0} - E_{A,1}) = 63 \text{ cm}^{-1}$ apart, this interaction also has to be taken into account. The interaction with all the other vibrational levels can be neglected.

3.7.1 Intensities of the Intersystem Bands

The spin-orbit interaction between the $A^1\Pi$ state and the $b^3\Sigma^+$ state mixes their wave functions and causes a shift of the rotational levels. If the interacting levels are much further apart than the magnitude of the interaction terms, we can calculate the effect of the interaction using first order perturbation theory. In this case, the contribution to the wave function of the $A^1\Pi, v = 0$ ($b^3\Sigma^+, v = 0$) state due to the interaction with the $b^3\Sigma^+$ ($A^1\Pi$) state is given by the interaction term divided by the energy separation of the interacting levels. The wave function of the $A^1\Pi$ state can be written as:

$$|\Psi'_{A,0}\rangle = C_{A,0}^s |\Psi_{A,0}\rangle + C_{A,0;b,0}^t |\Psi_{b,0}\rangle, \quad (3.9)$$

where $|C_{A,0}^s| \approx 1$, is the total amount of singlet character and where $|C_{A,0;b,0}^t| \equiv |C_{A,0}^t|$ is the total amount of triplet character in the wave function of the $A^1\Pi$ state. It is readily seen from the interaction terms given above that the triplet contribution to the wave functions of the e - and f -levels is equal, does not depend on J , and is given by

$$|C_{A,0}^t| = \frac{A_{so} \sqrt{q_{00}}}{\sqrt{2}(E_{b,0} - E_{A,0})}. \quad (3.10)$$

The wave function of the $b^3\Sigma^+$ state can be written as:

$$|\Psi'_{b,0}\rangle = C_{b,0}^t |\Psi_{b,0}\rangle + C_{b,0;A,0}^s(J, \mathcal{F}_i) |\Psi_{A,0}\rangle + C_{b,0;A,1}^s(J, \mathcal{F}_i) |\Psi_{A,1}\rangle, \quad (3.11)$$

where $|C_{b,0}^t| \approx 1$ is the total amount of triplet character and

$$\sqrt{|C_{b,0;A,0}^s(J, \mathcal{F}_i)|^2 + |C_{b,0;A,1}^s(J, \mathcal{F}_i)|^2} \equiv |C_{b,0}^s(J, \mathcal{F}_i)|$$

is the total amount of singlet character in the wave function of the $b^3\Sigma^+$ state. The singlet contribution to the wave function of the $b^3\Sigma^+$ state depends on the (J, \mathcal{F}_i) ($i = 1, 2, 3$) level. For the positive parity, $N = 2$, $F = 4$, $n = 4$ level that we used for the measurement of R_b we find, using the weights W^J as indicated in figure 3.4 ($W_1^J = 42.3\%$, $W_2^J = 0.3\%$ and $W_3^J = 57.4\%$),

$$|C_{b,0}^s| = 0.69 \frac{A_{so}}{\sqrt{2}} \sqrt{\frac{q_{00}}{(E_{b,0} - E_{A,0})^2} + \frac{q_{10}}{(E_{b,0} - E_{A,1})^2}}. \quad (3.12)$$

The expression for R_A can now be rewritten as:

$$R_A = \frac{A_{A,a}}{A_{A,X}} = \frac{|\langle \Psi'_{A,0} | \mu(r) | \Psi_{a,0} \rangle|^2 \lambda_{A,X}^3}{|\langle \Psi'_{A,0} | \mu(r) | \Psi_{X,0} \rangle|^2 \lambda_{A,a}^3} = |C_{A,0}^t|^2 \frac{A_{b,a} \lambda_{b,a}^3}{A_{A,X} \lambda_{A,a}^3} = \frac{|C_{A,0}^t|^2}{116}, \quad (3.13)$$

where $\mu(r)$ is the electronic transition dipole moment, $\lambda_{b,a} = 569$ nm, $\lambda_{A,a} = 599$ nm are the wavelengths of the $b^3\Sigma^+ - a^3\Pi$ and $A^1\Pi - a^3\Pi$ transitions, respectively. The ratio of the Einstein A -coefficients is calculated from the experimentally known lifetimes of the $A^1\Pi$ state (1.90 ns, [167]) and of the $b^3\Sigma^+$ state (190 ns, Section 3.3). The expression for R_b can now be rewritten as:

$$R_b = \frac{A_{b,X}}{A_{b,a}} = \frac{\sum_{i=0}^1 |\langle \Psi'_{b,0} | \mu(r) | \Psi_{X,i} \rangle|^2 \lambda_{b,a}^3}{|\langle \Psi'_{b,0} | \mu(r) | \Psi_{a,0} \rangle|^2 \lambda_{b,X}^3} = |C_{b,0}^s|^2 \frac{A_{A,X} \lambda_{A,X}^3}{A_{b,a} \lambda_{b,X}^3} = 106 |C_{b,0}^s|^2, \quad (3.14)$$

where $\lambda_{A,X} = 227.5$ nm and $\lambda_{b,X} = 223$ nm. The sum in the numerator results in the two terms given in equation 3.12, because the Franck-Condon matrix between the $A^1\Pi$ and $X^1\Sigma^+$ states is highly diagonal.

The parameter $H_0(v_A)$, introduced by Barrow and co-workers, describes the effect of the spin-orbit interaction between two specific vibrational levels and is equivalent to

$$H_0(v_A) = \frac{\xi(v_A, v_b = v_A - 1)}{\sqrt{2}} = A_{so} \sqrt{\frac{q_{v_A v_A - 1}}{2}}. \quad (3.15)$$

Barrow and co-workers did not discuss the dependence of the values for $H_0(v_A)$ on the square root of the Franck-Condon factors, and they therefore did not extract a single value for the spin-orbit interaction parameter A_{so} from the three values of $H_0(v_A)$ that they reported [144].

In the following, we determine the Franck-Condon factors $q_{v_A v_b}$ and A_{so} from

the measured $H_0(v_A)$ values [144], and then use these Franck-Condon factors to extract a value for A_{so} from our measurements of R_A and R_b . For this, a Morse potential is fitted to the term-values of the vibrational levels in the $A^1\Pi$ and $b^3\Sigma^+$ state, as listed in [144]. The parameters of the Morse potential are optimised to reproduce the measured vibrational levels to better than 0.3 cm^{-1} . This optimisation is independent of the equilibrium distance r_e . Next, the difference between the equilibrium distances of the $A^1\Pi$ and $b^3\Sigma^+$ state, $\Delta r_e = r_e(A) - r_e(b)$, is optimised such that the vibrational level dependence of $\sqrt{q_{v_A v_A - 1}}$ agrees with the observed vibrational level dependence of $H_0(v_A)$. We find the best agreement for $\Delta r_e = 0.0046 \text{ \AA}$, about half the value for Δr_e extracted from the reported values for B_e in the $A^1\Pi$ and $b^3\Sigma^+$ state [144] of 0.0094 \AA . Finally, we fit to the experimentally determined rotational constants reported in [144] using only $r_e(A)$ as a fit parameter. The data is reproduced to within 1% for $r_e(A) = 1.63098 \text{ \AA}$. Considering the simple model for the potentials, this is an excellent agreement. The value for A_{so} determined from this fitting procedure is $A_{so} = 8.9 \text{ cm}^{-1}$ and the corresponding Franck-Condon matrix is shown in Table 3.4. The uncertainty in the value of A_{so} is difficult to determine, as the main contribution to the total uncertainty stems from the assumption that the potentials can be approximated by Morse potentials. We estimate this uncertainty to be at least 2.5 cm^{-1} .

Table 3.4: Calculated Franck-Condon factors between the $A^1\Pi$ state and the $b^3\Sigma^+$ state. The elements highlighted in red are used to predict the three measured values for $H_0(v_A)$ given in [144].

$v_A \setminus v_b$	0	1	2	3	4	5	6
0	0.9936	0.0012	0.0051	0.0002	0.0000	0.0000	0.0000
1	0.0010	0.9831	0.0005	0.0144	0.0010	0.0000	0.0000
2	0.0051	0.0003	0.9650	0.0000	0.0264	0.0031	0.0000
3	0.0003	0.0142	0.0002	0.9364	0.0024	0.0391	0.0073
4	0.0001	0.0008	0.0267	0.0023	0.8950	0.0102	0.0498
5	0.0000	0.0004	0.0014	0.0425	0.0078	0.8390	0.0260
6	0.0000	0.0001	0.0009	0.0019	0.0615	0.0168	0.7680

Using the information from the Franck-Condon matrix shown in Table 3.4, the experimental value of $R_A = (6 \pm 2) \times 10^{-7}$ implies a value for $A_{so} = (10 \pm 2) \text{ cm}^{-1}$. The value of $R_b = (4.3 \pm 1.3) \times 10^{-3}$ implies a value for $A_{so} = (10.4 \pm 1.5) \text{ cm}^{-1}$. These two values for A_{so} , as well as the value for A_{so} extracted from the $H_0(v_A)$ values, all overlap within their error bars, yielding a final experimental value for $A_{so} = (10.0 \pm 1.1) \text{ cm}^{-1}$.

As mentioned in the previous section, we observe that the ratio of the visible to the UV fluorescence that is emitted from the $A^1\Pi, v = 1$ level is equal to that from the $A^1\Pi, v = 0$ level. Based on the derivation presented in this section we expect that the fractional emission in the visible from the $A^1\Pi, v = 1$ level is larger than the emission from the $A^1\Pi, v = 0$ level by a factor of

$$\left(\frac{E_{b,0} - E_{A,0}}{E_{b,1} - E_{A,1}}\right)^2 \frac{q_{11}}{q_{00}} + \left(\frac{E_{b,0} - E_{A,0}}{E_{b,0} - E_{A,1}}\right)^2 \frac{q_{10}}{q_{00}} = 1.23, \quad (3.16)$$

where the energy difference $(E_{b,1} - E_{A,1}) = 834 \text{ cm}^{-1}$, and where the values for the Franck-Condon factors are taken from Table 3.4. The predicted 23% increase in visible fluorescence is consistent with the experimental observation, within the experimental uncertainty of 15%. This highlights that the spin-orbit mixing is dominated by the interaction between vibrational levels that have the same vibrational quantum number.

3.7.2 Effect on the Fine Structure in the $b^3\Sigma^+, v = 0$ State

In first order perturbation theory, the shift of the energy levels is given by the square of the interaction matrix elements, divided by the energy separation of the interacting levels. The interaction is repulsive, and for the $A^1\Pi, v = 0$ state all rotational levels shift downwards by $A_{so}^2 q_{00} / [2(E_{b,0} - E_{A,0})]$. Such an overall shift is difficult to determine, and is absorbed in the value for the term-energy. In the $b^3\Sigma^+, v = 0$ state, the e -levels will all be shifted upward by about the same amount, but the f -levels will have a lower, J -dependent shift. ‘Curiously’, Hebb wrote originally in 1936, the shift of the levels in a $^3\Sigma^+$ state due to the spin-orbit interaction with a $^1\Pi$ state has the same J -dependence as the shift due to the spin-spin and spin-rotation interaction, and both effects cannot be distinguished [195]. The origin of the spin-spin and spin-rotation interaction in a $^3\Sigma$ state has first been described in a classic paper by Kramers [196], and more general expressions have been given soon after that by Schlapp [197]. Normally, the spin-spin and spin-rotation interactions are expected to be the dominant effects and the spin-orbit interaction with a nearby $^1\Pi$ state is expected to be only a second order correction. Both effects add up, and this means that the values for λ and γ as found from fitting the energy levels in the $b^3\Sigma^+, v = 0$ state should actually be interpreted as

$$\lambda = \lambda_{ss} + \frac{A_{so}^2 q_{00}}{4(E_{b,0} - E_{A,0})} \quad (3.17)$$

$$\gamma = \gamma_{sr} + \frac{BA_{so}^2 q_{00}}{2(E_{b,0} - E_{A,0})^2} \quad (3.18)$$

where λ_{ss} and γ_{sr} describe the contribution due to the spin-spin and spin-rotation interaction in the $b^3\Sigma^+$ state, respectively, and where the additional terms describe the contribution due to the spin-orbit interaction with the nearby $A^1\Pi$ state.

When we take the final experimental value for A_{so} , then the spin-orbit contribution to λ amounts to about +900 MHz. We conclude therefore that the value for λ_{ss} in the $b^3\Sigma^+, v = 0$ state is about -1800 MHz, and that about half of this value is cancelled by the spin-orbit interaction with the nearby $A^1\Pi$ state. The spin-orbit contribution to γ amounts only to +1.1 MHz, and this contribution can be neglected. For higher vibrational levels in the $b^3\Sigma^+$ state a slightly different behaviour is expected. The spin-orbit contribution to λ remains about +900 MHz for $v_b = 0 - 3$, but increases to about +1200 MHz for $v_b = 4$ due to the near-resonant interaction with the $v_A = 5$ level. For the $v_b = 6$ level, the near-resonant contribution to λ due to spin-orbit interaction with the $v_A = 7$ level is negative,

reducing the total spin-orbit contribution to λ to about +600 MHz. The $v_b = 5$ level is special, as the \mathcal{F}_3 levels of the $b^3\Sigma^+$ -state and the f -levels of $A, v_A = 6$ cross, between $J = 1$ and $J = 2$, making an interpretation in terms of a contribution to λ less meaningful. It is interesting to note that this crossing causes the J -levels that belong to low N -values in the $b^3\Sigma^+, v = 5$ state to be split considerably further than for the $b^3\Sigma^+, v = 0$ state, making J a good quantum number. This strong interaction opens a ‘doorway’ to efficiently drive transitions between the singlet and triplet manifolds [198, 199] and when J is a good quantum number, this can be done highly rotationally selective [200].

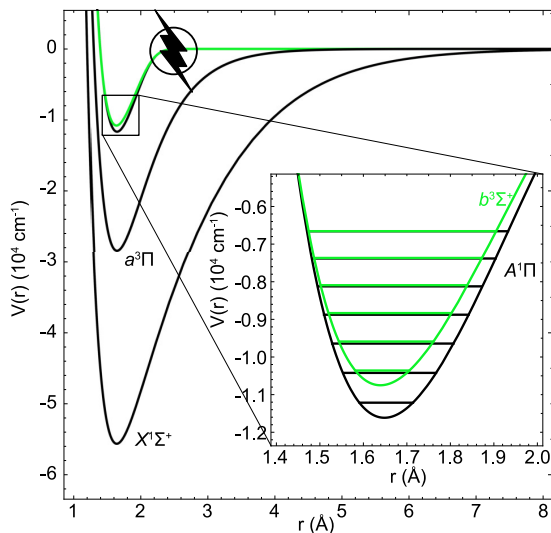


Figure 3.7: Calculated potential energy curves for the lowest singlet and triplet electronic states of AlF, using precise Expanded Morse Oscillator (EMO) functions. We obtain these EMO potentials by fitting to the point-wise RKR potentials generated by LeRoy’s program [143] and adjust the parameters to predict the vibrational levels with a high accuracy of 0.05 cm^{-1} (using the non-perturbed or de-perturbed values from the appendix from [144]) and from [145]. These potentials are much more precise than the simple Morse model we use in section 3.7, but do not allow us to treat the two electronic states independently to extract the spin-orbit interaction. *Ab initio* calculations indicate that the $A^1\Pi$ state has a barrier in the region marked with a flash, which cannot be reproduced with our EMO potentials. The inset shows a more detailed view of the $A^1\Pi$ and $b^3\Sigma^+$ potentials, with the vibrational levels indicated.

3.8 Conclusion

We investigated the $b^3\Sigma^+$ state of AlF and the spin-orbit interaction between this lowest electronically excited state in the triplet system and the first electronically excited singlet state, the $A^1\Pi$ state. First, we presented a low-resolution rotational spectrum of the $b^3\Sigma^+, v' = 0 \leftarrow a^3\Pi_1, v'' = 0$ transition and determined the radiative lifetime of the $b^3\Sigma^+, v = 0$ state to be 190(2) ns. Molecules in the $a^3\Pi, v = 0$ state can be efficiently detected using a (1+2)-REMPI scheme via the $b^3\Sigma^+, v = 0$ state even at relatively low laser intensity. Then, we used cw laser induced fluorescence excitation spectroscopy of the $b^3\Sigma^+, v' = 0 \leftarrow X^1\Sigma^+, v'' = 1$ transition to determine the fine and hyperfine structure of the $b^3\Sigma^+, v = 0$ state with a precision of about 10 MHz. The eigenvalues of the hyperfine Hamiltonian have been fitted to the experimentally determined line positions and all relevant spectroscopic constants have been determined. Hyperfine-resolved LIF spectra of the $b^3\Sigma^+, v' = 0 \leftarrow a^3\Pi, v'' = 0$ band, originating from all three spin-orbit manifolds in $a^3\Pi$, were used to improve the spin-orbit (A) and spin-spin (λ) interaction parameters that determine the relative spacing of the three Ω manifolds in the $a^3\Pi$ state.

Despite the highly-diagonal Franck-Condon matrix of the $b^3\Sigma^+ - a^3\Pi$ transition, laser cooling of AlF in the triplet manifold is challenging, due to the large number of rotational branches. This is further complicated by the spin-orbit interaction between the $A^1\Pi$ state and the $b^3\Sigma^+$ state, which is concluded to be governed by an interaction parameter A_{so} of about 10 cm^{-1} . The spin-orbit interaction mixes up to about 1% of the wave function of the $A^1\Pi$ state into the wave function of the hyperfine levels in the $v = 0$ level of the triplet state; the exact amount of mixing depends on the J, \mathcal{F}_i ($i = 1, 2, 3$) character of the hyperfine levels in the $b^3\Sigma^+$ state. By the same mechanism, about 1% of the wave function of the $b^3\Sigma^+$ state is mixed into the wave functions of the $A^1\Pi, v = 0$ state; the amount of triplet character is the same for all levels in the $A^1\Pi$ state. The triplet character of the $A^1\Pi, v = 0$ state, causes an $A^1\Pi, v = 0 \rightarrow a^3\Pi, v = 0$ loss below the 10^{-6} level from the main $A^1\Pi - X^1\Sigma^+$ laser cooling transition.

Chapter 4

Optical Cycling of AlF

4.1 Introduction

This chapter discusses calculations and experiments on optical cycling of AlF. The first part is dedicated to rate equation and optical Bloch equation modelling of multilevel systems. I further discuss the origin of dark states that can hinder optical cycling. In the second part, I present our measurement of the radiative lifetime of the metastable $a^3\Pi$ state and discuss the possibility of laser cooling of AlF to μK temperatures.

Our group performed experiments to measure the rate of optical cycling and could show deflection of a buffer-gas cooled molecular beam by radiation pressure force [88]. To understand the processes occurring in the experiment, we performed calculations that I present in the first part of this chapter. We want to model the experiment we performed as accurately as possible. The two experimental observables that we compare to calculations are:

- The number of scattered photons when a beam of AlF molecules with known forward velocity and velocity distribution interacts with a laser beam of known intensity profile at a single frequency with fixed polarisation.
- The resulting change in the transverse position of an AlF molecular beam interacting with such a laser.

In the first case, we must accurately determine the photon scattering rate as a function of the laser intensity; in the second case, we have to model the effect of momentum kicks arising due to the photon scattering on molecules in the beam.

Whilst the strong $A^1\Pi \leftarrow X^1\Sigma^+$ transition enables extremely large scattering forces to be exerted on the molecules, this large transition strength results in a temperature limit for Doppler cooling of about 2 mK. A cycling transition to a

Parts of this chapter are based on reference [88] – S. Hofsäss, *et al.*, “Optical cycling of AlF molecules.” In *New Journal of Physics* **23**(7), (2021), doi:10.1088/1367-2630/ac06e5, and reference [201] – N. Walter, *et al.*, “Spectroscopic characterisation of the $a^3\Pi$ state of aluminum monofluoride.” In *The Journal of Chemical Physics* **156**(12), (2022), doi:10.1063/5.0082601.

state with a long lifetime — often called a “narrow-line” transition — can then be used to further decrease the temperature down to the recoil limit. While the Doppler temperature is caused by heating from isotropic emission of many photons, the recoil temperature is caused by the energy from a single photon recoil. Narrow-line cooling is a very efficient technique and has been demonstrated for, e.g., strontium [202], calcium [203], ytterbium [150], and cadmium [151]. The $a^3\Pi$ state of AlF has a predicted lifetime in the ms range, which makes the $a^3\Pi - X^1\Sigma^+$ transition a suitable candidate for narrow-line cooling to the recoil limit. In the second part of this chapter, I present our measurement of the radiative lifetime of the $a^3\Pi_0$ and $a^3\Pi_1$ states in a pulsed-excitation//delayed-detection experiment. Based on this knowledge, we propose an experimental scheme for narrow-line cooling.

In sections 4.2 to 4.4 of this chapter, the states are labelled following the common convention of the laser cooling community, where excited state quantum numbers are designated with a prime (e.g. F') and ground state quantum numbers have no prime (e.g. F). In section 4.5 and all other chapters, the standard spectroscopic convention is used, where ground state quantum numbers have two primes (e.g. F'') and excited state quantum numbers have one prime (e.g. F').

4.2 Modelling Optical Cycling

Theoretical modelling of optical cycling in atoms and molecules is an essential tool to understand experimental results and to optimise experimental parameters.

Two theoretical approaches are common: a rate equation model or the full quantum mechanical treatment using the optical Bloch equations (OBE). For N energy levels, the rate equation model includes the solution of N equations, while there are $N(N-1)/2$ variables to solve for the OBEs. Therefore, the rate equation model is quicker and easier to solve. It yields useful information at low laser intensities and for the majority of the dynamics in magneto-optical traps. However, only the OBEs consider all quantum-mechanical coherences that are, for example, crucial to understand coherent dark states in the optical cycling process. These are especially important to study sub-Doppler cooling forces.

4.2.1 Rate Equations

Two-Level System

To start, it is instructive to study a rate equation model of the interaction of a monochromatic light field with a simple two-level system with spontaneous emission probability A and stimulated absorption and emission probability R , illustrated in figure 4.1a. The occupation probabilities for the lower (ground) and upper (excited) level are n_g and n_e , respectively. The pumping light is on reso-

nance with the transition. The rate equations are given by:

$$\begin{aligned}\frac{dn_g}{dt} &= -R(n_g - n_e) + An_e \\ \frac{dn_e}{dt} &= R(n_g - n_e) - An_e \\ 1 &= n_g + n_e.\end{aligned}\tag{4.1}$$

Solving the system of differential equations for the steady state, where $\frac{dn_g}{dt} = \frac{dn_e}{dt} = 0$, yields

$$n_e = \frac{R}{2R + A} = \frac{R/A}{1 + 2R/A}\tag{4.2}$$

The ratio $2R/A$ can be written as I/I_{sat} [204], where I is the laser intensity at the transition and I_{sat} is the two-level saturation intensity given by [205]

$$I_{\text{sat}} = \frac{\pi hc\Gamma}{3\lambda^3}.\tag{4.3}$$

In our two-level case, $\Gamma = A = 1/\tau$ is the spontaneous decay rate with τ being the spontaneous lifetime of the upper state. This results in the steady-state excited state population

$$n_e = \frac{1}{2} \frac{I/I_{\text{sat}}}{1 + I/I_{\text{sat}}}.\tag{4.4}$$

In the limit of high intensity, $I \gg I_{\text{sat}}$, the maximum excited state population is $n_e = 1/2$.

The steady-state scattering rate is defined by $R_{\text{ss}} = \Gamma n_e$, therefore the two-level steady state scattering rate is

$$R_{\text{ss}} = \frac{\Gamma}{2} \frac{I/I_{\text{sat}}}{1 + I/I_{\text{sat}}}.\tag{4.5}$$

If the light field is detuned from resonance by $\Delta = \omega - \omega_0$, I/I_{sat} must be scaled following a Lorentzian lineshape with full width at half maximum Γ [206]:

$$\left(\frac{I}{I_{\text{sat}}}\right)_{\text{eff}} = \frac{I}{I_{\text{sat}}} \frac{(\Gamma/2)^2}{\Delta^2 + (\Gamma/2)^2}\tag{4.6}$$

The steady-state scattering rate is then written as

$$\begin{aligned}
 R_{\text{ss}}(\Delta) &= \frac{\Gamma}{2} \frac{\frac{I}{I_{\text{sat}}} \frac{(\Gamma/2)^2}{\Delta^2 + (\Gamma/2)^2}}{1 + \frac{I}{I_{\text{sat}}} \frac{(\Gamma/2)^2}{\Delta^2 + (\Gamma/2)^2}} \\
 &= \frac{\Gamma}{2} \frac{I/I_{\text{sat}}}{\frac{\Delta^2 + (\Gamma/2)^2}{(\Gamma/2)^2} + I/I_{\text{sat}}} \\
 &= \frac{\Gamma}{2} \frac{I/I_{\text{sat}}}{1 + 4(\Delta/\Gamma)^2 + I/I_{\text{sat}}}.
 \end{aligned} \tag{4.7}$$

Multiple Ground States and Dark States

Before we consider the case of multiple states in the ground and excited states, it is also helpful to study the behaviour of a system with one excited state and several ground states, taken here as N_g . The ground states are coupled to the excited state via laser radiation, but are not coupled with each other. In this case, the rate equations are set up as [207]

$$\begin{aligned}
 \frac{dn_{g,j}}{dt} &= -R_j(n_{g,j} - n_e) + A_j n_e \\
 \frac{dn_e}{dt} &= \sum_{j=1}^{N_g} R_j(n_{g,j} - n_e) - \Gamma n_e \\
 1 &= n_e + \sum_{j=1}^{N_g} n_{g,j},
 \end{aligned} \tag{4.8}$$

where $n_{g,j}$ and n_e are the occupation probabilities of the ground states and the excited state, respectively. For a level j , R_j are the stimulated excitation and emission probabilities and A_j is the probability of spontaneous decay to this level j . Γ is defined as the sum of all A_j . The relative probability of one decay channel compared to the sum of all decay channels is called the branching ratio $p_i = A_i / \sum_j A_j = A_i / \Gamma$.

In the rate equations in (4.8), all transitions are resonant with the laser frequency: $R_j > 0$. If $R_j = 0$ for a state — either if the radiation is not resonant or the transition is not allowed — that state is called *dark*. For a three-level system with one excited state and one bright and one dark ground state with occupation probabilities n_e , n_g and n_d , respectively, the rate equations are then:

$$\begin{aligned}
 \frac{dn_g}{dt} &= -R_g(n_g - n_e) + A_g n_e \\
 \frac{dn_e}{dt} &= R_g(n_g - n_e) - (A_d + A_g)n_e \\
 \frac{dn_d}{dt} &= A_d n_e \\
 1 &= n_e + n_g + n_d,
 \end{aligned} \tag{4.9}$$

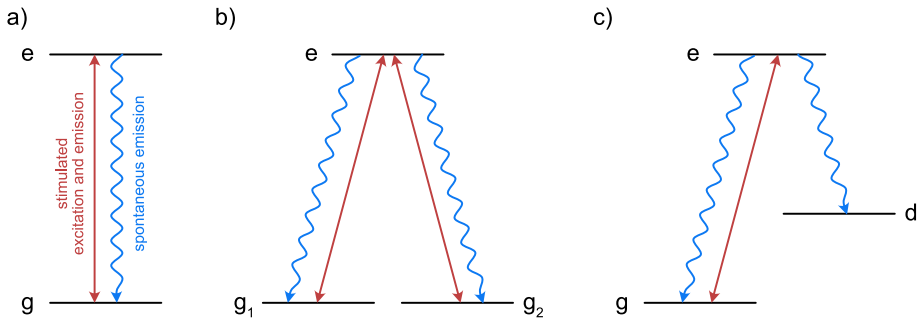


Figure 4.1: Energy level scheme for a two-level system on resonance (a), a three-level system on resonance (b), and a three-level system with one resonant ground state and one dark state (c).

where R_g is the excitation probability on the bright transition and A_g and A_d are the spontaneous decay probabilities to the bright and dark ground states, all of which are larger than zero. If we look at the steady state solution where the derivatives on the left sides are all zero, the third equation then immediately shows that $n_e = 0$ in the steady state. Substituting this in the first equation tells us that $n_g = 0$ and that, consequently, only the dark state is fully occupied and no photons are absorbed or emitted anymore. This result can also be easily expanded to the system with several bright ground states in (4.8). The excitation and decay channels for a three-level system with both ground states on resonance and with one dark state are illustrated in figures 4.1b and c. A more thorough discussion of different types of dark states based on quantum mechanics is presented in section 4.3.2 of this chapter.

Larger Systems

Rate equations can be set up for level systems of any size and different laser polarisations, as long as the respective transition probabilities between the involved states are known [205, 207, 208]. For the purpose of this chapter, discussing the full rate equations for such a level system is not necessary; it suffices to consider the excitation rate from ground to excited electronic states which determines the rate of photon scattering which is at the centre of the modelling of optical cycling.

For a system with substructure in the involved states, the excitation rates between a lower state l and an upper state u are given by: [205, 207, 208]

$$R_{l,u,p}(I_p) = \frac{\Gamma}{N_{\text{tot}}} \frac{f_{l,u,p} s_{p,\text{eff}}}{1 + s_{p,\text{eff}} + 4\Delta_{l,u,p}^2/\Gamma^2}, \quad (4.10)$$

where N_{tot} is the sum of all ground and excited states, p denotes the polarisation and Γ is the sum of the spontaneous decay probabilities on all channels. $\Delta_{l,u,p} = \omega_p - \omega_{l,u}$ is the detuning of the laser angular frequency ω_p from the resonance angular frequency $\omega_{l,u}$. The fractional transition strength of a dipole transition

$f_{l,u,p}$ can be calculated from the transition dipole moments between all lower and upper states ($\hat{\boldsymbol{\mu}}$ is the dipole moment operator and ϵ_p is the laser polarisation in the local coordinate system):

$$f_{l,u,p} = \frac{|\langle l | \hat{\boldsymbol{\mu}} \cdot \epsilon_p | u \rangle|^2}{\sum_k |\langle k | \hat{\boldsymbol{\mu}} | u \rangle|^2}. \quad (4.11)$$

The sum in the denominator is over all ground states. The saturation parameter is defined as $s_p = I_p/I_{\text{sat}}$. Here, we take into account that spontaneous emission can occur with σ^+ , π , and σ^- polarisation, while stimulated emission is fixed to the polarisation of the laser field [207]. The correction is included in the effective saturation parameter*

$$s_{p,\text{eff}} = s_p \frac{N_g + N_e}{6N_g}, \quad (4.12)$$

where N_g and N_e are the total number of ground and excited states, respectively. The total scattering rate is calculated as the sum over all hyperfine transitions:

$$R_{\text{tot}}(I_p) = \sum_{l,u} R_{l,u,p}(I_p). \quad (4.13)$$

4.2.2 Optical Bloch Equations

The optical Bloch equations can be derived from the Schrödinger equation and include all important quantum-mechanical properties. In the following, I use a two-level system to explain the fundamentals and then show how this has been expanded to treat multilevel systems.

This description is based on the books by Scully and Zubairy [209] and Foot [20]. Our starting point is the time-dependent Schrödinger equation

$$i\hbar \frac{d\Psi}{dt} = \hat{H}\Psi \quad (4.14)$$

and the Hamiltonian

$$\hat{H} = \hat{H}_0 + \hat{H}_I(t), \quad (4.15)$$

where \hat{H}_0 is the unperturbed Hamiltonian and $\hat{H}_I(t) = e\hat{\mathbf{r}} \cdot \mathbf{E}_0 \cos(\omega t)$ the Hamiltonian for the interaction with an oscillating electric field of amplitude \mathbf{E}_0 and angular frequency ω . The wave functions for an energy level are defined by

$$\Psi_n(\mathbf{r}, t) = \psi_n(\mathbf{r})e^{-i\omega_n t} = |n\rangle e^{-i\omega_n t}, \quad (4.16)$$

where $\omega_n = E_n/\hbar$ is the angular frequency associated with the energy of the state n and $\psi_n(\mathbf{r}) = |n\rangle$ is the spatial wave function of state n . In a two-level system, the spatial wave functions are eigenfunctions of the unperturbed Hamiltonian, but not stationary states of the full Hamiltonian. \hat{H}_0 is diagonal while $\hat{H}_0 + \hat{H}_I(t)$ is

*This formula is only valid if there are three possible decay transitions with the three polarisations for the excited states. It is therefore not valid for a two-level system where spontaneous emission can only occur to one ground state.

not. Therefore, the population will oscillate if initialised in the eigenstates of \hat{H}_0 . The wave function as a function of time is expressed as

$$\Psi(\mathbf{r}, t) = c_1 |1\rangle e^{-i\omega_1 t} + c_2 |2\rangle e^{-i\omega_2 t}, \quad (4.17)$$

The coefficients must obey $|c_1|^2 + |c_2|^2 = 1$.

Substituting the wave function (4.17) in the Schrödinger equation (4.14) yields a system of differential equations ($\omega_0 = \omega_2 - \omega_1$)

$$\begin{aligned} i\dot{c}_1 &= \Omega \cos(\omega t) e^{-i(\omega_0)t} c_2 \\ i\dot{c}_2 &= \Omega^* \cos(\omega t) e^{i(\omega_0)t} c_1. \end{aligned} \quad (4.18)$$

Ω is the *Rabi frequency*

$$\Omega = \frac{\langle 1 | e \hat{\mathbf{r}} \cdot \mathbf{E}_0 | 2 \rangle}{\hbar} = \frac{\langle 1 | \hat{\boldsymbol{\mu}} | 2 \rangle \cdot \mathbf{E}_0}{\hbar} = \frac{\boldsymbol{\mu}_{12} \cdot \mathbf{E}_0}{\hbar} \quad (4.19)$$

where we used that $\hat{\boldsymbol{\mu}} = e \cdot \hat{\mathbf{r}}$ is the electric dipole moment operator and $\boldsymbol{\mu}_{12}$ is defined as the transition dipole moment between states 1 and 2.[†]

Under the simplifying assumption of monochromatic radiation and applying the rotating-wave approximation — neglecting fast oscillating terms — the solution of equation (4.18) is

$$|c_2(t)|^2 = \frac{\Omega^2}{\Omega^2 + \Delta^2} \sin^2 \left(\frac{\sqrt{\Omega^2 + \Delta^2} t}{2} \right), \quad (4.20)$$

where $\Delta = \omega - \omega_0$ is the detuning of the incident radiation. Equation (4.20) describes the *Rabi oscillations*: at fixed detuning, the population oscillates between the two levels at a frequency proportional to the incident electric field strength. If the electric field strength and the interaction time t are fixed and the frequency detuning is changed, one obtains the Rabi spectral lineshape. A spectral line has the Rabi lineshape in cases where spontaneous emission can be neglected, such as microwave transitions between Λ -doublet states in the $a^3\Pi$ state, as shown in figure 2.5. If spontaneous emission is dominant, spectra have a Lorentzian lineshape determined by the spontaneous lifetime. The Rabi oscillations are not reproduced in the simple rate equation model described earlier (section 4.2.1).

The full Hamiltonian of the two-level system interacting with an oscillating electric field can also be written in matrix form:

$$\hat{H} = \begin{pmatrix} \omega_1 & \Omega \cos(\omega t) \\ \Omega^* \cos(\omega t) & \omega_2 \end{pmatrix}. \quad (4.21)$$

A unitary transformation can be applied to the wave functions and Hamiltonian to simplify solving a problem without changing the solution. It is obtained by

[†]Here, we used the dipole approximation where \mathbf{E}_0 can be taken out of the integral because the wavelength of the radiation is much larger than the size of the atom. Then, the electric field amplitude is uniform over the atomic wave function.

applying a unitary operator \hat{U} as follows:

$$|\tilde{\Psi}\rangle = \hat{U} |\Psi\rangle \quad (4.22)$$

$$\hat{H} = \hat{U} \hat{H} \hat{U}^\dagger - i\hat{U} \frac{d}{dt} \hat{U}^\dagger. \quad (4.23)$$

One possible unitary transformation leads to the dressed atom picture, where the energy of the photon is absorbed into the ground state of the two-level system. The unitary matrix is then given by

$$\hat{U} = \begin{pmatrix} e^{-i\omega t} & 0 \\ 0 & 1 \end{pmatrix}. \quad (4.24)$$

After applying equation (4.23) on the Hamiltonian (4.21), we obtain

$$\hat{H} = \begin{pmatrix} \omega + \omega_1 & e^{i\omega t} \Omega \cos(\omega t) \\ e^{-i\omega t} \Omega^* \cos(\omega t) & \omega_2 \end{pmatrix}. \quad (4.25)$$

By applying the rotating wave approximation and shifting the energies (diagonal elements) down by $(\omega + \omega_1)$, we arrive at the Hamiltonian in the dressed atom picture

$$\hat{H} = \begin{pmatrix} 0 & \Omega/2 \\ \Omega^*/2 & -\Delta \end{pmatrix}. \quad (4.26)$$

To set up the optical Bloch equations, we stay in the dressed atom picture as it saves us from inconvenient phase factors. For the sake of simplicity, however, the tilde marks will be omitted.

It is useful to introduce the density matrix formalism to describe the state of the system. The density matrix ρ for a two-level system is defined by

$$\rho = |\Psi\rangle \langle \Psi| = \begin{pmatrix} c_1 \\ c_2 \end{pmatrix} \begin{pmatrix} c_1^* & c_2^* \end{pmatrix} = \begin{pmatrix} |c_1|^2 & c_1 c_2^* \\ c_2 c_1^* & |c_2|^2 \end{pmatrix} = \begin{pmatrix} \rho_{11} & \rho_{12} \\ \rho_{21} & \rho_{22} \end{pmatrix}. \quad (4.27)$$

The diagonal elements are the populations of states 1 and 2 and the off-diagonal elements are coherences between the two states because of the driving electric field frequency. By construction, $\rho_{12} = \rho_{21}^*$. The elements of the density matrix are $\rho_{ij} = \langle i | \rho | j \rangle = \langle i | \Psi \rangle \langle \Psi | j \rangle = \langle \Psi | j \rangle \langle i | \Psi \rangle = \langle j | \langle i \rangle$.[‡]

The equation of motion for the density operator is [212]

$$\dot{\rho} = -\frac{i}{\hbar} [\hat{H}, \rho] + r(\rho), \quad (4.28)$$

where the first term represents coherent evolution of the wavefunction — the Rabi oscillations — and the second term represents dissipative incoherent decay processes. The square brackets stand for the commutator of two operators, $[\hat{A}, \hat{B}] = \hat{A}\hat{B} - \hat{B}\hat{A}$. The relaxation term can be calculated in different ways,

[‡]In some publications, $|i\rangle \langle j|$ is written as σ^{ij} , the atomic projection, raising, and lowering operators [210, 211].

depending on the size of the system [6, 20, 210, 212, 213]. For a two-level system, the excited state populations decay spontaneously with rate Γ and the coherences with probability $\Gamma/2$. Finally, together with the Hamiltonian (4.15), this yields the *optical Bloch equations*[§] for a two-level system where the upper level $|2\rangle$ can only decay to the lower level $|1\rangle$:

$$\begin{aligned}\dot{\rho}_{11} &= \Gamma\rho_{22} - g\rho_{21} - g^*\rho_{12} \\ \dot{\rho}_{22} &= -\Gamma\rho_{22} + g\rho_{21} + g^*\rho_{12} \\ \dot{\rho}_{12} &= -\left(\frac{\Gamma}{2} - i\Delta\right)\rho_{12} + g(\rho_{11} - \rho_{22})\end{aligned}\tag{4.29}$$

The Rabi frequency is included in the factor

$$g = \frac{i}{\hbar}\Omega,\tag{4.30}$$

and g^* is the complex conjugate. An example of the results of the optical Bloch equations for a two-level system, also including spontaneous decay, is shown in figure 4.2.

4.2.3 The Low Intensity Case

It is worth to consider the case of low laser intensity, where the OBEs transform into the rate equations. In this case, the upper level population is negligibly low. $\rho_{11} + \rho_{22} = 1$, therefore $\rho_{22} \ll 1$ and $\rho_{11} \simeq 1$, and the third equation of (4.29) simplifies to

$$\dot{\rho}_{12} = -\left(\frac{\Gamma}{2} - i\Delta\right)\rho_{12} + g.\tag{4.31}$$

If the laser intensity is very low and the Rabi frequency term $|g|$ is much smaller than $|\left(\frac{\Gamma}{2} - i\Delta\right)|$, this equation describes the relaxation of ρ_{12} to a quasi-equilibrium, which is reasonably achieved within a few $\tau = 1/\Gamma$. We can write

$$\rho_{12} = \frac{g}{\frac{\Gamma}{2} - i\Delta}.\tag{4.32}$$

$\rho_{12}^* = \rho_{21}$, and therefore we can re-write the optical Bloch equations

$$\begin{aligned}\dot{\rho}_{11} &= \Gamma\rho_{22} - \frac{4\Gamma|g|^2}{\Gamma^2 + 4\Delta^2} \\ \dot{\rho}_{22} &= -\Gamma\rho_{22} + \frac{4\Gamma|g|^2}{\Gamma^2 + 4\Delta^2}.\end{aligned}\tag{4.33}$$

This is identical to the rate equations (4.1) in the low-intensity limit when $n_e \ll 1$ and $n_g \simeq 1$. The second terms on the right sides of the equations describe

[§]The term is familiar to a physical chemist who has been exposed to magnetic resonance spectroscopy. The optical Bloch equations are similar to the *Bloch equations* for a spin-1/2 particle in an oscillating magnetic field.

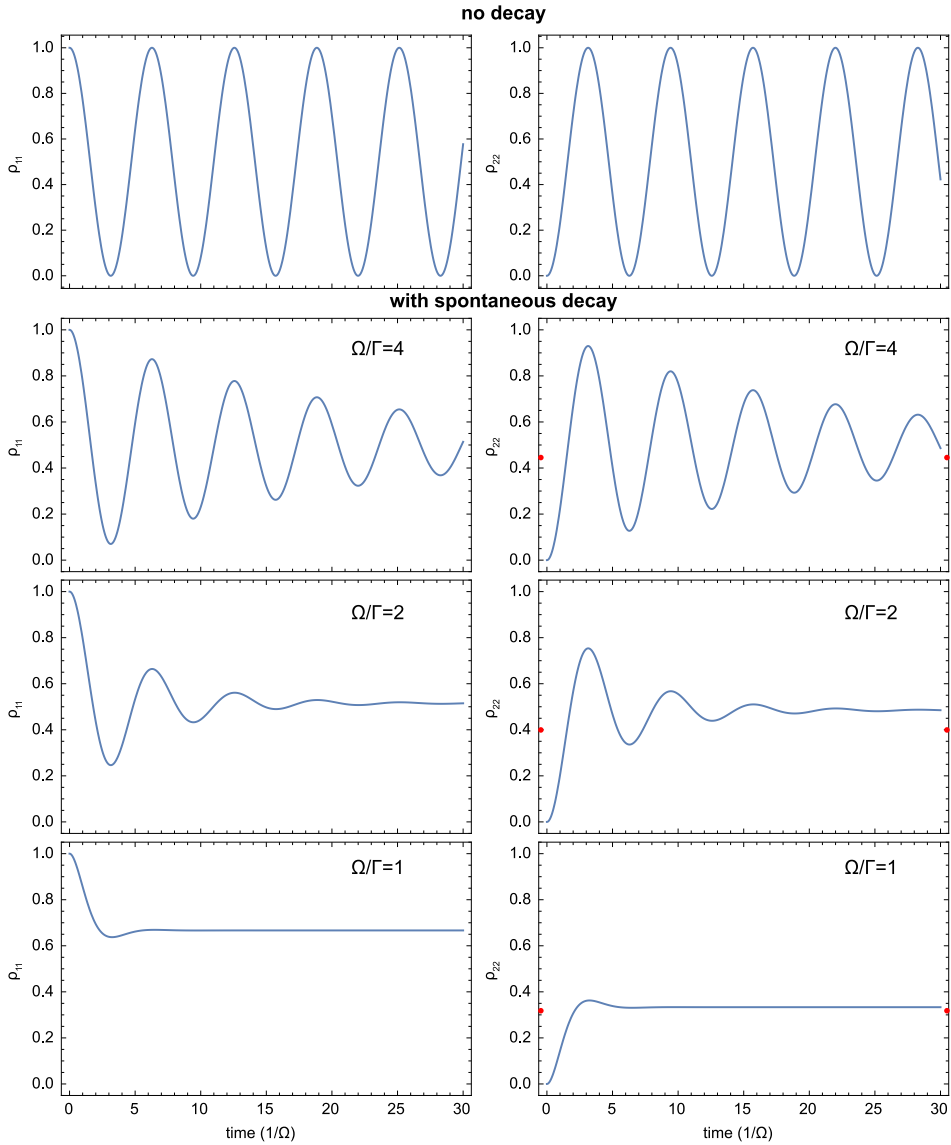


Figure 4.2: Population in the two levels (ρ_{11} and ρ_{22}) as a function of time (in units of the $1/\Omega$), as calculated using the optical Bloch equations. Top panel: without spontaneous decay term, all other panels: with spontaneous decay at different ratios of Ω/Γ to show the different decay behaviour and steady state populations. The red dots in the ρ_{22} panels indicate the steady-state excited state populations as obtained from the rate equations (eq. (4.4)). At lower intensities ($\Omega/\Gamma = 1$), the match between OBEs and rate equations is good and at high intensities ($\Omega/\Gamma = 4$), both models approach $\rho_{11} = \rho_{22} = 0.5$, although at a different pace.

excitation to the excited state; stimulated emission is negligible in the low-intensity limit.

4.3 Application to Multilevel Systems

For the treatment of a multilevel system like a real atom or molecule, the derived optical Bloch equations can be expanded to include multiple hyperfine levels and Zeeman sublevels in the ground and excited states as well as different laser polarisation configurations. Ungar *et al.* present a clear derivation of the equations in the case of multilevel atoms in an optical molasses [210]. Devlin and Tarbutt included magnetic fields to their equations to appropriately model magneto-optical trapping forces [211, 212, 214]. The latest publication [214] presents a generalised system of optical Bloch equations with multiple hyperfine components in both the ground and excited electronic states. Recently, a group at NIST has published a versatile Python package for the simulation of laser cooling that uses OBEs [215].

4.3.1 General

Since equation (4.28) holds for any system size, it is most useful to use this as a starting point for a computer program to solve the optical Bloch equations. The electric dipole interaction Hamiltonian can be calculated from first principles for all involved states [216]. The decay part can be derived from the Lindblad master equation [217], or calculated from formulae given in literature [6, 20, 210, 212, 213](the ones shown here are reproduced from Devlin's thesis [212]):

$$\begin{aligned}
 r_{eg} = r_{ge}^* &= -\frac{\Gamma}{2} \sum_{e', g', p} \langle e | \hat{\boldsymbol{\mu}} \cdot \boldsymbol{\epsilon}_p | g' \rangle \langle g' | \hat{\boldsymbol{\mu}} \cdot \boldsymbol{\epsilon}_p | e' \rangle \rho_{e'g} \\
 r_{ee'} &= -\frac{\Gamma}{2} \sum_{e'', g, p} (\langle e | \hat{\boldsymbol{\mu}} \cdot \boldsymbol{\epsilon}_p | g \rangle \langle g | \hat{\boldsymbol{\mu}} \cdot \boldsymbol{\epsilon}_p | e'' \rangle \rho_{e''e'} + \langle e' | \hat{\boldsymbol{\mu}} \cdot \boldsymbol{\epsilon}_p | g \rangle \langle g | \hat{\boldsymbol{\mu}} \cdot \boldsymbol{\epsilon}_p | e' \rangle \rho_{ee''}) \\
 r_{gg'} &= -\Gamma \sum_{e, e', p} \langle g | \hat{\boldsymbol{\mu}} \cdot \boldsymbol{\epsilon}_p | e \rangle \langle e' | \hat{\boldsymbol{\mu}} \cdot \boldsymbol{\epsilon}_p | g' \rangle \rho_{ee'}
 \end{aligned} \tag{4.34}$$

These equations can be applied to set up a coefficient matrix for the decay part of the optical Bloch equations.

Care is warranted in constructing the ground-ground coherences (off-diagonal elements that link different levels in the electronic ground state) that cannot be omitted in the optical Bloch equations — they are crucial for an accurate model. Independent of the approach, the decay matrix assumes a consistent form with matrix elements r_{ij} defined as:

$$\begin{aligned}
 r_{ge} &= -\frac{\Gamma}{2} \rho_{ge} \\
 r_{eg} &= -\frac{\Gamma}{2} \rho_{eg} \\
 r_{ee'} &= -\Gamma \rho_{ee'}
 \end{aligned} \tag{4.35}$$

where e and g stand for one ground or excited state, respectively. There is no simplified form of $r_{gg'}$ since it depends on the excited states and coherences these matrix elements couple to. The trace of the decay matrix must add up to zero since all population that decays from the excited states must end up in a ground state.

In appendix B, I show a method to check if a system of optical Bloch equations is set up correctly: their standard solution and the solution of the equations with the incident light polarisation and the initial population matrix rotated around the axis of light propagation have to be identical after rotation of the density matrix back by the same angle. Rotation of the initial density matrix (that has only non-zero elements along the diagonal) shifts population into the off-diagonal elements, thus making the initial behaviour more strongly dependent on off-diagonal elements in the decay matrix.[¶]

If the decay matrix is set up using quantum jump operators with the Lindblad formalism, $r_{gg'}$ are zero if $g \neq g'$ and the optical Bloch equations fail. This can also be detected with the aforementioned rotation test.

4.3.2 Dark States

A so-called dark state is a molecular state that does not couple to the light field. In the following, I introduce different kinds of dark states and what their implications are for optical cycling.

One hyperfine level with quantum number F consists of $2F + 1$ Zeeman sub-levels with $m_F = -F, -(F - 1), \dots, 0, \dots, F - 1, F$. The selection rules for a dipole-allowed transition between a quantum state with F in the ground state and F' in the excited state, for circularly (σ^+ or σ^-) or linearly (π) polarised light, are

$$\begin{aligned}\sigma^- : \Delta m_F &= -1 \\ \pi : \Delta m_F &= 0 \\ \sigma^+ : \Delta m_F &= 1.\end{aligned}\tag{4.36}$$

We can write a dark state $|d\rangle$ as superposition of states

$$|d\rangle = \sum_m c_m |\gamma, F, m\rangle,\tag{4.37}$$

where γ is a placeholder for all other quantum numbers to unambiguously define the states. For $|d\rangle$ to be a dark state, its coupling to any excited state must be zero. This means that the condition

$$\langle d | -\hat{\boldsymbol{\mu}} \cdot E | \gamma', F', m' \rangle = 0\tag{4.38}$$

has to be fulfilled for every excited state [218].

In the case of systems with $F' \leq F$, that will happen for optical cycling of molecules, dark states are always present for at least one polarisation. Two

[¶]Thus, we could discover a typing error in the decay matrix elements presented in the PhD thesis by Jack Devlin [212]. This error was corrected in equations (4.34).

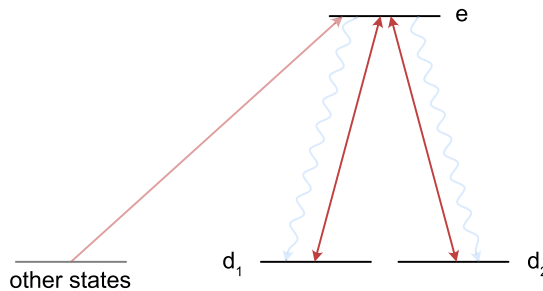


Figure 4.3: Scheme of a dark state of the second kind (“coherent dark state”) in a three-level system. Two (or more) ground states are only coupled to one common excited state by resonant laser radiation. The two ground states form a superposition state and the excited state e has zero occupation probability.

examples are: in the case where $F' = F = 1/2$, dark states only exist for circularly polarised light; in the case of $F' = F = 1$, dark states exist for all polarisations.

Dark states can be detrimental to laser cooling — after only a few photon scattering events, a molecule is pumped into a dark state. However, pumping a molecule into a dark state can be advantageous for sub-Doppler cooling, because no heating associated with photon scattering events takes place. Therefore, techniques to destabilise dark states as well as to engineer dark states have to be developed [219].

Two types of dark states can be distinguished. The first type are dark states that consist of only one $|\gamma, F, m\rangle$ state, the second kind are dark states that are coherent superposition states, often called “coherent dark states”. In this case, two or more ground states are coupled to the same excited state with resonant laser radiation of a certain polarisation. Then, a coherent superposition of the ground states is formed where all population will be trapped. If the system is initially in a different state, all population will be pumped to the coherent dark state. The population in the excited state is always zero and population can then not decay to other ground states anymore. The ground states must be degenerate for a coherent dark state to form [212, 220].[‡] A schematic picture of such a dark state of the second kind is presented in figure 4.3.

Dark states can be destabilised by making them time dependent [218]. Then, excited states are being populated and the system constantly scatters photons in its steady state. One way to achieve destabilisation for dark states of the second kind is by an energy splitting between the involved ground states. Such an energy splitting can be introduced by an external magnetic field. A magnetic field also destabilises a dark state of the first kind, if it is not aligned with the z -axis in the basis used. The magnetic field then transforms the polarisation so that there are no dark states.

[‡]One can also form a coherent dark state from non-degenerate ground states if two lasers (in the case of two ground states) are used. Then, the detunings of both states with respect to the addressing lasers must be the same [220].

Another way to destabilise both kinds of dark states is by using laser polarisation gradients, straightforwardly generated with counter-propagating laser beams of different polarisation. Then, the dark states depend on the position of the molecule in the laser beam and will not be stationary if the movement is fast enough. The dark state evolution can be written as [218]

$$|d(t)\rangle = \sum_m c_m(E(t)) |\gamma, F, m\rangle e^{-i\omega_m t}, \quad (4.39)$$

where $E(t)$ is the amplitude of the laser field and ω_m the angular frequency of the hyperfine levels.

An in-depth discussion on dark states can be found in the excellent review by Fitch and Tarbutt [219]. They present a method to determine the dark states analytically from the dipole interaction Hamiltonian. The wave function of the system is expanded from the ground states $|\gamma, F, m\rangle$ with energies $\hbar\omega_F$ and the excited states $|\gamma', F', m'\rangle$ with energies $\hbar\omega_{F'}$. Using the Hamiltonian for the interaction with a field of laser frequency ω_i and polarisation q with amplitude E_{-q}^i , the condition

$$\sum_{i,F,m,q} a_{F,m} e^{i\Delta_{i,F,F'} t} (-1)^{q+F'-m'} \begin{pmatrix} F' & 1 & F \\ -m' & q & m \end{pmatrix} \langle \gamma', F' || \mu || \gamma, F \rangle E_{-q}^i = 0 \quad (4.40)$$

is derived. Fitch and Tarbutt [219] derive their expressions in the interaction picture, therefore complex exponential terms are present.

Here, $\Delta_{i,F,F'} = \omega_i - (\omega_{F'} - \omega_F)$ and $\langle \gamma', F' || d || \gamma, F \rangle$ is the reduced dipole moment of the transition. This condition determines the ground state population vectors that result in no excited state population on interaction with the laser field. The equation can be written as a matrix equation $\mathbf{A} \cdot \vec{a} = 0$.** \vec{a} contains all coefficients $a_{F,m}$ and \mathbf{A} is a matrix with the elements

$$A_{(F',m'),(F,m)} = \sum_{i,q} e^{i\Delta_{i,F,F'} t} (-1)^{q+F'-m'} \begin{pmatrix} F' & 1 & F \\ -m' & q & m \end{pmatrix} \langle \gamma', F' || \mu || \gamma, F \rangle E_{-q}^i. \quad (4.41)$$

In the following, I will present two simple systems to demonstrate the influence of polarisation and hyperfine structure on dark states. Afterwards, I will present the results of optical Bloch equation calculations of the $A^1\Pi \leftarrow X^1\Sigma^+$ transition of AIF and how a relatively small hyperfine splitting in the ground state affects optical cycling considerably.

4.3.3 Simple Cases

To study the results of the OBEs for some exemplary cases, I choose a system similar to AIF, if only the fluorine atom had nuclear spin. The ground and excited

**i.e. the vectors \vec{a} make up the null space of \mathbf{A} — the operation of computing the null space is implemented in many code packages, such as Wolfram Mathematica.

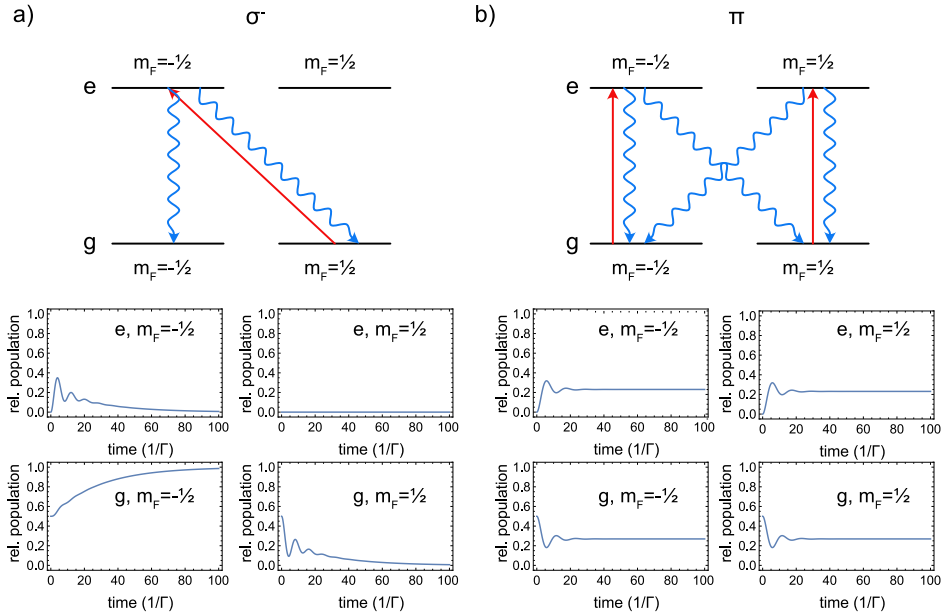


Figure 4.4: Simulation of a $F' = \frac{1}{2} \leftrightarrow F = \frac{1}{2}$ system, with resonant laser radiation at an intensity of $I = 1.8I_{\text{sat}}$. In panel (a), the system is driven with σ^- -polarised light. In this case, the $g, m_F = -\frac{1}{2}$ state is dark, all population accumulates in this state over time. In panel (b), the system is driven with π -polarised light. In this case, there is no dark state and the system reaches a steady state with non-zero excited state population.

state have $J(J') = 1, I(I') = \frac{1}{2}, \Lambda = 0$ and $\Lambda' = 1$, and $\Sigma(\Sigma') = 0$, like a Q(1) line of the $A^1\Pi \leftarrow X^1\Sigma^+$ transition.

Figure 4.4 shows the results of an OBE simulation of a $F' = \frac{1}{2} - F = \frac{1}{2}$ system, for σ^- - (a) and π -polarised (b) light. In the case of σ^- polarisation, the $m_F = -\frac{1}{2}$ level in the electronic ground state is dark and all population accumulates in this state (for σ^+ , the dark state would be $m_F = +\frac{1}{2}$). In the case of linearly polarised light, all states are bright and optical cycling is possible. This is the result predicted by (4.41).

In the case of a system with $F = \frac{1}{2}$ and $F = \frac{3}{2}$ in the ground state and $F' = \frac{1}{2}$ and $F' = \frac{3}{2}$ in the excited state, both types of dark states are predicted. If one then introduces a small energy difference between $F = \frac{1}{2}$ and $F = \frac{3}{2}$ levels in the ground state, the coherent dark states are destabilised. In the case of σ^- -polarised light, this leads to all population being pumped to $m_F = -\frac{3}{2}$, resulting in no additional photon scattering. However, in the case of π -polarised light, destabilisation of coherent dark states results in steady-state population in the excited state. Thanks to a small ground state hyperfine splitting, this system could be used for optical cycling, albeit at a rate limited by the size of the hyperfine interaction, which sets the destabilisation rate. The hyperfine interaction acts as

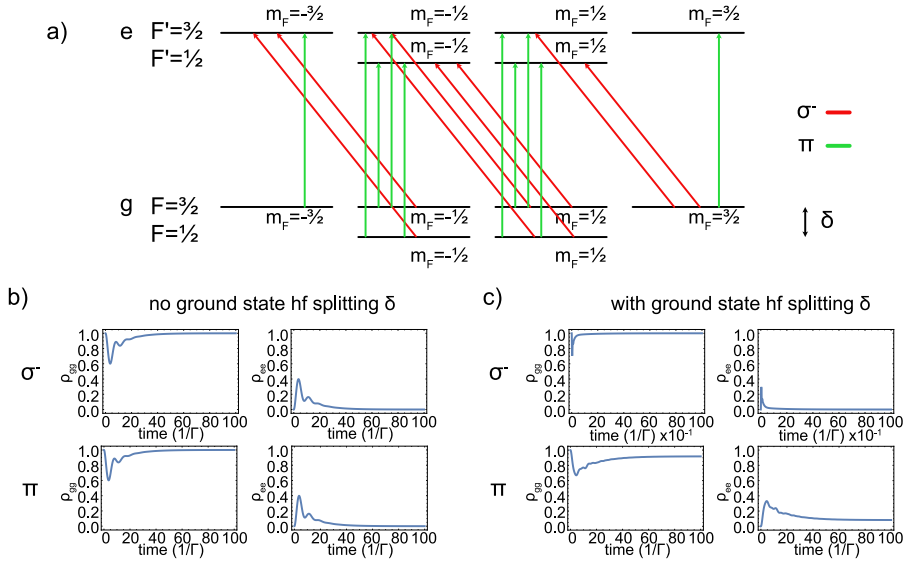


Figure 4.5: Simulation of a system with $F = \frac{1}{2}$ and $F = \frac{3}{2}$ in the ground state and $F' = \frac{1}{2}$ and $F' = \frac{3}{2}$ in the excited state, using resonant light at an intensity of $I = 1.8I_{\text{sat}}$. The level scheme in panel (a) shows the transitions that are driven with σ^- (red) and π (green) polarised light. For the sake of clarity, emission arrows are not shown. The population panels at the bottom show the total ground state population ρ_{gg} and total excited state population ρ_{ee} for both polarisations. In panel (b), the F and F' levels are degenerate and resonant with the laser radiation, in panel (c), a small ground-state hyperfine splitting δ is introduced.

an effective magnetic field that leads to precession of the coherent dark states. This case is presented in figure 4.5. An excited state hyperfine splitting does not have this influence since coherent dark states are linked by only one excited state. However, it can lower the scattering rate if it decreases the number of excited states that are accessible by resonant transitions.

4.3.4 The $A^1\Pi \leftarrow X^1\Sigma^+$ Transition of AlF

Now, we can apply the methods introduced to the $A^1\Pi \leftarrow X^1\Sigma^+$ transition of AlF. Every Q-line of this transition is rotationally closed and can be used for optical cycling. For the Q(1) line, there are 36 Zeeman sublevels in both the ground and excited electronic states. The electric dipole Hamiltonian of the Q(1) line was precisely calculated and the OBEs were set up as detailed previously. Whilst the $A^1\Pi \leftarrow X^1\Sigma^+$ transition includes many more states, compared to the simple model above, and two nuclei with nuclear spin, the main conclusions of the simple model are true. The $X^1\Sigma^+$, $J = 1$ hyperfine structure spans about 10 MHz, for the $A^1\Pi$, $J' = 1$ excited state it spans almost 500 MHz (chapter 2). Figure 4.6 shows the influence of the small ground state hyperfine splitting on the photon

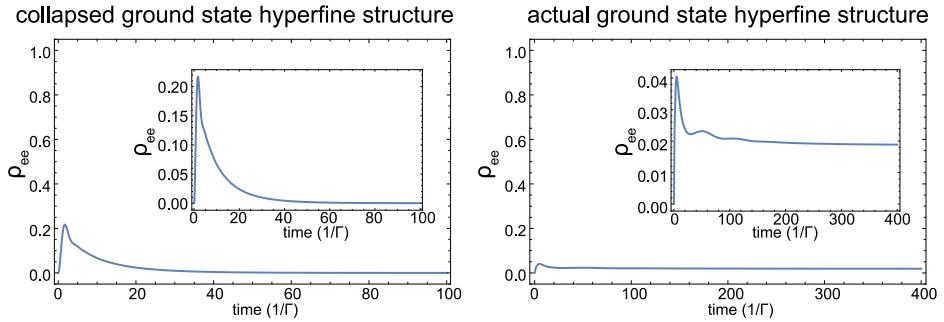


Figure 4.6: Simulation of optical cycling on the Q(1) line of the AlF $A^1\Pi \leftarrow X^1\Sigma^+$ system using optical Bloch equations. The laser radiation is resonant with the $F'_1 = 7/2, F' = 3 \leftarrow F_1 = 7/2, F = 3$ hyperfine transition and the intensity is $I = 8I_{\text{sat}}$. I only show the total excited state population ρ_{ee} , the total ground and excited state populations add up to 1. On the left, the ground state hyperfine structure was collapsed to zero. In this case, the system ends up in a dark state after several scattering cycles and there is no steady-state excited state population. In the case of the actual, spectroscopically determined hyperfine splittings in the ground state, there is a non-negligible steady state excited state population of approximately 2%, allowing for continuous optical cycling. This is presented in the zoomed-in inset.

scattering rate. If we assume no ground state hyperfine structure, the system ends up in a dark state after a few photon scattering cycles. In our actual molecule, the ground state hyperfine structure destabilises these dark states and leads to a non-negligible steady state excited state population — without the need for polarisation modulation. The dominant splitting in the ground state is caused by the hyperfine interaction of the Al nuclear spin, as discussed in chapter 2. Figure 4.7 shows the populations in all hyperfine states in the $X^1\Sigma^+$ and $A^1\Pi$ states as a function of time, showing that a steady state is reached after $1000/\Gamma$.

From this point on, and unless stated otherwise, I consider linear polarisation. For all laser polarisations other than pure circular, the steady-state scattering rate depends on the laser intensity. Calculating the result of the OBEs as a function of laser intensity therefore gives further insight and information to be used later on. Figure 4.7 shows the steady-state excited state population ρ_{ee} as a function of I/I_{sat} , for linearly polarised light. The excited state population reaches a maximum at $I/I_{\text{sat}} = 8$ and decreases for higher intensities. At these high intensities, the destabilising effect of the hyperfine structure on dark states is reduced by the strong coupling to the excited states via the light field. Then, the molecule follows the precessing dark state adiabatically and the excited state fraction decreases.

All coherent effects that lead to dark states and their destabilisation can not be captured by a simple rate model. This becomes clear from figure 4.8 that compares the saturation curves for the rate equations and OBEs. At low intensities, when

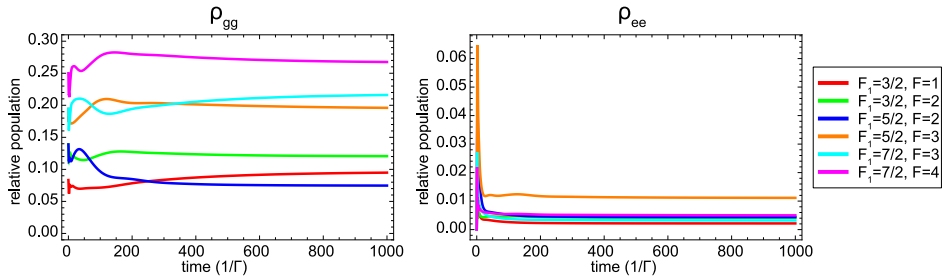


Figure 4.7: Populations of all F levels in the ground and excited states after excitation on the Q(1) line of the $A^1\Pi \leftarrow X^1\Sigma^+$ transition with $I = 8I_{\text{sat}}$. All 36 m_F -levels in the ground state have the same initial population. Therefore, the relative populations of the F -levels are weighted according to the degeneracy.

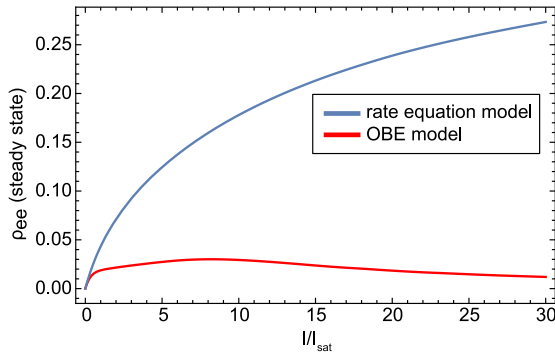


Figure 4.8: Saturation curves for the steady state excited state population as a function of intensity I/I_{sat} . The blue curve was calculated using a rate equation model, the red curve with optical Bloch equations.

the scattering rate is not limited by the hyperfine interaction, the models overlap well and the much simpler rate equations can be used for simulations. This is the case when the scattering rate is much less than $\Gamma/30$.

The total number of Zeeman sublevels that need to be included in the calculation increases when we progress to higher Q-lines, from 72 (Q(1)) to 216 (Q(4)). The computation time to solve the OBEs increases with the square of the number of included states, therefore this approach becomes impractical for higher Q-lines. However, we can use the intuition gained from previous sections, and knowledge of the hyperfine structure of the Q-lines, to make reasonable predictions for AIF. It is the ground state splitting which predominantly determines the maximum scattering rate, and this does not change significantly for higher rotational states. In the excited states, the hyperfine structure decreases in size with increasing J , so that a single laser frequency is closer to resonance with the different hyperfine transitions. In the absence of hyperfine interactions, there is always one dark state for a given polarisation and J on the Q-lines of AIF — the fraction of dark states therefore

decreases with J . We can thus reasonably assume that the higher Q(J) lines will scatter photons at increasing rates. This can be exploited for efficient slowing, but the high scattering rates might be detrimental for sub-Doppler cooling.

4.4 Application to the Experiment

In this section, I show how our calculations can be used to understand the effects of optical cycling on AIF molecules.

4.4.1 Scattered Photons in the Laser Profile

Now that we know the excited state population as a function of the laser intensity, we can also predict the actual photon scattering rate R_{phot} :

$$R_{\text{phot}}(I) = \Gamma \rho_{ee}(I). \quad (4.42)$$

The laser beam intensity profile $I(\mathbf{r})$ is known, either as analytical function or as image from a beam profiler, and can be converted to an *excited state population map* $\rho_{ee}(\mathbf{r})$. The maximum number of photons that a molecule scatters (ignoring losses) during its interaction with the laser beam is equal to the integral of the scattering rate over the interaction time t_i :

$$N_{\text{ph}}(t_i) = \Gamma \int_0^{t_i} \rho_{ee}(I(t')) dt'. \quad (4.43)$$

Applying a transformation of variables, this equation can be converted into the integral over the path through the beam. As a good approximation, we assume that the molecules only propagate in the forward direction, parallel to the x axis.

$$N_{\text{ph}}(x_i, y) = \frac{\Gamma}{v_0} \int_0^{x_i=v_0 \cdot t_i} \rho_{ee}(I(x', y)) dx', \quad (4.44)$$

where v_0 is the mean forward velocity of the molecules.

The cycling transition is not fully closed and losses to higher vibrational states are possible. The probability for the molecule to return to the vibrational ground state, p_0 , can be approximated from the ratio of Einstein A coefficients [167],

$$p_0 = \frac{A_{00}}{\sum_i A_{0i}} \approx \frac{A_{00}}{A_{00} + A_{01}} = 0.9953 \quad (4.45)$$

With equations (4.42) and (4.44), we have to correct the population in $v = 0$ for the probability of vibrational losses

$$R_{\text{phot,corr}}(\mathbf{r}) = \Gamma p_0^{N_{\text{ph}}(\mathbf{r})} \rho_{ee}(\mathbf{r}), \quad (4.46)$$

where $p_0^{N_{\text{ph}}(\mathbf{r})}$ is the remaining population in $v = 0$ at position \mathbf{r} along the trajectory. From this, we can then determine the average number of photons scattered

during the interaction with the laser,

$$\langle n_{\text{ph}} \rangle = \frac{1}{v_0} \int_x R_{\text{phot,corr}}(\mathbf{r}') dx'. \quad (4.47)$$

However, a similar result can be obtained following another path, as detailed in reference [88]. Based on a geometric distribution, the probability for a molecule to scatter exactly n photons (the maximal number is N_{ph}) is given by

$$p(n) = \begin{cases} (1 - r_v)r_v^{n-1} & (n < N_{\text{ph}}) \\ r_v^{n-1} & (n = N_{\text{ph}}) \\ 0 & (n > N_{\text{ph}}) \end{cases} \quad (4.48)$$

The average number of photons can be calculated by^{††}

$$\langle n_{\text{ph}} \rangle = \sum_{n=0}^{N_{\text{ph}}} np(n) = \sum_{n=0}^{N_{\text{ph}}-1} n(1 - r_v)r_v^{n-1} + N_{\text{ph}}r_v^{N_{\text{ph}}-1} = \frac{1 - r_v^{N_{\text{ph}}}}{1 - r_v} \quad (4.49)$$

The latter method takes less time to compute and is therefore preferred for simulations of many trajectories.

4.4.2 Experimental Observables

Number of Scattered Photons as Function of Laser Intensity

It is difficult to estimate the number of photons scattered per molecule from an experimental photon count rate without accurate knowledge of the number of molecules in the detection region, their velocity, and the photon detection efficiency. Fortunately, all these can be removed by using the number of photons counted when saturating a non-cycling “standard candle” transition of the same ground rotational state as calibration. In the case of the Q(1) line, this is the R(1) line. After a certain number of scattered photons on this transition, the molecules are optically pumped into another rotational state which does not interact with the laser field. This number can be calculated from $n_{\text{ph},\infty} = \frac{1}{1-p}$, where p is the probability to return to the same ground rotational state. This can be calculated from the Hönl-London factors [221] for all possible decay channels, as explained in section 2.6.3 of chapter 2. In the case of the R(1) line, 2.5 photons are scattered on average. In the case of a cycling transition, the number of scattered photons is limited by vibrational losses, the laser intensity and the interaction time. The Gaussian distribution of the laser intensity along y results in a spatially dependent scattering rate. Therefore, the experimental result is the *average* number of photons along the y axis. The axes are defined in figure 4.9.

To calculate the number of scattered photons, averaged over the interaction volume, we need to average all parallel trajectories through the interaction volume

^{††}The last step includes evaluating the sum using the partial sum formula for a geometric series.

of the molecular beam and the laser. A sketch of this region is shown in figure 4.9. The molecular beam passes a 2 mm aperture before entering the detector to ensure that the density in the beam is homogeneous and that the molecular beam is smaller than the laser beam; thus, the interaction volume does not change considerably as a function of laser intensity. The integral (4.47) is evaluated along the x -axis, for different values (y, z) . The average of the number of photons scattered on these trajectories is then calculated along y - the line of sight to the fluorescence detector.

The average number of photons scattered over the whole beam profile is a function of the peak intensity of the laser beam and the velocity of the molecules. Examples of the effective interaction volume at different v_0 are shown in figure 4.10. For $v_0 = 150 \text{ m s}^{-1}$, the scattering rate in the middle of the beam is skewed towards the molecule source (low x) because of pumping to $v = 1$. For higher v_0 , this effect is less pronounced because the short interaction time does not allow for enough photon scattering events. At very high v_0 , the number of scattered photons only depends on the interaction time.

Since the experiments on optical cycling will be described extensively in the upcoming thesis of Simon Hofsäss [193], details of the experiment will not be further discussed here. Figure 4.11a presents experimental results on the number of scattered photons as a function of laser peak intensity $I = \frac{2P}{\pi w^2}$ †† at 150 m s^{-1} and 300 m s^{-1} . At the higher velocity, the reduced interaction time of the molecules with the laser beam reduces the number of scattered photons. The OBE model, where we used the $\rho_{ee}(I)$ curve from figure 4.8, fits the experimental data well; as predicted from figure 4.8, the rate model drastically overestimates the photon scattering because coherences in the ground state that lead to a smaller excited state fraction are not included. In the experiment, we do not reach the limit of 213 photons given by losses to higher vibrational states that is also predicted by the rate model for 150 m s^{-1} . This is caused by the stabilisation of dark states at high laser intensities that reduces the scattering rate.

Some sources of uncertainty have not been considered in the simulation. While we assume a point source, the real phase space of the source adds uncertainty to the experimental data. We neglect Doppler shifts from the transverse velocity of the molecules because of the narrow aperture that was installed; Doppler shifts from momentum transfer from scattered photons to the molecule can be ignored. We approximate the laser beam with a Gaussian profile that is perfectly centred on the molecules — the alignment in the experiment was always optimised.

4.4.3 Monte Carlo Simulation of Transverse Deflection

To simulate the transverse deflection of a molecular beam caused by the interaction with resonant laser light, we use a Monte Carlo approach. While Devlin and Tarbutt [211,214] include the propagation of the molecules through the laser profile in their OBEs, we calculate the spatially resolved steady-state scattering rate and

†† P is the integrated laser power over the whole beam profile and w is the $1/e^2$ -radius of the beam. For an elliptical beam, w^2 needs to be replaced with $w_x w_y$, where w_x and w_y are the $1/e^2$ -semiaxes.

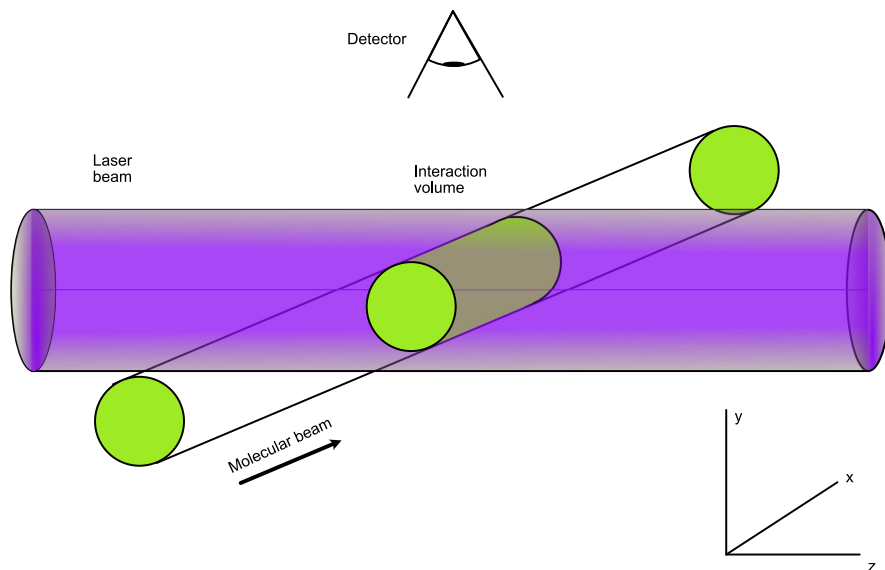


Figure 4.9: Sketch of the interaction region modelled to determine the average number of scattered photons per molecule.

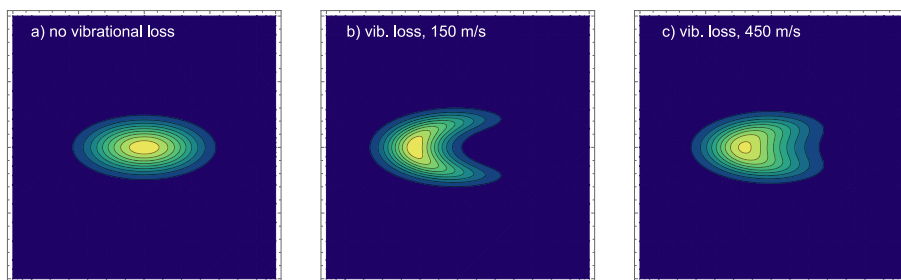


Figure 4.10: Dependence of the effective interaction volume on the molecule velocity. (a): no vibrational losses. (b) and (c): 150 m s^{-1} and 450 m s^{-1} , with vibrational losses.

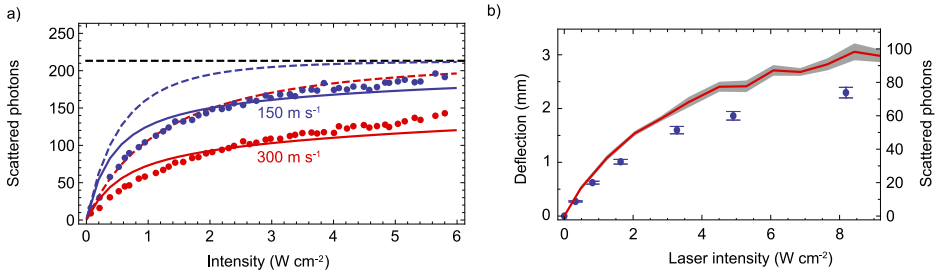


Figure 4.11: (a): Number of scattered photons on the Q(1) transition as a function of laser peak intensity (dots), simulation based on the OBE (solid line) and rate equation model (dashed line). Blue: 150 m s^{-1} , red: 300 m s^{-1} . (b): Transverse deflection of AIF molecules using optical cycling on the Q(2) transition. The blue dots show the experimentally determined deflection while the red line is the result of the Monte Carlo model using the result of a rate equation simulation for the steady-state excited state population. The grey shading is the error bar obtained from multiple runs of the simulation. The forward velocity of the molecules in the experiment is $270(20) \text{ m s}^{-1}$ and the distance between the pump and detection regions is 28 cm. Figures adapted from ref. [88].

then use a Monte Carlo trajectory simulation. We can use this simple approach because our experiment contains only one single laser beam on resonance with the cycling transition and polarisation gradients and polarisation forces do not need to be modelled.

For the Monte Carlo trajectory simulation, we need to generate a spatial scattering rate profile in the interaction region of the molecular beam and the deflection laser. In the case of the OBE, this can be done by fitting an appropriate function to the calculated points. In the case of the rate equation model, we skip the fitting step and can directly use the obtained function for the steady state scattering rate $R_{tot}(I(x, y))$ from equation (4.13) to calculate the scattering probability profile from the laser profile. This then serves as input for a three-dimensional trajectory simulation. We know from the OBE model that after only a few photon scattering events, the steady state is reached. Therefore, this approach is a good approximation.

We simulate the behaviour of the molecules at different laser beam peak intensities in order to compare the result to the experimental observations. Our simulation procedure is outlined in the following.

- For each intensity, 1000 molecules are generated. The velocities are distributed following a Gaussian distribution centred on the experimentally determined forward velocity, with a standard deviation according to the experimentally determined spread. A Gaussian was chosen because it fits best to the experimentally observed TOF profile.
- The transverse velocity distributions are calculated so that all molecules pass

through the 2 mm diameter aperture before the laser interaction region. This spatial distribution is assumed to be uniform.

- The time step is chosen to be $\tau = 1/\Gamma$. The position and transverse velocities of the molecules are updated for every time step.
- When a molecule enters the laser beam, the probability of a scattering event taking place is determined by $\rho_{ee}(I(x, y)) = R_{tot}(I(x, y))/\Gamma$. We generate a random number R_1 between 0 and 1 and compare it to $\rho_{ee}(I(x, y))$. If $R_1 < \rho_{ee}(I(x, y))$, a photon is scattered and the momentum $\hbar k$ (where $k = 2\pi/\lambda$ is the angular wavenumber) is transferred to the transverse movement of the molecule.
- In this case (if a photon is absorbed), another random number R_2 between 0 and 1 is used to determine if the molecule returns to $v = 0$ after emitting a photon or if it is lost to a higher vibrational state. The random number is compared with the experimentally determined probability p_v (eq. (4.45)) [167]. If $R_2 > q_{00}$, the molecule ends up in a dark state.
- The final position of the molecule in the detector is then calculated from the current forward and transverse velocities and the simulation for this molecule is terminated. If a molecule stays in a bright state until the end of the interaction with the laser, the final position is calculated at this point. The forward velocity of the molecules in the experiment of $270(20)\text{m s}^{-1}$ was used and the distance between the pump (deflection) region and the detection zone is 28 cm

The Doppler shift originating from the transverse movement of the molecules leads to a detuning of the laser frequency seen by the molecules. The detuning that we expect from the experimental setup is 2.5 MHz, far below the natural linewidth of the transition. It can therefore be ignored in the Monte Carlo simulation. The isotropic fluorescence of the molecules does not influence the mean deflection distance, but broadens the final spatial distribution. The focus of the investigation was on the total deflection distance, therefore these random momentum kicks were not incorporated. To be able to properly compare the experimental spatial distribution, they must be included in the code.

The algorithm was implemented in the MATLAB software and programming language. Because the molecule trajectories do not interact with each other, the trajectory simulation can be performed in parallel on separate cores of the processor to speed up the (brute-force) computation. In MATLAB, this is achieved with the `spmd` (single program, multiple data) command of the parallel computing toolbox. The result of this Monte Carlo simulation is compared with the experimental result in figure 4.11b. In the experiment, the displacement of the molecule cloud is determined from camera images [88].

4.5 Narrow-Line Laser Cooling of AlF

4.5.1 Introduction

The $A^1\Pi \leftarrow X^1\Sigma^+$ main cooling transition of AlF is perfectly suited to generate extremely large spontaneous scattering forces. On this transition, the molecule scatters many high-energy photons in a short time because of the 1.9 ns lifetime of the $A^1\Pi$ state. However, the minimum temperature achievable with Doppler cooling is the so-called Doppler limit $T_D = \frac{\hbar\Gamma}{2k_B}$ [6]. In the case of the $A^1\Pi \leftarrow X^1\Sigma^+$ transition of AlF, $T_D = 2$ mK. Lower temperatures can be achieved by sub-Doppler methods, such as Sisyphus cooling using polarisation gradients [222, 223] or velocity selective coherent population trapping [205]. The recoil temperature $T_R = \frac{(\hbar k)^2}{mk_B}$ [6] is the lowest temperature that can be achieved with laser cooling methods and is associated to one single photon recoil energy. The use of up to three pairs of counter-propagating laser beams in the three Cartesian coordinates is called optical molasses and efficiently reduces the temperature of an atom or molecule cloud. The particles accumulate at the intersection point of the beams. The addition of magnetic field gradients and the choice of appropriate laser polarisations allows to strongly confine the atoms in a magneto-optical trap (MOT) [9].

Sub-Doppler cooling methods were first devised for atoms [224] and applied to molecules [225] over two decades later. One technique that is frequently used is Sisyphus cooling [222, 223]. If the polarisations of two counter-propagating beams are linear and orthogonal to each other, they form a standing wave of polarisations that change between σ^+ and σ^- over space. As the molecules move through this standing wave, they experience a slowing force, just like going uphill (therefore called Sisyphus cooling, after the mythological figure). Population is transferred between different sub-levels of the ground state, which dissipates the energy. However, the timescale of this pumping process is much longer than the radiative lifetime of the excited state. Therefore, T_D can be surpassed. A good introduction to Sisyphus cooling can be found in Foot's book [20].

Narrow-line cooling — also called intercombination line cooling — exploits the lower scattering rate on transitions with a long excited-state lifetime. So far, it has only been demonstrated for atoms. First, the atoms are captured and cooled to the Doppler limit using the strong main cooling transition. Then, a second, narrow-line, transition that is normally too weak to trap atoms directly, is switched in. The Doppler limit of this transition is much lower, therefore the trapped atoms are cooled down to temperatures below the Doppler limit of the main transition. In some cases, T_D of the narrow-line transition is even lower than T_R . Many narrow-line cooling transitions work in the presence of magnetic fields, like in a MOT, whereas this is not always the case for other sub-Doppler techniques. It is important that the scattering rate on the narrow-line transition is much higher than the loss rate of trapped atoms from the MOT — otherwise, the atoms are not cooled.

Narrow line cooling is commonly used to cool alkaline earth atoms to ultralow temperatures and is an efficient tool to significantly increase the phase-space density of ultracold atomic gases. Direct laser cooling to quantum degeneracy has

been demonstrated this way [226]. However, this technique has not been demonstrated for molecules yet and crucially relies on the accurate determination of the lifetime of the metastable state used for cooling.

4.5.2 The Lifetime of the Metastable $a^3\Pi$ State

In this section I present a measurement of the radiative lifetime of the metastable $a^3\Pi_1, v = 0$ state. The spin-forbidden intercombination line $a^3\Pi_1, v' = 0 \leftarrow X^1\Sigma^+, v'' = 0$ can, in principle, be used to laser-cool AlF molecules to the recoil limit of a few μK , after pre-cooling on the much stronger $A^1\Pi, v' = 0 \leftarrow X^1\Sigma^+, v'' = 0$ transition. The Franck-Condon factors of the $a^3\Pi, v' = 0 \leftarrow X^1\Sigma^+, v'' = 0$ transitions are favourable and all Q-lines are rotationally closed, like for the main cooling cycle. The estimated lifetime of the $a^3\Pi_1, v = 0$ state is in the millisecond range, suggesting a T_D of a few nanokelvin, lower than the recoil limit [167]. This long lifetime comes about because spin-orbit coupling of the $a^3\Pi$ state to $^1\Pi$ and $^1\Sigma$ states makes the $a^3\Pi \leftarrow X^1\Sigma^+$ transition only weakly allowed. The narrow linewidth associated to the long lifetime makes high-resolution spectroscopy experiments possible that can serve as benchmark for quantum chemistry and open up opportunities for high-precision measurements of molecular properties and physics beyond the standard model.

Measuring the lifetime of metastable states in a molecular beam is challenging because the transition to the excited state is weak, making it difficult to populate the $a^3\Pi$ state efficiently. In addition, it is difficult to observe the spontaneous decay of long-lived states directly, because the molecules in the beam might leave the detection volume, or collisions with the background gas might redistribute the occupied levels. The measurement of the v -, J - and Ω -dependent lifetimes of the $a^3\Pi$ state of CO is a good example; initial measurements in the 1970s gave very different results ranging from 1 to 9 ms using a variety of techniques. These measurements could only give a lifetime averaged over multiple rotational states [227]. In 1997, Jongma *et al.* [228] used a supersonic molecular beam combined with two LIF detectors. The ratio of the two LIF signals as a function of the time-of-flight between them depends on the lifetime of the metastable state and gave a result of 3.4 ± 0.4 ms. By 2005, it became possible to confine molecules in electrostatic traps, loaded from Stark-decelerated molecular beams. By measuring the trap-loss due to the spontaneous decay to the ground-state, the lifetime of metastable states of molecules could be determined with very high accuracy and precision [229, 230]. This way, the lifetime of the $a^3\Pi_1, v = 0$ metastable state of CO could be determined to 2.63 ± 0.03 ms.

Here, we use an improved approach based on the one described by Jongma *et al.* [228], to determine the radiative lifetime of the $a^3\Pi_1$ state of AlF. This state is most relevant for narrow-line cooling applications, as the lifetimes of the $a^3\Pi_0$ and $a^3\Pi_2$ are approximately a factor 10 and 1000 longer, causing too few scattering events. We prepare the molecules in a single rotational level in the metastable state, detect the molecules in two spatially separated time-of-flight mass-spectrometer (TOF-MS) detectors and measure the ratio of the two ion signals as a function of the time-of-flight between the two detectors. The time-of-flight

between the detectors is varied by changing the velocity of the molecules and by changing the length of the molecular beam machine. To reduce potential systematic errors related to these changes, we also measure the ratio of the two ion signals for the much longer lived $a^3\Pi_0$ state, which serves as calibration for differences in the number of molecules passing through each detector and differences in the detection efficiencies. In the LIF experiments by Jongma *et al.* [228], such a reference measurement was not possible. The signal in the first TOF-MS detector (A), $S_{\Omega,A}$ is the product of the detection efficiency $\alpha_{\Omega,A}$ with the population in $a^3\Pi_0$ at this position n_Ω :

$$\begin{aligned} S_0(t=0) &= S_{0,A} = \alpha_{0,A}n_0 \\ S_1(t=0) &= S_{1,A} = \alpha_{1,A}n_1 \end{aligned} \quad (4.50)$$

In the second TOF-MS detector (B), the population has decayed to $n_\Omega e^{-\frac{\Delta t}{\tau_\Omega}}$ during the flight time Δt , with the lifetime τ_Ω , and the detection efficiency is $\alpha_{\Omega,B}$.

$$\begin{aligned} S_0(t=\Delta t) &= S_{0,B} = \alpha_{0,B}n_0 e^{-\frac{\Delta t}{\tau_0}} \\ S_1(t=\Delta t) &= S_{1,B} = \alpha_{1,B}n_1 e^{-\frac{\Delta t}{\tau_1}} \end{aligned} \quad (4.51)$$

The recorded signal in detector B is divided by the signal in detector A, eliminating the initial population n_Ω .

$$\frac{S_{1,B}}{S_{1,A}} = \frac{\alpha_{1,B} e^{-\frac{\Delta t}{\tau_1}}}{\alpha_{1,A}} \quad (4.52a)$$

$$\frac{S_{0,B}}{S_{0,A}} = \frac{\alpha_{0,B} e^{-\frac{\Delta t}{\tau_0}}}{\alpha_{0,A}} \quad (4.52b)$$

The experiment has to be designed such that the detection efficiencies of the TOF-MS are independent of the investigated spectral line. It is important to keep the laser beam shape and alignment identical for both transitions. Then,

$$\frac{\alpha_{1,B}}{\alpha_{1,A}} = \frac{\alpha_{0,B}}{\alpha_{0,A}} \quad (4.53)$$

holds and division of equation (4.52)a and (4.52)b yields a product of two exponential functions with the two parameters τ_0 and τ_1 :

$$\mathcal{R}(\Delta t) = \frac{S_{1,B}}{S_{1,A}} \left(\frac{S_{0,B}}{S_{0,A}} \right)^{-1} = e^{-\frac{\Delta t}{\tau_1}} e^{\frac{\Delta t}{\tau_0}} = e^{-\frac{\Delta t}{\tau_{\text{exp}}}} \quad (4.54)$$

where

$$\frac{1}{\tau_{\text{exp}}} = \frac{1}{\tau_1} - \frac{1}{\tau_0}. \quad (4.55)$$

The experimental setup is presented in figure 4.12. About 160 mm downstream from the laser ablation and gas nozzle, the molecular beam is intersected with the pulsed excitation laser (frequency-doubled Sirah PDA seeded by a Sirah

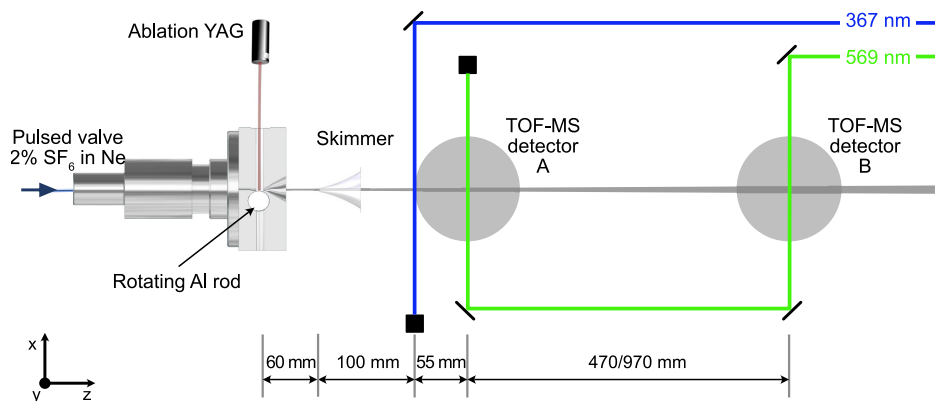


Figure 4.12: Experimental setup for the determination of the radiative lifetime of the $a^3\Pi_1$ state of AlF. First, the molecules are excited from the ground state to the $a^3\Pi_1, v = 0, J = 1$ or $a^3\Pi_0, v = 0, J = 1$ state with 367 nm UV light. The population in the respective state is probed by (1+2)-REMPI and TOF-MS detection at two positions, 470 or 970 mm apart.

Matisse titanium sapphire laser). The vertical spread of the molecular beam is confined by a 2 mm slit aperture in front of the excitation region. The size of the excitation laser beam was adjusted accordingly with an iris aperture, the remaining pulse energy was 3 mJ in a 3 mm spot. The validity of the requirement in equation (4.53) is guaranteed by precise alignment of the molecular beam and the lasers. Some 55 mm further, the first TOF-MS detector is installed, where the molecules are ionised using (1+2)-REMPI via the $b^3\Sigma^+$ state with a PDL (Radiant Dyes) around 569 nm. A second, similar TOF-MS detector using the same ionisation laser is installed either 470 or 970 mm downstream of the molecular beam. The ionisation laser beams were defined with 10 mm apertures to reduce scattered light on the TOF electrodes, the pulse energy was 7 mJ in detector B and 5 mJ in detector A. Ionisation takes place under electric field-free conditions. The laser timings are controlled with a precise timing card (National Instruments) in combination with LabView software.

Ion signal ratios (eq. (4.54)) were recorded at various time delays, made possible by using the different carrier gases helium, neon, argon, krypton and xenon and the two instrument lengths. The forward velocity of a gas in a supersonic beam is inversely proportional to the square root of the atomic mass. For one measurement, the frequency of the excitation laser is fixed to either the $R_1(0)$ or the $R_2(0)$ line. The ionisation laser timing is alternated during one experiment to interact with the molecule packet in either detector A or B. For each region, 2000 laser shots are averaged per data set. We observed that the normalised signal for helium as carrier gas was lower than predicted from measurements with heavier carrier gases. Reducing the gas pressure on the nozzle increased this signal. We assume that at high pressure, collisional redistribution happened in the molecular beam. For all other carrier gases, the backing pressure had no such influence. Thus,

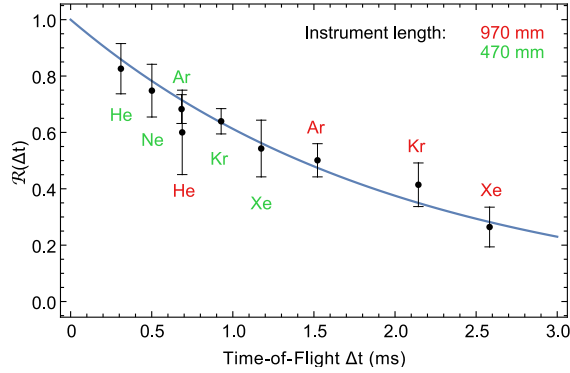


Figure 4.13: Data recorded to determine the radiative lifetime. The black dots show the normalised ion signal $\mathcal{R}(\Delta t)$. The error bars show the standard deviation of several measurements. The blue line is the exponential fit to the data points. The calculated lifetime of the $a^3\Pi_1, J = 1, e$ level is 1.89(15) ms.

all measurements that were considered to determine the lifetime were performed under collision-free conditions.

An exponential function (eqn. 4.54) was fitted to the ratio of the normalised signals for excitation to $\Omega = 1$ and $\Omega = 0$. The data and their fit are presented in figure 4.13. The error bars show the standard deviation obtained from averaging over the data from several days, thus giving a realistic estimate of the experimental error. To determine the lifetime of the $a^3\Pi_1$ state from the value of $\tau_{\text{exp}} = 2.04 \pm 0.16$ ms obtained in the fit, the ratio of the two lifetimes τ_0/τ_1 needs to be known. This can be obtained from the transition strengths of the two spectral lines used, $R_1(0)$ and $R_2(0)$. $I_{R_2(0)}/I_{R_1(0)}$ was experimentally determined to be 20.9 ± 1.0 . This difference in line intensity originates in the different coupling of the $a^3\Pi_0, v = 0, J = 1, e$ levels to the $X^1\Sigma^+, v = 0, N = 0$ state. As discussed in chapter 2, these lines obtain their intensity from spin-orbit mixing with $^1\Pi$ or $^1\Sigma^+$ pure singlet states. From the experimental intensity ratio, we can determine the relative amplitude and phase of the $^1\Sigma^+$ and $^1\Pi$ contributions to the $a^3\Pi_0, J = 1$ and $a^3\Pi_1, J = 1$ excited states. The ratio of the two lifetimes can be expressed as ratio of the decay rates of the excited states. These depend on the strengths of the possible rotational decay transitions,

$$\frac{\tau_0}{\tau_1} = \frac{\Gamma_1}{\Gamma_0} \approx \frac{\nu_{R_2(0)}^3 I_{R_2(0)} + \nu_{P_2(2)}^3 I_{P_2(2)}}{\nu_{R_1(0)}^3 I_{R_1(0)} + \nu_{P_1(2)}^3 I_{P_1(2)}}. \quad (4.56)$$

In a reasonable approximation, the transition frequencies can be assumed to be identical. Losses to higher vibrational states are not included because of the calculated Franck-Condon factor of 0.997 [142]. We can determine the lifetime ratio of $\frac{\tau_0}{\tau_1} = 13.2 \pm 1.1$. Inserting this into (4.55), together with the experimental value of τ_{exp} , yields lifetimes of $\tau_0 = 24.8 \pm 2.9$ ms for the $a^3\Pi_0, v = 0, J = 1, e$ level and $\tau_1 = 1.89 \pm 0.15$ ms for the $a^3\Pi_1, v = 0, J = 1, e$ level.

The full derivation can be found in the publication by Walter *et al.* [201]. The lifetime of the $a^3\Pi_2, v = 0, J = 2, e$ level was calculated to be 1600 ms [201]. In general, the spin-orbit coupling mechanism makes the lifetimes of the different rotational and parity states in the $a^3\Pi$ state strongly dependent on Ω , J and e/f .

4.5.3 Cooling Scheme

The recoil temperature that can be reached by narrow-line cooling on the $a^3\Pi \leftarrow X^1\Sigma^+$ transition is 3.1 μK . However, the maximum light force $F_{max} = \frac{\hbar k}{2\tau}$ exerted on a molecule on this transition is 0.8 times the gravitational force on an AIF molecule. Therefore, magneto-optical-trapping is impossible on this narrow transition. The scattering rate and therefore the light force may in principle be increased by using an additional quenching laser [231, 232]. The quenching laser opens up an additional loss channel to the short-lived excited state of the main cooling transition that effectively reduces the lifetime, thereby increasing the maximum scattering force possible. The excitation rate on this transition is proportional to the laser intensity and therefore, the linewidth of the triplet state also increases proportionally, $\Gamma_{\text{eff}} = \Gamma + r_{12}$, where r_{12} is the continuous excitation rate of the transition to the short-lived state. The quenching method has resulted in the first report of a Bose-Einstein-Condensate of ^{40}Ca in 2009 [226].

In our case, the quenching laser can reduce the lifetime of the $a^3\Pi$ state through excitation to the $A^1\Pi$ state, from where molecules decay rapidly to the electronic ground state. The $A^1\Pi \leftarrow a^3\Pi_1$ transition is about a factor 1000 weaker than the $A^1\Pi \leftarrow a^3\Pi_0$ transition, we therefore have to use the $a^3\Pi_0$ state with its very long lifetime for this proposed experiment. A cooling cycle of three transitions does not lead back to the same initial rotational level in the $X^1\Sigma^+, v = 0$ state — because of parity selection rules — and we propose a four-step cycle:

1. $a^3\Pi_0, v' = 0, J' = 0 \leftarrow X^1\Sigma^+, v'' = 0, J'' = 1$ ($P_1(1)$ line)
2. drive rf transitions in the $a^3\Pi_0, v = 0, J = 0$ level from e to f levels
3. $A^1\Pi, v = 0, J = 1 \leftarrow a^3\Pi_0, v' = 0, J' = 0$ ($R_1(0)$ line)
4. spontaneous decay on the Q(1) line of the $A^1\Pi, v = 0 \rightarrow X^1\Sigma^+, v'' = 0$ band.

In a preliminary experiment with PDA excitation on the $a^3\Pi_0, v' = 0, J' = 0 \leftarrow X^1\Sigma^+, v'' = 0, J'' = 1$ transition and cw excitation with more than 1 W in a $\approx 3\text{mm}$ beam on the $A^1\Pi, v = 0, J = 1 \leftarrow a^3\Pi_0, v' = 0, J' = 0$ transition, we could recover 2% of the population that was pumped to the $a^3\Pi_0, v' = 0, J' = 0$ level in the $X^1\Sigma^+, v'' = 0, J'' = 1$ level. The laser interacts with the molecules during 10 μs , which means that we can achieve an effective lifetime of $\approx 10 \mu\text{s}/0.02 = 500 \mu\text{s}$.

4.6 Conclusion

In this chapter, I have introduced the optical Bloch equations to model optical cycling in multilevel systems. I compared them to a simpler rate equation model

and showed the application to optical cycling of AlF. The optical Bloch equations allow us to understand the influences of dark states on optical cycling of AlF.

Laser cooling of AlF on the narrow $a^3\Pi \leftarrow X^1\Sigma^+$ transition is a possible way to reduce the temperature down to the recoil limit. We determined the radiative lifetime of the $a^3\Pi_1$ and $a^3\Pi_0$ levels to be $\tau_1 = 1.89 \pm 0.15$ ms and $\tau_0 = 24.8 \pm 2.9$ ms, respectively. I propose a possible narrow-line cooling scheme including quenching to the $A^1\Pi$ state to tune the lifetime of the $a^3\Pi_0$ state. Whilst this is likely to be experimentally extremely challenging because of the long lifetime, this type of scheme may work for other similar molecules like AlCl.

Chapter 5

Experimental Characterisation of Diatomic Monofluoride Molecule Formation in a Cryogenic Buffer Gas Cell

5.1 Introduction

Cryogenic buffer gas beams are the starting point for many cold molecule experiments, and the number of cold molecules emitted is a determining factor in what experiments are possible. In this chapter, I investigate the efficiency of cold molecule production in the same experimental setup for the species AlF, CaF, MgF, and YbF, which are all relevant for current or future ultracold physics experiments [167, 225, 233, 234]. We measure the brightness of the molecular beams using the two fluorine donor gases SF₆ and NF₃, and compare it with the observed brightness of atomic buffer gas beams of the metal reactant atoms. Differences in the chemical behaviour of the involved species lead to pronounced differences between the four metal monofluorides.

Most buffer gas sources are built with a specific molecule in mind, with specific geometries and requirements. This makes a direct comparison of the molecular beam properties from literature difficult. The experiments presented in this chapter serve as a remedy to this problem.

The number density and internal energy distribution of a molecular sample from a buffer gas beam depends on the mechanism of production of the molecules, on buffer gas cooling, the physical properties of the buffer gas cell, and the beam propagation outside the buffer gas cell. I discuss the influence of the experimental parameters laser ablation intensity, buffer gas flow and fluorine donor gas species

and flow on the beam brightness and velocity distribution and draw conclusions for future experiments.

Before the experiments are discussed, I give a short overview of the working principle of molecule sources and summarise the historical developments in the field of buffer gas cooling.

5.2 Molecule Sources

The production of molecular beams is more challenging than the production of atomic beams. The samples for most atom experiments can be purchased as a gas or readily brought to the gas phase by evaporation. Molecules, however, often have to be produced in-situ. Furthermore, the energy spacing of rotational lines in molecules is on the order of 1 K. Unless the molecules are produced cold, the population in a given internal state is very small compared to atoms.

Since the 1920s, molecular beams have proven to be a practical starting point for experiments to characterise and manipulate molecular samples [235, 236]. Molecules propagate in vacuum from a source point and encounter only negligible random collisions on their path. At sufficient distance from the source, they move ballistically and have a well-defined velocity distribution. Collision partners can actively be introduced downstream. The nearly ballistic motion of the molecules enables control and manipulation of their internal and external degrees of freedom. This can be done by a variety of methods, but the most powerful is to apply electromagnetic fields with high spatial and temporal resolution, such as laser light. Inhomogeneous line broadening can be reduced by translational and internal cooling and by beam collimation [237].

A cold and intense molecular beam is then the starting point for advanced cooling techniques down to or below the μK -range. A molecular beam can be produced in different ways, each offering specific advantages for the experiment to follow. A cold and fast molecule packet with a very narrow velocity distribution — a so-called supersonic jet — is produced by pulsed jet expansion into vacuum from a narrow orifice. In a buffer gas cell source, a dense beam of cold and slow molecules can be produced by cooling the molecules via collisions with cryogenic helium gas within an enclosed volume. The molecules are extracted from the cell hydrodynamically to form a molecular beam. In our experimental setups, a buffer gas beam typically contains 100 times more molecules than a supersonic beam; the molecules move slower in the laboratory frame but have a much wider velocity distribution.

To understand the different flow regimes that we observe in these two different sources, it is useful to introduce a flow metric called the Reynolds number [189]. This number is the ratio of inertial forces to viscous forces in a fluid and is defined by

$$Re = \frac{\rho w^2 d^2}{\mu w d} = \frac{\rho w d}{\mu}. \quad (5.1)$$

ρ is the gas density, w the flow velocity, μ is the viscosity and d the characteristic length scale, in our case the aperture diameter. The von Kármán relation connects

the Reynolds number to the Mach (Ma) and Knudsen (Kn) numbers

$$Ma \approx \frac{1}{2}KnRe, \quad (5.2)$$

where $Kn = \lambda/d$ (with the mean free path λ) and $Ma = w/c$.

For a monatomic or diatomic molecule gas, the mean thermal velocity of the particles is approximately the speed of sound in this gas ($c \approx 0.74\bar{v}$ and $0.8\bar{v}$, respectively) [189]. Therefore, $Ma \approx 1$ and, in consequence,

$$Re \approx \frac{2}{Kn} = \frac{2d}{\lambda_{b-b}} \quad (5.3)$$

where λ_{b-b} is the mean free path of the buffer gas. Equation 5.3 permits to estimate the flow regime from experimental parameters. The three possible types of flow are determined by Reynolds number ranges. If $Re \lesssim 1$, the flow is in the effusive regime, where no collisions occur at the aperture. The thermal distribution of the beam is identical to the one inside the gas reservoir. In the intermediate regime, $1 \lesssim Re \lesssim 100$, collisions occur at the aperture, but the flow is not hydrodynamic. Buffer gas cells mostly operate in this range. At $Re \gtrsim 100$, the flow is fully hydrodynamic (also called “supersonic”). The gas behaves like a fluid and is cooled via collisions in a supersonic expansion.

5.2.1 Supersonic Expansion

In a supersonic source, a gas (or gas mixture) expands adiabatically into vacuum. The energy of the random thermal motion is converted into translational energy in the forward direction by collisions so that the total energy is conserved [189, 238, 239]. A gas of interest can be mixed (“seeded”) into the carrier gas. If there are enough collisions, it is at thermal equilibrium and follows the gas flow. Target species can also be introduced via laser ablation or photodissociation at the expansion nozzle. Internal degrees of freedom (vibration and rotation) relax due to inelastic collisions with the cold carrier gas [237]. At high backing pressures, the collisional cooling can lead to clustering of the seeded gas; this has not been an issue in our experiments.

5.2.2 Cryogenic Buffer Gas Cell

A typical cryogenic buffer gas cell has a cross-section of a few cm^2 and is a few cm long. It is manufactured from solid metal and kept at a low temperature, typically with a helium cryostat. The species of interest is either produced or introduced and cooled by collisions with a cold buffer gas. Both translation and internal degrees of freedom are cooled. Applying the formulae from Hutzler *et al.* [189] yields that, in the case of AlF, after ~ 65 collisions with cold buffer gas, the molecules are within 10% of the buffer gas temperature. Under our experimental conditions with a mass flow rate of 1 standard cubic centimetre per minute (SCCM) of the buffer gas and a resulting number density of $7 \times 10^{20} \text{m}^{-3}$, the mean free path of AlF in He is $\sim 0.3 \text{mm}$ and thus the thermalisation length is less than 2 cm. Rotational

quenching takes place every 10-100 elastic collisions; vibrational quenching is several orders of magnitude slower. This suggests that the rotational temperature is close to the temperature of the buffer gas while the initial vibrational temperature is hardly influenced [240].*

5.3 Historical Overview

Experiments towards laser cooling of matter always depend on a reliable source of the atoms or molecules of interest. Because of the large optical forces that can be exerted on atoms, their sources do not need additional cooling steps before the laser cooling and trapping step. The first laser cooling successes were achieved with metal vapours that were ionised and confined in electrostatic traps [3, 4]. Early experiments on trapping of atoms in an optical molasses made use of an atom beam produced by laser ablation of solid metal [8]. In the following years, other, equally simple approaches for atom sources were used, such as effusive beam oven sources or even loading of a magneto-optical trap from the background vapour that was produced in an oven [243–246]. For molecules, a pre-cooled and slow sample is essential to efficiently load optical traps. In today’s molecular physics and physical chemistry, there are two frequently used approaches to produce slow and cold molecular beams: supersonic expansion and buffer gas cells.

Laser ablation of metals in the vicinity of a supersonic expansion orifice was initially used to make metal clusters seeded in a noble gas [247]; this method was later adapted to include reactant gasses in the expansion to form various di- and polyatomic molecules of spectroscopic interest [248–251]. The first fluorides that were produced from a reaction with SF₆ were YF [251] and CoF [252]. This method to produce metal fluorides was soon applied to two species of interest for laser cooling experiments, YbF [253] and CaF [254], by the group of Hinds, Tarbutt and Sauer. Using this supersonic source, this group succeeded in laser cooling of CaF in 2014 [63].

Before buffer gas cells were widely applied as molecule sources, researchers used other slowing and cooling techniques to obtain a cold and controlled sample beam from a supersonic expansion, such as Stark [37], Zeeman [38], or alternating gradient slowing [255].†

Buffer gas cooling of atoms and molecules was pioneered by the group of John Doyle, drawing on ideas by Messer and De Lucia [257]. His team at Harvard University started off by magnetically trapping different paramagnetic species in a closed cold cell that were subsequently cooled by collisions with a cold buffer gas with a temperature of less than 1 K [36, 258–263]. This method resulted in the production of an atomic Bose-Einstein condensate, by buffer gas and subsequent evaporative cooling [264].

*It is worth noting that, as pointed out by Polanyi and Woodall, the probability of rotational de-excitation depends on the energy spacing of the rotational levels following the relation $P_{J-1}^J \propto \exp(\frac{C\Delta E}{k_B T})$ [241, 242]. This is often referred to as the “energy gap law”.

†One particularly curious proposed method for slowing and speeding of a beam even employs a backward or forward rotating nozzle [256].

The Rempe group at the Max Planck Institute for Quantum Optics in Munich employed electric quadrupole guides to filter slow molecules from molecular beams of ammonia and formaldehyde. The group developed their setup to contain a buffer gas cell, where the sample gas is filled into the cryogenic cell with a capillary [265,266]. In 2002, Egorov *et al.* [267] published how they load a closed buffer gas cell from a thermal beam of Rb atoms. Maxwell *et al.* [188] — from the groups of John Doyle and David DeMille (Yale) — were then the first to report on a buffer gas cell as high-flux source of a beam of cold atoms or molecules. They thoroughly investigated beam properties as a function of buffer gas flow, for Na atoms as well as PbO molecules. This setup was improved with a “hydrodynamic enhancement” stage with a grid in the front that slowed and concentrated the sample molecules [268]. The Doyle group also reported on neon as suitable buffer gas [269] and demonstrated the extension of this technique to cool large molecules, using naphthalene [270]. The sizes of organic molecules that are successfully cooled in buffer gas cells have since increased up to the C₆₀ fullerene, as shown by the Ye group [271,272].

The buffer gas cooling technique was refined and applied to other species, such as CaH, using an extended slowing cell [273], and the reactive ThO molecule that was additionally cooled by an expansion [274]. In 2012, a comprehensive review on the current state of the art of buffer gas cells was published, emphasising the importance of this technique in the cold molecule community [189]. In the same issue of *Chemical Reviews*, an equally comprehensive review on the manipulation and control of supersonic molecular beams with electric and magnetic fields appeared [41].

The Tarbutt group at Imperial College made great progress working with buffer gas sources of YbF. They initially used the Harvard cell design [273] with a mixed powder target of reactant species, without reactant gas [208]. In two publications, members of this research group used a special buffer gas cell with large windows to use absorption imaging and absorption spectroscopy to precisely study diffusion and thermalisation of YbF molecules [275] and Yb atoms [234]. They showed that for YbF molecules formed by ablation of a mixed target of Yb and AlF₃, the molecules are created at the target surface and not further down in the plume. In his PhD thesis, Nicholas Bulleid developed a new design optimised for rapid extraction of the molecules from the cell and the method to produce YbF from a reaction of laser-ablated Yb metal with SF₆ [276,277]. Using this cell design with CaF, the group achieved chirped-frequency laser slowing and a CaF molecular MOT [225,278]. The source layout and its properties, together with gas-dynamics simulations, was published in a later article [190]. The same method to produce the molecules via reaction with SF₆ has then been adopted by the group at Harvard University [70]. Already before the London results on YbF and CaF, Shuman, Barry and DeMille reported on the first transverse laser cooling of a diatomic molecule, SrF, that they produced in a cryogenic buffer gas source from an SrF₂ target [61]. Later, they also demonstrated longitudinal slowing [279]. In the following years, they succeeded in magneto-optical trapping of SrF and further improved their method [68,280,281].

As currently many metal monofluorides are under investigation for opportunities towards ultracold science, a buffer gas source is now the method of choice in many groups. The new molecules that are currently being studied using a buffer gas source are MgF [282], AlF [167], BaF [283], SrF [284], and AlCl [77]. The experiments on BaF also use a cryogenic buffer gas cell of the common design, but without fluorine donor gas.

In the 2010 years, there was also progress at JILA in Boulder, USA, with a MOT of YO, also produced in a buffer gas source, from Y_2O_3 powder [62, 71, 285]. They progressed to sub-Doppler cooling and recently cooled the molecules to a record low of 6.1 μ K and transferred them into an optical lattice [286, 287].

Buffer gas cells are still also used for pure spectroscopy interests, like it was performed by Changala *et al.* [271] for frequency comb spectroscopy of buffer gas cooled polyatomic molecules and for BaH that was produced from BaH₂ and used for high-resolution optical spectroscopy [75, 288].

The different processes involved in the laser ablation of bulk solid aluminium have been thoroughly investigated by experiments and theory and will be discussed in a later section [289–293].

The question of where the reaction of an evaporated solid with the reactant gas happens has been addressed for the system of ablated graphite in the presence of NO to form CN by Sasaki and Watarai [294, 295]. They observe that the wavelength of the ablation laser has an influence on where the reaction product forms.

The kinetics of production of AlCl by ablation of Al and AlCl₃ in a buffer gas cell was investigated based on standard chemical kinetics [77].

Some efforts have been undertaken to simulate the processes during buffer gas cooling. In buffer gas cell environments, the gas densities are not high enough to allow for a purely hydrodynamic treatment, at least if the cooling process itself is the aim of the calculations. The typical densities in a buffer gas cell are in the so-called intermediate regime between hydrodynamic and molecular flow. This means that flow calculations based on the Navier-Stokes equation would not yield accurate results while at the same time, a full molecular dynamics treatment is not feasible because of the large number of particles involved. The densities of buffer gas and reactant gas differ by several orders of magnitude, which additionally challenges calculations. For a complete treatment that can also include internal energies, an approach called “direct simulation Monte Carlo” is the most suitable and promising [242, 296, 297]. In this method, a large number (around 10^{10}) of physical particles is grouped as a virtual particle, containing the sum of the properties of all physical particles, that collides with other particles. Still, this method involves significant computational efforts. The method has been refined with a more efficient self-consistent field algorithm to speed up calculations [298–300]. To appropriately calculate the translational and rotational cooling, the respective collision cross sections need to be determined accurately, as has been done by Karra *et al.* for AlF [301]. A simplified Monte Carlo approach was used by Gantner *et al.* to model the low-density limit [302]. If just the flow of a buffer gas is of interest, a simple computational fluid dynamics simulation is possible [225].

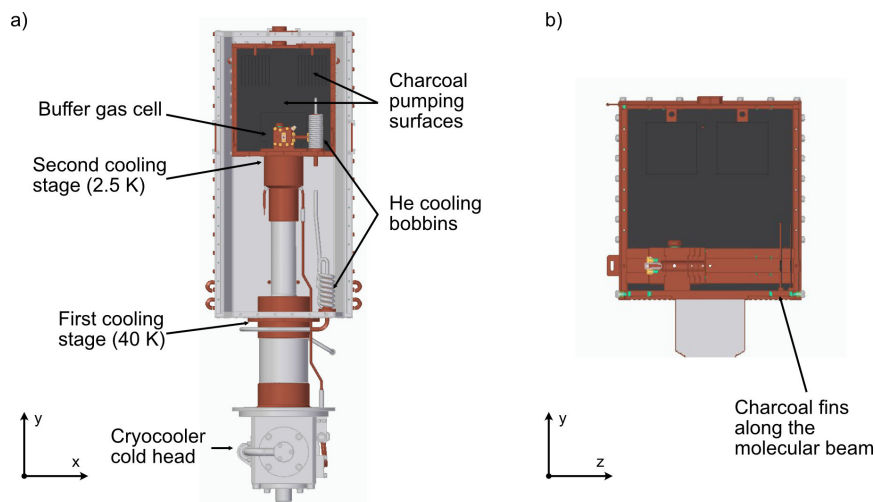


Figure 5.1: (a): CAD rendering of the whole experimental setup inside the vacuum chamber. The resulting molecule beam travels into the page. The front plates were removed to give a complete view of the inside of the source chamber. The gas lines and the target turning rod are not shown. (b): Cut along the direction of the molecular beam of the second stage radiation shield.

5.4 Experimental Setup

5.4.1 Cryogenic Buffer Gas Cell

In our cryogenic buffer gas cell setup, molecules are produced by laser ablation of metal in the presence of a fluorine donor gas and subsequently cooled by collisions with cold He buffer gas. The molecular beam produced this way is pulsed and has a length of a few ms passing through the fluorescence detector, visible in the LIF time-of-flight (TOF) traces in this chapter. The ablation laser pulse timing is the starting point of all these traces in this chapter. The buffer gas cell is kept at as low as 2.5 K by a two-stage closed-cycle He cryocooler, shown schematically in figure 5.1a.[‡] The first stage achieves temperatures down to as low as 40 K; we attach an aluminium radiation shield to it to reduce the heat load on the second stage. The second stage is made up by a copper box; its internal walls are coated with activated charcoal granulate that acts as a sorption pump for He buffer gas at temperatures below 10 K. The He needs to be pumped away very efficiently to allow a molecular beam to form and to prevent collisions further downstream.

To increase the pumping surface, we attach fins to the top of the copper radiation shield that are coated with activated charcoal as well. Additional charcoal-coated fins mounted along the molecular beam pump away helium from the wings of the molecular beam (shown in figure 5.1b). While the hanging fins turned out

[‡]To help understand the working principle of a conventional commercial He cryocooler, I provide a short description in appendix C.

to have only minor influence on the beam properties, the fins along the molecular beam increase the molecule flux. Saturation of the activated charcoal with reaction products of the buffer gas source — indicated by a discoloration around the aperture used to collimate the molecular beam — significantly reduced the molecule signal downstream. In this case, the fin can be easily replaced by another one with fresh charcoal coating. This is much simpler than replacing the whole outer plate of the charcoal shield and optimises maintenance considerably. The configuration of fins is shown in figure 5.1b. The gases (He, NF_3 and contaminants) need to be removed from the charcoal surface on a regular basis (normally after every experiment day), which is achieved by resistively heating the radiation shields to room temperature.

The temperatures of the two stages as well as the buffer gas cell are measured with silicon diodes (LakeShore DT-600) and recorded with a LakeShore temperature monitor. The warm-up process is monitored by two type-K thermocouples that are attached to both stages. As soon as a defined set point is reached, the cryocooler can be switched on automatically with a custom-programmed Eurotherm controller.

The cryogenic buffer gas cell used in our experiments is based on the design published by Truppe *et al.* [190]. The bore size of this buffer gas cell is smaller than most other buffer gas cells; the smaller volume will allow a shorter extraction time and a compact molecular pulse. We used different versions of the cell during the time of the investigations, but the changes in design only concerned the mounting and flexibility of parts - the materials and cell geometry stayed identical. The buffer gas cell is machined from oxygen-free copper. Cuts of the buffer gas cell along two directions are shown in figure 5.2 and an exploded view of the components is shown in figure 5.3.

The buffer gas cell has a circular cross-section with a diameter of 10 mm and a variable length of 30-60 mm. The molecules (or atoms) travel towards the cell orifice through a tube of variable length, whose influence on molecule thermalisation will be discussed later in the thesis. The pieces of this tube are either 5 or 10 mm long and can be interchanged flexibly. To enable optical access for in-cell absorption measurements, we drilled 3 mm diameter holes transverse to the molecular beam direction and sealed them with 5 mm fused silica windows on both sides. We observe that these windows get coated with material from the buffer gas source over several months of operation. The He buffer gas flows into the cell at the position furthest from the molecule orifice, at an angle with the molecular beam direction. The gas is pre-cooled in two copper pipe bobbins that are attached to each of the two cooling stages (pointed out in figure 5.1). The central piece of the buffer gas cell block is attached to the second stage of the closed-cycle cryocooler with four screws; we apply a small amount of Apiezon-N vacuum grease to the underside of the cell to ensure good thermal contact with the second stage of the cryocooler. In this piece, the cylindrical metal target threads into a copper target holder, which itself threads into the main block of the cell. The target holder rotates in the thread of the main cell block via a rotational feedthrough on the main vacuum chamber. In this way, we can access fresh spots for ablation of the atoms. Ablation of the metal is performed using a pulsed Nd:YAG laser

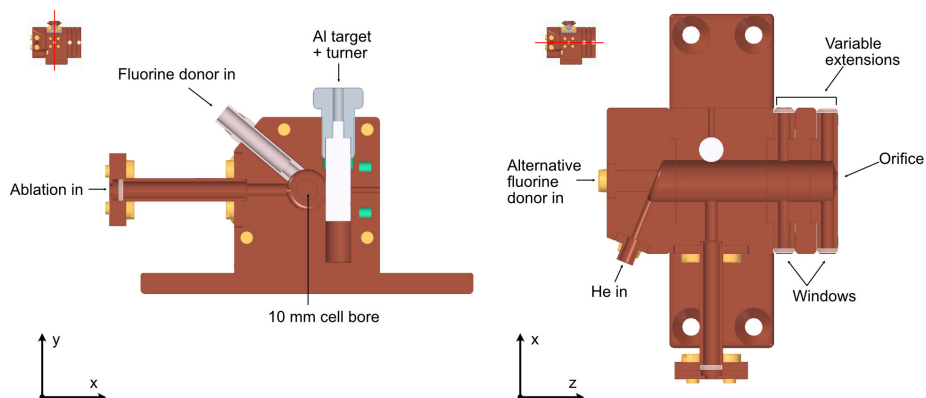


Figure 5.2: Cut views of the buffer gas cell. Left: cut perpendicular to the molecular beam direction, showing the region where Al is ablated and reacts with a fluorine donor gas. Right: cut along the molecular beam direction showing the path of the He buffer gas. In the back of the cell, an alternative fluorine donor gas inlet can be installed to change the flow dynamics. This was not used in the works presented in this thesis. The installed plug has a 1 mm hole to align lasers along the molecular beam axis.

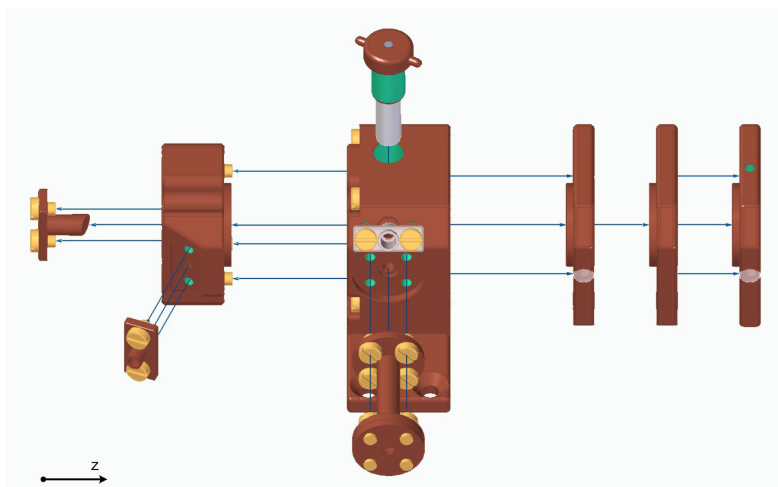


Figure 5.3: Exploded view of the buffer gas cell. All modular parts can be replaced by different options.

(Continuum Minilite II) with up to 40 mJ pulse energy in a pulse length of 5-7 ns, operated at a repetition rate of 1 Hz. The ablation laser enters through a window from the side that is attached on a 20 mm long pipe that avoids evaporated metal from depositing on the window and thus decreasing transmission. Between the metal target and the ablation laser window, the fluorine donor gas flows into the cell through a pipe that is insulated with PEEK (polyether ether ketone) plastic so that heat transfer from the pipe to the buffer gas cell is minimised — this also reduces the chance of the fluorine donor gases freezing and thus clogging the feeding pipe. The pipe temperature is monitored with a type-K thermocouple and is typically at 120 K.

The operating pressure of the source chamber is about 1.5×10^{-6} mbar in its warm state and about 1.5×10^{-8} mbar when cryogenic temperatures are reached. This is measured in the main vacuum chamber, outside the radiation shields. The pressure typically increases to $5-8 \times 10^{-8}$ mbar when we flow 1 or 2 SCCM of He. Unfortunately, we cannot measure the pressure inside the 2.5 K stage during operation.

Unless mentioned otherwise, all source characterisation experiments were performed using 15 mm of extension blocks on the buffer gas cell (amounting to a total length of 40 mm) with an output orifice diameter of 4 mm. We used a helium buffer gas flow of 1 SCCM and an NF_3 flow of 0.001 SCCM, the SF_6 flows are mentioned where applicable.

5.4.2 Source Characterisation Experiments

To compare the efficiency of cold molecule production for each species, we use two approaches: We measure the number of molecules produced outside the cell, N , by absorption spectroscopy. We measure both peak absorption and the transverse velocity distribution, from which we can deduce an estimate of the number of molecules produced and the on-axis source brightness. We also probe the molecules further downstream of the source using laser-induced fluorescence (LIF). We address rotationally open transitions so that each molecule scatters a known number of photons, from which we can deduce a second measure of the source brightness. In the same way, we can determine the number of atoms produced in the cell and compare this to the molecule number. Unfortunately, not all studied atom transitions are open and can be used as standard candle transitions.

The absorption method is relatively easy to implement and the calculation of the molecular beam density is straightforward. On the downside, absorption detection is not sensitive to low densities; at high densities, the molecular beam is optically dense and molecule numbers can only be determined from extrapolation. Fluorescence detection several centimetres downstream of the buffer gas cell is sensitive and has a large dynamic range that can record single photons as well as the highest numbers of photons we expect in the experiment. The calculation of the molecular beam density is more involved than for the absorption measurement because the wavelength dependence of the detection setup and the anisotropy of the fluorescence emission must be considered (*vide infra*).

In the case of Al, Ca and Yb, convenient optical transitions are accessible with our laser systems. This allows us to make useful comparisons between species under almost identical conditions. By observing the atom signal in presence of a fluorine-containing reactant gas, we can straightforwardly investigate the effect of the reactant gas. We combine this with the measured molecular state distribution downstream from the source. This information can be used to estimate the production efficiency of the molecules. This relies on the assumption that a negligible portion of the molecules observed are formed from atomic ions or clusters produced in the source, which we do not observe.

A scheme of the full experimental setup is shown in figure 5.4a. To be able to study different atomic and molecular species without having to break vacuum in between, we use a multi-species target, shown as an inset. The body of this target is made of Al and similar to the Al targets used before [88]. The Al cylinder includes a cylindrical bore into which rods of Ca, Mg, and Yb can be placed and secured by an Al cap.

We can detect the atoms and molecules using absorption spectroscopy with a weak probe beam inside the cell and at a variable distance 0-2 cm from the exit aperture. We detect the transmitted light with an amplified photodiode. We can optionally add a pump laser intersecting the molecules immediately outside the charcoal radiation shields, after which point most of the helium gas has been removed from the beam and rotational state-changing inelastic collisions of the sample molecules with the buffer gas are negligible.

The source chamber is separated from the downstream detection chambers with a gate valve. Downstream of the source chamber, two laser-induced fluorescence (LIF) zones are installed. The first one, LIF-1, is located $L_1 = 17$ cm downstream of the cell exit. It is primarily used as a region for optical pumping of populations to determine the velocity of the molecules using a pump-probe method [88]. The second zone, LIF-2, is located 44 cm downstream of the cell exit and is used for spectroscopy and beam brightness measurements. Before the molecular beam enters the field of view of the detection optics in LIF-2, the transverse velocity spread of the molecular beam is restricted by a square aperture of size 2×2 mm². In this case, this reduces the detected molecular beam to an opening angle of ≈ 4.5 mrad, which restricts a beam with a typical forward velocity of 200 ms⁻¹ to a transverse velocity spread of less than 1 ms⁻¹, thus reducing the Doppler broadening in our fluorescence spectra. Importantly, it also allows us to ensure the spatial extent of the molecular beam can be fully covered by the probe laser light, and that all fluorescence photons are generated close to the optimal location in our detector. This allows us to truly saturate the fluorescence.

Figure 5.4b shows the collection optics of LIF-2. The spatial extent of the laser beam profile exceeds that of the molecular beam aperture so that laser intensity changes do not influence the laser-molecule interaction volume. The e^{-2} intensity diameter is 2-3 mm, being small enough to ensure uniform imaging efficiency of the fluorescence onto the photomultiplier tube (PMT). With this setup, all molecules that enter the detection zone also interact with laser light. The solid angle subtended by the aperture at the buffer gas cell exit is $\approx 2.1 \times 10^{-5}$ sr; this can later be used to accurately determine the on-axis source brightness. We use

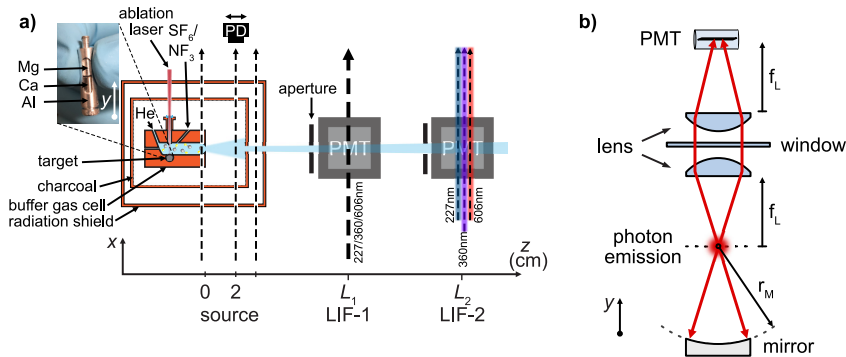


Figure 5.4: (a): Sketch of the experimental setup used in this study to characterise the atomic and molecular beams. (b): Optical layout of the fluorescence detector.

the same optical setup in the fluorescence detector for the detection of all atomic and molecular species. The wavelength span of the fluorescence light is from 227 to 606 nm and the collection efficiency of the LIF detector depends on this since the focal length of optical elements depends on λ . We use ray tracing simulations combined with the measured transmission and reflection losses of each optical component to account for this wavelength dependence. The quantum efficiencies were determined by illuminating the PMT directly with about 1 nW of light; the light intensity was attenuated from a well-measurable intensity by using a calibrated 10^{-3} optical filter. The PMT signal is then sent to a transimpedance amplifier with current-to-voltage conversion factor of 10^5 V A^{-1} . Thus, we can relate a voltage measured by our data acquisition hardware to the rate of fluoresced photons.

Anisotropy of the Fluorescence Emission

In general, fluorescence detection involves capturing a finite solid angle of the emission pattern of an atom or molecule. This effect makes it important to specify the detection direction \vec{R} relative to the electric field polarisation axis of the light, $\vec{\epsilon}$. Normally \vec{R} is perpendicular to the \vec{k} -vector of the light, and the anisotropy is defined by the angle θ , between \vec{R} and $\vec{\epsilon}$ in the plane normal to \vec{k} .

If we excite with linear polarisation, and let $\vec{\epsilon}$ define the z -axis, then emission of photons linearly polarised along z corresponds to π -polarised light. In this coordinate system, the detection efficiency of π -polarised light (which is emitted for transitions with $\Delta m = 0$) is proportional to $\sin^2 \theta$; the detection efficiency of σ^\pm light (which is emitted for transitions with $\Delta m = \pm 1$) is proportional to $(1 + \cos^2 \theta)/2$. For measuring the $^2\Sigma$ molecules (CaF, MgF, YbF) in fluorescence, we deliberately choose to excite $Q_{11}(0)$ lines, because the emission pattern from all Zeeman sublevels in the excited state is isotropic. We therefore neglect the influence of linear polarisation when calculating the molecular beam density in these cases. For AlF, the fluorescence on R-lines is known to exhibit a dependence on the linear polarisation angle, although this effect is at most 20% of the

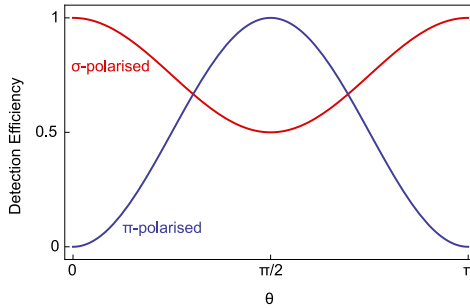


Figure 5.5: Detection efficiency of π - and σ^\pm -polarised photons as function of the angle θ between the direction of the fluorescence detector \vec{R} and the electric field polarisation axis of the excitation light $\vec{\epsilon}$ in the plane normal to the laser propagation direction \vec{k} .

fluorescence signal. To measure the AlF beam, we set $\vec{\epsilon} \parallel \vec{R}$, where the relative number of photons detected on the R(1) and P(1) lines was found to agree with predictions based on the Hönl-London factors. For measuring the Al, Ca and Yb atomic beams, we set $\vec{\epsilon} \perp \vec{R}$.

For the bosonic isotopes of Ca and Yb, the emission pattern follows that of a Hertzian dipole, and we correct the enhancement factor when observing perpendicular to the excitation light when calculating the measured atomic beam brightness.

For Al, we experimentally found less than 10% variation in the saturated fluorescence observed with the linear polarisation angle, and our experimental spectrum can be well reproduced by assuming isotropic emission. This is likely the result of angular momentum precession in the ground state during the interaction time with the laser, due to the ambient magnetic field in the detector.

5.4.3 Laser Systems

We use two different continuous laser systems for this study. The first is the Msquared Ti:Sa laser used previously. The IR fundamental can be frequency-doubled to generate UV light near 359 nm for detection of MgF, and near 399 nm for the detection of Yb. With an additional stage of frequency-doubling, we can produce deep UV light near 227 nm to detect AlF, Al and Ca.

The second laser system is the Coherent 899 ring dye laser (RDL) which generates light near 606 nm for detection of CaF and near 552 nm for the detection of YbF. The laser frequencies are monitored with our HighFinesse WS8-10 wavemeter that is calibrated to a temperature-stabilised HeNe laser. Details on the absolute accuracy of the wavemeter can be found in chapter 6.

In the following sections, I will present the experimental results of our investigations on the fluoride formation in a buffer gas source.

5.5 Results: Atomic Beams

For every atomic beam in our study, we need a well-characterised transition to study the brightness, velocity distribution and the influence of fluorine donor gas on both. In this section, I discuss the observations we made of atomic beams of Al, Ca and Yb. None of our available laser systems could be tuned to a frequency resonant with a strong Mg transition from the ground state.

5.5.1 Aluminium

To characterise the Al atom signal, we can use a transition close to the AlF optical cycling transition $A^1\Pi \leftarrow X^1\Sigma^+$, namely the $(3s^25d)^2D_{3/2} \leftarrow (3s^23p)^2P_{1/2}$ transition near 226.4 nm. The excited state lifetime τ_{ex} is 12.3 ns ($\Gamma/2\pi = 12.8$ MHz). Exciting this transition pumps 95% of the atomic population to the higher-energy spin-orbit doublet (fine structure) state $(3s^23p)^2P_{3/2}$. It lies 112 cm^{-1} above the ground state and decays at a rate that is negligible on the timescale of the experiments. Less than 1% of the Al atoms exiting the source initially occupy the $^2P_{3/2}$ state. They appear in the insufficiently thermalised part of the atomic pulse at early arrival times in the detector. Five percent of the atomic population gets pumped to other 2P and 2F states, which cannot decay to the $^2P_{1/2}$ electronic ground state by allowed dipole transitions. We neglect the effect of these states other than the fact that they slightly increase the optical pumping probability. The relevant electronic states and their hyperfine structure are presented in figure 5.6.

Hyperfine Structure

Spectra of the stable ^{27}Al isotope have a rich hyperfine structure, owing to the nuclear spin $I_{\text{Al}} = 5/2$. The hyperfine structure arises from interaction of the total electronic angular momentum $\mathbf{J} = \mathbf{L} + \mathbf{S}$ with the nuclear spin \mathbf{I} to give the total angular momentum $\mathbf{F} = \mathbf{I} + \mathbf{J}$. The states accessible by transitions in the wavelength region of our laser system are $(3s^23p)^2P_{1/2}$, $(3s^23p)^2P_{3/2}$ electronic ground states and the excited $(3s^25d)^2D_{3/2}$ and $(3s^27s)^2S_{1/2}$ states. The hyperfine parameters of the ground states have been reported [303], while those for the excited states are not known. With our versatile source of cold atoms and molecules and the flexible high-power tunable cw Ti:Sa laser system, we are able to record high-resolution spectra of the $^2D_{3/2} \leftarrow ^2P_{1/2}$, $^2D_{3/2} \leftarrow ^2P_{3/2}$, $^2S_{1/2} \leftarrow ^2P_{1/2}$, and $^2S_{1/2} \leftarrow ^2P_{3/2}$ transitions. All spectra are recorded using a weak probe intensity so that $I \ll I_{\text{sat}}$.

All recorded spectra are presented in figure 5.7. The transitions originating from the $^2P_{3/2}$ state could only be observed using residual fast moving atoms that do not thermalise with the buffer gas; this state is not populated in atoms thermalised to the buffer gas. Therefore, their spectra are Doppler-broadened considerably. We are able to assign all lines based on the previously known spectroscopic parameters and the hyperfine structure of the spectrum in 5.7a and b. The line centres are obtained from fits of Lorentzian curves. In the case of the

Table 5.1: Hyperfine parameters A and B for the states of Al investigated in this chapter. The literature values for the electronic ground states are reproduced from Chang’s work [303], where the hyperfine parameters are calculated from previously published spectroscopic data [306]. For states with $J = 1/2$, the second term in equation 5.4 is not defined, therefore B is set to 0.

	$A(\text{MHz, exp})$	$B(\text{MHz, exp})$	$A(\text{MHz, lit})$	$B(\text{MHz, lit})$
$(3s^27s)^2S_{1/2}$	33.18(13)	0	–	–
$(3s^25d)^2D_{3/2}$	–33.9(4)	1.9(2.5)	–	–
$(3s^23p)^2P_{3/2}$	94.3(1.0)	19.3(1.0)	94(0)	18.8(3)
$(3s^23p)^2P_{1/2}$	501.6(1.2)	0	502(0)	0

$2S_{1/2} \leftarrow^2 P_{3/2}$ transition, Gaussian curves were used to determine the line centres because of the dominant Doppler broadening of the beam of hot atoms and the small lifetime broadening. The simulated spectra in figure 5.7 have Lorentzian lineshapes, whose FWHM is the natural width of the excited states reported in the literature [304]. The residual broadening is a combination of the residual Doppler width of the molecules, Zeeman broadening due to uncontrolled magnetic fields in the instrument, and possible hyperfine pumping.

To fit the spectra, we assume the hyperfine energies, $E_i(J, I, F)$, are given by [305]

$$E_i = \frac{A_i C}{2} + B_i \frac{\frac{3}{4}C(C+1) - I(I+1)J(J+1)}{2I(2I-1)J(2J-1)}, \quad (5.4)$$

where A_i is the interaction strength between the nuclear spin \mathbf{I} and the electronic angular momentum \mathbf{J} , B_i is the quadrupole interaction coefficient, necessarily zero for $J < 1$, and $C = F(F+1) - I(I+1) - J(J+1)$. The index i labels the electronic state. The relative line strengths for transitions between a lower state F and an upper state F' are given, expressed using Wigner 6j-symbols, by [303]

$$I_{F',F} = |\sqrt{(2J'+1)(2J+1)} \times \begin{Bmatrix} L' & J' & S \\ J & L & 1 \end{Bmatrix} \times \sqrt{(2F'+1)(2F+1)} \times \begin{Bmatrix} J' & F' & I \\ F & J & 1 \end{Bmatrix}|^2 \quad (5.5)$$

From the fit, we find the hyperfine parameters for the four states. The values are presented in table 5.1. To obtain the presented values, we only used our experimental data and did not fix the values found in literature. I provide these in the table as a reference. The excited state hyperfine parameters are reported here for the first time. The 1.5 GHz splitting in the spectra in figure 5.7a and b originates from the large ground state hyperfine splitting of the $(3s^23p)^2P_{1/2}$ state while the splitting in the two features each is caused by the excited state hyperfine splitting that is one order of magnitude smaller. The $(3s^25d)^2D_{3/2}$ state is inverted. The spectra originating in the $(3s^23p)^2P_{3/2}$ state (figure 5.7c and d) are congested because the hyperfine parameters in the ground and excited state are of the same order of magnitude.

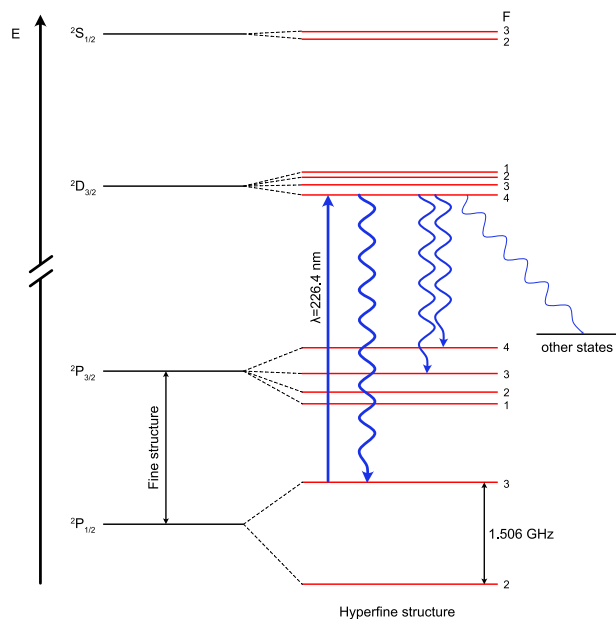


Figure 5.6: Scheme of the electronic states and hyperfine levels of Al that were observed in our experiments. Electronic energies are not to scale, the relative hyperfine splittings are shown to scale. We use the $^2D_{3/2}, F' = 4 \leftarrow ^2P_{1/2}, F = 3$ transition to detect Al atoms.

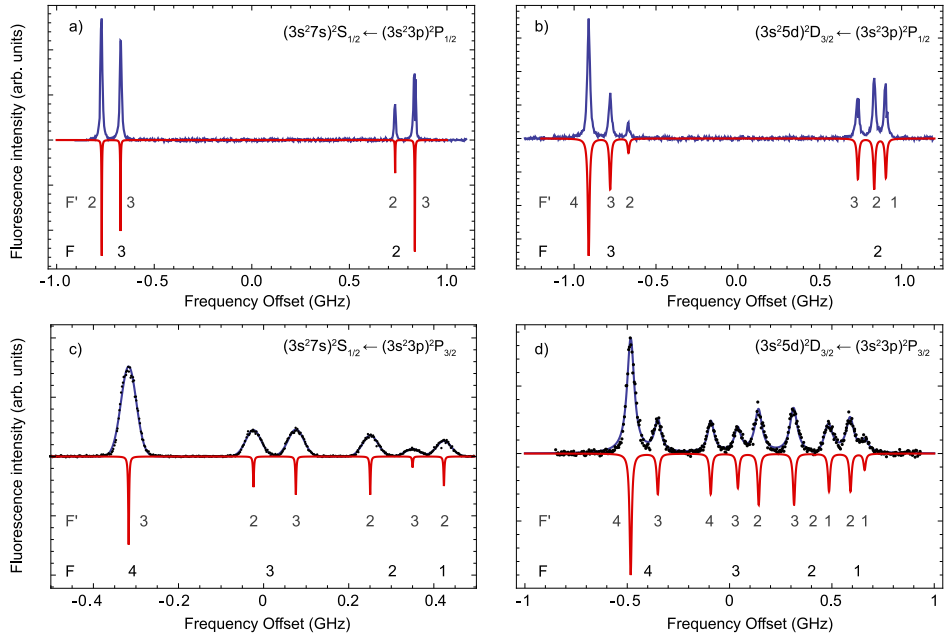


Figure 5.7: Hyperfine-resolved LIF spectra of four electronic transitions of Al. The term labels of the transitions are printed in the respective spectra. (a) and (b): experimental spectrum in blue, spectrum simulated from experimentally determined parameters in red. (c) and (d): experimental spectrum shown as black dots, Gaussian (c) or Lorentzian (d) fit in blue, and simulated spectrum in red. The ground-state (F) and excited-state (F') hyperfine quantum numbers of the transitions are given below the simulated spectra.

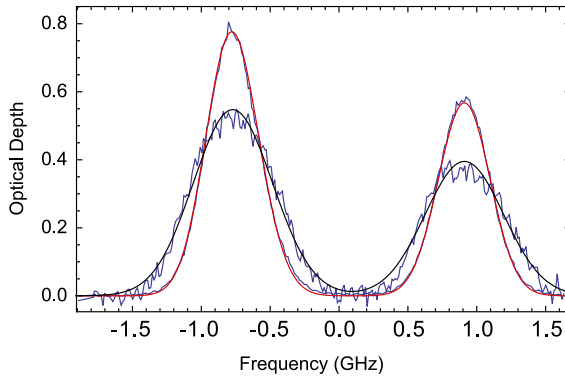


Figure 5.8: Aluminium absorption spectra recorded directly outside the cell exit (data blue, fit red) and 10 mm downstream (data blue, fit black). The Doppler broadening increases for the downstream position.

Measurement of Atomic Beam Properties

To investigate properties of the aluminium atomic beam, we choose the strong $^2D_{3/2} \leftarrow ^2P_{1/2}$ transition from the electronic ground state. We record absorption spectra of this transition directly outside the exit of the buffer gas cell and 10 mm downstream, presented in figure 5.8. There and in all following absorption plots, we show the optical depth $-\ln(I_t/I_0)$ on the ordinate axis, where I_t is the intensity transmitted through the sample and I_0 is the incoming intensity on the sample. The previously presented hyperfine structure is unresolved and we only observe the ground state hyperfine separation. We fit the data using the measured excited state hyperfine structure convolved with a Doppler broadening term with FWHM Γ_D . The transverse velocity width, $v_t = \Gamma_D \lambda / (2\pi)$, is approximately 80 m s^{-1} at $z = 0 \text{ mm}$ and 150 m s^{-1} at $z = 10 \text{ mm}$. This suggests that immediately outside the cell orifice, many collisions between the Al atoms and the He buffer gas and background gas occur, the atomic beam diverges and that the Al atoms are translationally heated up. Therefore, absorption measured directly outside the cell can only provide an upper bound to the beam brightness observed downstream.

To measure the atomic flux in fluorescence, we excite the $F' = 4 \leftarrow F = 3$ transition, since it is the strongest, best-resolved line. The $F' = 4$ excited state can decay back to the $F = 3$ initial state or to the $F = 3$ and 4 levels in the $^2P_{3/2}$ state. From the documented Einstein A coefficients of all possible decay transitions [304], the probability to decay back to the initial state is calculated to be $p = 0.837$ and therefore the average number of scattered photons on the $F' = 4 \leftarrow F = 3$ transition before the atom decays to the $^2P_{3/2}$ state is 6.12. In figure 5.9, the fluorescence signal on this transition in LIF-2 is plotted against the laser intensity, demonstrating that we can saturate the fluorescence. The inset shows the fluorescence signal with and without a high-intensity pump beam applied in LIF-1, demonstrating a pumping efficiency of approximately 90%.

In figure 5.10, the saturated fluorescence signal measured in LIF-2 is shown

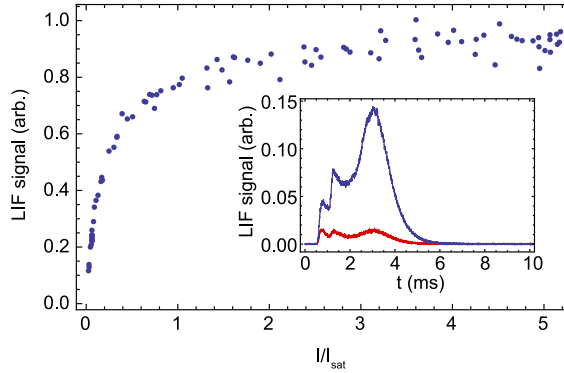


Figure 5.9: Fluorescence saturation curve of the $(3s^2 5d)^2 D_{3/2}, F' = 4 \leftarrow (3s^2 3p)^2 P_{1/2}, F = 3$ line of Al, demonstrating that we can bring fluorescence close to full saturation by optical pumping of the atoms. The inset shows the LIF TOF without (blue) and with (red) a pumping laser on the same transition in LIF-1.

together with the absorption measured after the buffer gas cell exit (inset). By integration of the LIF signal, we estimate that $6.1 \pm 0.8 \times 10^7$ atoms pass through the detection region, which corresponds to an on-axis brightness of the atomic beam of $3.0 \pm 0.4 \times 10^{12} \text{ sr}^{-1}$ per pulse. For this calculation, we assume that the atoms in the $F = 3$ state scatter 6 photons on average and that each Zeeman sublevel has equal population. Because of the hyperfine splitting in the ground state, atoms in $F = 2$ scatter no photons. From the absorption trace, we can also estimate the total number of atoms per pulse. We assume that the number of atoms in the detection region N behaves according to

$$\frac{dN}{dt} = v_f \cdot a \cdot n(t) \quad (5.6)$$

where v_f is the mean forward velocity, a the aperture area and $n(t)$ the time-dependent density in the absorption region. The latter can be obtained from the absorption $A = -\log(I/I_0)$ [§] from the relation

$$A(t) = n(t) \cdot \sigma_D \cdot x_i, \quad (5.7)$$

where x_i is the perpendicular absorption length through the beam and σ_D is the Doppler broadened absorption cross-section. The resonant absorption cross section is given by [206]

$$\sigma_{\text{abs}} = \frac{\lambda^2}{2\pi} \frac{2J' + 1}{2J + 1} \frac{\gamma_p}{\gamma_{\text{tot}}}, \quad (5.8)$$

where J and J' are the ground and excited state electronic angular momentum quantum numbers, γ_p is the partial spontaneous decay rate of the resonant transi-

[§]The absorption is defined with the decadic logarithm while the optical depth is defined with the natural logarithm: $OD = -\ln(I/I_0)$. Therefore, $A = OD/\ln(10)$.

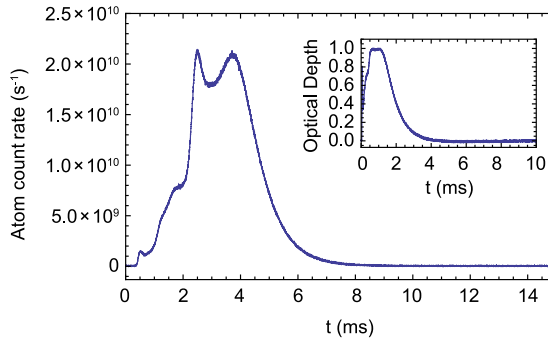


Figure 5.10: Fluorescence and absorption TOF traces of the Al beam, using light resonant with the $(3s^25d)^2D_{3/2}, F' = 4 \leftarrow (3s^23p)^2P_{1/2}, F = 3$ transition. The atom count rate was calculated from the LIF signal.

tion, and γ_{tot} is the total decay rate, including spontaneous decay to other levels. In the case of a closed transition, the factor $\gamma_p/\gamma_{\text{tot}}$ is 1. For the ${}^2D_{3/2} \leftarrow {}^2P_{1/2}$ transition of Al, the resonant absorption cross section is $1.4 \times 10^{-10} \text{cm}^2$. In cases of gas samples with a thermal velocity distribution, Doppler broadening makes the spectral line wider, but does not change the area under the absorption curve. Therefore, the resonant absorption cross section is reduced to the Doppler broadened absorption cross section [206]

$$\sigma_D = \frac{\sqrt{\pi}}{2} \frac{\gamma_{\text{tot}}}{\Gamma_D} \sigma_{\text{abs}}. \quad (5.9)$$

Using the measured transverse velocity spread at the exit of the source, and assuming $v_f = 200 \text{ms}^{-1}$, we find a total number of 2.8×10^{12} atoms per pulse. Combining this with the transverse velocity width measured downstream, we estimate the brightness of the atomic beam to be $4.1 \times 10^{12} \text{sr}^{-1}$ per pulse, which is in very good agreement with the LIF measurement.

5.5.2 Calcium

To determine the number of calcium atoms and their velocity distribution in the beam, we use the $(3p^64snp)^1P_1 \leftarrow (3p^64s^2)^1S_0$ transition[¶] at 227.6 nm, with an excited state lifetime $\tau_{Ca} = 14.1 \text{ns}$ ($\Gamma/2\pi = 11.3 \text{MHz}$). The LIF spectrum of this transition is shown in figure 5.11a. The strongest peak corresponds to the most abundant isotope ${}^{40}\text{Ca}$, minor peaks from the ${}^{42}\text{Ca}$, ${}^{43}\text{Ca}$, and ${}^{44}\text{Ca}$ isotopes (relative abundances 96.94%, 0.65%, 0.13%, and 2.09%, respectively) are visible at higher frequencies. Only the ${}^{43}\text{Ca}$ isotope has nonzero nuclear spin that gives rise to hyperfine structure. However, we do not detect structure at this low signal level.

[¶]The 1P_1 excited state has contributions from $4s7p$, $4s6p$ and $3d4p$ electronic configurations that are strongly mixed. This makes conventional labelling of the configuration of this level impossible and it is therefore written as $4snp$ [307].

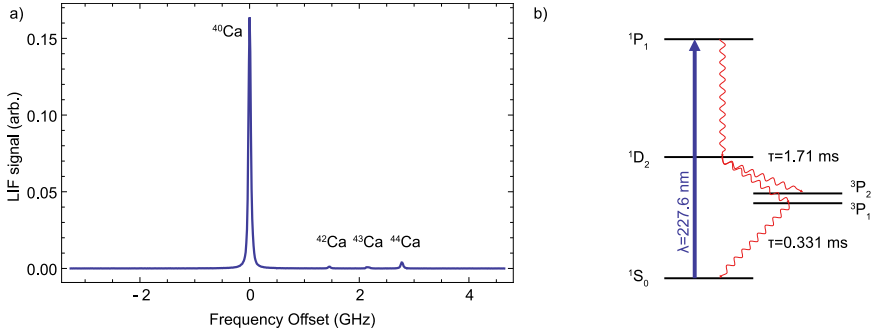


Figure 5.11: (a): LIF spectrum of the $(3p^6 4snp)^1P_1 \leftarrow (3p^6 4s^2)^1S_0$ line of Ca. The observed isotope peaks are labelled. (b): Scheme of the relevant energy levels and transitions.

For our purposes, we concentrate on the most abundant isotope in the following.

In figure 5.11b, the relevant energy levels for our study of the Ca atomic beam are shown. Exciting the atoms to the 1P_1 state pumps the population to the metastable $(3p^6 3d4s)^1D_2$ state. From the Einstein A coefficients reported from the NIST atomic spectra database [304], the average number of photons scattered on the $(3p^6 4snp)^1P_1 \leftarrow (3p^6 4s^2)^1S_0$ transition is calculated to be 1.7. In figure 5.12, the fluorescence signal in LIF-2 is plotted against peak laser intensity, demonstrating saturation of the fluorescence. Decay from the metastable 1D_2 state to the $(4s4p)^3P_{1,2}$ states is negligible during an interaction with a single laser beam, but is observable in a pump-probe measurement, where the flight time between the detectors is comparable to the decay time of 1.71 ms [308]. The 3P_1 state is populated with a probability of 83% and the 3P_2 state with a probability of 17%. The 3P_1 state decays to the ground state with a lifetime of 0.331 ms and the 3P_2 state decays with a lifetime of 118 min, which does not play a role on the experimental timescale. We observe approximately 30% of the population in LIF-2 when high intensity pump laser light is applied at LIF-1, which is shown as inset in figure 5.12. The percentage of atoms that have not yet decayed to the ground state is higher for the faster part of the molecular beam because of the shorter flight time. Compared to the case of Al shown in figure 5.9, the metastable states where the atoms are pumped to are shorter-lived.

Beam Properties

In figure 5.13, absorption spectra of the most abundant isotope peak of the $(3p^6 4snp)^1P_1 \leftarrow (3p^6 4s^2)^1S_0$ transition are plotted, recorded directly at the cell orifice or 20 mm downstream. From a Gaussian fit, we obtain the FWHM transverse velocity widths v_t of 75 m s^{-1} and 120 m s^{-1} , respectively. Figure 5.14 shows a time of flight trace of the Ca atoms in LIF-2. We calculate an estimated number of $1.7 \pm 0.2 \times 10^8$ atoms passing through the detection region per pulse, which corresponds to an on-axis brightness of $8.2 \pm 0.8 \times 10^{12} \text{ sr}^{-1}$ per pulse. Integrating the absorption trace recorded directly outside the buffer gas cell orifice shown as

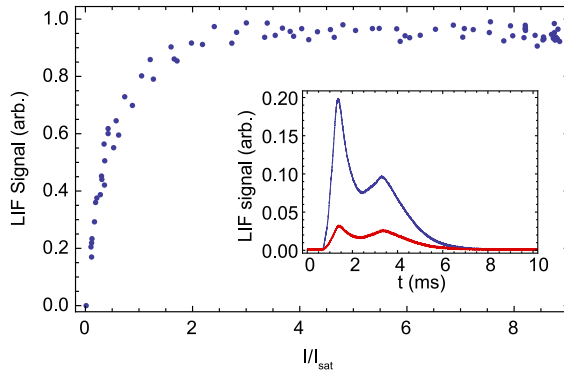


Figure 5.12: Fluorescence saturation curve of the $(3p^6 4snp)^1P_1 \leftarrow (3p^6 4s^2)^1S_0$ transition of Ca. The inset shows the LIF TOF without (blue) and with (red) a pumping laser on the same transition after the radiation shield.

an inset in figure 5.14, and using the Doppler broadened absorption cross-section, we obtain a number estimate of 3.34×10^{12} atoms per pulse. Using the transverse velocity spread calculated from the absorption spectrum, we can estimate the brightness from the absorption measurements as approximately $1.0 \times 10^{13} \text{ sr}^{-1}$ per pulse. We conclude that the brightness of the Ca atomic beam is within a factor two of the Al atomic beam brightness.

5.5.3 Ytterbium

We use the $(6s^2)^1S_0 \leftarrow (6s6p)^1P_1$ transition near 399 nm to study the Yb atomic beam. The excited state lifetime τ_{Yb} is 5.7 ns ($\Gamma/2\pi = 28$ MHz). We recorded a high-resolution LIF spectrum of this transition and used it to calibrate our wavemeter for high-resolution spectroscopy of MgF, presented in chapter 6. This spectrum, including the hyperfine structure of the odd isotopes, has been precisely characterised using a frequency comb [309]. Ablation of solid Yb metal in our source is very efficient and the pulse of the abundant isotopes directly after the cell orifice is optically dense, as presented in figure 5.15a. We therefore use the transition of the lowest abundance ^{168}Yb isotope (figure 5.15b) to estimate the number of atoms and to extract the Doppler width of the beam. The transverse velocity width FWHM at the cell orifice is 42 m s^{-1} , and 60 m s^{-1} when measured 18 mm downstream. The angular spread $\Delta\theta$ of the beam depends on the ratio of the masses of the buffer gas m_b and the sample gas m_s following $\Delta\theta \approx 2\sqrt{m_b/m_s}$ [189]. The high mass of Yb (173 u) leads to a much narrower beam compared to the other atoms studied in this chapter.

Beam Properties

As the $(6s^2)^1S_0 \leftarrow (6s6p)^1P_1$ transition is optically closed, it can therefore not be used as a standard candle transition with a defined average number of photons

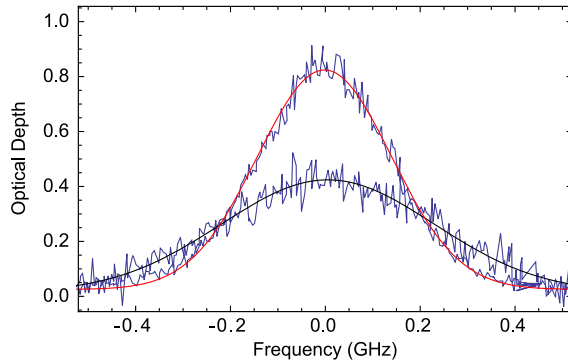


Figure 5.13: Absorption spectra of the ^{40}Ca peak of the $(3p^64snp)^1P_1 \leftarrow (3p^64s^2)^1S_0$ transition, recorded directly outside the cell exit (experimental data blue, fit red) and 20 mm downstream (experimental data blue, fit black).

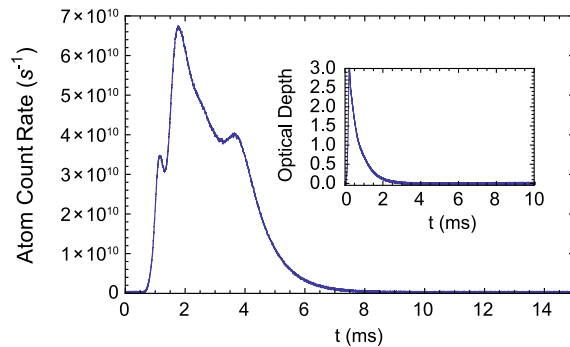


Figure 5.14: Fluorescence and absorption TOF traces of the Ca beam, using light resonant with the $(3p^64snp)^1P_1 \leftarrow (3p^64s^2)^1S_0$ transition of ^{40}Ca .

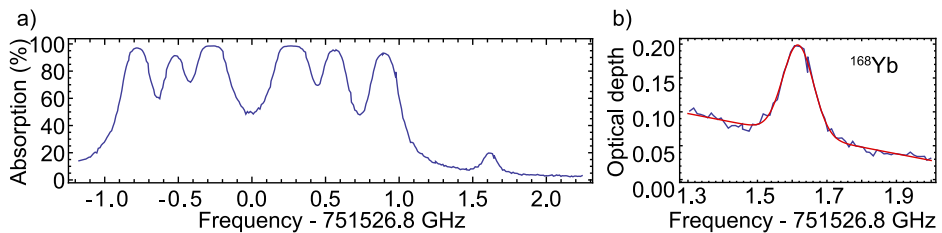


Figure 5.15: (a): Absorption spectrum of the $(6s^2)^1S_0 \leftarrow (6s6p)^1P_1$ transition, for all stable isotopes. Panel (b) shows a zoom-in on the ^{168}Yb peak.

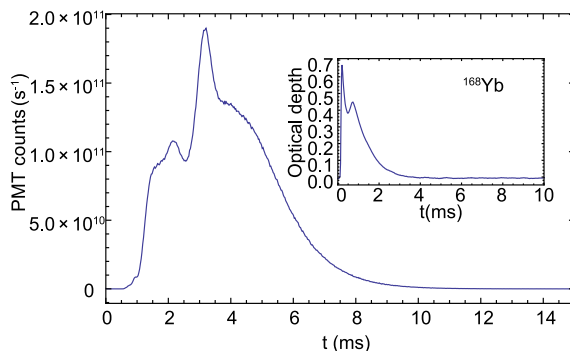


Figure 5.16: Fluorescence and absorption TOF traces of the ytterbium beam, using light resonant with the $(6s^2)^1S_0 \leftarrow (6s6p)^1P_1$ transition for the ^{174}Yb and ^{168}Yb isotopes, respectively. Because of the non-trivial conversion factor between observed photons and the number of atoms, the ordinate of the LIF plot is labelled with PMT counts.

scattered in saturation. To measure the source brightness in fluorescence, we measure the fluorescence in LIF-2 with a weak probe and model the number of photons detected using the measured laser intensity profile and the estimated velocity of the atomic beam, following the approach presented in section 4.4.1 of chapter 4 of this thesis.

Figure 5.16 shows a TOF profile obtained using the ^{174}Yb isotope, which will later be compared to the ^{174}YbF molecule. Assuming a velocity of 150 m s^{-1} , we estimate the beam brightness as $5.0 \times 10^{12} \text{ sr}^{-1}$ per pulse, in LIF-2. From the absorption measurements, we can extrapolate from the ^{168}Yb absorption signal (presented in the inset of figure 5.16) to the ^{174}Yb isotope, by taking into account the natural abundance ratio. This results in an estimated brightness of $1.7 \times 10^{13} \text{ sr}^{-1}$ per pulse in a single quantum state.

5.5.4 Influence of a Fluorine Donor Gas

The atomic beams are now well characterised. We see that the atomic beam LIF TOF profiles are similar for all three species; therefore, we assume that atoms behave similarly inside the cell. We can investigate the effect that influx of a fluorine donor gas has on the atomic beam from the buffer gas source. This gives an insight into how efficiently molecules are produced. Figure 5.17 shows the fluorescence TOF profiles of the atomic beams before and directly after introducing a flow of 0.002 SCCM NF_3 to the cell. For the Al atoms, there is an evident loss in signal, especially for the atoms with late arrival times in the detector. We typically observe a reduction of around 80% in the total number of atoms reaching the detector. For Ca and Yb, the effect of the seed gas is much less pronounced. We observe a 20% and 10% reduction in the atomic signal, respectively. These observations are reproducible over several days. We obtain qualitatively similar results when using SF_6 as the reactant gas.

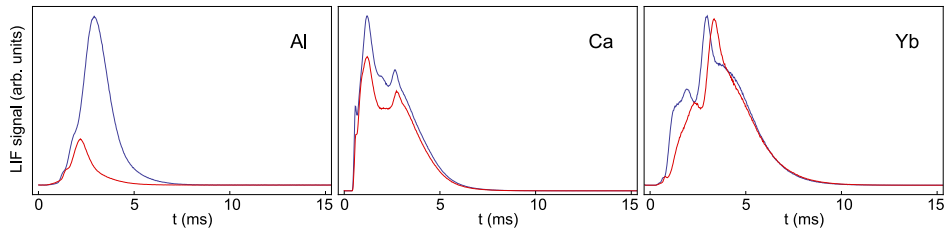


Figure 5.17: LIF signal traces of the Al, Ca and Yb atom beams without (blue) and with (red) NF_3 flow into the buffer gas cell, demonstrating the strong effect of a fluorine donor gas on the number of aluminium atoms in the beam.

5.6 Results: Molecular Beams

In this section, we determine the brightness of molecular beams of AlF , CaF , MgF and YbF and discuss the influence of experimental parameters on the molecular beam.

5.6.1 Standard Candle Transitions

To study the molecular buffer gas beams, we use rotationally open transitions as standard candles in saturated fluorescence. We focus on measuring the population in the rovibrational ground state which is predominantly populated in the buffer gas beam.

For AlF , we use the $A^1\Pi, v = 0 \leftarrow X^1\Sigma^+, v' = 0$ R(0) line, while for the other monofluorides CaF , MgF and YbF , we drive the $A^2\Pi_{1/2}, v = 0 \leftarrow X^2\Sigma^+ Q_1(0)$ line. In the absence of vibrational branching, each excitation scheme results in an average number of three scattered photons per molecule before they decay to the higher lying $N = 2$ states [254, 310].

5.6.2 Comparison of Molecular Beams

The left side of figure 5.18 shows the absorption spectra recorded directly after the buffer gas cell orifice for all four molecular species. The peak absorption of the AlF beam, presented in figure 5.18a, is an order of magnitude higher than for the other monofluoride species. Because of the high AlF molecule density, we can easily observe absorption 20 mm downstream, which is shown magnified in figure 5.18a. We observe the same broadening of the transverse velocity spread as seen for the atomic beams. As for the atoms, we extract the transverse velocity widths by fitting the absorption spectra to Doppler-broadened line shapes, and use these to predict the brightness of each molecular beam.

The right panels in figure 5.18 show saturation curves of the probing transitions. The insets show the results of pump-probe measurements for AlF , CaF , and MgF . For AlF , the large transition linewidth and small hyperfine structure in the $N = 0$ ground state permits efficient saturation, and we observe a pumping efficiency of 97%. For CaF , MgF and YbF , the ground state hyperfine structure

necessitates significant power broadening of the transition in order to fully saturate. In the case of YbF, the background due to rotational lines of other molecular isotopologues leads to an increase in the fluorescence above $I/I_{sat} = 100$ and we assume our conversion of fluorescence signal to molecule number is uncertain to within a factor 2.

Figure 5.19 shows a comparison of the maximum fluorescence signals obtained — under identical experimental conditions — for all four molecules. In the fluorescence traces, the PMT current is converted into a molecule count rate at the detector, using the calculated detection efficiencies. The MgF, CaF and YbF signals are magnified by a factor 5. From these signals and the absorption measurements shown in figure 5.21, we calculated the respective brightness in absorption and fluorescence.

In table 5.2, we summarise our estimates of the brightness of each atomic and molecular beam source. For the molecules, the given values correspond to the number of molecules in the rotational state probed by the detection transition. In both absorption and fluorescence, AlF is the brightest molecular species, while the atomic beam brightnesses are similar, within a factor two.

For AlF, we also recorded the molecular beam brightness by saturated fluorescence in rotational states up to $J = 3$. The resulting rotational state distribution is presented in figure 5.20. The relative populations do not follow a Boltzmann distribution well, pointing out that the molecules have not fully thermalised with the buffer gas. We estimate that 50% of the molecules populate the ground rotational level, and that the combined brightness when considering all rotational levels is consistent with that measured for atomic Al, suggesting that approximately all reacting Al atoms react to form AlF and no side products are formed in appreciable quantities.

The order of magnitude difference in molecule yield between AlF and the other monofluorides can be explained by the electronic structures of the atoms and molecules. Calcium and magnesium are group II metals with a fully occupied s orbital, ytterbium is a lanthanoid with fully occupied f and s orbitals, but aluminium is a group III metal with an unpaired p electron, making it a reactive radical. The gas-phase aluminium atoms react very strongly and efficiently with the fluorine donor gas, while for the other metal species, only a small percentage of the atoms reacts, as demonstrated in figure 5.17. While all studied monofluorides are stable molecules in the gas phase, only AlF possesses no unpaired electrons, making it much less reactive than the radicals CaF, MgF and YbF. The latter three are prone to the formation of difluorides. Theoretical calculations for CaF [311] predict that a considerable amount of CaF₂, comparable to or more than the amount of CaF, is formed in the reaction of ablated calcium and a fluorine donor gas, while the difluoride production is suppressed for Al.

5.6.3 Collision Cross Section of AlF and Helium

From the absorption trace (see figure 5.21), we can calculate the time constant of the signal decay τ that is related to the diffusion time τ_d and the pump-out time τ_p via $\tau^{-1} = \tau_d^{-1} + \tau_p^{-1}$ [283]. τ_p can be calculated as $\tau_p = V/C$ from the cell volume

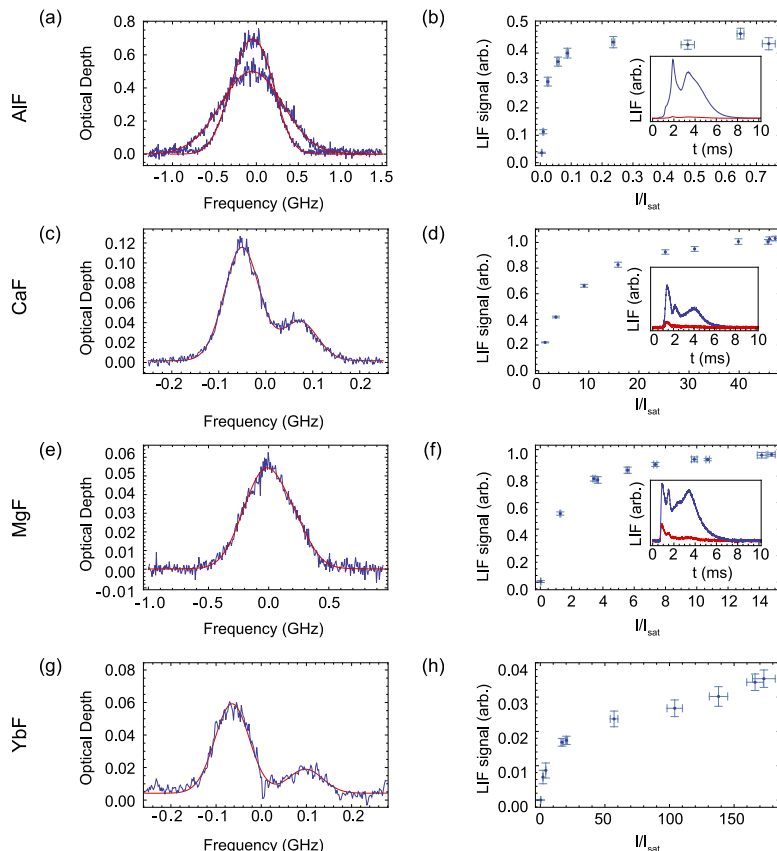


Figure 5.18: Absorption spectra recorded directly outside the cell orifice (in (a) also 20 mm downstream) of the molecular species (left column, (a), (c), (e), (g)) and saturation curves on the open standard candle transitions (right column). For AlF, CaF and MgF, the insets show the fluorescence signal without (blue) and with (red) pumping on the standard candle transitions in the LIF-1 zone, demonstrating that the molecules are indeed pumped away from the addressed transition. In the case of YbF, rotational lines from other isotopologues prevent saturation. The side peak at higher frequency is another hyperfine line that is not responsible for this.

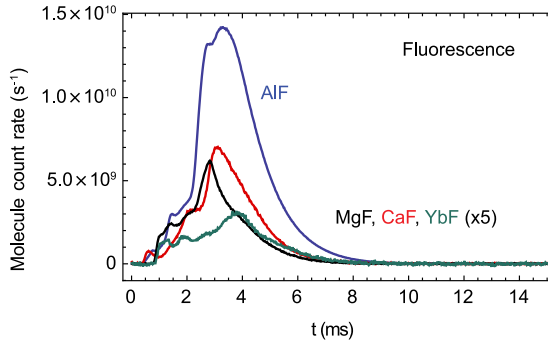


Figure 5.19: Comparison of the molecule count rates for all species, obtained from fluorescence measurements, as a function of arrival time in the detector. The signal for MgF, CaF and YbF is amplified by a factor five. Since all molecules scatter 3 photons on average, the LIF signals give a direct measure of the number of molecules.

Table 5.2: Brightness of the atomic and molecular beams, as determined from fluorescence and absorption. The combined uncertainties of the detection efficiencies lead to error bars for the LIF brightnesses of around 30%. In the case of Yb and YbF, the given values are expected to be accurate within a factor 2 because we cannot use open transitions saturated by optical pumping.

Species	Brightness at LIF (sr^{-1} per pulse)	Brightness in absorption (sr^{-1} per pulse)
Al	3.0×10^{12}	4.1×10^{12}
Ca	8.2×10^{12}	1×10^{13}
^{174}Yb	5.0×10^{12}	1.7×10^{13}
AlF	1.6×10^{12}	1.8×10^{12}
CaF	1.4×10^{11}	1.1×10^{11}
MgF	1.1×10^{11}	0.7×10^{11}
^{174}YbF	0.7×10^{11}	2.1×10^{11}

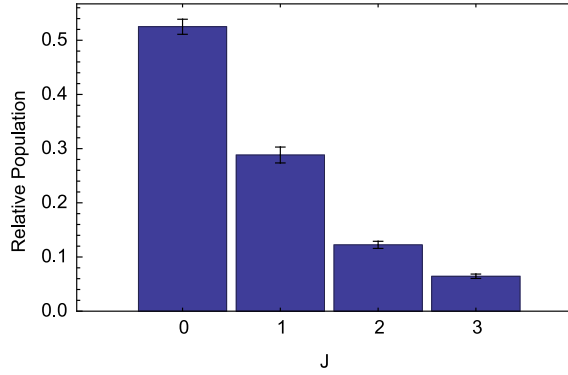


Figure 5.20: Distribution of the AlF population over the four lowest rotational levels in the vibrational ground state of the $X^1\Sigma^+$ state.

V and the aperture conductance $C = A_{\text{aperture}}\bar{v}_{\text{He}}/4$, where A_{aperture} is the cross section of the cell aperture and $\bar{v}_{\text{He}} = \sqrt{8k_B T/\pi m_{\text{He}}}$ is the mean thermal velocity of the helium buffer gas. The calculated pump-out time is $\tau_p = 7.94$ ms.

From an exponential fit, we determine $\tau = 0.81$ ms and thus calculate $\tau_d = 0.91$ ms. This means that before the molecule pulse produced in the buffer gas cell is pumped out, molecules will have diffused to the cell walls. The flux of molecules out of the cell is low but the beam is mostly effusive. The value for τ_d can now be used to calculate the thermally averaged elastic collision cross section of helium with AlF, $\sigma_{\text{He-AlF}}$, according to [189]

$$\sigma_{\text{He-AlF}} = \frac{9\pi\bar{v}_{\text{He}}\tau_d}{16A_{\text{cell}}n_{\text{He}}}, \quad (5.10)$$

where A_{cell} is the cross sectional area of the cell and n_{He} is the number density of helium in the cell, calculated by [189]

$$n_{\text{He}} = \frac{4f_{\text{He}}}{A_{\text{aperture}}\bar{v}_{\text{He}}}, \quad (5.11)$$

where f_{He} is the atom flow rate, defined by our mass flow controller. We obtain the collision cross section $\sigma_{\text{He-AlF}} = 108 \pm 5 \text{ \AA}^2$, which is in reasonable agreement with the value of 70.13 \AA^2 calculated by Karra *et al.* [301] for 20 K, using an *ab initio* potential energy surface. They also show that as the temperature decreases, the thermally averaged elastic collision cross section increases. A larger mismatch between theoretical and experimental values for these cross sections was reported for the He-YbF system [275].

5.6.4 Influence of the Ablation Laser Fluence

The process of ablation and its description involve the energy deposition and temperature evolution in the target, the mass removal mechanism and the expansion

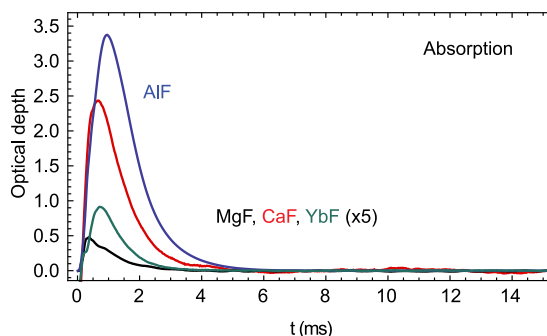


Figure 5.21: Comparison of the optical depth of the molecular beams, recorded at the buffer gas cell orifice. In both cases, the signal for MgF, CaF and YbF is amplified by a factor five. The optical depth depends on the width of the transitions and the wavelengths, it is therefore not a direct measure of the number of molecules.

of the vaporised metal [293]. The parameters that play a role in these processes are the melting and boiling point, the critical temperature and density as well as the latent heats of melting and vaporisation. The energy deposition in the metal also depends on the temperature-dependent reflectivity [292]. At low laser fluence (and low metal surface temperature), the material evaporates slowly. At higher laser fluence, the material starts to boil. At the nanosecond timescale that is of interest in our setup, the diffusion of gas bubbles necessary for boiling is kinetically hindered, therefore the metal undergoes so-called phase explosion [289, 290]. When the surface layer overheats, vapour and droplets are explosively released. Since aluminium was often used as model material for experimental and theoretical studies on ablation, recent results and data are available. The publication of Porneala and Willis [291] presents data and instructive images of an Al surface that is ablated by the fundamental of a Nd:YAG laser at 1064 nm at room temperature in air. The authors show that the onset of phase explosion happens at an ablation laser fluence of around 5 J cm^{-2} , which reflects in a steep increase of the amount of ablated material. This value agrees well with our experiment, where the onset is less steep and shifted to slightly higher fluence (figure 5.22). These effects can be explained by the difference in material properties at cryogenic temperatures and the buffer gas dynamics, as we only measure the LIF signal outside the buffer gas cell. Above the phase explosion threshold, a further increase in the laser fluence does not cause more material to be ablated because the dense metal vapour absorbs the light and effectively shields the surface [312, 313]. The vapour is ionised into a plasma, and at very high irradiances in the GW cm^{-2} range, the high temperatures result in the plasma becoming transparent [314]. The onset of this behaviour is expected to be just outside the experimentally accessible range. The phase explosion threshold was also reported on for the system of BaH creation from a solid BaH₂ target, by Tarallo *et al.* [288].

The influence of the energy of the Nd:YAG infrared ablation laser on the

number of atoms and molecules is shown in figure 5.22. The LIF signal is shown as function of the ablation pulse energy. In all cases, the laser spot size is approximately 0.7 mm, as determined from the size of the ablation spots on the metal rod. The presented data sets were recorded on different days; because of the day-to-day fluctuations in the buffer gas cell performance, an absolute comparison of the signal heights would not yield reliable information. We observe that the threshold energy for observing Al and AlF is between 10 and 15 mJ, and the signal from both species increases up to the maximum available pulse energy of 40 mJ. For all other metals, the threshold is 5 – 10 mJ, and we observe an optimum in the ablation energy of about 25 mJ.

The differences in the phase explosion threshold energy for the metals used in our study likely arise from the difference in the latent heat of vaporisation of the atomic species, where the value for Al is roughly a factor two larger than for Ca, Mg and Yb. The reflectivity of the bulk metal surfaces at room temperature — values for cryogenic temperatures are not reported — is around 93% for Al, Ca, and Mg [315,316], but 70% for Yb [317,318]. The latter is a possible explanation for the extraordinary amount of vaporised Yb atoms. The aluminium surface is passivated with a few-nanometer thin layer of alumina (Al_2O_3) [319] that has very low reflectivity and does not absorb the IR light, therefore, more energy can be absorbed by the metal, until the alumina layer is depleted after a few laser pulses.

The observed data for the atom ablation and knowledge from literature [291, 313] suggest that we can increase the number of ablated metal atoms with higher laser energy. The formation of plasma at high fluence, however, will alter the reaction probability and products because of its high temperature and ionic character. This might result in a lower number of product molecules. The decrease in molecule signal for CaF and YbF after an initial peak already indicates this.

5.6.5 Influence of the Fluorine Donor Gas

In the following, I focus on the AlF molecule because it is our primary species of interest for laser cooling applications and the observed effects proved to be similar for all species in our experiments. We compare the use of two reactant gases in our source, NF_3 and SF_6 . While the inert gas SF_6 is commonly used in experiments with monofluorides, theory suggests that the use of the more reactive and corrosive molecule NF_3 has advantages. We find that both produce a similar number of molecules when observed downstream of the source, within the range of day-to-day fluctuations of source operation with one fluorine donor gas. The molecule gas flow rates necessary to obtain maximum signal are similar for both NF_3 and SF_6 . Operating the source on NF_3 is more reliable and results in a slower beam for a longer period of operation. SF_6 can produce a similar beam brightness with a freshly cleaned cell, but after one day of operation, the TOF profile shifts to higher velocities. We assume that this is caused by the buildup of ablation products and sulphur-containing inorganic compounds on the internal buffer gas cell wall, thus hindering thermalisation of the helium buffer gas.

In figure 5.23, we use the compact Q-branch of AlF as a convenient means to probe the rotational distribution reaching LIF-2, and thereby gain insight into the

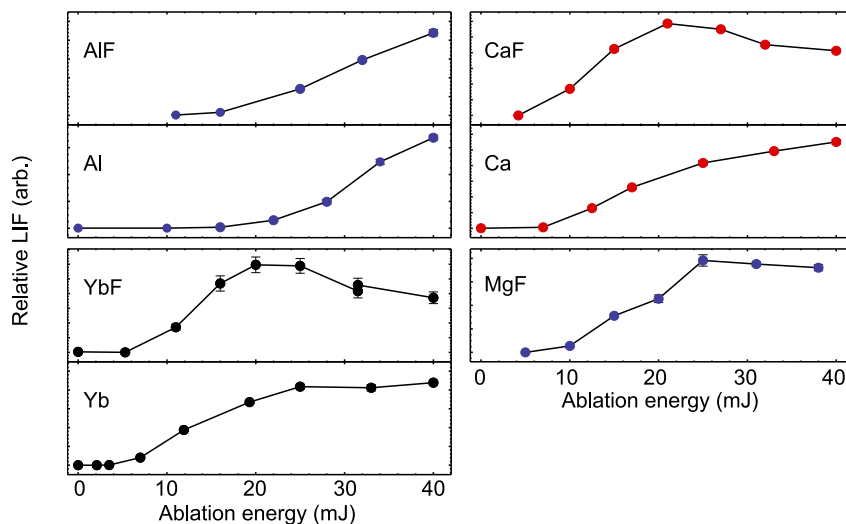


Figure 5.22: Fluorescence signals of all investigated species as a function of the ablation laser pulse energy.

thermalisation dynamics in the cell. We plot a series of Q-branch spectra, for which the gate in the molecule arrival time distribution that is integrated to obtain the spectrum was changed in 0.5 ms increments. Thus, we can understand the thermalisation in different parts of the molecular beam. The upper blue set of spectra are measurements taken with a clean cell and an SF₆ flow rate of 0.001 SCCM, whereas the red spectra are measurements with a flow rate of 0.0006 SCCM after one day of source operation without cleaning afterwards. The spectra show that at a higher flow rate and in the used cell, the molecules arrive earlier at the detector, and are distributed over many rotational states; we indeed observe molecules in $J = 13$ arriving 1 ms after the ablation pulse. The inset of the figure shows TOF fluorescence traces when saturating the R(0) line, demonstrating how the molecular pulse shifts towards higher velocities. We find that the onset of this reduced thermalisation occurs more rapidly as the flow rate increases, and that good thermalisation can only be recovered by cleaning ablation products from the buffer gas cell. The rotational spectra for different molecule arrival times also serve to show that translational and rotational energy of the AIF molecules are correlated - fast molecules are rotationally hotter than slow ones.

The sublimation point of SF₆ at standard pressure is -63.8°C , while the melting point of NF₃ at standard pressure is -208.5°C , which makes operation of the experiment with SF₆ more prone to pipe clogging and freezing. However, we observe that, using NF₃, the molecule signal persists for minutes after turning off the gas flow, while it disappears after only a couple of ablation shots for SF₆. This behaviour can therefore not be accounted for by freezing of the molecules to the Al surface, but might be explained by different adsorption behaviour. Like ammonia (NH₃) [320, 321], NF₃ dissociates into the elements on a metal surface [322]. At

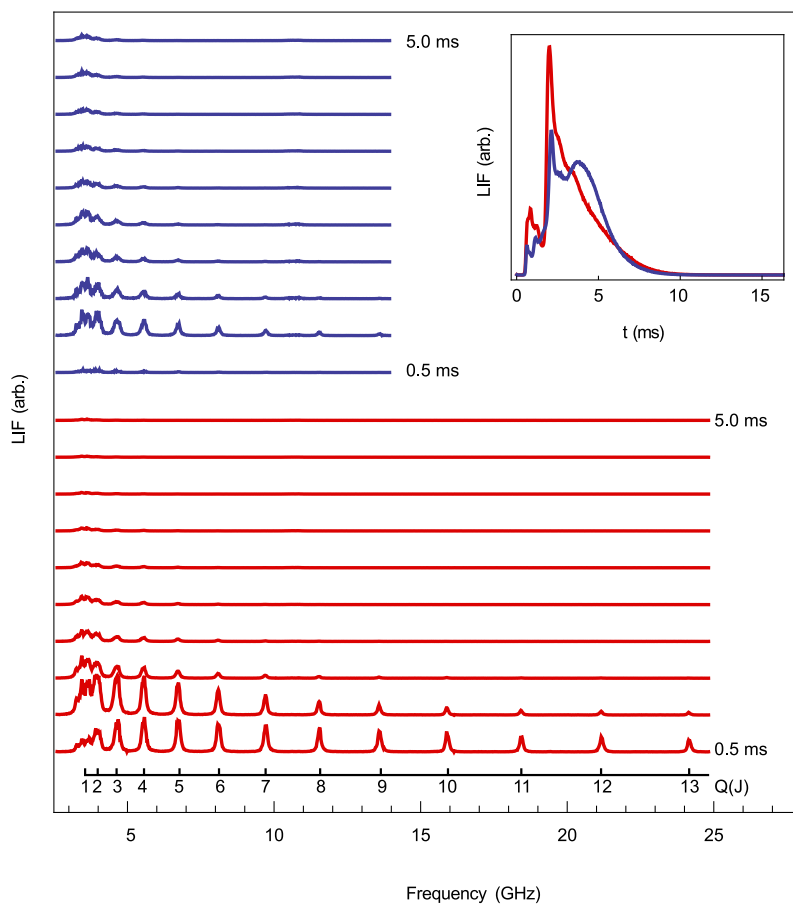


Figure 5.23: Q-branch spectra of the $A^1\Pi \leftarrow X^1\Sigma^+$ transition, recorded with a buffer gas cell that has been cleaned using Citranox acidic detergent (blue, top) or with a cell that had been operated for one day (red, bottom). The ruler on the bottom marks the different Q-lines. The inset shows the arrival time distributions in both cases, saturating the R(0) line.

cryogenic temperatures, the reaction will be very slow, but the equilibrium lies on the side of the elements. SF_6 is inert at cryogenic temperatures and does not interact with the metal surface. The precise dissociation reaction of NF_3 on a badly-defined metal surface has not been characterised. Additionally, it is not clear if this dissociation plays a role in the violent circumstances of laser ablation. A thorough investigation using surface science methods exceeds the scope of this work.

Parker *et al.* [323] reported experimentally determined activation energies of 5.9 kcal/mol (2990 K) and 9.5 kcal/mol (4780 K) for the reaction of aluminium atoms in the gas phase with NF_3 or SF_6 , respectively. From Doppler-broadened absorption spectra of Al atoms that were not cooled by a buffer gas, we could estimate a temperature of 3400 ± 1000 K. At this temperature, both reactions have a similar reaction rate, owing to the different pre-exponential factors in the Arrhenius equation [323]. More recent theoretical calculations on the reaction rates of AlF production, using an *ab initio* molecular dynamics approach and a tree-shaped reaction model based on Bayesian inference, predict that NF_3 reacts more efficiently with aluminium than SF_6 to form monofluoride molecules [311].^{||} This can be explained by the reactions' exothermicity. The energy for bond-breaking of NF_3 is 2.9 eV [324] and of SF_6 , it is 4.0 eV [325]. The binding energy of AlF is 6.9 eV, therefore the reaction involving NF_3 is more exothermic. However, the NF_3 reactant is predicted to yield more molecules at low velocities, which may be explained with the stereochemistry that allows for more efficient energy transfer between the metal atom and the fluorine atom. The publication by Liu *et al.* [311] furthermore predicts a broader velocity distribution of the reaction products from reaction with NF_3 than with SF_6 . The higher reaction rate should also lead to lower fluorine donor consumption. It is difficult to directly compare our experimental results with these theoretical predictions. The ablation process, metal vapour plume dynamics and the gas reactions at metal surfaces have not been modelled yet. The gas dynamics in the buffer gas cell has a strong influence on temperature and extraction behaviour of the molecules and can offset differences in reaction efficiency. Accurate modelling of the gas dynamics in a buffer gas cell can be performed using direct simulation Monte Carlo (DSMC) approaches that are unfortunately not yet available for our system [242, 297–299]. The combination of the high-level *ab initio* calculations for the reaction rate and an accurate gas dynamics simulation will, in future, give more in-depth insight into the inner workings of our buffer gas cell.

Sulphur hexafluoride and nitrogen trifluoride are not the only possible fluorine donors. We performed preliminary experiments using tetrafluoromethane (CF_4) as fluorine donor gas that lead to similar molecule yields as for NF_3 and SF_6 , and we therefore did not further pursue this avenue. Although the small amounts of the corrosive gas NF_3 that are used in our laboratory do not present any harm to people or equipment, CF_4 could be used as a less hazardous alternative.

Solid xenon difluoride (XeF_2), theoretically predicted to be a good candidate as fluorine donor molecule [311], did not prove as a viable option. At room temperature, the compound evaporates quickly into a hazardous gas, which makes

^{||}The same prediction is made for CaF production.

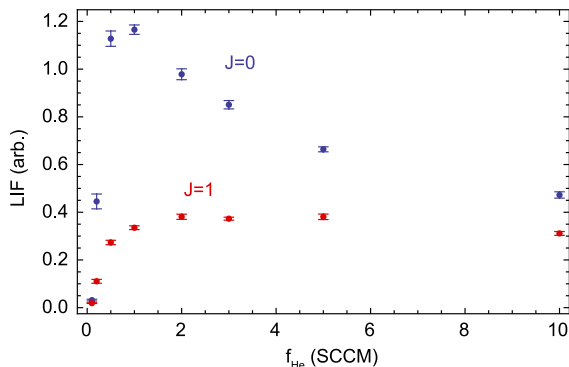


Figure 5.24: Influence of the helium buffer gas flow rate f_{He} on the fluorescence signal in LIF-2, detected on the R(0) line (blue) and the R(1) line (red).

handling dangerous. In one experiment, we put a couple of XeF_2 crystals in a CF40 chamber that was then connected to the buffer gas cell through a pipe. We could only control the flow rate using a needle valve. The observed fluorescence signal hinted towards efficient molecule production, but the large fluorine donor flow caused a very fast molecular beam. The signal quickly disappeared because XeF_2 froze out in the pipe.

5.6.6 Influence of the Helium Buffer Gas Flow Rate

We studied the behaviour of the fluorescence signal in LIF-2 as a function of the He buffer gas flow rate, as controlled by the mass flow controller. We detect the molecules using either the R(0) or the R(1) line of the $\text{A}^1\Pi \leftarrow \text{X}^1\Sigma^+$ transition. We observe that at a mass flow rate of 1 SCCM, the number of molecules in $J = 0$ is at its maximum and decreases for higher flow rates, while the number of molecules in $J = 1$ stays more or less constant at higher flow rates, as shown in figure 5.24. A flow rate of 1 SCCM is necessary for efficient extraction of the molecules from the buffer gas cell. Higher flow rates are detrimental to thermalisation in the cell, cause more collisions between molecules and buffer gas outside the cell and lead to a reduction in the number of ground-state molecules.

A similar experiment where we varied the mass flow rate of the fluorine donor gas suffered from irreproducible results over several days of measurements. From our current data, no positive influence of high flow rates on the resulting molecular beam can be confirmed.

At our standard conditions of 1 SCCM helium flow, we measured an extraction efficiency of 10-15% by comparison of absorption measurements inside the buffer gas cell and just outside the orifice.

5.6.7 Velocity Distribution of the Molecular Beam

Using the method described in ref. [88], we determined the velocity distributions of the Al and AlF beams in LIF-2. They are shown in figure 5.25, where the velocity

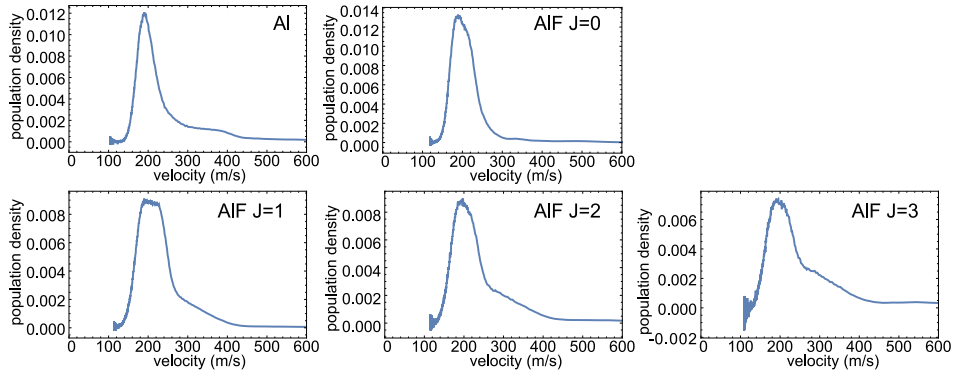


Figure 5.25: Velocity distributions of the atomic and molecular beam of Al and AIF. For AIF, the distribution was recorded and analysed for the four lowest rotational states.

distributions are shown up to $J = 3$. Fast molecules are formed predominantly in the higher rotational states and in $J = 0$, the relative amount of fast molecules is even lower than the amount of fast atoms. The velocity distributions' main peaks are broadened to higher velocity for the molecule compared to the atom, but the peak velocity of the distribution is always around 200 m s^{-1} .

In our fluorescence and absorption TOF profiles of both atomic and molecular beams, we often observe several distinct parts of the velocity distribution. For the absorption signal, these are not always clearly visible, but in the fluorescence signal, after the different parts of the velocity distribution had time to evolve, these peaks are obvious. We explain the different velocity regimes by different thermalisation efficiencies of parts of the ablation plume. Atoms that are ejected at an angle with a direct sight line to the cell orifice undergo significantly fewer collisions with the buffer gas than atoms ejected in the opposite direction. We observe that the peak structure of the fluorescence signal strongly depends on the alignment of the ablation laser on the metal rod, supporting this hypothesis.

5.6.8 Studying the Phase Space Distribution Using a Stark Decelerator

To gain additional insight into the molecular buffer gas source, we replaced the LIF detection zones with a Stark decelerator to map out the longitudinal phase space distribution (z, v_z) for AIF [37]. The decelerator consists of 133 electrode pairs spaced at 5.5 mm along the z -axis, whose orientation alternates between vertical and horizontal. We operate the decelerator in the “S=1” guiding mode, where the electrode configuration is switched synchronously with a molecule travelling at velocity v_z , which reaches the position of the decelerator z_0 at a variable in-coupling time t_i . In this way, molecules in a small region of phase space $(z_0 \pm \delta_z, v_z \pm \delta_v)$ at time t_i are guided through the machine and arrive at a defined time

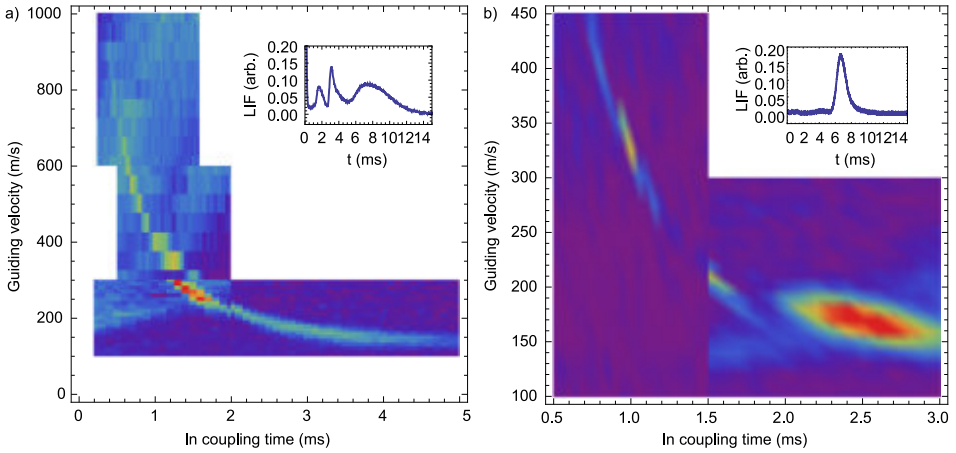


Figure 5.26: Phase space distribution of the AlF molecular beam. (a): Measured using a cell that has been used for several thousand ablation shots, with a broad and fast velocity distribution, shown as inset. (b): Measured in a freshly cleaned cell, with a narrow and slow velocity distribution. Note that the shown windows in phase space have different sizes.

in the LIF detection zone, located at a short distance from the final electrode pair. The acceptance region (δ_z, δ_y) is determined by the longitudinal electrode spacing. To map the phase space distribution $\rho(v_z, z, t)$, we scan v_z and t_i , and make use of the transformations $z(t) = z_0 - v_z(t_i - t)$ to compute ρ at an arbitrary time t .

Figure 5.26 shows two measurements of $\rho(z, v_z, t)$ for aluminium monofluoride molecules in the $J=1$ state, together with the LIF TOF recorded at the entrance of the Stark decelerator. In figure 5.26a, we used a cell in which several thousands of ablation shots were fired, but whose ablation products were recently cleaned. The second phase space measurement (5.26b) was performed after the cell had been cleaned for 15 minutes in an ultrasonic bath with an acidic detergent (Citranox) that removed the oxide layer from the copper surface. The molecules from the clean cell are concentrated in a small, defined region of phase space at low velocities, while the phase space distribution of the molecules from the used cell is very broad, has more than one peak and follows a $v_{\text{guiding}} \propto 1/t_{\text{coupling}}$ curve.

5.6.9 Further Observations

Over the course of our study on the formation of monofluorides in a cryogenic buffer gas cell, we made further observations that are useful for future experimental endeavours, but that have not been studied as thoroughly as the molecule formation.

Cell Length

Preliminary experiments with longer buffer gas cells showed that the rotational thermalisation of the AlF molecules is better, while at the same time, the signal level decreases. Since a systematic study of cell lengths involves frequently breaking vacuum, this had low priority. The final setup that was used for all data presented here was chosen because of good thermalisation and the opportunity to attach two windows to monitor the signal inside the cell.

Slowing Cell

We investigated the use of an extension (“slowing”) cell like the one used by the Harvard group, where a second stage of the buffer gas cell, with a grid at the exit, provides additional cooling [273]. We attached a 10 mm extension to the buffer gas cell, after the cell orifice, with a bore of 10 mm. To the end of the extension, we fixed a copper mesh with 60% transmission. Under standard operating conditions, this extension reduced the peak velocity of the molecular beam by 50 m s^{-1} , with the integrated absorption going down by approximately 30%. This suggests that the only signal loss is due to blocking by the grid. The slowing cell is a very useful approach to produce a slow molecular beam.

Excited State Chemistry

The Hutzler group at Caltech observed that excitation of the metal atoms to higher electronic states enhances the yield from the buffer gas source to produce YbOH from the reaction of solid ytterbium and $\text{Yb}(\text{OH})_3$ by one order of magnitude [326]. We tested if this approach is also applicable to AlF. We sent about 100 mW of UV light resonant with the $(3s^25d)^2D_{3/2} \leftarrow (3s^23p)^2P_{1/2}$ transition of Al longitudinally through the buffer gas cell. We could not observe any enhancement, on neither of the hyperfine transitions. For ytterbium, laser excitation promotes the singlet ground state to a more reactive triplet state. Ground-state aluminium, however, already is in a reactive doublet state, and excitation to another doublet state does not influence reactivity. Furthermore, for hot aluminium atoms, the energy input from the resonant photon is not necessary to overcome the activation energy. It is also important to note that the conditions and mechanisms of the AlF and YbOH formation reactions are different.

Mixed Powder Target

We investigated laser ablation of a mixed target of compacted aluminium and AlF_3 powders. Preliminary experiments showed similar yield and TOF profiles as for conventionally produced AlF molecules, but less stability over time. Tarallo *et al.* [288] have pointed out that the lower density of such a powder target can have disadvantages.

5.7 Conclusion and Outlook

In this chapter, I have presented our experiments towards a better understanding of reactions between laser-ablated metal atoms and a fluorine donor gas (SF_6 or NF_3) to form the metal monofluorides AlF , CaF , MgF and YbF in a buffer gas cell. These monofluorides are of interest for laser cooling and trapping experiments. Using well-characterised optical transitions in absorption and fluorescence, we precisely determine the number of molecules in molecular beams and compare it to the respective atomic beams. We observe that the majority of aluminium atoms ablated in the buffer gas cell is depleted by the reaction, while for CaF and YbF , only a small percentage of the metal signal gets depleted. Under identical experimental conditions, a factor 10 more AlF molecules are formed than CaF , MgF or YbF . The difference in reactivity is explained by the radical character of aluminium and the stability of the AlF molecule, while the other molecules are radicals that are formed from less reactive atoms. We compare our findings to recent theoretical results.

We investigate the influence of several experimental parameters on the molecular beam properties, namely the fluorine donor gas, ablation laser fluence and the buffer gas flow. Finally, we show that the build-up of ablation products on the buffer gas cell walls influences translational and rotational thermalisation.

Continuous loading of a magneto-optical trap from an oven source will increase the achievable densities considerably. In our laboratory, we started to use an electric furnace that was previously used for molecular beam epitaxy. By heating a mixed powder of aluminium and AlF_3 to a temperature between 500 and 620 °C — below the melting point of aluminium — we obtain a continuous and bright source of hot AlF molecules. From Q-branch spectra of the $\text{A}^1\Pi \leftarrow \text{X}^1\Sigma^+$ transition, we estimate a vibrational temperature of 1200 K and a rotational temperature of 650 K. In the lowest three vibrational levels, rotational states up to more than $J = 70$ can be detected. To buffer-gas cool these hot molecules, the oven must be attached to the buffer gas cell in a way that optimises molecular flow into the cell while at the same time keeping thermal contact to a minimum. This is a significant technical challenge that is worth being tackled.

Chapter 6

Hyperfine Resolved Optical Spectroscopy of the $A^2\Pi \leftarrow X^2\Sigma^+$ Transition in MgF

6.1 Introduction

In this chapter, I describe our spectroscopic study of magnesium monofluoride. This study was initially a part of the source characterisation study, but proved to be relevant in a more general sense. I will first explain the motivation behind a more thorough investigation of MgF. Then, after presenting the appropriate effective Hamiltonian, I will describe the rotational, fine- and hyperfine structure of the $A^2\Pi \leftarrow X^2\Sigma^+$ transition and how we calculated the radiative lifetime of the $A^2\Pi_{1/2}$ state from natural widths of hyperfine lines. We studied how the transition isotope shifts scale for different rotational states. Finally, we obtained dipole moments and an estimate on rotational losses caused by parity mixing by recording hyperfine spectra in an external electric field.

6.2 Motivation

The group II (alkaline earth) monofluorides CaF, SrF and BaF have been successfully laser-cooled in recent years [68, 70, 225], and magnesium monofluoride (MgF) was presented as a further promising candidate [73, 328, 329]. Compared to the previously studied group II monofluorides, it has a lower mass and a stronger

This chapter is based on reference [327] – M. Doppelbauer, *et al.*, “Hyperfine-resolved optical spectroscopy of the $A^2\Pi \leftarrow X^2\Sigma^+$ transition in MgF.” In *The Journal of Chemical Physics* **156**(13), (2022), doi:10.1063/5.0081902.

UV optical cycling transition, allowing to exert a larger radiation force. Diagonal Franck-Condon-factors and the narrow hyperfine structure make laser cooling technically feasible; only one repump laser and no sideband modulation is needed to scatter more than 10^4 photons per molecule [330]. First results on the exertion of radiative force on MgF molecules were published in 2022 [233].

The ground state of MgF is a $X^2\Sigma^+$ state and the electronic state used in the main cooling transition is a $A^2\Pi$ state. Unlike AlF, there is no intermediate metastable state in the cooling cycle.

Most available spectroscopic information dates back many decades ago: several groups recorded rotationally resolved absorption [331–335] and emission [335] spectra. Barber *et al.* studied the vibration-rotation emission in the electronic ground state [336]. The $X^2\Sigma^+$ electronic ground state hyperfine and rotational constants were precisely determined in the first four vibrational states from millimetre-wave spectra [337, 338].

In earlier literature, there was a debate on whether the $A^2\Pi$ state was inverted.* The discussion was resolved by S. Xu *et al.* [282], using optical absorption spectra of the $A^2\Pi \leftarrow X^2\Sigma^+$ transition; the $A^2\Pi$ state is a normal state. The absolute frequency values in their study, however, are systematically offset by -4.1 GHz compared to our calibrated measurements. In a more recent publication by the same group that studies the ^{25}MgF and ^{26}MgF isotopologues, we observe a systematic offset of $+2.3$ GHz. The research group only reports on the hyperfine structure of the $A^2\Pi_{1/2}, J' = 1/2, + \leftarrow X^2\Sigma^+, N'' = 1, -$ transition where the excited state hyperfine structure cannot be resolved. Therefore, they use an inappropriate Hamiltonian for their fitting of the spectra.

Theoretical studies on MgF include early works of Walker and Richards on spin-orbit coupling and Λ -doubling, [334, 339] studies on laser cooling by Kang *et al.*, [328] and an investigation of the hyperfine spectra and vibrational branching of the $A^2\Pi \leftarrow X^2\Sigma^+$ transition by L. Xu *et al.* [73]. Pelegrini *et al.* [340] calculated transition probabilities and radiative lifetimes for the $A^2\Pi \leftarrow X^2\Sigma^+$ transition and electric dipole moments for the $X^2\Sigma^+$ and $A^2\Pi$ states.

Here, I present hyperfine-resolved UV laser-induced fluorescence (LIF) spectra of MgF produced in a cryogenic buffer gas molecular beam. The large frequency calibration error present in the previous study by Xu *et al.* [282] is corrected by calibrating our wavemeter with known transition frequencies in Yb. The eigenvalues of an appropriate Hamiltonian are fitted to the measured hyperfine energy levels to derive precise spectroscopic constants for the $A^2\Pi$ state. We record and analyse transition isotope shifts between the two bosonic isotopologues and compare to predictions from mass scaling arguments. The spectral width of isolated lines is measured with high accuracy to determine the radiative lifetime of the $A^2\Pi$ state. The electric dipole moments of the ground and excited states are deduced from the Stark shifting of individual rotational lines in electric fields of up to 10.6 kV cm^{-1} . We then determine how opposite parity levels in the excited

*In a normal $^2\Pi$ state, the $^2\Pi_{1/2}$ state is lower in energy than the $^2\Pi_{3/2}$ state; it is the other way around for an inverted state. The spin-orbit coupling constant A is positive in the first case and negative in the latter.

state mix in an external electric field. This effect can result in large losses from the optical cycling scheme, if stray electric fields are not well-controlled.

The group II metal monofluorides are interesting candidates for laser cooling because of the single, unpaired, and metal-centred electron that is polarised away from the fluorine atom. The internuclear distance and potential energy curves of the ground and first excited states are very similar. This leads to a very diagonal Franck-Condon matrix which reduces the number of vibrational repump lasers required to scatter a large number of photons. Measurements of the fine and hyperfine structure and the electric dipole moments provide information about the spin density at the fluorine nucleus and the charge distribution. This provides information to better understand the bonding structure in these molecules [341]. We compare our results to the other group II monofluoride molecules, CaF, SrF and BaF that have been studied in detail.

6.3 Hamiltonian

The energy levels of MgF can be described by an effective Hamiltonian that operates in a given vibrational state with energy E_0 :

$$\begin{aligned}
 H = & BN^2 - DN^4 + AL \cdot \mathbf{S} + \gamma \mathbf{N} \cdot \mathbf{S} \\
 & - \frac{1}{2}p(N_+S_+ + N_-S_-) + \frac{1}{2}q(N_+^2 + N_-^2) \\
 & + aL_zI_z + b_F\mathbf{S} \cdot \mathbf{I} + \frac{1}{3}c(3S_zI_z - \mathbf{S} \cdot \mathbf{I}) \\
 & - \frac{1}{2}d(S_+I_+ + S_-I_-)
 \end{aligned} \tag{6.1}$$

In the Hamiltonian, B is the rotational, D the centrifugal distortion, A the spin-orbit coupling, γ the spin-rotation, and p and q are the Λ -doubling constants. The hyperfine interaction is described by the constants a, b_F, c and d . In the $X^2\Sigma^+$ ground state, $\Lambda = 0$ and therefore $A = p = q = a = d = 0$.

Figure 6.1 shows the relevant levels and transitions in absence of hyperfine structure. For a given value of J , the level with the lowest energy is labelled \mathcal{F}_1 . We use $\Delta J_{\mathcal{F}', \mathcal{F}''}(N'')$ to label the transitions. The energies of the J -levels in the ground state can be calculated using,

$$E(N) = E_0 + BN(N+1) \begin{cases} +\gamma N/2 & \text{for } J = N + 1/2 \\ -\gamma(N+1)/2 & \text{for } J = N - 1/2, \end{cases} \tag{6.2}$$

and in the $A^2\Pi$ state using the formula,

$$\begin{aligned}
 E(J) = & E_0 - \frac{1}{2}\gamma + B \left(J(J+1) - \frac{3}{4} \right) \\
 & \mp \sqrt{\left(\frac{1}{2}(A + \gamma) - B \right)^2 + \left(B - \frac{1}{2}\gamma \right)^2 \left(J(J+1) - \frac{3}{4} \right)}.
 \end{aligned} \tag{6.3}$$

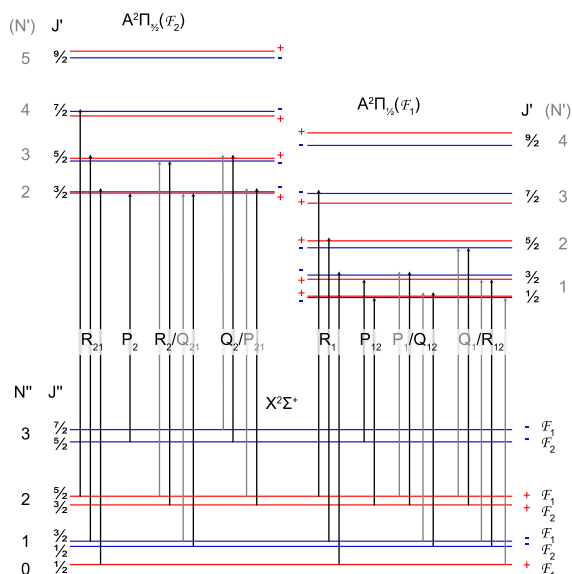


Figure 6.1: Schematic energy level diagram for a regular $2\Pi - 2\Sigma^+$ system, where p and q are both positive. Positive parity states are shown in red while negative parity states are shown blue (not to scale). N' is not well defined for low- J' . For clarity, where the spacings are small, arrowheads extending above (below) a doublet pair mark a transition to the upper (lower) doublet.

Here, the minus (plus) sign applies for the $\mathcal{F}_1(\mathcal{F}_2)$ levels respectively. In the case of $J' = 1/2$, the expression (6.3) reduces to

$$E\left(J' = \frac{1}{2}\right) = E_0 - \frac{1}{2}\gamma - \frac{1}{2}(A + \gamma) + B. \quad (6.4)$$

When comparing transition frequencies of different isotopologues, an explicit form for the energy E_0 is required. Here we assume,

$$E_0 = T_e + \omega_e(v + 1/2) - \omega_e x_e(v + 1/2)^2, \quad (6.5)$$

with T_e the potential energy minimum of an electronic state, and the remaining terms describing the vibrational energy up to second order in the vibrational quantum number v .

6.4 Experimental Setup and Absolute Frequency Calibration

The spectrometer used for this study has been described in chapter 5 and is shown in figure 5.4. The Mg rod is ablated by 20 mJ of a pulsed Nd:YAG laser (Continuum Minilite II, 1064 nm) radiation focused to a waist diameter of 0.4 mm. The hot Mg atoms react with NF_3 gas (0.001 SCCM flow rate, 100 K) to form MgF molecules. The molecules are cooled by collisions with the cryogenic He buffer gas which is flowing into the 40 mm long cell continuously at a rate of 1 SCCM. This helium flow also extracts the pulse of molecules from the cell into a molecular beam with a rotational temperature of about 4 K and a mean forward velocity of typically 160 m s^{-1} . The forward velocity increases to 160 m s^{-1} over several thousand ablation shots, but can be restored to its original value by cleaning the cell. The molecules are detected by laser-induced fluorescence (LIF) 44 cm downstream from the buffer gas cell aperture [88, 182]. The transverse velocity spread of the molecular beam is reduced to about 1 m s^{-1} by a $2 \times 2 \text{ mm}^2$ square aperture placed at the entrance to the LIF detector. Here, a continuous wave (cw) 359 nm laser beam from the second harmonic of a titanium sapphire laser intersects the molecular beam perpendicularly. We ensure that any Doppler shift arising from misalignment of the probe beam is below 10 MHz by measuring spectra with and without retroreflecting the laser. The LIF is imaged onto a photomultiplier tube (PMT, Hamamatsu R928) and the resulting photo-current is amplified to give a time-dependent fluorescence signal. We measure and stabilise the fundamental wavelength of the titanium sapphire laser using a wavemeter (HighFinesse WS8-10), which has an absolute accuracy of 20 MHz and a measurement resolution of 0.4 MHz. The wavemeter is calibrated using a temperature-stabilised HeNe laser (SIOS), whose absolute frequency is known to within 5 MHz. Additionally, we determine the $(6s6p)^1P_1 \leftarrow (6s^2)^1S_0$ transition frequency and isotope shifts of Yb by applying high-resolution laser spectroscopy to a pulsed buffer gas beam of Yb atoms. These frequencies are known with an absolute and relative uncertainty of better than 1 MHz [309]. Our experimental spectrum is presented in figure

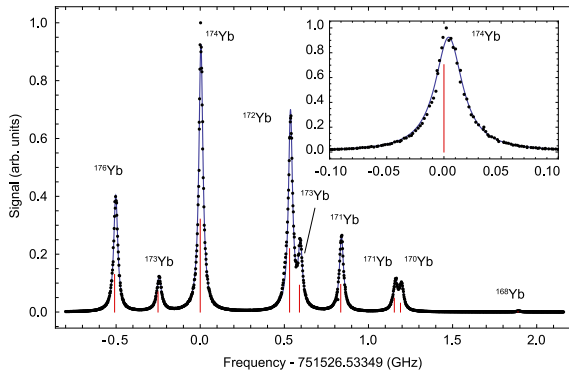


Figure 6.2: Laser induced fluorescence spectrum of the $(6s6p)^1P_1 \leftarrow (6s^2)^1S_0$ transition in Yb used to verify the accuracy of our wavemeter. The black dots present the data recorded in this study and the blue curve shows a fit using Lorentzian lineshapes. The red sticks represent the line positions obtained by Kleinert *et al.* [309] with an absolute accuracy of better than 1 MHz. The inset shows the spectral line from the ^{174}Yb isotope in more detail.

6.2. The lines under the spectrum show the transition frequencies measured by Kleinert *et al.* [309]. In our spectrum, the line-centres are determined from a fit to multiple Lorentzian lineshapes and listed in Table 6.1. We reproduce the absolute transition frequencies within 10 MHz and the relative frequencies (isotope shifts) to within 1 MHz over the range of several GHz. Since the deviation between our measured line centres and the published values is within the absolute accuracy of the wavemeter, we use the calibration from the HeNe laser without further correction. We found it was necessary to add a constant flow of dry nitrogen gas through the doubling cavity, in order to avoid absorption of the fundamental light by water vapour. This effect was particularly pronounced near the $Q_1(0)$ fundamental frequency of 834.3255 THz.

To determine the electric dipole moment of MgF in the $A^2\Pi$ and $X^2\Sigma^+$ states, we install transparent copper mesh electrodes below and above the molecular beam to apply electric fields to the molecules inside the LIF detector. The distance between the electrodes is measured to be 9.0(3) mm. The voltage on the electrodes is supplied by a high-voltage power supply (Spellman SL1200) and measured with a calibrated high-voltage probe and multimeter with a combined relative accuracy of 10^{-4} .

6.5 Isotope Shifts, Spectroscopic Constants, Hyperfine Structure, and Λ -Doubling

The vibrational, rotational, fine and hyperfine structure of the ground electronic state of MgF is well known. To improve the spectroscopic parameters for the rotational, fine and hyperfine structure of the $A^2\Pi$ state, we record low- J rota-

Table 6.1: The measured $(6s6p)^1P_1 \leftarrow (6s^2)^1S_0$ transition frequencies of Yb relative to the transition frequency of ^{174}Yb as determined by Kleinert *et al.* [309]. For the isotopes with a nuclear spin of $I \neq 0$, F' is given in brackets. The last column gives the absolute frequency differences of the isotope shifts between the two measurements with a standard deviation of 1.3 MHz.

Isotope	Isotope shift (MHz) [309]	This study (MHz)	Δf
176	-508.89±0.09	-502.11±0.13	6.78
173 ($F' = 5/2$)	-250.78±0.33	-243.79±0.43	6.99
174	0	4.16±0.05	4.16
172	531.11±0.09	536.51±0.08	5.40
173 ($F' = 7/2$)	589.75±0.24	595.14±0.24	5.39
171 ($F' = 3/2$)	835.19±0.20	839.57±0.20	4.38
171 ($F' = 1/2$)	1153.68±0.25	1160.96±0.54	7.28
170	1190.36±0.49	1196.78±0.63	6.42
168	1888.80±0.11	1892.44±0.11	3.64

tional lines of the $A^2\Pi \leftarrow X^2\Sigma^+$ transition. Figure 6.3 shows overview spectra of all recorded lines in both the $\Omega = 1/2$ and $\Omega = 3/2$ manifolds, together with their assignment. The isotope shifts between ^{26}MgF and ^{24}MgF are discussed in section 6.5.1. From section 6.5.2 onwards, we focus on the most abundant ^{24}MgF isotope, summarising the results of our measurements, and point out some important differences with the other group II monofluorides.

6.5.1 Isotope Shifts

We use a Mg metal ablation target with a natural isotopic abundance of 79%, 10% and 11% for ^{24}Mg , ^{25}Mg , and ^{26}Mg , respectively. ^{24}Mg and ^{26}Mg are bosons with a nuclear spin $I(^{24}\text{Mg}) = 0$ and $I(^{26}\text{Mg}) = 0$ whereas ^{25}Mg is a fermion with a nuclear spin $I(^{25}\text{Mg}) = 5/2$. Fluorine has one stable isotope with a nuclear spin of $I(^{19}\text{F}) = 1/2$.

Figure 6.4 shows a typical spectrum when exciting the $R_2/Q_{21}(1)$ line. In this example we scan over the three MgF isotopologues, and observe isotope shifts of -3.35 GHz (^{25}MgF) and -6.48 GHz (^{26}MgF), relative to ^{24}MgF . The inset of figure 6.4 shows the more complex hyperfine structure of ^{25}MgF . Each rotational line is split into two groups of hyperfine lines separated by about 1GHz, which are both further split by a few hundred MHz. The larger splitting arises from the Fermi contact interaction between the electron and ^{25}Mg nuclear spin in the ground electronic state [337]. We did not analyse the excited state in detail in this study.

The shift in transition frequencies between isotopologues is characteristic to a molecular species. This molecular isotope shift can be used as an additional means of identification, and to reveal small deviations from the Born-Oppenheimer approximation. Since ^{24}MgF and ^{26}MgF exhibit the same hyperfine structure, the shift in the gravity centre of a rotational line can be found straightforwardly by

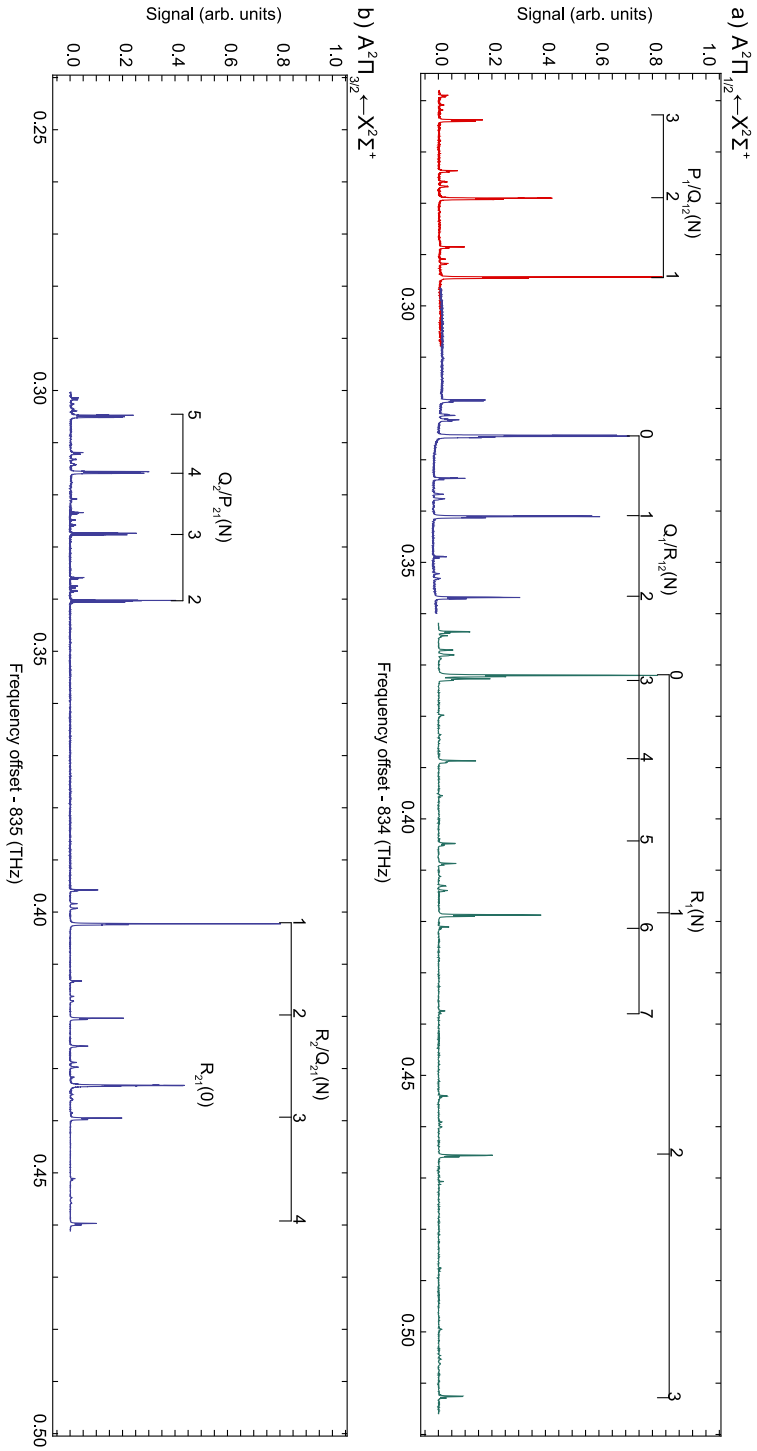


Figure 6.3: Overview spectra over several rotational lines of the $A^2\Pi_{1/2} \leftarrow X^2\Sigma^+$ (a) and $A^2\Pi_{3/2} \leftarrow X^2\Sigma^+$ (b) branches. The ^{24}MgF peaks of the observed lines are marked with their assigned label and quantum number N'' . In panel (a), data sets recorded on different days are presented in different colours. Spectra are taken in pieces over longer periods of time, therefore the relative intensities of the different rotational lines are not representative of the rotational temperature or the transition strengths.

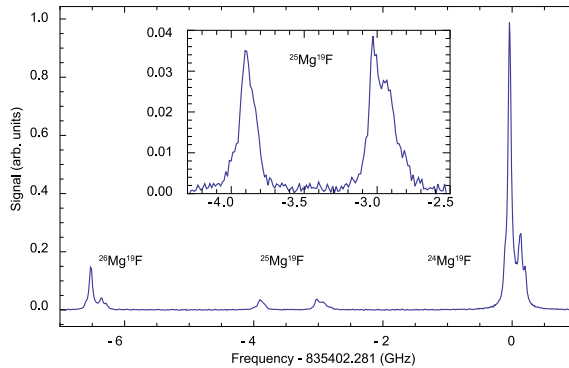


Figure 6.4: Isotope shift of the $R_2/Q_{21}(1)$ line of MgF. The ^{26}Mg and ^{24}Mg isotopes are bosons with $I = 0$, while ^{25}Mg is a fermion with $I = 5/2$ and has a more complex hyperfine structure. A zoom-in on the ^{25}MgF isotope is shown as an inset.

comparing the positions of equivalent hyperfine peaks. We define the transition isotope shift, $\delta\nu_i$, as,

$$\delta\nu_i = \nu_i(^{26}\text{MgF}) - \nu_i(^{24}\text{MgF}) \quad (6.6)$$

with $\nu_i(j)$ being the absolute frequency of the optical transition i in isotopologue j . Within the Born-Oppenheimer approximation, the isotope shift comes about through changes to the relevant reduced masses in the molecular system. For the rovibrational constants, the relevant reduced mass is that computed from the two atomic masses, m_{Mg} and m_{F} ,

$$m_{\text{mol}} = \frac{m_{\text{Mg}}m_{\text{F}}}{m_{\text{Mg}} + m_{\text{F}}} \quad (6.7)$$

We define $\rho = \sqrt{m_{\text{mol}}(^{24}\text{MgF})/m_{\text{mol}}(^{26}\text{MgF})}$, which has the value of about 0.983. To predict the isotope shifts, we use equations (6.2), (6.3) and (6.5) to calculate the energy differences, applying the following relations,

$$\begin{aligned} B^* &= \rho^2 B, \\ \omega_e^* &= \rho\omega_e, \quad \omega_e x_e^* = \rho^2 \omega_e x_e, \end{aligned} \quad (6.8)$$

where the asterisks refer to the constants for ^{26}MgF . The constants $\omega_e, \omega_e x_e$ for the ground state are taken from the work of Barber *et al.* [336] while the constants for the excited state were taken from the work of Gu *et al.*[†] The remaining values are taken from tables 6.2 and 6.3 in the subsequent sections of this chapter. From the difference in vibrational constants we expect an isotope shift of -7.15 GHz,

[†]These values were obtained from a private communication with the authors of reference [233], where we pointed out that their published constants were wrong.

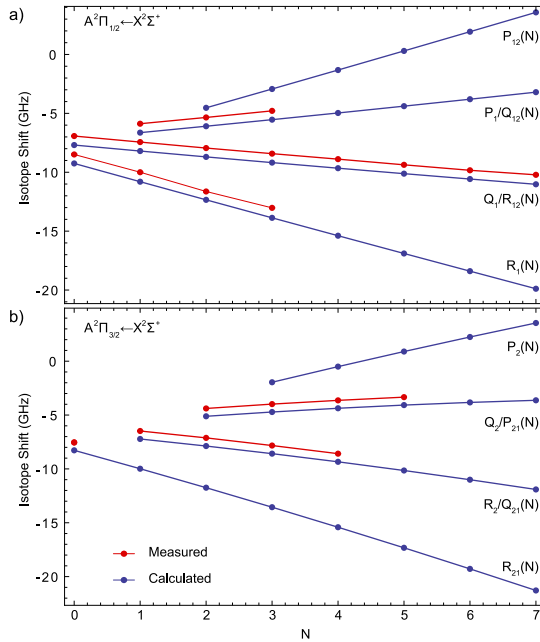


Figure 6.5: Isotope shifts of the $A^2\Pi \leftarrow X^2\Sigma^+$ transition in MgF. The blue joined points are calculated as described in the text, and the red joined points are from our dataset. (a) the $A^2\Pi_{1/2} \leftarrow X^2\Sigma^+$ branches. (b) the $A^2\Pi_{3/2} \leftarrow X^2\Sigma^+$ branches.

the contribution from the rotational energy is dependent on N'' and the rotational line in question.

In figure 6.5, we plot the calculated $\delta\nu_i$ values for the four branches of the $A^2\Pi_{1/2} \leftarrow X^2\Sigma^+$ (a) and $A^2\Pi_{3/2} \leftarrow X^2\Sigma^+$ (b) transitions. We plot the predicted values up to $N = 7$, and compare with those available from our measurements. We observe a systematic difference between the measured and calculated values, with a mean of 762 MHz and a standard deviation of 30 MHz. The rotational dependence of the isotope shift is well described by the first of the relations (6.8). An inaccuracy of about 3 cm^{-1} in any one of the vibrational constants would be required to account for the observed systematic difference, which seems unlikely. According to Hougen [342], we should also include a term $B\langle L_{\perp}^2 \rangle$ in the definition of E_0 , which accounts for the component of the electronic orbital angular momentum perpendicular to the internuclear axis. A non-zero value of $\langle L_{\perp}^2 \rangle$ would increase the discrepancy, by up to 540 MHz.

We so far have ignored any change in T_e between the isotopes as this is normally neglected by making the Born-Oppenheimer approximation.[‡] However, Watson [343] built on the work of Dunham [344], Van Vleck [345] and Ross *et al.* [346] and derived a general expression for the mass-dependent shift in the

[‡]The studious reader will note that in the published version of this work [327], we included a formula to account for this shift. The description in this thesis is considered superior.

Dunham coefficients of diatomic molecules:

$$Y_{kl} = \mu_C^{-(k+2l)/2} U_{kl} \left(1 + \frac{m_e \Delta_{kl}^a}{m_a} + \frac{m_e \Delta_{kl}^b}{m_b} + \mathcal{O}(m_e^2/m_i^2) \right), \quad (6.9)$$

where m_e is the electron mass, m_a and m_b are the masses of the atoms a and b and μ_C is the charge-modified reduced mass

$$\mu_C = \frac{m_a m_b}{m_a + m_b - C m_e}, \quad (6.10)$$

with C being the charge number of the molecule. The constants Δ_{kl}^i ($i = a, b$) and U_{kl} are isotopically invariant. This formula is known to describe rovibrational isotope shifts in CO well, for which there are data with different isotopes of C and O [346].

Normally, the term in brackets in (6.9) is very close to 1 and can be neglected, but it can be significant for the electronic energy term $Y_{00} = T_e$, because here, the prefactor U_{00} is large. With $k = l = 0$, equation (6.9) becomes

$$Y_{00} = U_{00} \left(1 + \frac{m_e \Delta_{00}^{\text{Mg}}}{m_{\text{Mg}}} + \frac{m_e \Delta_{00}^{\text{F}}}{m_{\text{F}}} + \mathcal{O}(m_e^2/m_i^2) \right), \quad (6.11)$$

where U_{00} is the electronic energy when the masses of the nuclei are infinite. If the full 762 MHz discrepancy is explained by the isotopic contribution to the electronic energy, the ratio $Y_{00}^{(26)}/Y_{00}^{(24)}$ for the two magnesium isotopes ^{26}Mg and ^{24}Mg is equal to $1 + (762 \text{ MHz}/T_e^{(24)})$. By applying equation (6.11), we find

$$\frac{Y_{00}^{(26)}}{Y_{00}^{(24)}} \approx 1 + \frac{m_e \Delta_{00}^{\text{Mg}}}{m_{\text{Mg}}^{(26)}} - \frac{m_e \Delta_{00}^{\text{Mg}}}{m_{\text{Mg}}^{(24)}} = 1 + m_e \Delta_{00}^{\text{Mg}} \left(\frac{1}{m_{\text{Mg}}^{(26)}} - \frac{1}{m_{\text{Mg}}^{(24)}} \right), \quad (6.12)$$

where we kept first-order terms only. From this, we can determine $\Delta_{00}^{\text{Mg}} = -0.52$. It is also possible that the specific mass shift contribution to T_e or the field shift of the Mg nucleus are responsible for the additional shift. These can only be derived by more sophisticated calculations, and our values provide an important benchmark in this regard.

6.5.2 Spectroscopic Constants of the $A^2\Pi$ State

To determine the spin-orbit, rotational, spin-rotation, Λ -doubling, and hyperfine constants of the $A^2\Pi$ state, we record 25 hyperfine-resolved rotational lines of the $A^2\Pi_{1/2} \leftarrow X^2\Sigma^+$ and $A^2\Pi_{3/2} \leftarrow X^2\Sigma^+$ transitions. The lines are slightly broadened by a small, uncompensated ambient magnetic field of 0.8 G in the LIF detector, and the effect of optical pumping between hyperfine and rotational states (discussed in section 6.6); they are fitted using a sum of Lorentzian lineshapes. Using a Voigt profile did not change the fit residuals significantly. In this way, we determine the centres of 56 hyperfine lines for $N'' \leq 4$, the observed frequencies of which are listed in Table E.1 in Appendix E. These line centres were used in a least-squares

Table 6.2: Spectroscopic parameters of the $X^2\Sigma^+$ state of MgF, reproduced from the work of Anderson *et al.* [337]. In the original article, the hyperfine structure parameter of the fluorine nucleus $b(\text{F}) = b_F(\text{F}) - c(\text{F})/3$ was used.

Parameter	Value (MHz)
$E_0(X^2\Sigma^+)$	0.0
B	15496.8125(29)
D	0.03238(16)
γ	50.697(49)
$b_F(\text{F})$	214.2(1.7)
$c(\text{F})$	178.5(3.0)

Table 6.3: Experimentally determined spectroscopic constants of the $A^2\Pi$ state of MgF and their standard deviation (SD); $\text{SD}\cdot\sqrt{Q}$ includes correlations between parameters [180]. The Λ -doubling parameters p and q , and the spin-orbit (A) and spin rotation (γ) constants are strongly correlated. We state their linear combinations $p + 2q$ and $A + \gamma$ that are well constrained by the fit.

Parameter	Value (MHz)	SD	$\text{SD}\sqrt{Q}$
$E_0(A^2\Pi) - \frac{1}{2}\gamma$	834855315.2	3	4
$A + \gamma$	1091346	3	3
B	15788.2	0.3	0.4
γ	-53	16	136
$p + 2q$	15	2	2
$a(\text{F})$	109	6	7
$b_F(\text{F}) + 2c/3$	-52	14	16
$d(\text{F})$	135	7	7

fit to determine spectroscopic parameters for the $A^2\Pi$ state, and we list the best fitted values in Table 6.3. In our analysis, we fixed the ground state parameters to those determined by Anderson *et al.* [337], and reproduce these in Table 6.2 for reference. The $A^2\Pi$ state is well approximated by a Hund's case (a) coupling scheme for the angular momenta. Relevant details regarding the Hamiltonian are provided in Appendix D. The Λ -splitting is determined by the linear combination $p + 2q$, and the hyperfine splittings are determined by the parameters a , $b_F + 2c/3$ and d [169].[§] To independently measure p and q , or b_F and c , requires exciting to higher J levels where the Hund's case (a) approximation breaks down. These parameter pairs are otherwise strongly correlated when fitted separately and so we state the linear combinations in Table 6.3. The same reasoning applies for the parameters A and γ .

[§]Note that b_F is related to b and c in equation 6.5 of Frosch and Foley [169] by $b_F = b + c/3$.

6.5.3 Hyperfine Structure

Figure 6.6 a and b show hyperfine-resolved spectra of the $P_1/Q_{12}(1)$ and $Q_1(0)$ lines of the $A^2\Pi_{1/2} \leftarrow X^2\Sigma^+$ transition respectively. These lines originate from different rotational levels in the $X^2\Sigma^+$ ground state and reach opposite parity levels in the same $J' = 1/2$ level of the excited state. The structure of the $P_1/Q_{12}(1)$ line is dominated by the ground state fine and hyperfine interactions, and the excited state hyperfine interaction is not resolved. However, in the negative parity Λ -doublet, the excited state splitting is 179 MHz, and we resolve both the ground and excited state hyperfine structure in our spectra of the $Q_1(0)$ line (figure 6.6 b). This is caused by a dependence of the magnetic hyperfine interaction on the sign of Λ , and therefore a difference in the linear combinations of Λ states [169]. The magnetic hyperfine constant $d(F)$ encapsulates this effect, and its influence on the hyperfine splittings is illustrated in the level scheme of figure 6.7.

The hyperfine parameters a , b_F , c and d are related to properties of the electronic wavefunction in the molecule. A first-order approximation was initially described by Frosch and Foley [169] and then subsequently simplified and corrected by Dousmanis [347].[¶] The interaction between the electron and nuclear magnetic moment can be split into two parts: one part is sensitive to the electron density at the nucleus, contained in b_F and the other is sensitive to the orbital and spin wavefunction away from the nucleus, which determines a , c and d . The coordinates of the electron relative to the interacting nucleus are expressed in the form (r_1, χ) , where r_1 is the distance from the nucleus and χ is the opening angle subtended with respect to the internuclear axis. The coordinates are illustrated in figure 6.8. According to Dousmanis,^{||}

$$\begin{aligned}
 a &= \frac{\mu_0}{2\pi} \mu_B \mu(F) \langle 1/r_1^3 \rangle, \\
 b_F &= b + c/3 = \frac{4}{3} \mu_0 \mu_B \mu(F) \psi^2(0), \\
 c &= \frac{3}{4\pi} \mu_0 \mu_B \mu(F) \left\langle \frac{3 \cos^2 \chi - 1}{r_1^3} \right\rangle, \\
 d &= \frac{3}{4\pi} \mu_0 \mu_B \mu(F) \langle \sin^2 \chi / r_1^3 \rangle.
 \end{aligned}
 \tag{6.13}$$

Here, $\mu(F) = 5.25\mu_N$ is the magnetic moment of the fluorine nucleus [348], μ_N is the nuclear magneton, and μ_B is the Bohr magneton. The angled brackets denote expectation values of the $A^2\Pi$ electronic wavefunction, and $\psi^2(0)$ represents its probability density at the fluorine nucleus. From the value of a we find a typical radius $\tilde{r} = \langle r_1^{-3} \rangle^{-1/3} = 0.88 \text{ \AA}$, roughly half the internuclear equilibrium separation of 1.75 \AA . Approximating $\langle \sin^2 \chi / r_1^3 \rangle \approx \langle \sin^2 \chi \rangle / \tilde{r}^3$ leads to a typical value $\tilde{\chi} = 65.3^\circ$. A wavefunction uniformly distributed over χ has $\tilde{\chi} = 54.5^\circ$. These observations suggest that, much like in the ground electronic state, there is appreciable electron density between the two nuclei.

[¶]In particular, we note the correction to the value of d , acknowledged by Frosch and Foley.

^{||}Here we use SI units, and our equations relate to the CGS units of Dousmanis by a factor $\mu_0/(4\pi)$.

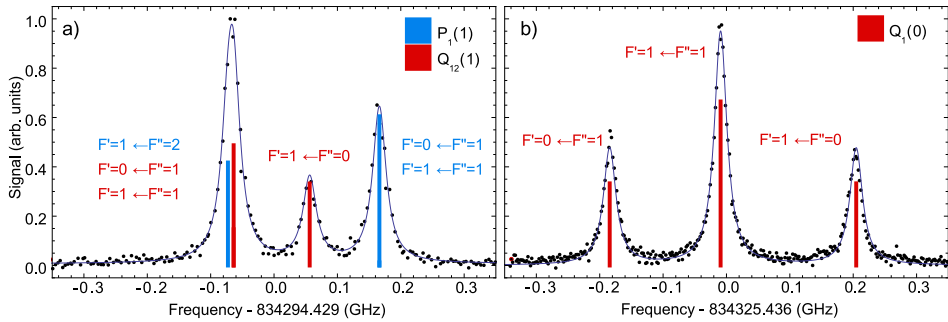


Figure 6.6: Hyperfine resolved spectra of the $P_1/Q_{12}(1)$ (a) and $Q_1(0)$ (b) lines. Experimental data is shown as black dots and the line positions simulated from the fitted spectroscopic constants are shown as colored bars. The dark blue lines are Lorentzian fits to the experimental data to determine the line-centre.

This is in stark contrast with the other group II monofluorides CaF, SrF and BaF, where there is no resolvable interaction with the fluorine spin [341, 349–352], and upper limits of a few MHz have been inferred for $d(F)$. It is only for the fermionic isotopologues of these molecules, where the metal nucleus has non-zero spin, that structure has been observed, and $d(^{87}\text{Sr})$, $d(^{135}\text{Ba})$, and $d(^{137}\text{Ba})$ could be determined [353, 354].

Finally, we note that the hyperfine interaction causes mixing between the $X^2\Sigma^+(N=3, F=2)$ and $X^2\Sigma^+(N=1, F=2)$ states, and between the $A^2\Pi(J=1/2, F=1)$ and $A^2\Pi(J=3/2, F=1)$ states. This mixing results in losses from the $P_{11}/Q_{12}(1)$ optical cycling transition. For ^{24}MgF we calculate a branching ratio of 1.6×10^{-6} for ^{24}MgF to the $N=3$ states. For ^{25}MgF these losses are estimated to be an order of magnitude larger. A more detailed analysis of this effect is given in Appendix D.

6.5.4 Λ -Doubling

In their discussion of the Λ -doubling in MgF, Walker and Richards derived values of p and q for MgF by extrapolation of the Λ -splitting observed at $J'+1/2 > 16$ [339]. Their analysis gives $p + 2q = -50.3$ MHz, which disagrees with our result in both the sign of the interaction and the magnitude. This discrepancy is likely due to the omission of the spin-rotation interaction in their analysis of the $^2\Sigma^+ \leftarrow ^2\Sigma^+$ bands of MgF, and due to insufficient resolution in the $A^2\Pi \leftarrow X^2\Sigma^+$ absorption spectra. We here provide an improved measurement and update their discussion of the origin of Λ -doubling in the group II monofluorides. In Table 6.4, we compare measured values of $p + 2q$ with the values obtained according to Van Vleck's pure precession approximation [355, 356]. The approximation is valid when the Λ -doubling is dominated by the interaction with a single $^2\Sigma$ state, whose σ molecular

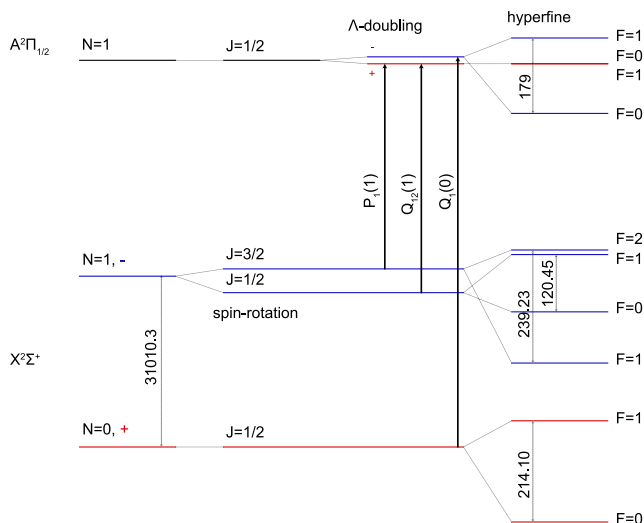


Figure 6.7: Energy level scheme of the hyperfine states involved in the $P_1/Q_{12}(1)$ (a) and $Q_1(0)$ transitions shown in figure 6.6 (a) and (b). Energy differences are given in MHz. The two hyperfine states in the positive parity doublet in $A^2\Pi_{1/2}$, $J = 1/2$ are not resolved; the calculation from spectroscopic constants determines the spacing to be 0.4 MHz.

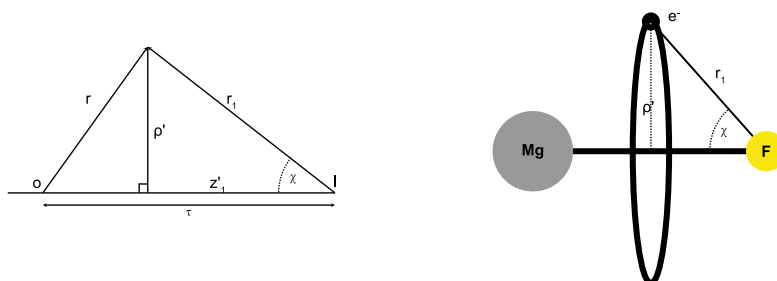


Figure 6.8: Scheme of the coordinates of the electron with respect to the nucleus, used to calculate the hyperfine structure parameters a , b_F , c and d .

Table 6.4: A comparison of the experimentally obtained Λ -doubling constants of the $A^2\Pi$ state $p + 2q$, with the value of $p_{vv} + 2q_{vv}$ as discussed in the text, for the group II monofluorides. All values are stated in MHz, and for MgF we use values obtained in this study. Sources of spectroscopic data are shown in the column headings where needed. The value labelled with the superscript a is from the work presented here. For the values labelled with the supersci, only p was reported in the publications and q was assumed to be zero.

	MgF [333]	CaF [358]	SrF [359, 360]	BaF [361]
$10^{-3}(p + 2q)$ (Exp.)	0.015 ^a	-1.32	-3.90 ^b	-7.67 ^b
$10^{-3}(p_{vv} + 2q_{vv})$	-0.25	-1.31	-4.17	-6.66

orbital is mainly derived from an atomic p orbital [357]. Under this assumption,

$$\begin{aligned}
 p = p_{vv} &= \frac{2ABl(l+1)}{E_{\Pi} - E_{\Sigma}} \quad , \\
 q = q_{vv} &= \frac{2B^2l(l+1)}{E_{\Pi} - E_{\Sigma}} \quad .
 \end{aligned}
 \tag{6.14}$$

Here, $l = 1$ is the orbital angular momentum of the unpaired electron, and $E_{\Pi} - E_{\Sigma}$ is the energy difference between the interacting states. Equations (6.14) apply for the interaction with a Σ^+ state, with the sign reversing when the interaction is with a Σ^- state. In the table we give $p_{vv} + 2q_{vv}$ values for pure precession with the nearby $B^2\Sigma^+$ states which are higher in energy, and this appears to work well for the heavier monofluorides CaF, SrF and BaF. The trend in the Λ -doubling parameters $p_{vv} + 2q_{vv}$ is primarily caused by the increasing spin-orbit interaction while moving from heavy to light nuclei. In the case of MgF, the interaction changes sign and is an order of magnitude smaller than expected from the interaction with the $B^2\Sigma^+$ state. Therefore, Λ -doubling in MgF is more complex than for the heavier group II monofluorides and may comprise interactions with many Σ -states. *Ab initio* calculations by Kang *et al.* [328] imply that the $B^2\Sigma^+$ state of MgF is of mixed character, which may explain the marked difference in Λ -doubling compared to the heavier group II monofluorides.

6.6 Radiative Lifetime of the $A^2\Pi$, $v' = 0$ Level

So far, the radiative lifetime of the $A^2\Pi$ state is known only theoretically [340]. We determine the lifetime experimentally by measuring the $Q_1(0)$ spectral line shape (figure 6.6 b) at low laser intensity. This line is convenient because the hyperfine structure in both ground and excited states is fully resolved, and the ground $N = 0$ rotational level contains the largest population of slow molecules for which the residual Doppler broadening is smallest. For these measurements, we reduced the expected Doppler broadening to 1 MHz by replacing the $2 \times 2 \text{ mm}^2$ square molecular beam aperture in the detector with a 1 mm slit. We measure spectra at several probe laser intensities, and extract the full width at half-maximum

(FWHM) for each line with a Lorentzian fitting function. Figure 6.9 plots the linewidths for the three hyperfine components of the $Q_1(0)$ line against the peak laser intensity together with linear fits (solid lines). Linear fits to the data show that each line broadens differently with increasing laser intensity. This broadening occurs at laser intensities well below the predicted two-level saturation intensity, $I_s = \pi hc\Gamma/3\lambda^3 = 62 \text{ mW cm}^{-2}$, and is the result of optical pumping between rotational and hyperfine states of the molecule, which we discuss in the following paragraph.

In general, the spectrum of an open transition will broaden when the number of photon scattering events is sufficient to optically pump the molecule to a state not addressed by the laser. This broadening can occur at an arbitrarily low laser intensity I , provided that the interaction time t_i is large enough. In the absence of hyperfine structure, molecules are pumped to $N'' = 2$ on the $Q_1(0)$ line after an average of three scattering events. With the inclusion of hyperfine structure, molecules are pumped to both $N'' = 2$ and also between hyperfine levels of $N'' = 0$, further reducing the number of scattering events. For our experiments where the typical laser interaction time is $t_i = 10 \mu\text{s}$, this effect becomes significant even when $I \sim 10^{-3}I_s$. To verify our understanding, we simulate the interaction with the laser using rate equations, the measured hyperfine splittings, and the branching ratios for each hyperfine decay channel. We assume all three polarisation components are excited with equal probability; this is a reasonable approximation given the magnetic field in the detector mixes the ground states by spin precession during the interaction time with the laser. We fit the simulated spectra with the same Lorentzian model, and find that the model predicts the relative broadening rates within the experimental uncertainties. A complete quantitative treatment of this effect requires detailed information about the laser profile and the collection optics, which is beyond the requirements of this paper. We refer the interested reader to the work of Wall *et al.* [254] as an example.

To estimate an upper bound for the true Lorentzian linewidth $\Gamma/(2\pi)$, where $\Gamma = 1/\tau_0$ and τ_0 is the radiative lifetime of the $A^2\Pi$, $v' = 0$ level, we use the spectrum taken at a peak intensity of $80 \mu\text{W cm}^{-2}$, shown in figure 6.6 b. Here the FWHM of the individual hyperfine lines are consistent within the uncertainties, indicating that the effect of optical pumping is small. We fit the data to a sum of three Voigt profiles, finding a Lorentzian FWHM of $\Gamma/(2\pi) = 22.0(5) \text{ MHz}$ and a Gaussian FWHM of $3.8(1.8) \text{ MHz}$. The ground state splitting can be estimated from our experimental spectra, and compared to the precise measurements of Anderson *et al.* to estimate an uncertainty on the linearity of the laser scan. We find agreement within $\pm 1 \text{ MHz}$, consistent with the Yb measurements presented in Section 6.4. The Gaussian contribution to the lineshape arises from the Doppler effect, residual Zeeman shifts and laser frequency instability. To estimate its systematic uncertainty, we measured the $(3s^27s)^2S_{1/2} \leftarrow (3s^23p)^2P_{1/2}$ narrow transition in a buffer gas beam of atomic aluminium. The atoms are produced in the same beam machine, with a forward velocity similar to the MgF molecules. The probe light at 225.8 nm is generated from the fourth harmonic of the same titanium sapphire laser, which increases the laser frequency noise by at least a factor two. The sensitivity to Doppler shifts arising from the shorter probe wavelength is increased

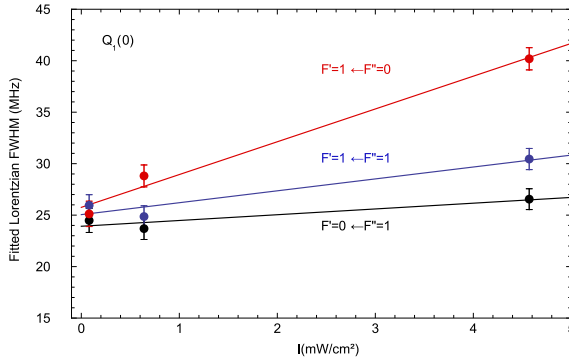


Figure 6.9: Dependence of the linewidth of the three hyperfine lines of the $Q_1(0)$ spectrum as a function of the peak laser intensity. The hyperfine lines broaden differently with increasing intensity because of hyperfine and rotational pumping. Straight lines are linear fits to the data. The relative slopes agree well with simulations using rate equations.

by a factor 1.6 relative to the $Q_1(0)$ line in MgF. The Al transition has a natural linewidth of 2.5 MHz [362], and using this value we arrive at an upper bound of the Gaussian FWHM contribution of 9.2(2) MHz at the Al detection wavelength. We therefore vary the Gaussian contribution in the final fit between 1 and 4.6 MHz, and find that this changes the fitted value of $\Gamma/(2\pi)$ by at most 1 MHz. From this, we estimate a lower bound for the radiative lifetime of the $A^2\Pi, v' = 0$ state to be $\tau_0 = 1/\Gamma = (7.23 \pm 0.16_{stat} \pm 0.33_{sys})$ ns, in agreement with the theoretical prediction by Pelegrini *et al.* [340] of 7.16 ns. The uncertainty is dominated by the systematic uncertainty in the Gaussian contribution to the spectral lineshape.

6.7 Electric Dipole Moment Measurements

The application of an external electric field \mathbf{E} in the detector introduces an additional term,

$$H_{Stark} = -\boldsymbol{\mu}_i \cdot \mathbf{E}, \quad (6.15)$$

to the Hamiltonian given in Equation (6.1). Here, $\boldsymbol{\mu}_i$ is the vector dipole moment operator in electronic state i . From the Stark splitting and shifting of the LIF spectra we can determine the magnitude of the dipole moments $|\boldsymbol{\mu}_A|$ and $|\boldsymbol{\mu}_X|$.

The Stark Hamiltonian (6.15) couples nearby molecular states of opposite parity having the same total angular momentum projection M_F onto an axis parallel to \mathbf{E} . To calculate the energies under an applied field, we diagonalise the Hamiltonian matrix constructed using the relevant Hund's case basis functions, including all levels with $J \leq 9/2$. In the electronic ground state, the Stark Hamiltonian mainly mixes states separated by one unit of the quantum number N'' . For the electric fields applied in this study of up to 10.6 kV/cm, the Stark shift is

quadratic. For the excited states, the dominant interaction is between the closely spaced Λ -doublet levels. The interaction is strong compared to this splitting and results in a linear Stark shift even for low electric field strengths. The Stark effect overcomes the hyperfine interaction at modest electric field strengths of about 0.1 kV/cm, after which the levels separate by their value of the angular momentum projection $M_{J'}$.

Figure 6.10 a and b show spectra of the $R_{21}(0)$ and $Q_1(0)$ lines, respectively, under field-free conditions and with an electric field of 4.44 kV cm^{-1} applied in the detector. The total span of each spectrum is determined by the Stark effect of the excited state, and the small shift in the gravity centre is due to the ground state Stark shift. With the laser polarisation oriented perpendicular to the electric field, we excite and observe all four $M_{J'}$ components of the $R_{21}(0)$ lines in figure 6.10 a. We measure spectra at various applied fields and fit the modelled spectra to extract best fit values for the dipole moments, obtaining $\mu_A = 3.20 \pm 0.01_{stat} \pm 0.22_{sys} \text{ D}$ and $\mu_X = 2.88 \pm 0.03_{stat} \pm 0.20_{sys} \text{ D}$. The systematic uncertainty is dominated by the determination of the electric field between the mesh electrodes. We assume a measurement uncertainty of 0.3 mm in the mesh separation of 9 mm, and with finite element modelling we estimate a reduction of 2% in the electric field strength relative to infinite plate electrodes of the same separation. The combination of these effects far exceeds the statistical uncertainty from the fitting procedure. Simulated spectra using the best fit values are shown inverted in figure 6.10a and b, demonstrating good quantitative agreement with the measurements. The FWHM of the lines measured at low and high field are consistent within 1 MHz, from which we deduce that spatial inhomogeneity of the electric field across the probe beam is below 0.1%.

To examine the behaviour of the energy levels in MgF in electric fields in more detail, we show the simulated Stark shifts for low- J levels at high, moderate and small electric field strengths in figure 6.11. Between 10 and 100 kV/cm (left panel), different rotational levels interact significantly; this leads to avoided crossings between the excited states, indicated by circles in the figure 6.11. At intermediate fields up to 10 kV/cm (centre panel), the Stark effect of the ground state becomes comparable to the excited state. At electric fields below 0.25 kV/cm (right panel), mixing in the ground state is negligible, whereas in the excited state the nearby Λ -states mix significantly. The $X^2\Sigma^+$ ground state dipole moment has been predicted theoretically [340,363–367]. The values obtained by different methods range from 2.67 D [340] to 3.126 D [366]. We note that our measured value of μ_X is in good agreement with the theoretical value obtained by Fowler and Sadlej [364], $\mu_X = 2.8611 \text{ D}$, using the complete active space self-consistent field (CASSCF) method. Pelegriani *et al.* also calculated $\mu_A = 4.23 \text{ D}$, which is in poor agreement with our experimental results. Table 6.5 compares our experimental values to those of other group II monofluorides. Steimle *et al.* [354] reported two different values of the electric dipole moment for the $A^2\Pi_{1/2}$ and $A^2\Pi_{3/2}$ states of BaF, which can be explained by interactions with other states. Within the statistical uncertainty of 0.3%, our Stark shifted spectra of MgF are well described by a single dipole moment for the $A^2\Pi$ state. This suggests very little influence of nearby perturbing states on the dipole moment, in contrast to BaF.

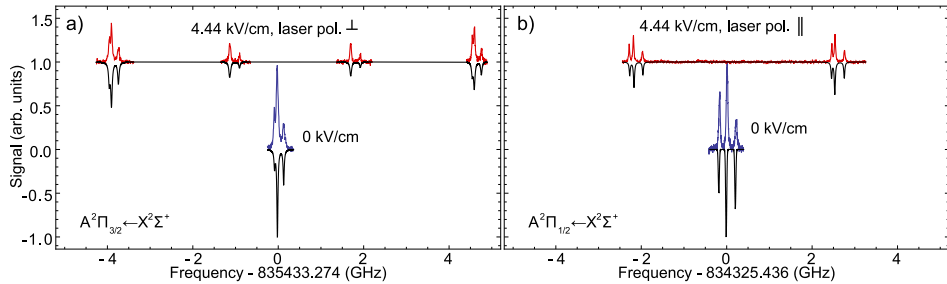


Figure 6.10: Stark effect measurement of the $R_{21}(0)$ (a) and $Q_1(0)$ (b) lines of the $A^2\Pi \leftarrow X^2\Sigma^+$ transition in MgF. The field-free spectra are shown in blue and when an electric field of 4.44 kV cm^{-1} is applied in red. The simulated spectra assuming $\mu_X = 2.88(20)$ D and $\mu_A = 3.20(22)$ D for the ground and excited state dipole moments, respectively, are shown in black.

6.8 Electric Field Induced Rotational Branching

The laser cooling scheme for MgF relies on the parity (P) and angular momentum (J) selection rules of electric dipole transitions. In zero electric field, optical cycling is possible on the $P_1/Q_{12}(1)$ transition, which excites molecules from the $N'' = 1$ ground states to the $J' = 1/2, P' = +$ excited states. However, a small electric field E results in an exchange of population, ϵ^2 , between excited states of opposite parity. The relative transition strength from $N'' = 1$ becomes $1 - \epsilon^2$ when exciting the states of mostly positive character, and these states decay to $N'' = 0, 2$ with probability ϵ^2 . In addition, excitation to the states with mostly negative parity character becomes weakly allowed, with a relative transition strength ϵ^2 . These states decay to $N'' = 0, 2$ with near unit probability. This second loss channel cannot be neglected, because efficient optical cycling requires frequency sidebands to address the ground state hyperfine splitting, causing the weak transitions to be driven near resonance. As a result, we estimate the loss probability from the cooling cycle due to uncontrolled electric fields, to lowest order in ϵ , as $\mathcal{P}_{\text{loss}} \approx 2\epsilon^2$.

In figure 6.12, we plot $\mathcal{P}_{\text{loss}}$ versus the electric field strength for the two possible values of F' , using our measured spectroscopic constants. We fit the data below 5 V/cm to $\mathcal{P}_{\text{loss}} = \alpha_{F'} |E|^2$, finding that $\alpha_0 = 4 \times 10^{-5} \text{ cm}^2/\text{V}^2$ and $\alpha_1 = 2 \times 10^{-4} \text{ cm}^2/\text{V}^2$. For the $P_1/Q_{12}(1)$ cooling transition, electric fields of 18 V cm^{-1} and 9 V cm^{-1} lead to a mixing of the parity eigenstates of about 1.4%, for $F' = 0$ and 1, respectively. At this level, losses from the optical cycle due to parity mixing match losses to the $v'' = 1$ vibrational manifold in the $X^2\Sigma^+$ state predicted by Ref. [340]. We note that such electric field induced losses have already been observed experimentally in SrF [281] and AlF [88].

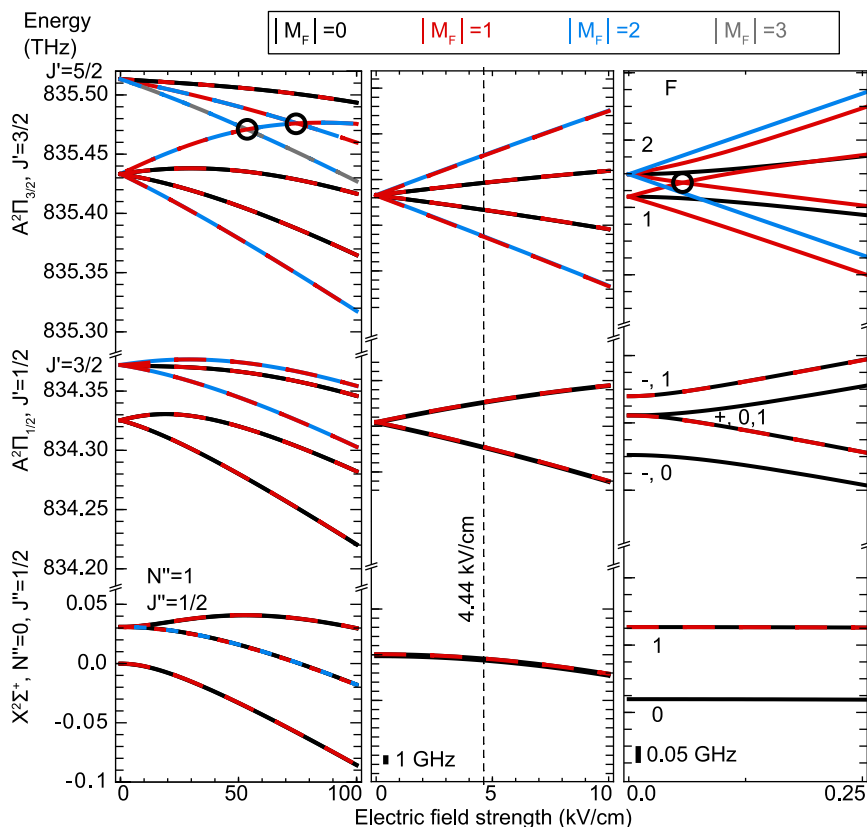


Figure 6.11: Calculated Stark shifts of the $X^2\Sigma^+$, $N'' = 0$, $J'' = 1/2$, $A^2\Pi_{1/2}$, $J' = 1/2$, and $A^2\Pi_{3/2}$, $J' = 3/2$ levels. The left panel shows the shifts up to 100 kV cm^{-1} , the centre shows the region of $0\text{--}10 \text{ kV cm}^{-1}$ and the right panel a zoom-in to $0\text{--}0.25 \text{ kV cm}^{-1}$. Avoided crossings are marked with black circles. The different $|M_F|$ components are colour-coded. If the Stark curves of two states with the same $|M_F|$ overlap at the resolution of the figure, they are shown as dashed lines. The electric field used in the spectra in figure 6.10 (a) and (b) is indicated with a dashed vertical line.

Table 6.5: Reported dipole moments of group II monofluorides, in Debye. Values for MgF are from this study.

Parameter	MgF	CaF	SrF	BaF
$\mu(X^2\Sigma^+)$	2.88(20)	3.07(7) [368]	3.4963(4) [369]	3.170(3) [370]
$\mu(A^2\Pi_{1/2})$	3.20(22)			1.50(2) [354]
$\mu(A^2\Pi_{3/2})$	3.20(22)	2.45(6) [371]	2.064(50) [341]	1.31(2) [354]

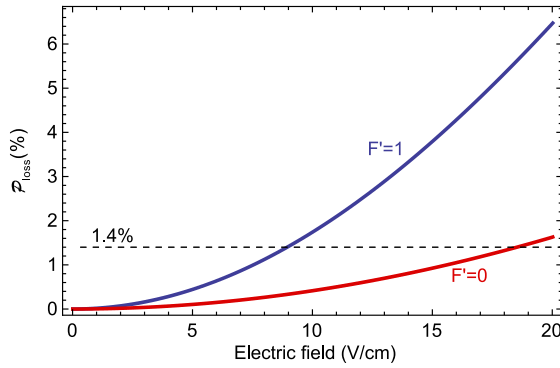


Figure 6.12: Calculated loss of population due to mixing of opposite parity levels, ϵ^2 , for the different hyperfine levels of the $A^2\Pi$, $J' = 1/2$ states in an electric field. This results in unwanted rotational branching to $N'' = 0$ and 2 in the ground state when driving the $P_1/Q_{12}(1)$ laser cooling transition. The $|M_{F'}| = 0, 1$ levels in $F' = 1$ are shown in blue, the $F' = 0, |M_{F'}| = 0$ level is shown in red. The dashed line indicates the level of expected losses due to vibrational branching to $v'' = 1$. The quadratic loss coefficients $\alpha_{F'}$ are $\alpha_0 = 4 \times 10^{-5} \text{cm}^2/\text{V}^2$ and $\alpha_1 = 2 \times 10^{-4} \text{cm}^2/\text{V}^2$.

6.9 Conclusion

We recorded hyperfine-resolved cw LIF spectra of 25 low- J lines of the $A^2\Pi \leftarrow X^2\Sigma^+$ transition in MgF, and analysed the ^{24}MgF isotopologue in detail. By fitting the eigenvalues of the effective Hamiltonian to the measured line positions, we determined the spectroscopic parameters of the $A^2\Pi$ state that are relevant for laser cooling experiments: rotational, fine- and hyperfine structure constants. We calibrated our wavemeter using the precisely known Yb $(6s6p)^1P_1 \leftarrow (6s^2)^1S_0$ transition frequencies [309], and correct a -4.1 GHz systematic error in the line frequencies presented by Xu *et al.* [282]. Transition isotope shifts between the ^{24}MgF and ^{26}MgF isotopologues were recorded and the different contributions were discussed. We studied the broadening of the hyperfine lines due to optical pumping and recorded high-resolution spectra of the $Q_1(0)$ line to determine the radiative lifetime of the $A^2\Pi$, $v' = 0$ level to be $\tau_0 = 7.23(36)$ ns.

By studying the fluorescence spectra under an applied electric field, we experimentally determined the dipole moments of the $X^2\Sigma^+$ and $A^2\Pi$ states. Our value for the ground state, $\mu_X = 2.88 \pm 0.03_{stat} \pm 0.20_{sys}$ D, is in good agreement with the value predicted by *ab initio* calculations [363–367]. Using our value of $\mu_A = 3.20 \pm 0.01_{stat} \pm 0.22_{sys}$ D, we predict the electric field strength at which parity-mixing in the excited states limits optical cycling on the $P_1/Q_{12}(1)$ line. We find that 9 V cm^{-1} is sufficient for unwanted rotational branching to match the expected vibrational branching. To scatter more than 10^4 photons, stray electric fields have to be controlled to below the 1 V cm^{-1} level. Coincidentally, the hyperfine structure in the $J' = 1/2, P' = +1$ level is less than 1 MHz, which simplifies the laser cooling scheme significantly. On the contrary, the hyperfine splitting in the $J' = 1/2, P' = -1$ level is large, which increases the separation between opposite parity hyperfine levels. This reduces the sensitivity of the optical cycling scheme to stray electric fields substantially.

There are a number of notable differences between MgF and the heavier group II monofluorides CaF, SrF and BaF. First, the sign of the Λ -splitting is inverted in MgF, and its magnitude is about 100 times smaller. Second, MgF has the largest dipole moment in the $A^2\Pi$ state, whereas it has the smallest dipole moment in its ground state. Third, the interaction of the electronic angular momentum with the fluorine nuclear spin leads to a resolvable hyperfine structure in the excited state of MgF, and from our measured hyperfine constants we can infer that the electronic wavefunction has significant probability density between the nuclei. This supports the conclusions of Anderson *et al.* [337] regarding the greater covalency of the chemical bonding in MgF.

Finally, we note that our measurements form a stringent set of benchmarks for precise quantum chemical calculations on MgF. The hyperfine constants and dipole moment measurements are strong benchmarks for molecular orbital calculations of the $X^2\Sigma^+$ and $A^2\Pi$ states, while the transition isotope shifts presented constrain vibrational constants and deviations from the Born-Oppenheimer approximation.

Summary

Ultracold molecules have great potential for future applications in physics and chemistry. In this thesis, I presented a set of studies that establish aluminium monofluoride (AlF) as a promising candidate for laser cooling and trapping experiments of cold molecules.

An experimental apparatus based on a pulsed supersonic expansion source for AlF molecules and interaction zones with continuous or pulsed laser, radio frequency and microwave radiation is used for a first spectroscopic investigation. We resolved the hyperfine structure of the $a^3\Pi$ state using Λ -doublet transitions between hyperfine states, helping us to understand the hyperfine structure in the $A^1\Pi$ state. The spin-forbidden $A^1\Pi \leftarrow a^3\Pi$ transition is detected for the first time. This transition is a potential loss channel from the $A^1\Pi - X^1\Sigma^+$ cycling transition. However, the experimentally determined loss channel is negligible and below the 10^{-6} level.

The next study focuses on spectroscopic studies of the $b^3\Sigma^+$ state. We measure and explain its fine and hyperfine structure and investigate the spin-orbit mixing with the $A^1\Pi$ state, which explains the coupling between the triplet and singlet states.

Optical cycling can be modelled using rate equations or the optical Bloch equations. These, in combination with trajectory simulations, can explain our experimental observations on optical cycling. Using the optical Bloch equations, we can demonstrate that the hyperfine splitting of the $X^1\Sigma^+$ state of AlF destabilises dark states, which is crucial to maintain optical cycling. The $a^3\Pi \leftarrow X^1\Sigma^+$ transition of AlF can, in principle, be used for narrow-line cooling. The lifetime of the $a^3\Pi_0, v = 0, J = 1, e$ level is experimentally determined to be $\tau_1 = 1.89 \pm 0.15$ ms; the resulting scattering rate is probably too low for efficient narrow-line cooling.

To achieve dense samples of ultracold molecules, it is important to understand and optimise the formation processes in the cryogenic source. We compare the formation of AlF, CaF, MgF and YbF from the reaction of ablated metal with a fluorine donor gas in the same buffer gas cell setup. We show that, under the same experimental conditions, a beam of AlF is one order of magnitude brighter than the other molecular beams. The radical atom aluminium reacts to form the stable molecule AlF, while the other studied species are radical molecules formed from stable atoms.

In a last study, we perform high-resolution spectroscopy of the $A^2\Pi \leftarrow X^2\Sigma^+$ transition of MgF and establish important spectroscopic information — hyperfine

and Λ -doubling parameters as well as dipole moments — that will guide future laser-cooling experiments of this molecule.

Samenvatting

Ultrakoude moleculen bieden uiteenlopende mogelijkheden voor toekomstige toepassingen in de natuur- en scheikunde. In dit proefschrift presenteer ik verschillende onderzoeken waaruit blijkt dat het aluminium monofluoride molecuul (AlF) een veelbelovende kandidaat is voor laser-koeling en voor aansluitende experimenten met ingevangen, koude moleculen.

Voor het eerste spectroscopische onderzoek is een molecuulbundel opstelling gebruikt waarin AlF is geproduceerd in een gepulste supersone expansie en is onderzocht met zowel gepulste als continue lasers, en met radiofrequente en microgolf straling. We hebben de hyperfijnstructuur in de $a^3\Pi$ toestand kunnen ontrafelen door nauwkeurig de opsplitsingen tussen de Λ -niveau's te meten, en dit heeft geholpen om vervolgens de hyperfijnstructuur in de $A^1\Pi$ toestand te kunnen begrijpen. We hebben voor de eerste keer de $A^1\Pi \leftarrow a^3\Pi$ overgang waargenomen. Deze overgang kan in principe een verlieskanaal vormen voor de $A^1\Pi \leftarrow X^1\Sigma^+$ laser-koelings overgang, maar met een gemeten verlies op het 10^{-6} niveau is dit kanaal verwaarloosbaar.

Het volgende spectroscopische onderzoek betreft de $b^3\Sigma^+$ toestand, waarvoor we ook de fijnstructuur en de hyperfijnstructuur hebben bepaald. We hebben in detail de spin-baan koppeling met de $A^1\Pi$ toestand gekarakteriseerd, en kunnen daardoor de koppeling tussen de triplet en singlet toestand kwantitatief beschrijven.

Het proces van herhaalde absorptie en emissie van optische straling op een gestloten overgang (“optical cycling”) kan gemodelleerd worden met een set van reële, lineaire differentiaalvergelijkingen of met optische Bloch vergelijkingen. Samen met de simulatie van moleculaire trajectoriën, kunnen met deze vergelijkingen de experimentele waarnemingen van optical cycling goed verklaard worden. Met behulp van de optische Bloch vergelijkingen hebben we kunnen laten zien dat de hyperfijnstructuur in de $X^1\Sigma^+$ toestand van AlF de zogenaamde donkere niveau's destabiliseert, hetgeen essentieel is om het proces van optical cycling aan de gang te houden. De $a^3\Pi \leftarrow X^1\Sigma^+$ overgang kan in principe gebruikt worden om de AlF moleculen naar een nog lagere temperatuur te koelen dan op de $A^1\Pi \leftarrow X^1\Sigma^+$ overgang mogelijk is. We hebben de stralings-levensduur van het $a^3\Pi_0, v = 0, J = 1, e$ -niveau experimenteel echter gevonden als $\tau_1 = 1.89 \pm 0.15\text{ms}$, en dit maakt het aantal fotonen dat per seconde verstrooid kan worden op deze overgang waarschijnlijk te klein voor efficiënte laser-koeling.

Om nog grotere hoeveelheden koude moleculen bij nog hogere dichtheden te verkrijgen, is het belangrijk om het productie-proces van deze moleculen in de cryogene bron beter te begrijpen, teneinde dit verder te kunnen optimaliseren. We hebben de productie van AlF, CaF, MgF and YbF in een reactie van het laser-verdampte metaal met een fluor-houdend gas onderzocht in één en dezelfde cryogene buffer-gas cel. We hebben laten zien dat onder dezelfde experimentele condities, de bundel van AlF moleculen die gevormd wordt een grootte-orde meer intens is dan de bundel van de andere genoemde twee-atomige moleculen. Het reactieve Al atoom reageert met het fluor-houdende gas en produceert het stabiele molecuul AlF, terwijl de andere genoemde moleculen zelf reactief zijn en gevormd worden uitgaande van minder reactieve atomen.

Het laatste onderzoek beschreven in dit proefschrift betreft hoge resolutie spectroscopie aan de $A^2\Pi \leftarrow X^2\Sigma^+$ overgang van MgF. Dit heeft gedetailleerde spectroscopische informatie opgeleverd — parameters die de hyperfijnstructuur en de Λ -opsplitsing beschrijven alsmede elektrische dipool momenten — die belangrijk is voor toekomstige laser-koelings experimenten aan dit molecuul.

Appendix A

Transition Frequencies in the $a^3\Pi, v = 0$ State

Table A.1 lists the 138 measured radio-frequency and microwave transitions in the $a^3\Pi, v = 0$ state of AlF. The measured transition frequency f_o is listed in the first column, followed by the experimental uncertainty δf_o (in MHz). The latter includes the statistical uncertainty from the fit and a systematic uncertainty determined by the Zeeman broadening of the line due to the small residual magnetic field in the interaction region. The third column lists δf_{loop} , which is used as an experimental consistency check. A combination of three transitions probe an interval that can also be measured directly, in a single transition. Their difference should be zero within the total combined experimental uncertainty. We list this deviation from zero for each line that is part of such a loop as δf_{loop} . This deviation from zero is never larger than the combined experimental uncertainty of the four lines that make up a loop. The next twelve columns list the Ω , J , parity (p) and F labels of the levels involved in the transition, together with their calculated g_F -factors. The labels with (without) a prime refer to the upper (lower) level of the transition. However, this labelling scheme is not unique because there can be multiple levels with the same parity and F quantum number within a given J and Ω . To be able to distinguish levels with the same quantum numbers and parity, we introduce an index n . The lowest energy level for a given value of F and p gets the index $n = 1$ and is in the $a^3\Pi_0$ manifold. The column with the header d^2 (D^2) lists the calculated square of the reduced dipole moment d of the transition in Debye². These transition strengths vary over four orders of magnitude. The difference between the observed and calculated transition frequency, $f_o - f_c$ is given (in MHz) in the second to last column. The last column lists the difference between the calculated g_F -factors of the upper and the lower level of the transition. This value correlates with the experimental uncertainty to determine the line center, because transitions with larger $\delta g = g'_F - g_F$ show more Zeeman broadening. We use all 138 transitions in the fit to the eigenvalues of the Hamiltonian to determine the 24 spectroscopic parameters given in Table 2.1.

Table A.1: Observed and calculated rf and microwave transition frequencies in the $a^3\Pi, v = 0$ state of AlF, transition dipole moments and magnetic g_F factors.

f_o (MHz)	δf_o	δf_{loop}	Ω'	J'	p'	F'	n'	g'_F	Ω	J	p	F	n	g_F	d^2 (D^2)	f_o-f_c	g'_F-g_F
9815.516	0.003	0.003	0	0	-	3	1	-0.028	0	0	+	2	1	-0.022	0.0050	-0.004	-0.006
9818.512	0.003	0.003	0	0	-	3	1	-0.028	0	0	+	3	1	-0.016	0.1100	-0.001	-0.012
9822.671	0.003	0.003	0	0	-	2	1	-0.039	0	0	+	3	1	-0.016	0.0050	0.002	-0.023
9819.673	0.003	0.003	0	0	-	2	1	-0.039	0	0	+	2	1	-0.022	0.0750	-0.003	-0.017
9686.817	0.005	0.004	0	1	+	2	2	-0.024	0	1	-	3	3	0.025	0.0350	-0.006	-0.049
9692.796	0.004	0.007	0	1	+	1	1	-0.040	0	1	-	2	3	0.035	0.0222	-0.002	-0.075
9807.485	0.003	0.003	0	1	+	2	3	0.015	0	1	-	3	3	0.025	0.0028	-0.004	-0.010
9808.913	0.003	0.004	0	1	+	3	2	0.011	0	1	-	3	3	0.025	0.0459	-0.007	-0.014
9812.306	0.002	0.007	0	1	+	2	3	0.015	0	1	-	2	3	0.035	0.0327	-0.006	-0.020
9821.992	0.004	0.001	0	1	+	4	1	0.006	0	1	-	3	3	0.025	0.0355	0.002	-0.019
9822.583	0.004	0.003	0	1	+	3	3	0.008	0	1	-	3	3	0.025	0.0025	0.004	-0.017
9827.406	0.003	0.003	0	1	+	3	3	0.008	0	1	-	2	3	0.035	0.0253	0.005	-0.027
9841.880	0.003	0.001	0	1	+	3	2	0.011	0	1	-	4	1	0.007	0.0101	-0.004	0.004
9845.927	0.004	0.003	0	1	+	2	3	0.015	0	1	-	3	2	0.009	0.0066	-0.007	0.006
9854.960	0.005	0.001	0	1	+	4	1	0.006	0	1	-	4	1	0.007	0.0107	0.006	-0.001
9861.027	0.005	0.003	0	1	+	3	3	0.008	0	1	-	3	2	0.009	0.0073	0.004	-0.001
9894.181	0.001	0.007	0	1	+	3	1	-0.040	0	1	-	1	1	-0.036	0.0026	0.001	-0.004
9899.272	0.002	0.004	0	1	+	2	2	-0.024	0	1	-	2	2	-0.023	0.0050	0.004	-0.001
10013.696	0.002	0.007	0	1	+	2	3	0.015	0	1	-	1	1	-0.036	0.0096	0.003	0.051
10021.372	0.003	0.004	0	1	+	3	2	0.011	0	1	-	2	2	-0.023	0.0155	0.008	0.034
9749.561	0.003	0.001	0	2	-	4	2	0.017	0	2	+	5	1	0.016	0.0018	0.002	0.001
9760.598	0.004	0	0	2	-	3	5	0.022	0	2	+	4	3	0.020	0.0014	-0.002	0.002
9840.139	0.004	0.001	0	2	-	5	1	0.016	0	2	+	5	1	0.016	0.0031	0.002	0.000
9851.702	0.003	0	0	2	-	4	3	0.020	0	2	+	4	3	0.020	0.0024	0.003	0.000
9853.710	0.002	0	0	2	-	1	2	-0.038	0	2	+	2	4	0.007	0.0018	0.003	-0.045
9854.234	0.003	0.001	0	2	-	4	2	0.017	0	2	+	4	2	0.019	0.0010	-0.003	-0.002
9877.260	0.005	0	0	2	-	3	4	0.015	0	2	+	3	4	0.017	0.0026	-0.005	-0.002
9881.786	0.004	0	0	2	-	2	5	0.021	0	2	+	2	5	0.027	0.0018	-0.005	-0.006
9944.813	0.004	0.001	0	2	-	5	1	0.016	0	2	+	4	2	0.019	0.0035	-0.002	-0.003
9953.603	0.003	0	0	2	-	4	3	0.020	0	2	+	3	5	0.025	0.0027	-0.001	-0.005
9966.078	0.002	0	0	2	-	2	4	0.006	0	2	+	1	2	-0.045	0.0015	-0.004	0.051
1.079	0.002	0.001	1	1	-	1	7	-0.227	1	1	+	1	7	-0.227	1.2300	0.002	0.000
6.484	0.002	0.007	1	1	-	3	13	0.039	1	1	+	2	12	0.073	0.0014	0.001	-0.034
10.902	0.002	0.005	1	1	-	2	11	-0.151	1	1	+	2	11	-0.149	2.6900	0.002	-0.002
13.428	0.003	0.005	1	1	+	3	14	0.150	1	1	-	3	14	0.148	7.4000	-0.007	0.002
21.379	0.001	0.007	1	1	-	2	12	0.074	1	1	+	2	12	0.073	0.6420	-0.003	0.001
21.744	0.001	0.006	1	1	-	3	13	0.039	1	1	+	3	13	0.038	0.4910	-0.003	0.001
21.826	0.003	0.002	1	1	+	4	13	0.113	1	1	-	4	13	0.113	9.0800	-0.006	0.000
36.644	0.002	0.005	1	1	-	2	12	0.074	1	1	+	3	13	0.038	0.0018	-0.001	0.036
74.353	0.004	0.004	1	1	-	4	13	0.113	1	1	+	3	14	0.150	0.0458	0.006	-0.037
101.298	0.004	0.002	1	1	+	1	7	-0.227	1	1	-	2	11	-0.151	0.0128	0.003	-0.076
109.610	0.005	0.004	1	1	+	4	13	0.113	1	1	-	3	14	0.148	0.1050	-0.004	-0.035
113.279	0.004	0.005	1	1	-	1	7	-0.227	1	1	+	2	11	-0.149	0.0373	0.007	-0.078
120.377	0.008	0.005	1	1	+	2	12	0.073	1	1	-	1	7	-0.227	3.6300	0.001	0.300
142.835	0.007	0.002	1	1	-	2	12	0.074	1	1	+	1	7	-0.227	3.6500	0.001	0.301
188.903	0.005	0.007	1	1	+	3	14	0.150	1	1	-	2	12	0.074	3.8100	0.001	0.076
196.856	0.006	0.005	1	1	-	3	14	0.148	1	1	+	2	12	0.073	3.8300	0.007	0.075
203.805	0.006	0.007	1	1	+	3	14	0.150	1	1	-	3	13	0.039	0.1010	0.005	0.111
207.488	0.007	0.006	1	1	+	3	13	0.038	1	1	-	2	11	-0.151	5.4200	0.004	0.189
212.117	0.006	0.005	1	1	-	3	14	0.148	1	1	+	3	13	0.038	0.0245	0.005	0.110
222.754	0.005	0.006	1	1	+	2	12	0.073	1	1	-	2	11	-0.151	0.0459	0.007	0.224
240.135	0.007	0.005	1	1	-	3	13	0.039	1	1	+	2	11	-0.149	5.4000	0.004	0.188
255.034	0.006	0.005	1	1	-	2	12	0.074	1	1	+	2	11	-0.149	0.0321	0.004	0.223
299.902	0.006	0.004	1	1	-	4	13	0.113	1	1	+	3	13	0.038	5.4700	0.009	0.075
299.985	0.006	0.004	1	1	+	4	13	0.113	1	1	-	3	13	0.039	5.4100	0.006	0.074
430.512	0.010	0.005	1	1	-	3	14	0.148	1	1	+	2	11	-0.149	0.0160	0.015	0.297
433.038	0.010	0.005	1	1	+	3	14	0.150	1	1	-	2	11	-0.151	0.0099	0.007	0.301
5.823	0.002	0.002	1	2	+	4	14	0.055	1	2	-	4	14	0.054	1.9800	0.006	0.001
20.560	0.005	0	1	2	-	2	13	0.002	1	2	+	1	8	-0.154	1.0800	0.000	0.156
23.798	0.003	0	1	2	-	4	15	0.076	1	2	+	4	15	0.075	3.8900	-0.009	0.001
25.431	0.001	0	1	2	-	2	14	0.075	1	2	+	1	9	0.077	0.9420	-0.005	-0.002
28.224	0.001	0	1	2	+	3	15	0.039	1	2	-	3	15	0.039	0.5000	0.003	0.000
46.617	0.003	0	1	2	-	3	15	0.039	1	2	+	2	13	0.001	1.6200	-0.006	0.038
49.659	0.002	0	1	2	-	3	16	0.076	1	2	+	2	14	0.076	1.0800	-0.003	0.000
61.370	0.003	0.002	1	2	+	4	15	0.075	1	2	-	4	14	0.054	0.0343	0.009	0.021
93.480	0.003	0.002	1	2	-	5	13	0.061	1	2	+	4	15	0.075	0.0760	-0.012	-0.014
115.544	0.003	0	1	2	+	5	13	0.061	1	2	-	4	14	0.054	1.1700	0.009	0.007
116.955	0.003	0	1	2	+	1	9	0.077	1	2	-	1	8	-0.152	0.0034	-0.004	0.229
120.115	0.002	0.002	1	2	+	4	14	0.055	1	2	-	3	15	0.039	1.6400	0.002	0.016
133.810	0.004	0	1	2	-	3	16	0.076	1	2	+	2	13	0.001	0.0116	-0.008	0.075
149.029	0.003	0.002	1	2	-	5	13	0.061	1	2	+	4	14	0.055	1.1100	-0.007	0.006
175.662	0.004	0.002	1	2	+	4	15	0.075	1	2	-	3	15	0.039	0.0403	0.005	0.036
181.424	0.004	0	1	2	+	3	16	0.076	1	2	-	2	13	0.002	0.0011	-0.005	0.074
26.397	0.002	0	1	3	-	4	16	0.040	1	3	+	4	16	0.039	1.0400	0.007	0.001
58.145	0.003	0	1	3	+	5	15	0.047	1	3	-	5	14	0.040	0.3110	-0.011	0.007
58.206	0.002	0	1	3	+	5	14	0.039	1	3	-	4	16	0.040	0.6560	-0.011	-0.001
89.015	0.002	0	1	3	-	4	16	0.040	1	3	+	3	17	0.040	0.7340	-0.002	0.000
110.090	0.003	0	1	3	+	5	15	0.047	1	3	-	4	16	0.040	0.0051	-0.007	0.007
0.294	0.003	0	1	7	+	8	17	0.016	1	7	-	8	17	0.016	0.9120	0.000	0.000
5.226	0.003	0	1	7	-	9	13	0.015	1	7	+	8	17	0.016	0.0178	-0.004	-0.001
5.362	0.002	0	1	7	-	7	18	0.017	1	7	+	8	16	0.015	0.0801	0.000	0.002
8.043	0.003	0	1	7	-	9	14	0.015	1	7	+	8	17	0.016	0.0134	0.001	

Continuation of Table A.1

f_o (MHz)	δf_o	δf_{loop}	Ω'	J'	p'	F'	n'	g'_F	Ω	J	p	F	n	g_F	d^2 (D ²)	f_o-f_c	g'_F-g_F
33.727	0.003	0.002	1	7	+	9	13	0.014	1	7	-	9	14	0.015	0.5340	-0.002	-0.001
45.060	0.002		1	7	-	6	20	0.020	1	7	+	7	18	0.017	0.0606	0.000	0.003
46.428	0.003		1	7	+	9	13	0.014	1	7	-	8	16	0.016	0.0736	0.002	-0.002
55.504	0.002	0.002	1	7	-	5	22	0.025	1	7	+	6	21	0.021	0.0212	-0.001	0.004
62.319	0.002	0.002	1	7	-	5	23	0.025	1	7	+	6	21	0.021	0.0097	-0.003	0.004
72.488	0.003		1	7	-	8	16	0.016	1	7	+	7	18	0.017	0.0877	0.002	-0.001
75.855	0.002		1	7	-	5	22	0.025	1	7	+	6	20	0.020	0.0291	0.000	0.005
78.724	0.003		1	7	+	9	14	0.015	1	7	-	8	16	0.016	0.0006	0.008	-0.001
80.565	0.003	0.002	1	7	-	4	24	0.031	1	7	+	5	23	0.025	0.0006	-0.004	0.006
88.363	0.002	0.002	1	7	-	5	22	0.025	1	7	+	5	23	0.025	0.3950	0.000	0.000
95.180	0.003	0.002	1	7	-	5	23	0.025	1	7	+	5	23	0.025	0.2150	0.000	0.000
102.205	0.002		1	7	-	6	20	0.020	1	7	+	5	23	0.025	0.0154	0.001	-0.005
106.043	0.003	0.002	1	7	+	10	10	0.013	1	7	-	10	10	0.013	1.1700	0.004	0.000
109.587	0.003		1	7	-	6	21	0.021	1	7	+	5	23	0.025	0.0157	0.002	-0.004
112.727	0.003	0.002	1	7	+	10	10	0.013	1	7	-	9	14	0.015	0.0172	0.005	-0.002
131.992	0.003	0.002	1	7	-	4	24	0.031	1	7	+	4	24	0.031	0.4810	-0.005	0.000
139.792	0.001	0.002	1	7	-	5	22	0.025	1	7	+	4	24	0.031	0.0206	0.001	-0.006
146.608	0.002	0.001	1	7	-	5	23	0.025	1	7	+	4	24	0.031	0.0244	0.000	-0.006
0.524	0.006		2	4	+	5	28	0.166	2	4	-	5	28	0.166	4.5000	0.001	0.000
0.569	0.006		2	4	+	4	30	0.210	2	4	-	4	30	0.210	3.9700	-0.002	0.000
1.721	0.005		2	7	-	10	22	0.041	2	7	+	10	22	0.041	4.5700	0.002	0.000
2.034	0.006		2	7	-	9	26	0.046	2	7	+	9	26	0.046	4.1700	0.001	0.000
2.779	0.004	0.001	2	7	-	9	25	0.044	2	7	+	9	25	0.044	3.8800	-0.002	0.000
3.086	0.004	0.004	2	7	-	8	29	0.050	2	7	+	8	29	0.050	3.5500	-0.002	0.000
3.397	0.003	0.001	2	7	-	8	28	0.048	2	7	+	8	28	0.048	3.3000	-0.004	0.000
3.556	0.004		2	7	-	5	34	0.075	2	7	+	5	34	0.075	2.1800	-0.006	0.000
3.666	0.100	0.004	2	7	-	7	30	0.054	2	7	+	7	30	0.054	2.8200	-0.006	0.000
3.666	0.100	0.004	2	7	-	7	31	0.056	2	7	+	7	31	0.056	3.0300	-0.005	0.000
3.684	0.100		2	7	-	6	32	0.062	2	7	+	6	32	0.062	2.4400	-0.007	0.000
3.720	0.005		2	7	-	4	35	0.095	2	7	+	4	35	0.095	1.9100	-0.007	0.000
3.754	0.004		2	7	-	5	35	0.078	2	7	+	5	35	0.078	2.3300	-0.004	0.000
3.861	0.004		2	7	-	6	33	0.064	2	7	+	6	33	0.064	2.6200	-0.008	0.000
85.166	0.004		2	7	+	9	25	0.044	2	7	-	8	29	0.050	0.0096	-0.001	-0.006
118.002	0.004		2	7	-	6	32	0.062	2	7	+	5	34	0.075	0.2400	-0.002	-0.013
129.340	0.004		2	7	-	5	35	0.078	2	7	+	4	35	0.095	0.0494	0.000	-0.017
137.062	0.004		2	7	-	6	33	0.064	2	7	+	5	35	0.078	0.1540	0.000	-0.014
139.858	0.004		2	7	-	7	30	0.054	2	7	+	6	32	0.062	0.3070	-0.002	-0.008
148.712	0.005		2	7	+	7	31	0.056	2	7	-	6	33	0.064	0.2030	0.011	-0.008
153.672	0.004		2	7	+	8	28	0.048	2	7	-	7	30	0.054	0.3170	0.008	-0.006
168.989	0.004	0.004	2	7	+	8	29	0.050	2	7	-	7	31	0.056	0.1940	0.004	-0.006
174.809	0.004	0.001	2	7	+	9	25	0.044	2	7	-	8	28	0.048	0.2700	0.004	-0.004
175.737	0.004	0.004	2	7	-	8	29	0.050	2	7	+	7	31	0.056	0.1940	-0.007	-0.006
180.986	0.004	0.001	2	7	-	9	25	0.044	2	7	+	8	28	0.048	0.2700	0.000	-0.004
195.015	0.004		2	7	-	9	26	0.046	2	7	+	8	29	0.050	0.1260	-0.009	-0.004
200.643	0.005		2	7	-	10	22	0.041	2	7	+	9	25	0.044	0.1650	-0.003	-0.003
64825.398	0.001		0	2	+	2	5	0.027	0	1	-	2	3	0.035	3.7500	-0.001	-0.008
64825.964	0.001		0	2	+	3	4	0.017	0	1	-	3	3	0.025	5.4100	0.003	-0.008
64830.784	0.002		0	2	+	3	4	0.017	0	1	-	2	3	0.035	0.1730	0.001	-0.018
65067.937	0.002		0	2	+	4	3	0.020	0	1	-	3	2	0.009	11.4000	-0.004	0.011
65074.328	0.002		0	2	+	5	1	0.016	0	1	-	4	1	0.007	14.3000	-0.001	0.009
66466.114	0.001		1	2	+	2	14	0.076	1	1	-	2	12	0.074	2.8500	0.000	0.002
66471.700	0.001		1	2	+	3	15	0.039	1	1	-	3	13	0.039	4.2300	0.000	0.000
66563.594	0.002		1	2	+	4	14	0.055	1	1	-	3	13	0.039	5.5000	-0.001	0.016

Appendix B

Sanity Check for OBEs

A useful sanity check for a system of optical Bloch equations is to rotate the polarization of the incident light and the initial density matrix around the axis of light propagation. Then, one solves the equations as before for the changed input. After a rotation back by the same angle, the resulting populations as a function of time have to be identical to those of the system without polarization rotation [210].

Rotating the light polarization by a certain angle means rotating the dipole interaction Hamiltonian. Rotation is defined by the generator of rotation

$$R(\theta) = e^{-i\theta\mathbf{n}\cdot\mathbf{J}}, \quad (\text{B.1})$$

where θ is the angle of rotation, \mathbf{n} is the unit vector along the rotation axis and \mathbf{J} is the total angular momentum operator. In the case of transitions between hyperfine states, the relevant angular momentum is \mathbf{F} and can be inserted for \mathbf{J} . For our purpose, it is sufficient to only look at rotation around the axes of the cartesian coordinate system, and we can write

$$R(\theta) = e^{-i\theta\mathbf{J}_i}, \quad (\text{B.2})$$

where $i \in \{x, y, z\}$. The π polarization of the Hamiltonian is aligned with z , therefore we only consider rotation around x or y . To calculate the matrix elements of the angular momentum operator, it is useful to introduce the raising and lowering operators

$$\begin{aligned} J_+ &= J_x + iJ_y \\ J_- &= J_x - iJ_y \end{aligned} \quad (\text{B.3})$$

and their matrix elements are defined by [372]

$$\langle J, m | J_{\pm} | J', m' \rangle = \sqrt{J(J+1) - m'(m' \pm 1)} \delta_{JJ'} \delta_{m, m' \pm 1}, \quad (\text{B.4})$$

where J is the eigenvalue of \mathbf{J}^2 and m is the eigenvalue of J_z . The matrix elements of J_z are defined as

$$\langle J, m | J_z | J', m' \rangle = m' \delta_{jj'} \delta_{mm'} \quad (\text{B.5})$$

Knowing this, we can rotate a matrix M by an angle θ by applying

$$M' = R(\theta)MR(\theta)^\dagger \tag{B.6}$$

and the inverse rotation is defined by

$$M = R(\theta)^\dagger MR(\theta). \tag{B.7}$$

Appendix C

Closed-Cycle He Cryocooler

The commercial closed-cycle He cryocooler used for cooling of our buffer gas cell setup is based on the fundamental design that was first presented in 1960 by Gifford and McMahon [373,374]. Good introductions into the working principle of Gifford-McMahon-type and other cryocoolers can be found in the book by Walker [375] and the review by de Waele [376].

A Gifford-McMahon-type (GM) cryocooler's cooling principle is based on the expansion of compressed helium in a pulsed manner, controlled by switching valves and a displacer piston. A compressor provides high He pressure. Two valves separate the compressor from the cold head, an inlet and an outlet valve. In the cold head, there are two volumes that are connected so that fluid can flow freely between the two. One is the regenerator, which consists of porous metal that can quickly exchange thermal energy with the He. The other is a cylinder with a displacer piston that takes up about three quarters of the volume and that can move freely. A tight seal prevents fluid from passing on the side of the displacer. The compressor cycle and the cold head cycle frequencies are not coupled. The four-step operation is shown in figure C.1 and described in the following, using the nomenclature by Walker [375].

1. Pressure build-up:

The inlet valve is open while the displacer is at the bottom of the cylinder. Hot, compressed helium fills the regenerator and the volume above the displacer.

2. Intake stroke:

While the inlet valve is still open, the displacer moves to the top, pushing helium through the regenerator to the space below the displacer. In the regenerator, the gas cools down and reduces its volume. Maximum pressure is maintained by additional gas flowing in.

3. Pressure release and expansion:

The inlet valve is closed and the outlet valve open. The gas can now expand freely and takes the required energy from the system (gas volume + cold head).

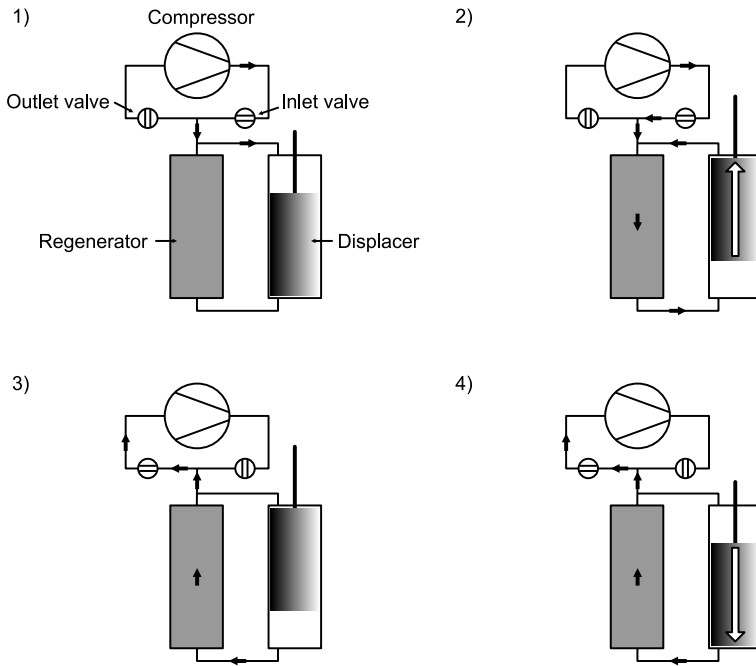


Figure C.1: Scheme of the cooling cycle of a GM-type refrigerator. Drawing based on [375] and the Sumitomo SRDK series manual.

4. Exhaust stroke:

The outlet valve is still open and the displacer moves down again. This pushes the cold, low-pressure gas through the regenerator, thus cooling down the metal matrix.

Because the He expansion and the compressor repetition rates are independent, one can use relatively inexpensive commercial compressors for the helium, as opposed to, e.g., pulse-tube cryocoolers.

The refrigerator used in our experiment has two cooling stages that can achieve different temperatures. There, the first stage cools down the second stage, enabling a lower temperature (see figure 5.9 of Walker [375]).

Between the cooling surface and the cold head, a volume of liquid helium in a reservoir can be used as a buffer for rapid temperature fluctuations.

The Sumitomo RDK-415DP cold head used for many of the experiments in this thesis has a refrigeration capacity of 35 W at 50 kelvin in the first stage and 1.4 W at 4.2 K in the second stage.

Appendix D

Hamiltonian of $A^2\Pi$ States of MgF

To understand the influence of the different spectroscopic parameters in the Hamiltonian (6.1), we discuss subspaces of the Hund's case (a) basis $|\Omega, J, P, F\rangle$ relevant for the excited $A^2\Pi$ states. Mixing between $|\Omega, J, P, F\rangle$ states is restricted to be within subspaces with the same P and F due to parity and angular momentum selection rules. The pure spin-orbit and rotational Hamiltonian, H_{Ω_i, Ω_k} , has diagonal elements,

$$H_{\Omega, \Omega}(J) = (\Omega - 1)A + B[J(J + 1) - 2\Omega + 5/4] + (\Omega - 3/2)\gamma \quad (\text{D.1})$$

and off-diagonals,

$$H_{\frac{1}{2}, \frac{3}{2}}(J) = H_{\frac{3}{2}, \frac{1}{2}}(J) = -(B - \gamma/2) \sqrt{J(J + 1) - 3/4} \quad . \quad (\text{D.2})$$

Each $F = 0, P$ subspace contains a single state and these do not mix. There are three states in a $|\Omega, J, P = \pm, F = 1\rangle$ subspace, and we order these states as $|\Omega, J\rangle = |1/2, 1/2\rangle, |1/2, 3/2\rangle, |3/2, 3/2\rangle$. The combined Hamiltonian $H(F = 1, P = \pm)$, which includes the hyperfine and Λ -doubling interactions, is given by,

$$\left(\begin{array}{ccc} H_{\frac{1}{2}, \frac{1}{2}}\left(\frac{1}{2}\right) \mp \frac{\tilde{p}}{2} + \frac{a}{6} - \frac{\tilde{b}}{12} \mp \frac{d}{6} & h.c. & h.c. \\ -\frac{\sqrt{2}a}{3} + \frac{\tilde{b}}{3\sqrt{2}} \mp \frac{d}{3\sqrt{2}} & H_{\frac{1}{2}, \frac{1}{2}}\left(\frac{3}{2}\right) \pm \tilde{p} - \frac{a}{6} + \frac{\tilde{b}}{12} \mp \frac{d}{3} & h.c. \\ \frac{\tilde{b}}{\sqrt{6}} & H_{\frac{1}{2}, \frac{3}{2}}\left(\frac{3}{2}\right) - \sqrt{3}q - \frac{\tilde{b}}{2\sqrt{3}} & H_{\frac{3}{2}, \frac{3}{2}}\left(\frac{3}{2}\right) - \frac{a}{2} - \frac{\tilde{b}}{4} \end{array} \right), \quad (\text{D.3})$$

Here, $\tilde{b} = b_F + 2c/3$, $\tilde{b} = b_F - c/3$, $\tilde{p} = p + 2q$, and $h.c.$ refers to the Hermitian conjugate. By applying perturbation theory to the Hamiltonian (D.3), mixing of the $|\Omega = 1/2, J = 1/2\rangle$ and $|\Omega = 1/2, J = 3/2\rangle$ states due to the hyperfine inter-

action can be calculated. To second order, the population mixing ζ is,

$$\zeta = 2 \left(\frac{\tilde{b} - d - 2a}{18B - 2a - d + \tilde{b} + 9\tilde{p}} \right)^2 \approx \frac{1}{2} \left(\frac{1\tilde{b} - 2a - d}{3} \frac{1}{3B} \right)^2 \quad (\text{D.4})$$

The resulting loss from the cycling transition due to hyperfine mixing in the excited state, η_A is,

$$\eta_A = \frac{S(\text{P}_{12})}{S(\text{P}_{12}) + S(\text{R}_{12}) + S(\text{Q}_1)} \zeta \quad (\text{D.5})$$

Here, $S(\mathcal{L})$ is the Hönl-London factor for decay from $\Omega = 1/2, J = 3/2$ by transition \mathcal{L} , and we note that only the P₁₂ path results in loss from the $N = 1$ ground states. Using our spectroscopic parameters, the loss probability from $F = 1$ is $\eta_A = 1.2 \times 10^{-6}$. Loss can also occur via mixing with the $|\Omega = 3/2, J = 3/2\rangle$ states, but this is suppressed by about a factor $(A/B)^2$ and we neglect this term. A similar calculation for the ground state can be used to calculate the hyperfine mixing between $N'' = 1$ and $N'' = 3$, and results in a total loss $\eta_X \approx 0.4 \times 10^{-6}$ from the cooling cycle. Therefore, the total loss probability from the $|\Omega = 1/2, J = 1/2, P = +1, F = 1\rangle$ excited states from hyperfine mixing is $\eta = 1.6 \times 10^{-6}$.

To complete our discussion, we consider now the subspaces with $F \geq 2$, each of which contains four states. For $F = 2, P = \pm$, the combined Hamiltonian matrix is

$$\begin{pmatrix} H_{\frac{1}{2}, \frac{1}{2}}(\frac{3}{2}) - \frac{\tilde{b}}{20} \pm \tilde{p} + \frac{a}{10} \pm \frac{d}{5} & h.c. & h.c. & h.c. \\ \frac{1}{5} \sqrt{\frac{3}{2}} \tilde{b} - \frac{\sqrt{6}a}{5} \pm \frac{1}{5} \sqrt{\frac{3}{2}} d & H_{\frac{1}{2}, \frac{1}{2}}(\frac{5}{2}) + \frac{\tilde{b}}{20} \mp \frac{3\tilde{p}}{2} - \frac{a}{10} \pm \frac{3d}{10} & h.c. & h.c. \\ H_{\frac{1}{2}, \frac{3}{2}}(\frac{3}{2}) + \frac{\sqrt{3}\tilde{b}}{10} \mp \sqrt{3}q & -\frac{\tilde{b}}{5\sqrt{2}} & H_{\frac{3}{2}, \frac{3}{2}}(\frac{3}{2}) + \frac{3\tilde{b}}{20} + \frac{3a}{10} & h.c. \\ \frac{\sqrt{3}\tilde{b}}{5} & H_{\frac{1}{2}, \frac{3}{2}}(\frac{5}{2}) - \frac{\sqrt{2}\tilde{b}}{5} \pm 3\sqrt{2}q & -\frac{\tilde{b}}{5} - \frac{2a}{5} & H_{\frac{3}{2}, \frac{3}{2}}(\frac{5}{2}) - \frac{3\tilde{b}}{20} - \frac{3a}{10} \end{pmatrix}, \quad (\text{D.6})$$

where the ordering of states is $|\Omega, J\rangle = |1/2, 3/2\rangle, |1/2, 5/2\rangle, |3/2, 3/2\rangle, |3/2, 5/2\rangle$. The eigenenergies of equation (D.3) and (D.6) are, to first order, the diagonals of the matrices, and can be used to accurately determine $a, \tilde{b}, d, \tilde{p}$. The parameters \tilde{b} and q contribute only as a second order correction to the energies, and appear as terms $\mathcal{O}\left(\frac{\tilde{b}^2}{A}, \frac{q^2}{A}, \frac{B}{A}\tilde{b}, \frac{B}{A}q\right)$ or smaller. As a result, an experiment just capable of resolving \tilde{b} or \tilde{p} would require about two orders of magnitude higher resolution to resolve similar values for \tilde{b} and q , for low- J lines. The off-diagonal matrix elements H_{Ω_i, Ω_k} increase approximately linearly with J , which magnifies the role of the q and $\tilde{b} = b_F - c/3$ parameters as J increases. The role of all 6 parameters will be significant in spectra of high- J lines of MgF.

Appendix E

MgF Linelist

Table E.1: Fitted line positions used for the determination of the spectroscopic constants of the $A^2\Pi$ state, presented in Table 6.3. We show the observed line frequencies, the deviation observed-calculated (o-c) and their assignment. The presence of O- and S-lines with $\Delta J = 2$ is a result of the hyperfine interaction in the ground state, which mixes different J -states and breaks the ($\Delta J = 0, 1$) selection rule. The statistical uncertainty on the individual hyperfine lines is below 1 MHz. On different days, the gravity center of a rotational line is reproducible to within 10 MHz.

Label	Observed (MHz)	o-c	Ω	J'	F'	N''	J''	F''
P ₁₂ (3)	834186158	7	1/2	3/2	1	3	5/2	2
	834186384	6	1/2	3/2	2	3	5/2	3
O ₁ (3)	834186100	3	1/2	3/2	2	3	7/2	3
P ₁ (1)	834294356	1	1/2	1/2	1	1	3/2	2
	834294595	1	1/2	1/2	1	1	3/2	1
	834294595	0	1/2	1/2	0	1	3/2	1
Q ₁₂ (1)	834294485	0	1/2	1/2	1	1	1/2	0
P ₁ (2)	834278982	0	1/2	3/2	2	2	5/2	3
	834279000	-3	1/2	3/2	2	2	5/2	2
	834279038	-2	1/2	3/2	1	2	5/2	2
Q ₁₂ (2)	834279126	-3	1/2	3/2	2	2	3/2	1
	834279167	0	1/2	3/2	1	2	3/2	1
	834279257	3	1/2	3/2	2	2	3/2	2
Q ₁ (0)	834325252	3	1/2	1/2	0	0	1/2	1
	834325426	-4	1/2	1/2	1	0	1/2	1
	834325639	-5	1/2	1/2	1	0	1/2	0
Q ₁ (1)	834341073	-4	1/2	3/2	2	1	3/2	2
	834341204	-6	1/2	3/2	1	1	3/2	1
	834341319	3	1/2	3/2	2	1	3/2	1
R ₁₂ (1)	834340972	-8	1/2	3/2	1	1	1/2	1

Q ₁ (3)	834372660	-2	1/2	7/2	3	3	7/2	3
	834372717	3	1/2	7/2	4	3	7/2	4
R ₁₂ (3)	834372822	-1	1/2	7/2	3	3	5/2	2
	834372939	-4	1/2	7/2	3	3	5/2	3
	834373029	4	1/2	7/2	4	3	5/2	3
R ₁ (0)	834372011	8	1/2	3/2	2	0	1/2	1
	834372047	6	1/2	3/2	1	0	1/2	1
	834372256	1	1/2	3/2	1	0	1/2	0
R ₁ (1)	834418742	1	1/2	5/2	3	1	3/2	2
	834419025	-4	1/2	5/2	2	1	3/2	1
S ₁₂ (1)	834418793	-6	1/2	5/2	2	1	1/2	1
R ₁ (2)	834465601	5	1/2	7/2	4	2	5/2	3
S ₁₂ (2)	834465923	-1	1/2	7/2	3	2	3/2	2
	834465670	-2	1/2	7/2	3	2	5/2	2
Q ₂ (2)	835340294	-8	3/2	3/2	1	2	3/2	1
	835340370	1	3/2	3/2	2	2	3/2	1
	835340428	1	3/2	3/2	1	2	3/2	2
	835340494	0	3/2	3/2	2	2	3/2	2
P ₂₁ (2)	835340215	-6	3/2	3/2	2	2	5/2	3
	835340234	-9	3/2	3/2	2	2	5/2	2
R ₂ (1)	835402172	-1	3/2	3/2	1	1	1/2	1
	835402247	7	3/2	3/2	2	1	1/2	1
	835402296	3	3/2	3/2	1	1	1/2	0
Q ₂₁ (1)	835402162	-2	3/2	3/2	1	1	3/2	2
	835402236	5	3/2	3/2	2	1	3/2	2
	835402405	2	3/2	3/2	1	1	3/2	1
	835402471	0	3/2	3/2	2	1	3/2	1
R ₂ (3)	835439653	7	3/2	7/2	3	3	5/2	2
	835439771	5	3/2	7/2	3	3	5/2	3
	835439802	1	3/2	7/2	4	3	5/2	3
Q ₂₁ (3)	835439488	-1	3/2	7/2	4	3	7/2	4
	835439517	-3	3/2	7/2	4	3	7/2	3
R ₂ (4)	835459901	-5	3/2	9/2	4	4	7/2	3
R ₂₁ (0)	835433178	2	3/2	3/2	1	0	1/2	1
	835433245	2	3/2	3/2	2	0	1/2	1
	835433392	2	3/2	3/2	1	0	1/2	0

Bibliography

- [1] T. Hänsch and A. Schawlow. “Cooling of gases by laser radiation.” In *Optics Communications* **13**(1), (1975), 68–69. doi:10.1016/0030-4018(75)90159-5.
- [2] A. Ashkin. “Trapping of atoms by resonance radiation pressure.” In *Physical Review Letters* **40**(12), (1978), 729–732. doi:10.1103/PhysRevLett.40.729.
- [3] W. Neuhauser, M. Hohenstatt, P. Toschek, and H. Dehmelt. “Optical-sideband cooling of visible atom cloud confined in parabolic well.” In *Physical Review Letters* **41**(4), (1978), 233–236. doi:10.1103/PhysRevLett.41.233.
- [4] D. J. Wineland, R. E. Drullinger, and F. L. Walls. “Radiation-pressure cooling of bound resonant absorbers.” In *Physical Review Letters* **40**(25), (1978), 1639–1642. doi:10.1103/PhysRevLett.40.1639.
- [5] D. J. Wineland. “Nobel Lecture: Superposition, entanglement, and raising Schrödinger’s cat.” In *Reviews of Modern Physics* **85**(3), (2013), 1103–1114. doi:10.1103/RevModPhys.85.1103.
- [6] H. J. Metcalf and P. van der Straten. *Laser Cooling and Trapping*. Graduate Texts in Contemporary Physics. New York: Springer (1999). ISBN 978-0-387-98728-6. doi:10.1007/978-1-4612-1470-0.
- [7] C. S. Adams and E. Riis. “Laser cooling and trapping of neutral atoms.” In *Progress in Quantum Electronics* **21**(1), (1997), 1–79. doi:10.1016/S0079-6727(96)00006-7.
- [8] S. Chu, L. Hollberg, J. E. Bjorkholm, A. Cable, and A. Ashkin. “Three-dimensional viscous confinement and cooling of atoms by resonance radiation pressure.” In *Physical Review Letters* **55**(1), (1985), 48–51. doi:10.1103/PhysRevLett.55.48.
- [9] E. L. Raab, M. Prentiss, A. Cable, S. Chu, and D. E. Pritchard. “Trapping of Neutral Sodium Atoms with Radiation Pressure.” In *Physical Review Letters* **59**(23), (1987), 2631–2634. doi:10.1103/PhysRevLett.59.2631.
- [10] A. Ashkin. “Acceleration and Trapping of Particles by Radiation Pressure.” In *Physical Review Letters* **24**(4), (1970), 156–159. doi:10.1103/PhysRevLett.24.156.

- [11] J. P. Gordon and A. Ashkin. “Motion of atoms in a radiation trap.” In *Physical Review A* **21**(5), (1980), 1606–1617. doi:10.1103/PhysRevA.21.1606.
- [12] S. Chu, J. E. Bjorkholm, A. Ashkin, and A. Cable. “Experimental Observation of Optically Trapped Atoms.” In *Physical Review Letters* **57**(3), (1986), 314–317. doi:10.1103/PhysRevLett.57.314.
- [13] R. Grimm, M. Weidemüller, and Y. B. Ovchinnikov. “Optical Dipole Traps for Neutral Atoms.” In *Advances in Atomic, Molecular and Optical Physics* **42**(C), (2000), 95–170. doi:10.1016/S1049-250X(08)60186-X.
- [14] L. Anderegg, L. W. Cheuk, Y. Bao, S. Burchesky, W. Ketterle, K.-K. Ni, and J. M. Doyle. “An optical tweezer array of ultracold molecules.” In *Science* **365**(6458), (2019), 1156–1158. doi:10.1126/science.aax1265.
- [15] G. Quémener and P. S. Julienne. “Ultracold molecules under control!” In *Chemical Reviews* **112**(9), (2012), 4949–5011. doi:10.1021/cr300092g.
- [16] W. D. Phillips. “Nobel Lecture: Laser cooling and trapping of neutral atoms.” In *Reviews of Modern Physics* **70**(3), (1998), 721–741. doi:10.1103/RevModPhys.70.721.
- [17] T. P. Heavner, E. A. Donley, F. Levi, G. Costanzo, T. E. Parker, J. H. Shirley, N. Ashby, S. Barlow, and S. R. Jefferts. “First accuracy evaluation of NIST-F2.” In *Metrologia* **51**(3), (2014), 174–182. doi:10.1088/0026-1394/51/3/174.
- [18] S. L. Campbell, R. B. Hutson, G. E. Marti, A. Goban, N. Darkwah Oppong, R. L. McNally, L. Sonderhouse, J. M. Robinson, W. Zhang, B. J. Bloom, and J. Ye. “A Fermi-degenerate three-dimensional optical lattice clock.” In *Science* **358**(6359), (2017), 90–94. doi:10.1126/science.aam5538.
- [19] W. B. Cairncross and J. Ye. “Atoms and molecules in the search for time-reversal symmetry violation.” In *Nature Reviews Physics* **1**(8), (2019), 510–521. doi:10.1038/s42254-019-0080-0.
- [20] C. J. Foot. *Atomic Physics*. Oxford: Oxford University Press (2005). ISBN 9780198506959.
- [21] C. Adams, M. Sigel, and J. Mlynek. “Atom optics.” In *Physics Reports* **240**(3), (1994), 143–210. doi:10.1016/0370-1573(94)90066-3.
- [22] F. Richter, D. Becker, C. Bény, T. A. Schulze, S. Ospelkaus, and T. J. Osborne. “Ultracold chemistry and its reaction kinetics.” In *New Journal of Physics* **17**(5), (2015), 055005. doi:10.1088/1367-2630/17/5/055005.
- [23] J. Pérez-Ríos. *An Introduction to Cold and Ultracold Chemistry*. Cham: Springer International Publishing (2020). ISBN 978-3-030-55935-9. doi:10.1007/978-3-030-55936-6.

- [24] B. R. Heazlewood and T. P. Softley. “Towards chemistry at absolute zero.” In *Nature Reviews Chemistry* **5**(2), (2021), 125–140. doi:10.1038/s41570-020-00239-0.
- [25] I. F. Silvera and J. T. M. Walraven. “Stabilization of Atomic Hydrogen at Low Temperature.” In *Physical Review Letters* **44**(3), (1980), 164–168. doi:10.1103/PhysRevLett.44.164.
- [26] V. Bagnato and D. Kleppner. “Bose-Einstein condensation in low-dimensional traps.” In *Physical Review A* **44**(11), (1991), 7439–7441. doi:10.1103/PhysRevA.44.7439.
- [27] I. F. Silvera. “Prospects for Bose-Einstein condensation in atomic hydrogen and other gases.” In *Journal of Low Temperature Physics* **89**(1-2), (1992), 287–296. doi:10.1007/BF00692601.
- [28] I. F. Silvera. “The quest for Bose-Einstein condensation in atomic hydrogen.” In *Journal of Low Temperature Physics* **101**(1-2), (1995), 49–58. doi:10.1007/BF00754561.
- [29] K. B. Davis, M. O. Mewes, M. R. Andrews, N. J. van Druten, D. S. Durfee, D. M. Kurn, and W. Ketterle. “Bose-Einstein Condensation in a Gas of Sodium Atoms.” In *Physical Review Letters* **75**(22), (1995), 3969–3973. doi:10.1103/PhysRevLett.75.3969.
- [30] M. H. Anderson, J. R. Ensher, M. R. Matthews, C. E. Wieman, and E. A. Cornell. “Observation of Bose-Einstein Condensation in a Dilute Atomic Vapor.” In *Science* **269**(5221), (1995), 198–201. doi:10.1126/science.269.5221.198.
- [31] M. A. Norcia, C. Politi, L. Klaus, E. Poli, M. Sohmen, M. J. Mark, R. N. Bisset, L. Santos, and F. Ferlaino. “Two-dimensional supersolidity in a dipolar quantum gas.” In *Nature* **596**(7872), (2021), 357–361. doi:10.1038/s41586-021-03725-7.
- [32] A. E. Leanhardt, T. A. Pasquini, M. Saba, A. Schirotzek, Y. Shin, D. Kielpinski, D. E. Pritchard, and W. Ketterle. “Cooling Bose-Einstein Condensates Below 500 Picokelvin.” In *Science* **301**(5639), (2003), 1513–1515. doi:10.1126/science.1088827.
- [33] T. Kovachy, J. M. Hogan, A. Sugarbaker, S. M. Dickerson, C. A. Donnelly, C. Overstreet, and M. A. Kasevich. “Matter wave lensing to picokelvin temperatures.” In *Physical Review Letters* **114**(14), (2015), 143004. doi:10.1103/PhysRevLett.114.143004.
- [34] C. Deppner, W. Herr, M. Cornelius, P. Stromberger, T. Sternke, C. Grzeschik, A. Grote, J. Rudolph, S. Herrmann, M. Krutzik, A. Wenzlawski, R. Corgier, E. Charron, D. Guéry-Odelin, N. Gaaloul, C. Lämmerzahl, A. Peters, P. Windpassinger, and E. M. Rasel. “Collective-Mode Enhanced Matter-Wave Optics.” In *Physical Review Letters* **127**(10), (2021), 100401. doi:10.1103/PhysRevLett.127.100401.

- [35] M. R. Tarbutt. “Laser cooling of molecules.” In *Contemporary Physics* **59**(4), (2018), 356–376. doi:10.1080/00107514.2018.1576338.
- [36] J. D. Weinstein, R. DeCarvalho, T. Guillet, B. Friedrich, and J. M. Doyle. “Magnetic trapping of calcium monohydride molecules at millikelvin temperatures.” In *Nature* **395**(6698), (1998), 148–150. doi:10.1038/25949.
- [37] H. Bethlem, G. Berden, and G. Meijer. “Decelerating Neutral Dipolar Molecules.” In *Physical Review Letters* **83**(8), (1999), 1558–1561. doi:10.1103/PhysRevLett.83.1558.
- [38] N. Vanhaecke, U. Meier, M. Andrist, B. H. Meier, and F. Merkt. “Multi-stage Zeeman deceleration of hydrogen atoms.” In *Physical Review A* **75**(3), (2007), 031402. doi:10.1103/PhysRevA.75.031402.
- [39] E. Narevicius, A. Libson, C. G. Parthey, I. Chavez, J. Narevicius, U. Even, and M. G. Raizen. “Stopping Supersonic Beams with a Series of Pulsed Electromagnetic Coils: An Atomic Coilgun.” In *Physical Review Letters* **100**(9), (2008), 093003. doi:10.1103/PhysRevLett.100.093003.
- [40] E. Narevicius, A. Libson, C. G. Parthey, I. Chavez, J. Narevicius, U. Even, and M. G. Raizen. “Stopping supersonic oxygen with a series of pulsed electromagnetic coils: A molecular coilgun.” In *Physical Review A* **77**(5), (2008), 051401. doi:10.1103/PhysRevA.77.051401.
- [41] S. Y. T. van de Meerakker, H. L. Bethlem, N. Vanhaecke, and G. Meijer. “Manipulation and Control of Molecular Beams.” In *Chemical Reviews* **112**(9), (2012), 4828–4878. doi:10.1021/cr200349r.
- [42] A. N. Nikolov, J. R. Ensher, E. E. Eyler, H. Wang, W. C. Stwalley, and P. L. Gould. “Efficient Production of Ground-State Potassium Molecules at Sub-mK Temperatures by Two-Step Photoassociation.” In *Physical Review Letters* **84**(2), (2000), 246–249. doi:10.1103/PhysRevLett.84.246.
- [43] A. J. Kerman, J. M. Sage, S. Sainis, T. Bergeman, and D. DeMille. “Production and State-Selective Detection of Ultracold RbCs Molecules.” In *Physical Review Letters* **92**(15), (2004), 153001. doi:10.1103/PhysRevLett.92.153001.
- [44] K. M. Jones, E. Tiesinga, P. D. Lett, and P. S. Julienne. “Ultracold photoassociation spectroscopy: Long-range molecules and atomic scattering.” In *Reviews of Modern Physics* **78**(2), (2006), 483–535. doi:10.1103/RevModPhys.78.483.
- [45] C. P. Koch and M. Shapiro. “Coherent Control of Ultracold Photoassociation.” In *Chemical Reviews* **112**(9), (2012), 4928–4948. doi:10.1021/cr2003882.
- [46] T. Köhler, K. Góral, and P. S. Julienne. “Production of cold molecules via magnetically tunable Feshbach resonances.” In *Reviews of Modern Physics* **78**(4), (2006), 1311–1361. doi:10.1103/RevModPhys.78.1311.

- [47] J. M. Sage, S. Sainis, T. Bergeman, and D. DeMille. “Optical Production of Ultracold Polar Molecules.” In *Physical Review Letters* **94**(20), (2005), 203001. doi:10.1103/PhysRevLett.94.203001.
- [48] C. Ospelkaus, S. Ospelkaus, L. Humbert, P. Ernst, K. Sengstock, and K. Bongs. “Ultracold Heteronuclear Molecules in a 3D Optical Lattice.” In *Physical Review Letters* **97**(12), (2006), 120402. doi:10.1103/PhysRevLett.97.120402.
- [49] C. Weber, G. Barontini, J. Catani, G. Thalhammer, M. Inguscio, and F. Minardi. “Association of ultracold double-species bosonic molecules.” In *Physical Review A* **78**(6), (2008), 061601. doi:10.1103/PhysRevA.78.061601.
- [50] K.-K. Ni, S. Ospelkaus, M. H. G. de Miranda, A. Pe’er, B. Neyenhuis, J. J. Zirbel, S. Kotochigova, P. S. Julienne, D. S. Jin, and J. Ye. “A High Phase-Space-Density Gas of Polar Molecules.” In *Science* **322**(5899), (2008), 231–235. doi:10.1126/science.1163861.
- [51] J. Deiglmayr, A. Grochola, M. Repp, K. Mörzlbauer, C. Glück, J. Lange, O. Dulieu, R. Wester, and M. Weidemüller. “Formation of Ultracold Polar Molecules in the Rovibrational Ground State.” In *Physical Review Letters* **101**(13), (2008), 133004. doi:10.1103/PhysRevLett.101.133004.
- [52] M. Viteau, A. Chotia, M. Allegrini, N. Bouloufa, O. Dulieu, D. Comparat, and P. Pillet. “Optical pumping and vibrational cooling of molecules.” In *Science* **321**(5886), (2008), 232–234. doi:10.1126/science.1159496.
- [53] C. Haimberger, J. Kleinert, P. Zabawa, A. Wakim, and N. P. Bigelow. “Formation of ultracold, highly polar $X^1\Sigma^+$ NaCs molecules.” In *New Journal of Physics* **11**(5), (2009), 055042. doi:10.1088/1367-2630/11/5/055042.
- [54] A.-C. Voigt, M. Taglieber, L. Costa, T. Aoki, W. Wieser, T. W. Hänsch, and K. Dieckmann. “Ultracold Heteronuclear Fermi-Fermi Molecules.” In *Physical Review Letters* **102**(2), (2009), 020405. doi:10.1103/PhysRevLett.102.020405.
- [55] C.-H. Wu, J. W. Park, P. Ahmadi, S. Will, and M. W. Zwierlein. “Ultracold Fermionic Feshbach Molecules of $^{23}\text{Na}^{40}\text{K}$.” In *Physical Review Letters* **109**(8), (2012), 085301. doi:10.1103/PhysRevLett.109.085301.
- [56] M.-S. Heo, T. T. Wang, C. A. Christensen, T. M. Rvachov, D. A. Cotta, J.-H. Choi, Y.-R. Lee, and W. Ketterle. “Formation of ultracold fermionic NaLi Feshbach molecules.” In *Physical Review A* **86**(2), (2012), 021602. doi:10.1103/PhysRevA.86.021602.
- [57] F. Wang, X. He, X. Li, B. Zhu, J. Chen, and D. Wang. “Formation of ultracold NaRb Feshbach molecules.” In *New Journal of Physics* **17**(3), (2015), 035003. doi:10.1088/1367-2630/17/3/035003.

- [58] M. D. Di Rosa. “Laser-cooling molecules: Concept, candidates, and supporting hyperfine-resolved measurements of rotational lines in the A-X(0,0) band of CaH.” In *European Physical Journal D* **31**(2), (2004), 395–402. doi:10.1140/epjd/e2004-00167-2.
- [59] B. K. Stuhl, B. C. Sawyer, D. Wang, and J. Ye. “Magneto-optical Trap for Polar Molecules.” In *Physical Review Letters* **101**(24), (2008), 243002. doi:10.1103/PhysRevLett.101.243002.
- [60] E. S. Shuman, J. F. Barry, D. R. Glenn, and D. DeMille. “Radiative Force from Optical Cycling on a Diatomic Molecule.” In *Physical Review Letters* **103**(22), (2009), 223001. doi:10.1103/PhysRevLett.103.223001.
- [61] E. S. Shuman, J. F. Barry, and D. DeMille. “Laser cooling of a diatomic molecule.” In *Nature* **467**(7317), (2010), 820–823. doi:10.1038/nature09443.
- [62] M. T. Hummon, M. Yeo, B. K. Stuhl, A. L. Collopy, Y. Xia, and J. Ye. “2D Magneto-Optical Trapping of Diatomic Molecules.” In *Physical Review Letters* **110**(14), (2013), 143001. doi:10.1103/PhysRevLett.110.143001.
- [63] V. Zhelyazkova, A. Cournol, T. E. Wall, A. Matsushima, J. J. Hudson, E. A. Hinds, M. R. Tarbutt, and B. E. Sauer. “Laser cooling and slowing of CaF molecules.” In *Physical Review A* **89**(5), (2014), 053416. doi:10.1103/PhysRevA.89.053416.
- [64] J. Lim, J. R. Almond, M. A. Trigatzis, J. A. Devlin, N. J. Fitch, B. E. Sauer, M. R. Tarbutt, and E. A. Hinds. “Laser Cooled YbF Molecules for Measuring the Electron’s Electric Dipole Moment.” In *Physical Review Letters* **120**(12), (2018), 123201. doi:10.1103/PhysRevLett.120.123201.
- [65] I. Kozyryev, L. Baum, K. Matsuda, B. L. Augenbraun, L. Anderegg, A. P. Sedlack, and J. M. Doyle. “Sisyphus Laser Cooling of a Polyatomic Molecule.” In *Physical Review Letters* **118**(17), (2017), 173201. doi:10.1103/PhysRevLett.118.173201.
- [66] B. L. Augenbraun, Z. D. Lasner, A. Frenett, H. Sawaoka, C. Miller, T. C. Steimle, and J. M. Doyle. “Laser-cooled polyatomic molecules for improved electron electric dipole moment searches.” In *New Journal of Physics* **22**(2), (2020), 022003. doi:10.1088/1367-2630/ab687b.
- [67] D. Mitra, N. B. Vilas, C. Hallas, L. Anderegg, B. L. Augenbraun, L. Baum, C. Miller, S. Raval, and J. M. Doyle. “Direct laser cooling of a symmetric top molecule.” In *Science* **369**(6509), (2020), 1366–1369. doi:10.1126/science.abc5357.
- [68] J. F. Barry, D. J. McCarron, E. B. Norrgard, M. H. Steinecker, and D. DeMille. “Magneto-optical trapping of a diatomic molecule.” In *Nature* **512**(7514), (2014), 286–289. doi:10.1038/nature13634.

- [69] H. J. Williams, S. Truppe, M. Hambach, L. Caldwell, N. J. Fitch, E. A. Hinds, B. E. Sauer, and M. R. Tarbutt. “Characteristics of a magneto-optical trap of molecules.” In *New Journal of Physics* **19**(11), (2017), 113035. doi:10.1088/1367-2630/aa8e52.
- [70] L. Anderegg, B. L. Augenbraun, E. Chae, B. Hemmerling, N. R. Hutzler, A. Ravi, A. Collopy, J. Ye, W. Ketterle, and J. M. Doyle. “Radio Frequency Magneto-Optical Trapping of CaF with High Density.” In *Physical Review Letters* **119**(10), (2017), 103201. doi:10.1103/PhysRevLett.119.103201.
- [71] A. L. Collopy, S. Ding, Y. Wu, I. A. Finneran, L. Anderegg, B. L. Augenbraun, J. M. Doyle, and J. Ye. “3D Magneto-Optical Trap of Yttrium Monoxide.” In *Physical Review Letters* **121**(21), (2018), 213201. doi:10.1103/PhysRevLett.121.213201.
- [72] N. B. Vilas, C. Hallas, L. Anderegg, P. Robichaud, A. Winnicki, D. Mitra, and J. M. Doyle. “Magneto-optical trapping and sub-Doppler cooling of a polyatomic molecule.” In *Nature* **606**(7912), (2022), 70–74. doi:10.1038/s41586-022-04620-5.
- [73] L. Xu, Y. Yin, B. Wei, Y. Xia, and J. Yin. “Calculation of vibrational branching ratios and hyperfine structure of $^{24}\text{Mg}^{19}\text{F}$ and its suitability for laser cooling and magneto-optical trapping.” In *Physical Review A* **93**(1), (2016), 013408. doi:10.1103/PhysRevA.93.013408.
- [74] T. Chen, W. Bu, and B. Yan. “Radiative deflection of a BaF molecular beam via optical cycling.” In *Physical Review A* **96**(5), (2017), 053401. doi:10.1103/PhysRevA.96.053401.
- [75] G. Z. Iwata, R. L. McNally, and T. Zelevinsky. “High-resolution optical spectroscopy with a buffer-gas-cooled beam of BaH molecules.” In *Physical Review A* **96**(2), (2017), 022509. doi:10.1103/PhysRevA.96.022509.
- [76] E. B. Norrgard, E. R. Edwards, D. J. McCarron, M. H. Steinecker, D. DeMille, S. S. Alam, S. K. Peck, N. S. Wadia, and L. R. Hunter. “Hyperfine structure of the $B^3\Pi_1$ state and predictions of optical cycling behavior in the $X \rightarrow B$ transition of TIF.” In *Physical Review A* **95**(6), (2017), 062506. doi:10.1103/PhysRevA.95.062506.
- [77] T. N. Lewis, C. Wang, J. R. Daniel, M. Dhital, C. J. Bardeen, and B. Hemmerling. “Optimizing pulsed-laser ablation production of AlCl molecules for laser cooling.” In *Physical Chemistry Chemical Physics* **23**(39), (2021), 22785–22793. doi:10.1039/D1CP03515K.
- [78] B. L. Augenbraun, Z. D. Lasner, A. Frenett, H. Sawaoka, A. T. Le, J. M. Doyle, and T. C. Steimle. “Observation and laser spectroscopy of ytterbium monomethoxide, YbOCH_3 .” In *Physical Review A* **103**(2), (2021), 022814. doi:10.1103/PhysRevA.103.022814.

- [79] R. F. Garcia Ruiz, R. Berger, J. Billowes, C. L. Binnersley, M. L. Bissell, A. A. Breier, A. J. Brinson, K. Chrysalidis, T. E. Cocolios, B. S. Cooper, K. T. Flanagan, T. F. Giesen, R. P. de Groote, S. Franchoo, F. P. Gustafsson, T. A. Isaev, Á. Koszorús, G. Neyens, H. A. Perrett, C. M. Ricketts, S. Rothe, L. Schweikhard, A. R. Vernon, K. D. Wendt, F. Wienholtz, S. G. Wilkins, and X. F. Yang. “Spectroscopy of short-lived radioactive molecules.” In *Nature* **581**(7809), (2020), 396–400. doi:10.1038/s41586-020-2299-4.
- [80] S. M. Udrescu, A. J. Brinson, R. F. G. Ruiz, K. Gaul, R. Berger, J. Billowes, C. L. Binnersley, M. L. Bissell, A. A. Breier, K. Chrysalidis, T. E. Cocolios, B. S. Cooper, K. T. Flanagan, T. F. Giesen, R. P. de Groote, S. Franchoo, F. P. Gustafsson, T. A. Isaev, Á. Koszorús, G. Neyens, H. A. Perrett, C. M. Ricketts, S. Rothe, A. R. Vernon, K. D. A. Wendt, F. Wienholtz, S. G. Wilkins, and X. F. Yang. “Isotope Shifts of Radium Monofluoride Molecules.” In *Physical Review Letters* **127**(3), (2021), 033001. doi:10.1103/PhysRevLett.127.033001.
- [81] I. C. Lane. “Ultracold fluorine production via Doppler cooled BeF.” In *Physical Chemistry Chemical Physics* **14**(43), (2012), 15078–15087. doi:10.1039/c2cp42709e.
- [82] R. Mitra, V. S. Prasanna, B. K. Sahoo, N. R. Hutzler, M. Abe, and B. P. Das. “Study of HgOH to Assess Its Suitability for Electron Electric Dipole Moment Searches.” In *Atoms* **9**(1), (2021), 7. doi:10.3390/atoms9010007.
- [83] M. Li, J. Klos, A. Petrov, and S. Kotochigova. “Emulating optical cycling centers in polyatomic molecules.” In *Communications Physics* **2**(1), (2019), 148. doi:10.1038/s42005-019-0245-2.
- [84] J. Klos and S. Kotochigova. “Prospects for laser cooling of polyatomic molecules with increasing complexity.” In *Physical Review Research* **2**(1), (2020), 013384. doi:10.1103/PhysRevResearch.2.013384.
- [85] C. E. Dickerson, H. Guo, G.-Z. Zhu, E. R. Hudson, J. R. Caram, W. C. Campbell, and A. N. Alexandrova. “Optical Cycling Functionalization of Arenes.” In *The Journal of Physical Chemistry Letters* **12**(16), (2021), 3989–3995. doi:10.1021/acs.jpcllett.1c00733.
- [86] D. Mitra, Z. D. Lasner, G.-Z. Zhu, C. E. Dickerson, B. L. Augenbraun, A. D. Bailey, A. N. Alexandrova, W. C. Campbell, J. R. Caram, E. R. Hudson, and J. M. Doyle. “Pathway Towards Optical Cycling and Laser Cooling of Functionalized Arenes.” (2022). doi:10.48550/ARXIV.2202.01685.
- [87] G.-Z. Zhu, D. Mitra, B. L. Augenbraun, C. E. Dickerson, M. J. Frim, G. Lao, Z. D. Lasner, A. N. Alexandrova, W. C. Campbell, J. R. Caram, J. M. Doyle, and E. R. Hudson. “Functionalizing Aromatic Compounds with Optical Cycling Centers.” (2022). doi:10.48550/ARXIV.2202.01881.

- [88] S. Hofsäss, M. Doppelbauer, S. C. Wright, S. Kray, B. G. Sartakov, J. Pérez-Ríos, G. Meijer, and S. Truppe. “Optical cycling of AlF molecules.” In *New Journal of Physics* **23**(7), (2021), 075001. doi:10.1088/1367-2630/ac06e5.
- [89] L. De Marco, G. Valtolina, K. Matsuda, W. G. Tobias, J. P. Covey, and J. Ye. “A degenerate Fermi gas of polar molecules.” In *Science* **363**(6429), (2019), 853–856. doi:10.1126/science.aau7230.
- [90] L. D. Carr, D. DeMille, R. V. Krems, and J. Ye. “Cold and ultracold molecules: Science, technology and applications.” In *New Journal of Physics* **11**, (2009), 055049–055087. doi:10.1088/1367-2630/11/5/055049.
- [91] R. V. Krems. “Molecules near absolute zero and external field control of atomic and molecular dynamics.” In *International Reviews in Physical Chemistry* **24**(1), (2005), 99–118. doi:10.1080/01442350500167161.
- [92] R. V. Krems. “Cold controlled chemistry.” In *Physical Chemistry Chemical Physics* **10**(28), (2008), 4079. doi:10.1039/b802322k.
- [93] S. Ospelkaus, K.-K. Ni, D. Wang, M. H. G. de Miranda, B. Neyenhuis, G. Quémener, P. S. Julienne, J. L. Bohn, D. S. Jin, and J. Ye. “Quantum-State Controlled Chemical Reactions of Ultracold Potassium-Rubidium Molecules.” In *Science* **327**(5967), (2010), 853–857. doi:10.1126/science.1184121.
- [94] K.-K. Ni, S. Ospelkaus, D. Wang, G. Quémener, B. Neyenhuis, M. H. G. de Miranda, J. L. Bohn, J. Ye, and D. S. Jin. “Dipolar collisions of polar molecules in the quantum regime.” In *Nature* **464**(7293), (2010), 1324–1328. doi:10.1038/nature08953.
- [95] M. G. Hu, Y. Liu, D. D. Grimes, Y. W. Lin, A. H. Gheorghe, R. Vexiau, N. Bouloufa-Maafa, O. Dulieu, T. Rosenband, and K.-K. Ni. “Direct observation of bimolecular reactions of ultracold KRb molecules.” In *Science* **366**(6469), (2019), 1111–1115. doi:10.1126/science.aay9531.
- [96] L. W. Cheuk, L. Anderegg, Y. Bao, S. Burchesky, S. S. Yu, W. Ketterle, K.-K. Ni, and J. M. Doyle. “Observation of collisions between two ultracold ground-state CaF molecules.” In *Physical Review Letters* **125**(4), (2020), 43401. doi:10.1103/PhysRevLett.125.043401.
- [97] S. Jurgilas, A. Chakraborty, C. J. H. Rich, B. E. Sauer, M. D. Frye, J. M. Hutson, and M. R. Tarbutt. “Collisions in a dual-species magneto-optical trap of molecules and atoms.” In *New Journal of Physics* **23**(7), (2021), 075004. doi:10.1088/1367-2630/ac0c9a.
- [98] S. Jurgilas, A. Chakraborty, C. J. H. Rich, L. Caldwell, H. J. Williams, N. J. Fitch, B. E. Sauer, M. D. Frye, J. M. Hutson, and M. R. Tarbutt. “Collisions between Ultracold Molecules and Atoms in a Magnetic Trap.” In *Physical Review Letters* **126**(15), (2021), 153401. doi:10.1103/PhysRevLett.126.153401.

- [99] Y. Segev, M. Pitzer, M. Karpov, N. Akerman, J. Narevicius, and E. Narevicius. “Collisions between cold molecules in a superconducting magnetic trap.” In *Nature* **572**(7768), (2019), 189–193. doi:10.1038/s41586-019-1446-2.
- [100] J. J. Gilijamse, S. Hoekstra, S. Y. T. van de Meerakker, G. C. Groenenboom, and G. Meijer. “Near-Threshold Inelastic Collisions Using Molecular Beams with a Tunable Velocity.” In *Science* **313**(5793), (2006), 1617–1620. doi:10.1126/science.1131867.
- [101] S. Y. T. van de Meerakker and G. Meijer. “Collision experiments with Stark-decelerated beams.” In *Faraday Discussions* **142**, (2009), 113. doi:10.1039/b819721k.
- [102] T. de Jongh, M. Besemer, Q. Shuai, T. Karman, A. van der Avoird, G. C. Groenenboom, and S. Y. van de Meerakker. “Imaging the onset of the resonance regime in low-energy NO-He collisions.” In *Science* **368**(6491), (2020), 626–630. doi:10.1126/science.aba3990.
- [103] T. de Jongh, Q. Shuai, G. L. Abma, S. Kuijpers, M. Besemer, A. van der Avoird, G. C. Groenenboom, and S. Y. T. van de Meerakker. “Mapping partial wave dynamics in scattering resonances by rotational de-excitation collisions.” In *Nature Chemistry* **14**(5), (2022), 538–544. doi:10.1038/s41557-022-00896-2.
- [104] S. Willitsch, M. T. Bell, A. D. Gingell, S. R. Procter, and T. P. Softley. “Cold Reactive Collisions between Laser-Cooled Ions and Velocity-Selected Neutral Molecules.” In *Physical Review Letters* **100**(4), (2008), 043203. doi:10.1103/PhysRevLett.100.043203.
- [105] M. T. Bell, A. D. Gingell, J. M. Oldham, T. P. Softley, and S. Willitsch. “Ion-molecule chemistry at very low temperatures: cold chemical reactions between Coulomb-crystallized ions and velocity-selected neutral molecules.” In *Faraday Discussions* **142**, (2009), 73. doi:10.1039/b818733a.
- [106] A. D. Gingell, M. T. Bell, J. M. Oldham, T. P. Softley, and J. N. Harvey. “Cold chemistry with electronically excited Ca^+ Coulomb crystals.” In *The Journal of Chemical Physics* **133**(19), (2010), 194302. doi:10.1063/1.3505142.
- [107] D. DeMille, J. M. Doyle, and A. O. Sushkov. “Probing the frontiers of particle physics with tabletop-scale experiments.” In *Science* **357**(6355), (2017), 990–994. doi:10.1126/science.aal3003.
- [108] M. S. Safronova, D. Budker, D. Demille, D. F. Kimball, A. Derevianko, and C. W. Clark. “Search for new physics with atoms and molecules.” In *Reviews of Modern Physics* **90**(2), (2018), 25008. doi:10.1103/RevModPhys.90.025008.

- [109] W. B. Cairncross, D. N. Gresh, M. Grau, K. C. Cossel, T. S. Roussy, Y. Ni, Y. Zhou, J. Ye, and E. A. Cornell. “Precision Measurement of the Electron’s Electric Dipole Moment Using Trapped Molecular Ions.” In *Physical Review Letters* **119**(15), (2017), 153001. doi:10.1103/PhysRevLett.119.153001.
- [110] J. J. Hudson, D. M. Kara, I. J. Smallman, B. E. Sauer, M. R. Tarbutt, and E. A. Hinds. “Improved measurement of the shape of the electron.” In *Nature* **473**(7348), (2011), 493–496. doi:10.1038/nature10104.
- [111] J. Baron, W. C. Campbell, D. DeMille, J. M. Doyle, G. Gabrielse, Y. V. Gurevich, P. W. Hess, N. R. Hutzler, E. Kirilov, I. Kozyryev, B. R. O’Leary, C. D. Panda, M. F. Parsons, E. S. Petrik, B. Spaun, A. C. Vutha, and A. D. West. “Order of Magnitude Smaller Limit on the Electric Dipole Moment of the Electron.” In *Science* **343**(6168), (2014), 269–272. doi:10.1126/science.1248213.
- [112] V. Andreev, D. G. Ang, D. DeMille, J. M. Doyle, G. Gabrielse, J. Haefner, N. R. Hutzler, Z. Lasner, C. Meisenhelder, B. R. O’Leary, C. D. Panda, A. D. West, E. P. West, and X. Wu. “Improved limit on the electric dipole moment of the electron.” In *Nature* **562**(7727), (2018), 355–360. doi:10.1038/s41586-018-0599-8.
- [113] P. Aggarwal, H. L. Bethlem, A. Borschevsky, M. Denis, K. Esajas, P. A. B. Haase, Y. Hao, S. Hoekstra, K. Jungmann, T. B. Meijknecht, M. C. Mooij, R. G. E. Timmermans, W. Ubachs, L. Willmann, and A. Zapara. “Measuring the electric dipole moment of the electron in BaF.” In *The European Physical Journal D* **72**(11), (2018), 197. doi:10.1140/epjd/e2018-90192-9.
- [114] N. R. Hutzler. “Polyatomic molecules as quantum sensors for fundamental physics.” In *Quantum Science and Technology* **5**(4), (2020), 044011. doi:10.1088/2058-9565/abb9c5.
- [115] I. Kozyryev, L. Baum, K. Matsuda, and J. M. Doyle. “Proposal for Laser Cooling of Complex Polyatomic Molecules.” In *ChemPhysChem* **17**(22), (2016), 3641–3648. doi:10.1002/cphc.201601051.
- [116] I. Kozyryev and N. R. Hutzler. “Precision Measurement of Time-Reversal Symmetry Violation with Laser-Cooled Polyatomic Molecules.” In *Physical Review Letters* **119**(13), (2017), 133002. doi:10.1103/PhysRevLett.119.133002.
- [117] T. A. Isaev, S. Hoekstra, and R. Berger. “Laser-cooled RaF as a promising candidate to measure molecular parity violation.” In *Physical Review A* **82**(5), (2010), 052521. doi:10.1103/PhysRevA.82.052521.
- [118] T. A. Isaev, A. V. Zaitsevskii, and E. Eliav. “Laser-coolable polyatomic molecules with heavy nuclei.” In *Journal of Physics B: Atomic, Molecular and Optical Physics* **50**(22), (2017), 225101. doi:10.1088/1361-6455/aa8f34.

- [119] P. Yu and N. R. Hutzler. “Probing Fundamental Symmetries of Deformed Nuclei in Symmetric Top Molecules.” In *Physical Review Letters* **126**(2), (2021), 023003. doi:10.1103/PhysRevLett.126.023003.
- [120] J. Veldhoven, J. Küpper, H. L. Bethlem, B. Sartakov, A. J. A. Roij, and G. Meijer. “Decelerated molecular beams for high-resolution spectroscopy.” In *The European Physical Journal D* **31**(2), (2004), 337–349. doi:10.1140/epjd/e2004-00160-9.
- [121] E. R. Hudson, H. J. Lewandowski, B. C. Sawyer, and J. Ye. “Cold Molecule Spectroscopy for Constraining the Evolution of the Fine Structure Constant.” In *Physical Review Letters* **96**(14), (2006), 143004. doi:10.1103/PhysRevLett.96.143004.
- [122] S. Truppe, R. Hendricks, S. Tokunaga, H. Lewandowski, M. Kozlov, C. Henkel, E. Hinds, and M. Tarbutt. “A search for varying fundamental constants using hertz-level frequency measurements of cold CH molecules.” In *Nature Communications* **4**(1), (2013), 2600. doi:10.1038/ncomms3600.
- [123] G. Barontini, L. Blackburn, V. Boyer, F. Butuc-Mayer, X. Calmet, J. R. Crespo López-Urrutia, E. A. Curtis, B. Darquié, J. Dunningham, N. J. Fitch, E. M. Forgan, K. Georgiou, P. Gill, R. M. Godun, J. Goldwin, V. Guarrera, A. C. Harwood, I. R. Hill, R. J. Hendricks, M. Jeong, M. Y. H. Johnson, M. Keller, L. P. Kozhiparambil Sajith, F. Kuipers, H. S. Margolis, C. Mayo, P. Newman, A. O. Parsons, L. Prokhorov, B. I. Robertson, J. Rodewald, M. S. Safronova, B. E. Sauer, M. Schioppo, N. Sherrill, Y. V. Stadnik, K. Szymaniec, M. R. Tarbutt, R. C. Thompson, A. Tofful, J. Tunesi, A. Vecchio, Y. Wang, and S. Worm. “Measuring the stability of fundamental constants with a network of clocks.” In *EPJ Quantum Technology* **9**(1), (2022), 12. doi:10.1140/epjqt/s40507-022-00130-5.
- [124] M. Duda, X.-Y. Chen, A. Schindewolf, R. Bause, J. von Milczewski, R. Schmidt, I. Bloch, and X.-Y. Luo. “Transition from a polaronic condensate to a degenerate Fermi gas of heteronuclear molecules.” (2021). doi:10.48550/ARXIV.2111.04301.
- [125] J. Stuhler, A. Griesmaier, T. Koch, M. Fattori, T. Pfau, S. Giovanazzi, P. Pedri, and L. Santos. “Observation of Dipole-Dipole Interaction in a Degenerate Quantum Gas.” In *Physical Review Letters* **95**(15), (2005), 150406. doi:10.1103/PhysRevLett.95.150406.
- [126] T. Lahaye, C. Menotti, L. Santos, M. Lewenstein, and T. Pfau. “The physics of dipolar bosonic quantum gases.” In *Reports on Progress in Physics* **72**(12), (2009), 126401. doi:10.1088/0034-4885/72/12/126401.
- [127] M. Schmitt, M. Wenzel, F. Böttcher, I. Ferrier-Barbut, and T. Pfau. “Self-bound droplets of a dilute magnetic quantum liquid.” In *Nature* **539**(7628), (2016), 259–262. doi:10.1038/nature20126.

- [128] A. Micheli, G. K. Brennen, and P. Zoller. “A toolbox for lattice-spin models with polar molecules.” In *Nature Physics* **2**(5), (2006), 341–347. doi:10.1038/nphys287.
- [129] R. Barnett, D. Petrov, M. Lukin, and E. Demler. “Quantum magnetism with multicomponent dipolar molecules in an optical lattice.” In *Physical Review Letters* **96**(19), (2006), 3–6. doi:10.1103/PhysRevLett.96.190401.
- [130] H. P. Büchler, E. Demler, M. Lukin, A. Micheli, N. Prokof’ev, G. Pupillo, and P. Zoller. “Strongly correlated 2D quantum phases with cold polar molecules: Controlling the shape of the interaction potential.” In *Physical Review Letters* **98**(6), (2007), 060404. doi:10.1103/PhysRevLett.98.060404.
- [131] A. V. Gorshkov, S. R. Manmana, G. Chen, J. Ye, E. Demler, M. D. Lukin, and A. M. Rey. “Tunable superfluidity and quantum magnetism with ultracold polar molecules.” In *Physical Review Letters* **107**(11), (2011), 115301. doi:10.1103/PhysRevLett.107.115301.
- [132] B. Yan, S. A. Moses, B. Gadway, J. P. Covey, K. R. Hazzard, A. M. Rey, D. S. Jin, and J. Ye. “Observation of dipolar spin-exchange interactions with lattice-confined polar molecules.” In *Nature* **501**(7468), (2013), 521–525. doi:10.1038/nature12483.
- [133] S. A. Moses, J. P. Covey, M. T. Miecnikowski, D. S. Jin, and J. Ye. “New frontiers for quantum gases of polar molecules.” In *Nature Physics* **13**(1), (2017), 13–20. doi:10.1038/nphys3985.
- [134] R. Sawant, L. Caldwell, J. Aldegunde, D. Jaksch, P. D. Gregory, J. Mur-Petit, M. R. Tarbutt, J. M. Hutson, E. M. Bridge, B. E. Sauer, J. A. Blackmore, and S. L. Cornish. “Ultracold molecules for quantum simulation: rotational coherences in CaF and RbCs.” In *Quantum Science and Technology* **4**(1), (2018), 014010. doi:10.1088/2058-9565/aace35.
- [135] J. A. Blackmore, L. Caldwell, P. D. Gregory, E. M. Bridge, R. Sawant, J. Aldegunde, J. Mur-Petit, D. Jaksch, J. M. Hutson, B. E. Sauer, M. R. Tarbutt, and S. L. Cornish. “Ultracold molecules for quantum simulation: rotational coherences in CaF and RbCs.” In *Quantum Science and Technology* **4**(1), (2018), 014010. doi:10.1088/2058-9565/aace35.
- [136] D. DeMille. “Quantum Computation with Trapped Polar Molecules.” In *Physical Review Letters* **88**(6), (2002), 067901. doi:10.1103/PhysRevLett.88.067901.
- [137] S. F. Yelin, K. Kirby, and R. Côté. “Schemes for robust quantum computation with polar molecules.” In *Physical Review A* **74**(5), (2006), 050301. doi:10.1103/PhysRevA.74.050301.
- [138] A. André, D. DeMille, J. M. Doyle, M. D. Lukin, S. E. Maxwell, P. Rabl, R. J. Schoelkopf, and P. Zoller. “A coherent all-electrical interface between polar molecules and mesoscopic superconducting resonators.” In *Nature Physics* **2**(9), (2006), 636–642. doi:10.1038/nphys386.

- [139] R. Sawant, J. A. Blackmore, P. D. Gregory, J. Mur-Petit, D. Jaksch, J. Aldegunde, J. M. Hutson, M. R. Tarbutt, and S. L. Cornish. “Ultracold polar molecules as qudits.” In *New Journal of Physics* **22**(1), (2020), 013027. doi:10.1088/1367-2630/ab60f4.
- [140] H. C. Ko, M. A. Greenbaum, J. A. Blauer, and M. Farber. “The Enthalpy of Formation and Entropy of Aluminum(I) Fluoride(g).” In *The Journal of Physical Chemistry* **69**(7), (1965), 2311–2316. doi:10.1021/j100891a030.
- [141] S. R. Langhoff, C. W. Bauschlicher, and P. R. Taylor. “Theoretical studies of AlF, AlCl, and AlBr.” In *The Journal of Chemical Physics* **88**(9), (1988), 5715–5725. doi:10.1063/1.454531.
- [142] N. Wells and I. C. Lane. “Electronic states and spin-forbidden cooling transitions of AlH and AlF.” In *Physical Chemistry Chemical Physics* **13**(42), (2011), 19018–19025. doi:10.1039/c1cp21313j.
- [143] R. J. Le Roy. “RKR1: A computer program implementing the first-order RKR method for determining diatomic molecule potential energy functions.” In *Journal of Quantitative Spectroscopy and Radiative Transfer* **186**, (2017), 158–166. doi:10.1016/j.jqsrt.2016.03.030.
- [144] R. F. Barrow, I. Kopp, and C. Malmberg. “The electronic spectrum of gaseous AlF.” In *Physica Scripta* **10**(1-2), (1974), 86–102. doi:10.1088/0031-8949/10/1-2/008.
- [145] M. Yousefi and P. F. Bernath. “Line Lists for AlF and AlCl in the $X^1\Sigma^+$ Ground State.” In *The Astrophysical Journal Supplement Series* **237**(1), (2018), 8. doi:10.3847/1538-4365/aacc6a.
- [146] G. Grynberg and J.-Y. Courtois. “Proposal for a Magneto-Optical Lattice for Trapping Atoms in Nearly-Dark States.” In *Europhysics Letters (EPL)* **27**(1), (1994), 41–46. doi:10.1209/0295-5075/27/1/008.
- [147] D. Boiron, C. Triché, D. R. Meacher, P. Verkerk, and G. Grynberg. “Three-dimensional cooling of cesium atoms in four-beam gray optical molasses.” In *Physical Review A* **52**(5), (1995), R3425–R3428. doi:10.1103/PhysRevA.52.R3425.
- [148] D. Rio Fernandes, F. Sievers, N. Kretzschmar, S. Wu, C. Salomon, and F. Chevy. “Sub-Doppler laser cooling of fermionic 40 K atoms in three-dimensional gray optical molasses.” In *EPL (Europhysics Letters)* **100**(6), (2012), 63001. doi:10.1209/0295-5075/100/63001.
- [149] P. G. H. Sandars. “Measurability of the Proton Electric Dipole Moment.” In *Physical Review Letters* **19**(24), (1967), 1396–1398. doi:10.1103/PhysRevLett.19.1396.
- [150] S. Saskin, J. T. Wilson, B. Grinkemeyer, and J. D. Thompson. “Narrow-Line Cooling and Imaging of Ytterbium Atoms in an Optical

- Tweezer Array.” In *Physical Review Letters* **122**(14), (2019), 143002. doi:10.1103/PhysRevLett.122.143002.
- [151] A. Yamaguchi, M. Safronova, K. Gibble, and H. Katori. “Narrow-line Cooling and Determination of the Magic Wavelength of Cd.” In *Physical Review Letters* **123**(11), (2019), 113201. doi:10.1103/PhysRevLett.123.113201.
- [152] S. Schiller, D. Bakalov, and V. I. Korobov. “Simplest Molecules as Candidates for Precise Optical Clocks.” In *Physical Review Letters* **113**(2), (2014), 023004. doi:10.1103/PhysRevLett.113.023004.
- [153] S. S. Kondov, C. H. Lee, K. H. Leung, C. Liedl, I. Majewska, R. Moszynski, and T. Zelevinsky. “Molecular lattice clock with long vibrational coherence.” In *Nature Physics* **15**(11), (2019), 1118–1122. doi:10.1038/s41567-019-0632-3.
- [154] J. L. Highberger, C. Savage, J. H. Biegging, and L. M. Ziurys. “Heavy-Metal Chemistry in Proto-Planetary Nebulae: Detection of MgNC, NaCN, and AlF toward CRL 2688.” In *The Astrophysical Journal* **562**(2), (2001), 790–798. doi:10.1086/323231.
- [155] M. Agúndez, J. P. Fonfría, J. Cernicharo, C. Kahane, F. Daniel, and M. Guélin. “Molecular abundances in the inner layers of IRC +10216.” In *Astronomy and Astrophysics* **543**, (2012), A48. doi:10.1051/0004-6361/201218963.
- [156] T. Kamiński, R. Tylenda, K. M. Menten, A. Karakas, J. M. Winters, A. A. Breier, K. T. Wong, T. F. Giesen, and N. A. Patel. “Astronomical detection of radioactive molecule ^{26}AlF in the remnant of an ancient explosion.” In *Nature Astronomy* **2**(10), (2018), 778–783. doi:10.1038/s41550-018-0541-x.
- [157] S. P. So and W. G. Richards. “A theoretical study of the excited electronic states of AlF.” In *Journal of Physics B: Atomic and Molecular Physics* **7**(14), (1974), 1973–1980. doi:10.1088/0022-3700/7/14/021.
- [158] D. E. Woon and E. Herbst. “Quantum chemical predictions of the properties of known and postulated neutral interstellar molecules.” In *Astrophysical Journal, Supplement Series* **185**(2), (2009), 273–288. doi:10.1088/0067-0049/185/2/273.
- [159] G. D. Rochester. “The Absorption Spectrum of Aluminum Fluoride (AlF).” In *Physical Review* **56**(4), (1939), 305–307. doi:10.1103/PhysRev.56.305.
- [160] H. C. Rowlinson and R. F. Barrow. “The Absorption Spectrum of Aluminium Monofluoride in the Schumann Region.” In *Proceedings of the Physical Society. Section A* **66**(8), (1953), 771–772. doi:10.1088/0370-1298/66/8/116.
- [161] S. M. Naudé and T. J. Hugo. “THE EMISSION SPECTRUM OF ALUMINUM MONOFLUORIDE I.” In *Canadian Journal of Physics* **31**(7), (1953), 1106–1114. doi:10.1139/p53-095.

- [162] S. M. Naudé and T. J. Hugo. “The Emission Spectrum of Aluminum Monofluoride.” In *Physical Review* **90**(2), (1953), 318–318. doi:10.1103/PhysRev.90.318.
- [163] S. M. Naudé and T. J. Hugo. “THE EMISSION SPECTRUM OF ALUMINUM MONOFLUORIDE. II.” In *Canadian Journal of Physics* **32**(3), (1954), 246–258. doi:10.1139/p54-023.
- [164] S. Rosenwaks, R. Steele, and H. Broida. “Observation of a³Π–X¹Σ intercombination emission in AlF.” In *Chemical Physics Letters* **38**(1), (1976), 1–4. doi:10.1016/0009-2614(76)80270-9.
- [165] I. Kopp, B. Lindgren, and C. Malmberg. “Rotational analysis of the a³Π–X¹Σ⁺ Transition of AlF.” In *Physica Scripta* **14**(4), (1976), 170–174. doi:10.1088/0031-8949/14/4/008.
- [166] J. M. Brown, I. Kopp, C. Malmberg, and B. Rydh. “An Analysis of Hyperfine Interactions in the Electronic Spectrum of AlF.” In *Physica Scripta* **17**(2), (1978), 55–67. doi:10.1088/0031-8949/17/2/003.
- [167] S. Truppe, S. Marx, S. Kray, M. Doppelbauer, S. Hofsäss, H. C. Schewe, N. Walter, J. Pérez-Ríos, B. G. Sartakov, and G. Meijer. “Spectroscopic characterization of aluminum monofluoride with relevance to laser cooling and trapping.” In *Physical Review A* **100**(5), (2019), 052513. doi:10.1103/PhysRevA.100.052513.
- [168] R. S. Freund and W. Klemperer. “Radio-Frequency Spectrum of the a³Π State of Carbon Monoxide.” In *The Journal of Chemical Physics* **43**(7), (1965), 2422–2428. doi:10.1063/1.1697141.
- [169] R. A. Frosch and H. M. Foley. “Magnetic Hyperfine Structure in Diatomic Molecules.” In *Physical Review* **88**(6), (1952), 1337–1349. doi:10.1103/PhysRev.88.1337.
- [170] R. N. Zare, A. L. Schmeltekopf, W. J. Harrop, and D. L. Albritton. “A direct approach for the reduction of diatomic spectra to molecular constants for the construction of RKR potentials.” In *Journal of Molecular Spectroscopy* **46**(1), (1973), 37–66. doi:10.1016/0022-2852(73)90025-8.
- [171] J. M. Brown, E. A. Colbourn, J. K. G. Watson, and F.D. Wayne. “An Effective Hamiltonian for Diatomic Molecules.” In *J. Mol. Spect.* **74**, (1979), 294–318. doi:10.1016/0022-2852(79)90059-6.
- [172] J. M. Brown and A. J. Merer. “Lambda-type doubling parameters for molecules in Π electronic states of triplet and higher multiplicity.” In *Journal of Molecular Spectroscopy* **74**(3), (1979), 488–494. doi:10.1016/0022-2852(79)90172-3.
- [173] C. Brazier, R. Ram, and P. Bernath. “Fourier transform spectroscopy of the A³Π–X³Σ[−] transition of NH.” In *Journal of Molecular Spectroscopy* **120**(2), (1986), 381–402. doi:10.1016/0022-2852(86)90012-3.

- [174] W. Gordy and R. L. Cook. *Microwave Molecular Spectra*. New York, Chichester, Brisbane, Toronto, Singapore: John Wiley & Sons, Inc., third edn. (1984). ISBN 0471086819.
- [175] J. M. Brown and A. Carrington. *Rotational Spectroscopy of Diatomic Molecules*. Cambridge: Cambridge University Press (2003). ISBN 9780511814808. doi:10.1017/CBO9780511814808.
- [176] C. H. Townes and A. L. Schawlow. *Microwave Spectroscopy*. New York: Dover (1975). ISBN 048661798X.
- [177] T. Klaus, S. Takano, and G. Winnewisser. “Laboratory measurement of the $N=1\leftarrow 0$ rotational transition of NH at 1 THz.” In *Astronomy and Astrophysics* **322**, (1997), L1–L4.
- [178] D. V. Dearden, R. D. Johnson, and J. W. Hudgens. “New Rydberg states of aluminum monofluoride observed by resonance-enhanced multiphoton ionization spectroscopy.” In *Journal of Physical Chemistry* **95**(11), (1991), 4291–4296. doi:10.1021/j100164a022.
- [179] J. Brown, J. Hougen, K.-P. Huber, J. Johns, I. Kopp, H. Lefebvre-Brion, A. Merer, D. Ramsay, J. Rostas, and R. Zare. “The labeling of parity doublet levels in linear molecules.” In *Journal of Molecular Spectroscopy* **55**(1-3), (1975), 500–503. doi:10.1016/0022-2852(75)90291-X.
- [180] J. K. G. Watson. “Rounding errors in the reporting of least-squares parameters.” In *Journal of Molecular Spectroscopy* **66**(3), (1977), 500–502. doi:10.1016/0022-2852(77)90308-3.
- [181] C. Zhang, C. Zhang, L. Cheng, T. C. Steimle, and M. R. Tarbutt. “Inner-shell excitation in the YbF molecule and its impact on laser cooling.” In *Journal of Molecular Spectroscopy* **386**, (2022), 111625. doi:10.1016/j.jms.2022.111625.
- [182] M. Doppelbauer, N. Walter, S. Hofsäss, S. Marx, H. C. Schewe, S. Kray, J. Pérez-Ríos, B. G. Sartakov, S. Truppe, and G. Meijer. “Characterisation of the $b^3\Sigma^+, v = 0$ state and its interaction with the $A^1\Pi$ state in aluminium monofluoride.” In *Molecular Physics* **119**(1-2), (2021), e1810351. doi:10.1080/00268976.2020.1810351.
- [183] P. G. Dodsworth and R. F. Barrow. “Triplet electronic states of aluminium monofluoride.” In *Proceedings of the Physical Society. Section A* **67**(1), (1954), 94–95. doi:10.1088/0370-1298/67/1/115.
- [184] P. G. Dodsworth and R. F. Barrow. “The triplet band systems of aluminium monofluoride.” In *Proceedings of the Physical Society. Section A* **68**(9), (1955), 824–828. doi:10.1088/0370-1298/68/9/307.
- [185] R. F. Barrow, I. Kopp, and R. Scullman. “Singlet electronic states of aluminium monofluoride.” In *Proceedings of the Physical Society* **82**(4), (1963), 635–636. doi:10.1088/0370-1328/82/4/125.

- [186] I. Kopp and R. F. Barrow. “Electronic states of gaseous AlF.” In *Journal of Physics B: Atomic and Molecular Physics* **3**(10), (1970), 1235–1257. doi:10.1088/0022-3700/3/10/020.
- [187] M. A. Duncan, T. G. Dietz, and R. E. Smalley. “Two-color photoionization of naphthalene and benzene at threshold.” In *The Journal of Chemical Physics* **75**(5), (1981), 2118–2125. doi:10.1063/1.442315.
- [188] S. E. Maxwell, N. Brahm, R. DeCarvalho, D. R. Glenn, J. S. Helton, S. V. Nguyen, D. Patterson, J. Petricka, D. DeMille, and J. M. Doyle. “High-Flux Beam Source for Cold, Slow Atoms or Molecules.” In *Physical Review Letters* **95**(17), (2005), 173201. doi:10.1103/PhysRevLett.95.173201.
- [189] N. R. Hutzler, H. I. Lu, and J. M. Doyle. “The buffer gas beam: An intense, cold, and slow source for atoms and molecules.” In *Chemical Reviews* **112**, (2012), 4803–4827. doi:10.1021/cr200362u.
- [190] S. Truppe, M. Hambach, S. M. Skoff, N. E. Bülleid, J. S. Bumby, R. J. Hendricks, E. A. Hinds, B. E. Sauer, and M. R. Tarbutt. “A buffer gas beam source for short, intense and slow molecular pulses.” In *Journal of Modern Optics* **65**(5-6), (2018), 648–656. doi:10.1080/09500340.2017.1384516.
- [191] H. G. Hedderich and P. F. Bernath. “The infrared emission spectrum of gaseous AlF.” In *Journal of Molecular Spectroscopy* **153**(1-2), (1992), 73–80. doi:10.1016/0022-2852(92)90458-Z.
- [192] P. Nolan and F. A. Jenkins. “Intensities in the $^3\Pi$, $^3\Sigma$ Band of PH.” In *Physical Review* **50**(10), (1936), 943–949. doi:10.1103/PhysRev.50.943.
- [193] S. Hofsäss. Ph.D. thesis (2022).
- [194] I. Kovács. *Rotational Structure in the Spectra of Diatomic Molecules*. Budapest: Akadémiai Kiadó (1969).
- [195] M. H. Hebb. “On Λ -type doubling in $^3\Pi$ states of diatomic molecules intermediate between Hund’s cases a and b.” In *Physical Review* **49**(8), (1936), 610–618. doi:10.1103/PhysRev.49.610.
- [196] H. A. Kramers. “Zur Struktur der Multiplett-S-Zustände in zweiatomigen Molekülen. I.” In *Zeitschrift für Physik* **53**(5-6), (1929), 422–428. doi:10.1007/BF01347762.
- [197] R. Schlapp. “Fine structure in the $^3\Sigma$ ground state of the oxygen molecule, and the rotational intensity distribution in the atmospheric oxygen band.” In *Physical Review* **51**(5), (1937), 342–345. doi:10.1103/PhysRev.51.342.
- [198] J. H. Blokland, J. Riedel, S. Putzke, B. G. Sartakov, G. C. Groenenboom, and G. Meijer. “Producing translationally cold, ground-state CO molecules.” In *The Journal of Chemical Physics* **135**(11), (2011), 114201. doi:10.1063/1.3637037.

- [199] N. Bartels, T. Schäfer, J. Hühnert, R. W. Field, and A. M. Wodtke. “Production of a beam of highly vibrationally excited CO using perturbations.” In *The Journal of Chemical Physics* **136**(21), (2012), 214201. doi:10.1063/1.4722090.
- [200] N. Walter, J. Seifert, S. Truppe, H. C. Schewe, B. G. Sartakov, and G. Meijer. “Spectroscopic characterization of singlet–triplet doorway states of aluminum monofluoride.” In *The Journal of Chemical Physics* **156**(18), (2022), 184301. doi:10.1063/5.0088288.
- [201] N. Walter, M. Doppelbauer, S. Marx, J. Seifert, X. Liu, J. Pérez-Ríos, B. G. Sartakov, S. Truppe, and G. Meijer. “Spectroscopic characterization of the $a^3\Pi$ state of aluminum monofluoride.” In *The Journal of Chemical Physics* **156**(12), (2022), 124306. doi:10.1063/5.0082601.
- [202] H. Katori, T. Ido, Y. Isoya, and M. Kuwata-Gonokami. “Magneto-optical trapping and cooling of strontium atoms down to the photon recoil temperature.” In *Physical Review Letters* **82**(6), (1999), 1116–1119. doi:10.1103/PhysRevLett.82.1116.
- [203] E. A. Curtis, C. W. Oates, and L. Hollberg. “Quenched narrow-line laser cooling of ^{40}Ca to near the photon recoil limit.” In *Physical Review A* **64**(3), (2001), 031403. doi:10.1103/PhysRevA.64.031403.
- [204] W. Demtröder. *Laser Spectroscopy 1*. Berlin, Heidelberg: Springer, fifth edn. (2014). ISBN 978-3-642-53858-2. doi:10.1007/978-3-642-53859-9.
- [205] M. R. Tarbutt. “Magneto-optical trapping forces for atoms and molecules with complex level structures.” In *New Journal of Physics* **17**(1), (2015), 015007. doi:10.1088/1367-2630/17/1/015007.
- [206] D. Budker, D. F. Kimball, and D. P. DeMille. *Atomic Physics. An Exploration through Problems and Solutions*. Oxford: Oxford University Press, second edn. (2008). ISBN 9780199532421.
- [207] J. R. Almond. *Laser cooling of YbF molecules for an improved measurement of the electron electric dipole moment*. Doctoral thesis, Imperial College London (2017).
- [208] M. R. Tarbutt, B. E. Sauer, J. J. Hudson, and E. A. Hinds. “Design for a fountain of YbF molecules to measure the electron’s electric dipole moment.” In *New Journal of Physics* **15**(5), (2013), 053034. doi:10.1088/1367-2630/15/5/053034.
- [209] M. O. Scully and M. S. Zubairy. *Quantum Optics*. Cambridge: Cambridge University Press (1997). ISBN 9780521435956. doi:10.1017/CBO9780511813993.
- [210] P. J. Ungar, D. S. Weiss, E. Riis, and S. Chu. “Optical molasses and multi-level atoms: theory.” In *Journal of the Optical Society of America B* **6**(11), (1989), 2058. doi:10.1364/JOSAB.6.002058.

- [211] J. A. Devlin and M. R. Tarbutt. “Three-dimensional Doppler, polarization-gradient, and magneto-optical forces for atoms and molecules with dark states.” In *New Journal of Physics* **18**(12), (2016), 123017. doi:10.1088/1367-2630/18/12/123017.
- [212] J. A. Devlin. *Progress towards a more sensitive measurement of the electron electric dipole moment with YbF*. Doctoral thesis, Imperial College London (2015).
- [213] P. M. Farrell, W. R. MacGillivray, and M. C. Standage. “Quantum-electrodynamic calculation of hyperfine-state populations in atomic sodium.” In *Physical Review A* **37**(11), (1988), 4240–4251. doi:10.1103/PhysRevA.37.4240.
- [214] J. A. Devlin and M. R. Tarbutt. “Laser cooling and magneto-optical trapping of molecules analyzed using optical Bloch equations and the Fokker-Planck-Kramers equation.” In *Physical Review A* **98**(6), (2018), 063415. doi:10.1103/PhysRevA.98.063415.
- [215] S. Eckel, D. S. Barker, E. B. Norrgard, and J. Scherschligt. “PyLCP: A Python package for computing laser cooling physics.” In *Computer Physics Communications* **270**, (2022), 108166. doi:10.1016/j.cpc.2021.108166.
- [216] S. C. Wright. *A Microwave Trap for Atoms and Molecules*. Doctoral thesis, Imperial College London (2020).
- [217] D. Manzano. “A short introduction to the Lindblad master equation.” In *AIP Advances* **10**(2), (2020), 025106. doi:10.1063/1.5115323.
- [218] D. J. Berkeland and M. G. Boshier. “Destabilization of dark states and optical spectroscopy in Zeeman-degenerate atomic systems.” In *Physical Review A* **65**(3), (2002), 033413. doi:10.1103/PhysRevA.65.033413.
- [219] N. J. Fitch and M. R. Tarbutt. “Laser-cooled molecules.” In *Advances in Atomic, Molecular and Optical Physics* **70**, (2021), 157–262. doi:10.1016/bs.aamop.2021.04.003.
- [220] B. D. Agap’ev, M. B. Gornyi, B. G. Matisov, and Y. V. Rozhdestvenskii. “Coherent population trapping in quantum systems.” In *Physics-Uspekhi* **36**(9), (1993), 763–793. doi:10.1070/PU1993v036n09ABEH002306.
- [221] G. Herzberg. *Molecular Spectra and Molecular Structure. I. Spectra of Diatomic Molecules*. New York: D. Van Nostrand Company, Inc. (1950). doi:10.1119/1.1932852.
- [222] J. Dalibard and C. Cohen-Tannoudji. “Laser cooling below the Doppler limit by polarization gradients: simple theoretical models.” In *Journal of the Optical Society of America B* **6**(11), (1989), 2023. doi:10.1364/josab.6.002023.

- [223] B. Sheehy, S. Q. Shang, P. Van Der Straten, S. Hatamian, and H. Metcalf. “Magnetic-field-induced laser cooling below the Doppler limit.” In *Physical Review Letters* **64**(8), (1990), 858–861. doi:10.1103/PhysRevLett.64.858.
- [224] P. D. Lett, R. N. Watts, C. I. Westbrook, W. D. Phillips, P. L. Gould, and H. J. Metcalf. “Observation of Atoms Laser Cooled below the Doppler Limit.” In *Physical Review Letters* **61**(2), (1988), 169–172. doi:10.1103/PhysRevLett.61.169.
- [225] S. Truppe, H. J. Williams, M. Hambach, L. Caldwell, N. J. Fitch, E. A. Hinds, B. E. Sauer, and M. R. Tarbutt. “Molecules cooled below the Doppler limit.” In *Nature Physics* **13**(12), (2017), 1173–1176. doi:10.1038/nphys4241.
- [226] S. Kraft, F. Vogt, O. Appel, F. Riehle, and U. Sterr. “Bose-Einstein Condensation of Alkaline Earth Atoms: ^{40}Ca .” In *Physical Review Letters* **103**(13), (2009), 130401. doi:10.1103/PhysRevLett.103.130401.
- [227] T. C. James. “Transition Moments, Franck—Condon Factors, and Lifetimes of Forbidden Transitions. Calculation of the Intensity of the Cameron System of CO.” In *The Journal of Chemical Physics* **55**(8), (1971), 4118–4124. doi:10.1063/1.1676710.
- [228] R. T. Jongma, G. Berden, and G. Meijer. “State-specific lifetime determination of the $a^3\Pi$ state in CO.” In *Journal of Chemical Physics* **107**(18), (1997), 7034–7040. doi:10.1063/1.474946.
- [229] S. van de Meerakker, N. Vanhaecke, M. van der Loo, G. Groenenboom, and G. Meijer. “Direct Measurement of the Radiative Lifetime of Vibrationally Excited OH Radicals.” In *Physical Review Letters* **95**(1), (2005), 013003. doi:10.1103/PhysRevLett.95.013003.
- [230] J. J. Gilijamse, S. Hoekstra, S. A. Meek, M. Metsälä, S. Y. T. van de Meerakker, G. Meijer, and G. C. Groenenboom. “The radiative lifetime of metastable CO ($a^3\Pi, v = 0$).” In *The Journal of Chemical Physics* **127**(22), (2007), 221102. doi:10.1063/1.2813888.
- [231] T. Binnewies, G. Wilpers, U. Sterr, F. Riehle, J. Helmcke, T. E. Mehlstäubler, E. M. Rasel, and W. Ertmer. “Doppler Cooling and Trapping on Forbidden Transitions.” In *Physical Review Letters* **87**(12), (2001), 123002. doi:10.1103/PhysRevLett.87.123002.
- [232] E. A. Curtis, C. W. Oates, and L. Hollberg. “Quenched narrow-line second- and third-stage laser cooling of ^{40}Ca .” In *Journal of the Optical Society of America B* **20**(5), (2003), 977. doi:10.1364/josab.20.000977.
- [233] R. Gu, K. Yan, D. Wu, J. Wei, Y. Xia, and J. Yin. “Radiative force from optical cycling on magnesium monofluoride.” In *Physical Review A* **105**(4), (2022), 042806. doi:10.1103/PhysRevA.105.042806.

- [234] N. E. Bulleid, S. M. Skoff, R. J. Hendricks, B. E. Sauer, E. A. Hinds, and M. R. Tarbutt. “Characterization of a cryogenic beam source for atoms and molecules.” In *Physical Chemistry Chemical Physics* **15**(29), (2013), 12299. doi:10.1039/c3cp51553b.
- [235] H. Pauly. *Atom, Molecule, and Cluster Beams I*, vol. 28 of *Springer Series on Atomic, Optical, and Plasma Physics*. Berlin, Heidelberg: Springer (2000). ISBN 978-3-642-08623-6. doi:10.1007/978-3-662-04213-7.
- [236] B. Friedrich and H. Schmidt-Böcking, eds.. *Molecular Beams in Physics and Chemistry. From Otto Stern’s Pioneering Exploits to Present-Day Feats*. Cham: Springer International Publishing, first edn. (2021). ISBN 978-3-030-63962-4. doi:10.1007/978-3-030-63963-1.
- [237] G. Scoles, ed.. *Atomic and Molecular Beam Methods, Volume 1*. New York, Oxford: Oxford University Press (1988).
- [238] M. D. Morse. “Supersonic Beam Sources.” In *Experimental Methods in the Physical Sciences*, vol. 29, pp. 21–47. San Diego: ACADEMIC PRESS INC. (1996). ISBN 978-0-12-475976-3. doi:10.1016/S0076-695X(08)60784-X.
- [239] W. Demtröder. *Laser Spectroscopy 2*. Berlin, Heidelberg: Springer, fifth edn. (2015). ISBN 978-3-662-44640-9. doi:10.1007/978-3-662-44641-6.
- [240] W. C. Campbell and J. M. Doyle. “Cooling, Trap Loading, and Beam Production Using a Cryogenic Helium Buffer Gas.” In R. V. Krems, B. Friedrich, and W. C. Stwalley, eds., *Cold Molecules. Theory, Experiment, Applications*, chap. 13, pp. 473–508. Boca Raton: CRC Press (2009). ISBN 9780429149504.
- [241] J. C. Polanyi and K. B. Woodall. “Mechanism of Rotational Relaxation.” In *The Journal of Chemical Physics* **56**(4), (1972), 1563. doi:10.1063/1.1677406.
- [242] M. J. Doppelbauer, O. Schullian, J. Loreau, N. Vaeck, A. van der Avoird, C. J. Rennick, T. P. Softley, and B. R. Heazlewood. “Using a direct simulation Monte Carlo approach to model collisions in a buffer gas cell.” In *The Journal of Chemical Physics* **146**(4), (2017), 044302. doi:10.1063/1.4974253.
- [243] Z. T. Lu, K. L. Corwin, M. J. Renn, M. H. Anderson, E. A. Cornell, and C. E. Wieman. “Low-velocity intense source of atoms from a magneto-optical trap.” In *Physical Review Letters* **77**(16), (1996), 3331–3334. doi:10.1103/PhysRevLett.77.3331.
- [244] S. E. Park, H. S. Lee, E.-J. Shin, T. Y. Kwon, S. H. Yang, and H. Cho. “Generation of a slow and continuous cesium atomic beam for an atomic clock.” In *Journal of the Optical Society of America B* **19**(11), (2002), 2595. doi:10.1364/JOSAB.19.002595.

- [245] J. Schoser, A. Batär, R. Löw, V. Schweikhard, A. Grabowski, Y. B. Ovchinnikov, and T. Pfau. “Intense source of cold Rb atoms from a pure two-dimensional magneto-optical trap.” In *Physical Review A* **66**(2), (2002), 023410. doi:10.1103/PhysRevA.66.023410.
- [246] C. Slowe, L. Vernac, and L. V. Hau. “High flux source of cold rubidium atoms.” In *Review of Scientific Instruments* **76**(10), (2005), 103101. doi:10.1063/1.2069651.
- [247] D. E. Powers, S. G. Hansen, M. E. Geusic, A. C. Puiiu, J. B. Hopkins, T. G. Dietz, M. A. Duncan, P. R. Langridge-Smith, and R. E. Smalley. “Supersonic metal cluster beams: Laser photoionization studies of Cu₂.” In *Journal of Physical Chemistry* **86**(14), (1982), 2556–2560. doi:10.1021/j100211a002.
- [248] B. Simard, S. A. Mitchell, M. R. Humphries, and P. A. Hackett. “High-resolution spectroscopy and photophysics of refractory molecules at low temperature: The C¹Σ⁺-X¹Σ⁺ system of ZrO.” In *Journal of Molecular Spectroscopy* **129**(1), (1988), 186–201. doi:10.1016/0022-2852(88)90269-X.
- [249] M. Ebben, G. Meijer, and J. J. ter Meulen. “Laser evaporation as a source of small free radicals.” In *Applied Physics B Photophysics and Laser Chemistry* **50**(1), (1990), 35–38. doi:10.1007/BF00330090.
- [250] C. J. Whitham, B. Soep, J. P. Visticot, and A. Keller. “Observation and spectroscopy of metallic free radicals produced by reactive collisions during a supersonic expansion.” In *The Journal of Chemical Physics* **93**(2), (1990), 991–1000. doi:10.1063/1.459126.
- [251] D. A. Fletcher, K. Y. Jung, C. T. Scurlock, and T. C. Steimle. “Molecular beam pump/probe microwave-optical double resonance using a laser ablation source.” In *The Journal of Chemical Physics* **98**(3), (1993), 1837–1842. doi:10.1063/1.464218.
- [252] A. G. Adam, L. P. Fraser, W. D. Hamilton, and M. C. Steeves. “Gas-phase electronic spectroscopy of cobalt monofluoride.” In *Chemical Physics Letters* **230**(1-2), (1994), 82–86. doi:10.1016/0009-2614(94)01149-4.
- [253] M. R. Tarbutt, J. J. Hudson, B. E. Sauer, E. A. Hinds, V. A. Ryzhov, V. L. Ryabov, and V. F. Ezhov. “A jet beam source of cold YbF radicals.” In *Journal of Physics B: Atomic, Molecular and Optical Physics* **35**(24), (2002), 5013–5022. doi:10.1088/0953-4075/35/24/306.
- [254] T. E. Wall, J. F. Kanem, J. J. Hudson, B. E. Sauer, D. Cho, M. G. Boshier, E. A. Hinds, and M. R. Tarbutt. “Lifetime of the A(*v*' = 0) state and Franck-Condon factor of the A – X(0 – 0) transition of CaF measured by the saturation of laser-induced fluorescence.” In *Physical Review A* **78**(6), (2008), 062509. doi:10.1103/PhysRevA.78.062509.
- [255] M. R. Tarbutt, H. L. Bethlem, J. J. Hudson, V. L. Ryabov, V. A. Ryzhov, B. E. Sauer, G. Meijer, and E. A. Hinds. “Slowing Heavy, Ground-State

- Molecules using an Alternating Gradient Decelerator.” In *Physical Review Letters* **92**(17), (2004), 173002. doi:10.1103/PhysRevLett.92.173002.
- [256] M. Gupta and D. Herschbach. “Slowing and speeding molecular beams by means of a rapidly rotating source.” In *Journal of Physical Chemistry A* **105**(9), (2001), 1626–1637. doi:10.1021/jp002640u.
- [257] J. K. Messer and F. C. De Lucia. “Measurement of pressure-broadening parameters for the CO-He system at 4 K.” In *Physical Review Letters* **53**(27), (1984), 2555–2558. doi:10.1103/PhysRevLett.53.2555.
- [258] J. M. Doyle, B. Friedrich, J. Kim, and D. Patterson. “Buffer-gas loading of atoms and molecules into a magnetic trap.” In *Physical Review A* **52**(4), (1995), R2515–R2518. doi:10.1103/PhysRevA.52.R2515.
- [259] J. Kim, B. Friedrich, D. P. Katz, D. Patterson, J. D. Weinstein, R. DeCarvalho, and J. M. Doyle. “Buffer-gas loading and magnetic trapping of atomic Europium.” In *Physical Review Letters* **78**(19), (1997), 3665–3668. doi:10.1103/PhysRevLett.78.3665.
- [260] J. D. Weinstein, R. DeCarvalho, J. Kim, D. Patterson, B. Friedrich, and J. M. Doyle. “Magnetic trapping of atomic chromium.” In *Physical Review A* **57**(5), (1998), R3173–R3175. doi:10.1103/PhysRevA.57.R3173.
- [261] J. D. Weinstein, R. Decarvalho, K. Amar, A. Boca, B. C. Odom, B. Friedrich, and J. M. Doyle. “Spectroscopy of buffer-gas cooled vanadium monoxide in a magnetic trapping field.” In *Journal of Chemical Physics* **109**(7), (1998), 2656–2661. doi:10.1063/1.476864.
- [262] R. DeCarvalho, J. M. Doyle, B. Friedrich, T. Guillet, J. Kim, D. Patterson, and J. D. Weinstein. “Buffer-gas loaded magnetic traps for atoms and molecules: A primer.” In *European Physical Journal D* **7**(3), (1999), 289–309. doi:10.1007/s100530050572.
- [263] W. C. Campbell, E. Tsikata, H.-I. Lu, L. D. van Buuren, and J. M. Doyle. “Magnetic trapping and Zeeman relaxation of $\text{NH} (X^3\Sigma^-)$.” In *Physical Review Letters* **98**(21), (2007), 213001. doi:10.1103/PhysRevLett.98.213001.
- [264] S. C. Doret, C. B. Connolly, W. Ketterle, and J. M. Doyle. “Buffer-Gas Cooled Bose-Einstein Condensate.” In *Physical Review Letters* **103**(10), (2009), 103005. doi:10.1103/PhysRevLett.103.103005.
- [265] L. D. van Buuren, C. Sommer, M. Motsch, S. Pohle, M. Schenk, J. Bayerl, P. W. H. Pinkse, and G. Rempe. “Electrostatic Extraction of Cold Molecules from a Cryogenic Reservoir.” In *Physical Review Letters* **102**(3), (2009), 033001. doi:10.1103/PhysRevLett.102.033001.
- [266] C. Sommer, L. D. van Buuren, M. Motsch, S. Pohle, J. Bayerl, P. W. H. Pinkse, and G. Rempe. “Continuous guided beams of slow and internally cold polar molecules.” In *Faraday Discussions* **142**, (2009), 203. doi:10.1039/b819726a.

- [267] D. Egorov, T. Lahaye, W. Schöllkopf, B. Friedrich, and J. M. Doyle. “Buffer-gas cooling of atomic and molecular beams.” In *Physical Review A* **66**(4), (2002), 043401. doi:10.1103/PhysRevA.66.043401.
- [268] D. Patterson and J. M. Doyle. “Bright, guided molecular beam with hydrodynamic enhancement.” In *The Journal of Chemical Physics* **126**(15), (2007), 154307. doi:10.1063/1.2717178.
- [269] D. Patterson, J. Rasmussen, and J. M. Doyle. “Intense atomic and molecular beams via neon buffer-gas cooling.” In *New Journal of Physics* **11**(5), (2009), 055018. doi:10.1088/1367-2630/11/5/055018.
- [270] D. Patterson, E. Tsikata, and J. M. Doyle. “Cooling and collisions of large gas phase molecules.” In *Physical Chemistry Chemical Physics* **12**(33), (2010), 9736–9741. doi:10.1039/c002764b.
- [271] P. B. Changala, B. Spaun, D. Patterson, J. M. Doyle, and J. Ye. “Sensitivity and resolution in frequency comb spectroscopy of buffer gas cooled polyatomic molecules.” In *Applied Physics B* **122**(12), (2016), 292. doi:10.1007/s00340-016-6569-7.
- [272] P. B. Changala, M. L. Weichman, K. F. Lee, M. E. Fermann, and J. Ye. “Rovibrational quantum state resolution of the C 60 fullerene.” In *Science* **363**(6422), (2019), 49–54. doi:10.1126/science.aav2616.
- [273] H. I. Lu, J. Rasmussen, M. J. Wright, D. Patterson, and J. M. Doyle. “A cold and slow molecular beam.” In *Physical Chemistry Chemical Physics* **13**(42), (2011), 18986–18990. doi:10.1039/c1cp21206k.
- [274] N. R. Hutzler, M. F. Parsons, Y. V. Gurevich, P. W. Hess, E. Petrik, B. Spaun, A. C. Vutha, D. DeMille, G. Gabrielse, and J. M. Doyle. “A cryogenic beam of refractory, chemically reactive molecules with expansion cooling.” In *Physical Chemistry Chemical Physics* **13**(42), (2011), 18976. doi:10.1039/c1cp20901a.
- [275] S. M. Skoff, R. J. Hendricks, C. D. J. Sinclair, J. J. Hudson, D. M. Segal, B. E. Sauer, E. A. Hinds, and M. R. Tarbutt. “Diffusion, thermalization, and optical pumping of YbF molecules in a cold buffer-gas cell.” In *Physical Review A* **83**(2), (2011), 023418. doi:10.1103/PhysRevA.83.023418.
- [276] N. E. Bulleid. *Slow, cold beams of polar molecules for precision measurements*. Doctoral thesis, Imperial College London (2013).
- [277] T. E. Wall. “Preparation of cold molecules for high-precision measurements.” In *Journal of Physics B: Atomic, Molecular and Optical Physics* **49**(24), (2016), 243001. doi:10.1088/0953-4075/49/24/243001.
- [278] S. Truppe, H. J. Williams, N. J. Fitch, M. Hambach, T. E. Wall, E. A. Hinds, B. E. Sauer, and M. R. Tarbutt. “An intense, cold, velocity-controlled molecular beam by frequency-chirped laser slowing.” In *New Journal of Physics* **19**(2), (2017), 022001. doi:10.1088/1367-2630/aa5ca2.

- [279] J. F. Barry, E. S. Shuman, E. B. Norrgard, and D. DeMille. “Laser Radiation Pressure Slowing of a Molecular Beam.” In *Physical Review Letters* **108**(10), (2012), 103002. doi:10.1103/PhysRevLett.108.103002.
- [280] D. J. McCarron, E. B. Norrgard, M. H. Steinecker, and D. DeMille. “Improved magneto-optical trapping of a diatomic molecule.” In *New Journal of Physics* **17**(3), (2015), 035014. doi:10.1088/1367-2630/17/3/035014.
- [281] E. Norrgard, D. McCarron, M. Steinecker, M. Tarbutt, and D. DeMille. “Submillikelvin Dipolar Molecules in a Radio-Frequency Magneto-Optical Trap.” In *Physical Review Letters* **116**(6), (2016), 063004. doi:10.1103/PhysRevLett.116.063004.
- [282] S. Xu, M. Xia, Y. Yin, R. Gu, Y. Xia, and J. Yin. “Determination of the normal $A^2\Pi$ state in MgF with application to direct laser cooling of molecules.” In *The Journal of Chemical Physics* **150**(8), (2019), 084302. doi:10.1063/1.5083898.
- [283] R. Albrecht, M. Scharwaechter, T. Sixt, L. Hofer, and T. Langen. “Buffer-gas cooling, high-resolution spectroscopy, and optical cycling of barium monofluoride molecules.” In *Physical Review A* **101**(1), (2020), 013413. doi:10.1103/PhysRevA.101.013413.
- [284] P. Aggarwal, Y. Yin, K. Esajas, H. L. Bethlem, A. Boeschoten, A. Borschevsky, S. Hoekstra, K. Jungmann, V. R. Marshall, T. B. Meijknecht, M. C. Mooij, R. G. E. Timmermans, A. Touwen, W. Ubachs, and L. Willmann. “Deceleration and Trapping of SrF Molecules.” In *Physical Review Letters* **127**(17), (2021), 173201. doi:10.1103/PhysRevLett.127.173201.
- [285] M. Yeo, M. T. Hummon, A. L. Collopy, B. Yan, B. Hemmerling, E. Chae, J. M. Doyle, and J. Ye. “Rotational State Microwave Mixing for Laser Cooling of Complex Diatomic Molecules.” In *Physical Review Letters* **114**(22), (2015), 223003. doi:10.1103/PhysRevLett.114.223003.
- [286] S. Ding, Y. Wu, I. A. Finneran, J. J. Burau, and J. Ye. “Sub-Doppler Cooling and Compressed Trapping of YO Molecules at μK Temperatures.” In *Physical Review X* **10**(2), (2020), 21049. doi:10.1103/PhysRevX.10.021049.
- [287] Y. Wu, J. J. Burau, K. Mehling, J. Ye, and S. Ding. “High Phase-Space Density of Laser-Cooled Molecules in an Optical Lattice.” In *Physical Review Letters* **127**(26), (2021), 263201. doi:10.1103/PhysRevLett.127.263201.
- [288] M. G. Tarallo, G. Z. Iwata, and T. Zelevinsky. “BaH molecular spectroscopy with relevance to laser cooling.” In *Physical Review A* **93**(3), (2016), 032509. doi:10.1103/PhysRevA.93.032509.
- [289] C. L. Chan and J. Mazumder. “One-dimensional steady-state model for damage by vaporization and liquid expulsion due to laser-material interaction.” In *Journal of Applied Physics* **62**(11), (1987), 4579–4586. doi:10.1063/1.339053.

- [290] A. Miotello and R. Kelly. “Laser-induced phase explosion: new physical problems when a condensed phase approaches the thermodynamic critical temperature.” In *Applied Physics A: Materials Science & Processing* **69**(7), (1999), S67–S73. doi:10.1007/s003390051357.
- [291] C. Porneala and D. A. Willis. “Observation of nanosecond laser-induced phase explosion in aluminum.” In *Applied Physics Letters* **89**(21), (2006), 211121. doi:10.1063/1.2393158.
- [292] A. Gragossian, S. H. Tavassoli, and B. Shokri. “Laser ablation of aluminum from normal evaporation to phase explosion.” In *Journal of Applied Physics* **105**(10), (2009), 103304. doi:10.1063/1.3131689.
- [293] J. Terragni and A. Miotello. “Laser Ablation of Aluminum Near the Critical Regime: A Computational Gas-Dynamical Model with Temperature-Dependent Physical Parameters.” In *Micromachines* **12**(3), (2021), 300. doi:10.3390/mi12030300.
- [294] K. Sasaki and H. Watarai. “Dynamics of Laser-Ablation Plume and Ambient Gas Visualized by Laser-Induced Fluorescence Imaging Spectroscopy.” In *Japanese Journal of Applied Physics* **45**(No. 16), (2006), L447–L449. doi:10.1143/JJAP.45.L447.
- [295] K. Sasaki and H. Watarai. “Reaction between laser ablation plume and ambient gas studied by laser-induced fluorescence imaging spectroscopy.” In *Journal of Physics: Conference Series* **59**(1), (2007), 60–63. doi:10.1088/1742-6596/59/1/013.
- [296] G. A. Bird. *Molecular Gas Dynamics and the Direct Simulation of Gas Flows*. Oxford: Oxford University Press (2003). ISBN 9780198561958.
- [297] O. Schullian, J. Loreau, N. Vaeck, A. van der Avoird, B. Heazlewood, C. Rennick, and T. Softley. “Simulating rotationally inelastic collisions using a direct simulation Monte Carlo method.” In *Molecular Physics* **113**(24), (2015), 3972–3978. doi:10.1080/00268976.2015.1098740.
- [298] O. Schullian and B. R. Heazlewood. “Beyond direct simulation Monte Carlo (DSMC) modelling of collision environments.” In *Molecular Physics* **117**(21), (2019), 3076–3087. doi:10.1080/00268976.2019.1602740.
- [299] O. Schullian, H. S. Antila, and B. R. Heazlewood. “A variable time step self-consistent mean field DSMC model for three-dimensional environments.” In *The Journal of Chemical Physics* **156**(12), (2022), 124309. doi:10.1063/5.0083033.
- [300] Y. Takahashi, D. Shlivko, G. Woolls, and N. R. Hutzler. “Simulation of cryogenic buffer gas beams.” In *Physical Review Research* **3**(2), (2021), 023018. doi:10.1103/PhysRevResearch.3.023018.

- [301] M. Karra, M. T. Cretu, B. Friedrich, S. Truppe, G. Meijer, and J. Pérez-Ríos. “Dynamics of translational and rotational thermalization of AlF molecules via collisions with cryogenic helium.” In *Physical Review A* **105**(2), (2022), 022808. doi:10.1103/PhysRevA.105.022808.
- [302] T. Gantner, M. Koller, X. Wu, G. Rempe, and M. Zeppenfeld. “Buffer-gas cooling of molecules in the low-density regime: comparison between simulation and experiment.” In *Journal of Physics B: Atomic, Molecular and Optical Physics* **53**(14), (2020), 145302. doi:10.1088/1361-6455/ab8b42.
- [303] E. S. Chang. “Energy Levels of Atomic Aluminum with Hyperfine Structure.” In *Journal of Physical and Chemical Reference Data* **19**(1), (1990), 119–125. doi:10.1063/1.555870.
- [304] A. Kramida, Yu. Ralchenko, J. Reader, and NIST ASD Team. NIST Atomic Spectra Database (ver. 5.9), [Online]. Available: <https://physics.nist.gov/asd> [2022, May 18]. National Institute of Standards and Technology, Gaithersburg, MD. (2021).
- [305] L. Davis, B. T. Feld, C. W. Zabel, and J. R. Zacharias. “The Hyperfine Structure and Nuclear Moments of the Stable Chlorine Isotopes.” In *Physical Review* **76**(8), (1949), 1076–1085. doi:10.1103/PhysRev.76.1076.
- [306] K. B. S. Eriksson and H. B. S. Isberg. “The spectrum of atomic aluminium, Al I.” In *Arkiv för fysik* **23**, (1963), 527–542.
- [307] J. Sugar and C. Corliss. “Atomic Energy Levels of the Iron-Period Elements: Potassium through Nickel.” In *Journal of Physical and Chemical Reference Data* **14**(Suppl. 2), (1985), 51–105.
- [308] M. Mills, P. Puri, Y. Yu, A. Derevianko, C. Schneider, and E. R. Hudson. “Efficient repumping of a Ca magneto-optical trap.” In *Physical Review A* **96**(3), (2017), 033402. doi:10.1103/PhysRevA.96.033402.
- [309] M. Kleinert, M. E. Gold Dahl, and S. Bergeson. “Measurement of the Yb I $^1S_0 - ^1P_1$ transition frequency at 399 nm using an optical frequency comb.” In *Physical Review A* **94**(5), (2016), 052511. doi:10.1103/PhysRevA.94.052511.
- [310] E. GharibNezhad, A. Shayesteh, and P. F. Bernath. “Einstein A coefficients for rovibronic lines of the $A^2\Pi \rightarrow X^2\Sigma^+$ and $B'^2\Sigma^+ \rightarrow X^2\Sigma^+$ transitions of MgH.” In *Monthly Notices of the Royal Astronomical Society* **432**(3), (2013), 2043–2047. doi:10.1093/mnras/stt510.
- [311] X. Liu, W. Wang, S. C. Wright, M. Doppelbauer, G. Meijer, S. Truppe, and J. Pérez-Ríos. “The chemistry of AlF and CaF production in buffer gas sources.” In *The Journal of Chemical Physics* **157**(7), (2022), 074305. doi:10.1063/5.0098378.
- [312] D. Bäuerle. *Laser Processing and Chemistry*. Berlin, Heidelberg: Springer, fourth edn. (2011). ISBN 978-3-642-17612-8. doi:10.1007/978-3-642-17613-5.

- [313] A. H. Lutey. “An improved model for nanosecond pulsed laser ablation of metals.” In *Journal of Applied Physics* **114**(8), (2013), 83108. doi:10.1063/1.4818513.
- [314] M. von Allmen. *Laser-Beam Interactions with Materials. Physical Principles and Applications*, vol. 2 of *Springer Series in Materials Science*. Berlin, Heidelberg: Springer, first edn. (1987). ISBN 978-3-642-97009-2. doi:10.1007/978-3-642-97007-8.
- [315] C. L. Foiles. “Electrical Resistivity, Thermoelectrical Power and Optical Properties · Ag - Ca: Datasheet from Landolt-Börnstein - Group III Condensed Matter · Volume 15B: “Electrical Resistivity, Thermoelectrical Power and Optical Properties” in SpringerMaterials (https://doi.org/10.1007/10201705_31).” doi:10.1007/10201705_31. Copyright 1985 Springer-Verlag Berlin Heidelberg.
- [316] C. L. Foiles. “Electrical Resistivity, Thermoelectrical Power and Optical Properties · Ir - Mn: Datasheet from Landolt-Börnstein - Group III Condensed Matter · Volume 15B: “Electrical Resistivity, Thermoelectrical Power and Optical Properties” in SpringerMaterials (https://doi.org/10.1007/10201705_34).” doi:10.1007/10201705_34. Copyright 1985 Springer-Verlag Berlin Heidelberg.
- [317] C. L. Foiles. “Electrical Resistivity, Thermoelectrical Power and Optical Properties · Sn - Zr: Datasheet from Landolt-Börnstein - Group III Condensed Matter · Volume 15B: “Electrical Resistivity, Thermoelectrical Power and Optical Properties” in SpringerMaterials (https://doi.org/10.1007/10201705_38).” doi:10.1007/10201705_38. Copyright 1985 Springer-Verlag Berlin Heidelberg.
- [318] C. L. Foiles. “Electrical Resistivity, Thermoelectrical Power and Optical Properties · Figs. 102 - 139: Datasheet from Landolt-Börnstein - Group III Condensed Matter · Volume 15B: “Electrical Resistivity, Thermoelectrical Power and Optical Properties” in SpringerMaterials (https://doi.org/10.1007/10201705_42).” doi:10.1007/10201705_42. Copyright 1985 Springer-Verlag Berlin Heidelberg.
- [319] J. Gorobez, B. Maack, and N. Nilius. “Growth of Self-Passivating Oxide Layers on Aluminum—Pressure and Temperature Dependence.” In *physica status solidi (b)* **258**(5), (2021), 2000559. doi:10.1002/pssb.202000559.
- [320] G. Ertl and M. Huber. “Mechanism and kinetics of ammonia decomposition on iron.” In *Journal of Catalysis* **61**(2), (1980), 537–539. doi:10.1016/0021-9517(80)90403-0.
- [321] G. Ertl. “Primary steps in catalytic synthesis of ammonia.” In *Journal of Vacuum Science & Technology A: Vacuum, Surfaces, and Films* **1**(2), (1983), 1247–1253. doi:10.1116/1.572299.

- [322] R. Miotto, A. C. Ferraz, and G. P. Srivastava. “Dissociative adsorption of NF_3 on $\text{Si}(001)-(2\times 1)$.” In *Surface Science* **454**(1), (2000), 152–156. doi:10.1016/S0039-6028(00)00163-1.
- [323] J. K. Parker, N. L. Garland, and H. H. Nelson. “Kinetics of the Reaction $\text{Al} + \text{SF}_6$ in the Temperature Range 499–813 K.” In *The Journal of Physical Chemistry A* **106**(2), (2002), 307–311. doi:10.1021/jp012895n.
- [324] G. T. Armstrong, S. Marantz, and C. F. Coyle. “HEAT OF FORMATION OF NITROGEN TRIFLUORIDE AND THE N-F BOND ENERGY.” In *Journal of the American Chemical Society* **81**(14), (1959), 3798–3798. doi:10.1021/ja01523a077.
- [325] T. Kiang and R. N. Zare. “Stepwise Bond Dissociation Energies in Sulfur Hexafluoride.” In *Journal of the American Chemical Society* **102**(12), (1980), 4024–4029. doi:10.1021/ja00532a008.
- [326] A. Jadbabaie, N. H. Pilgram, J. Kłos, S. Kotochigova, and N. R. Hutzler. “Enhanced molecular yield from a cryogenic buffer gas beam source via excited state chemistry.” In *New Journal of Physics* **22**(2), (2020), 022002. doi:10.1088/1367-2630/ab6eae.
- [327] M. Doppelbauer, S. C. Wright, S. Hofsäss, B. G. Sartakov, G. Meijer, and S. Truppe. “Hyperfine-resolved optical spectroscopy of the $\text{A}^2\Pi \leftarrow \text{X}^2\Sigma^+$ transition in MgF .” In *The Journal of Chemical Physics* **156**(13), (2022), 134301. doi:10.1063/5.0081902.
- [328] S. Kang, Y. Gao, F. Kuang, T. Gao, J. Du, and G. Jiang. “Theoretical study of laser cooling of magnesium monofluoride using ab initio methods.” In *Physical Review A* **91**(4), (2015), 042511. doi:10.1103/PhysRevA.91.042511.
- [329] E. Chae. “Entanglement *via* rotational blockade of MgF molecules in a magic potential.” In *Physical Chemistry Chemical Physics* **23**(2), (2021), 1215–1220. doi:10.1039/D0CP04042H.
- [330] M. Xia, R. Gu, K. Yan, D. Wu, L. Xu, Y. Xia, and J. Yin. “Destabilization of dark states in MgF molecules.” In *Physical Review A* **103**(1), (2021), 013321. doi:10.1103/PhysRevA.103.013321.
- [331] F. A. Jenkins and R. Grinfeld. “The Spectrum of MgF .” In *Physical Review* **45**(4), (1934), 229–233. doi:10.1103/PhysRev.45.229.
- [332] C. A. Fowler. “New Absorption Spectra of the Alkaline Earth Fluorides.” In *Physical Review* **59**(8), (1941), 645–652. doi:10.1103/PhysRev.59.645.
- [333] R. F. Barrow and J. R. Beale. “Rotational analysis of electronic bands of gaseous MgF .” In *Proceedings of the Physical Society* **91**(2), (1967), 483–488. doi:10.1088/0370-1328/91/2/328.

- [334] T. E. Walker and W. G. Richards. “The nature of the first excited electronic state in MgF.” In *Journal of Physics B: Atomic and Molecular Physics* **1**(6), (1968), 1061–1065. doi:10.1088/0022-3700/1/6/308.
- [335] M. M. Novikov and L. V. Gurvich. “The electronic spectra of MgF and MgF⁺.” In *Journal of Applied Spectroscopy* **14**(6), (1971), 820–822. doi:10.1007/BF00606831.
- [336] B. E. Barber, K. Q. Zhang, B. Guo, and P. F. Bernath. “Vibration-rotation emission spectrum of MgF.” In *Journal of Molecular Spectroscopy* **169**(2), (1995), 583–589. doi:10.1006/jmsp.1995.1047.
- [337] M. A. Anderson, M. D. Allen, and L. M. Ziurys. “Millimeter-wave spectroscopy of MgF: Structure and bonding in alkaline-earth monofluoride radicals.” In *The Journal of Chemical Physics* **100**(2), (1994), 824–830. doi:10.1063/1.466565.
- [338] M. A. Anderson, M. D. Allen, and L. M. Ziurys. “Millimeter and submillimeter rest frequencies for the MgF radical.” In *The Astrophysical Journal* **425**, (1994), L53. doi:10.1086/187309.
- [339] T. E. H. Walker and W. G. Richards. “The assignment of molecular orbital configurations on the basis of Λ -type doubling.” In *Journal of Physics B: Atomic and Molecular Physics* **3**(2), (1970), 271–279. doi:10.1088/0022-3700/3/2/020.
- [340] M. Pelegrini, C. S. Vivacqua, O. Roberto-Neto, F. R. Ornellas, and F. B. Machado. “Radiative transition probabilities and lifetimes for the band systems $A^2\Pi-X^2\Sigma^+$ of the isovalent molecules BeF, MgF and CaF.” In *Brazilian Journal of Physics* **35**(4 A), (2005), 950–956. doi:10.1590/S0103-97332005000600007.
- [341] J. Kändler, T. Martell, and W. E. Ernst. “Electric dipole moments and hyperfine structure of SrF $A^2\Pi$ and $B^2\Sigma^+$.” In *Chemical Physics Letters* **155**(4-5), (1989), 470–474. doi:10.1016/0009-2614(89)87188-X.
- [342] J. T. Hougen. “The Calculation of rotational energy levels and rotational line intensities in diatomic molecules.” Tech. Rep., National Bureau of Standards, Gaithersburg, MD (1970). doi:10.6028/NBS.MONO.115.
- [343] J. K. Watson. “The isotope dependence of diatomic Dunham coefficients.” In *Journal of Molecular Spectroscopy* **80**(2), (1980), 411–421. doi:10.1016/0022-2852(80)90152-6.
- [344] J. L. Dunham. “The Energy Levels of a Rotating Vibrator.” In *Physical Review* **41**(6), (1932), 721–731. doi:10.1103/PhysRev.41.721.
- [345] J. H. Van Vleck. “On the Isotope Corrections in Molecular Spectra.” In *The Journal of Chemical Physics* **4**(6), (1936), 327–338. doi:10.1063/1.1749853.

- [346] A. H. M. Ross, R. S. Eng, and H. Kildal. “Heterodyne measurements of $^{12}\text{C}^{18}\text{O}$, $^{13}\text{C}^{16}\text{O}$, and $^{13}\text{C}^{18}\text{O}$ laser frequencies; mass dependence of Dunham coefficients.” In *Optics Communications* **12**(4), (1974), 433–438. doi:10.1016/0030-4018(74)90139-4.
- [347] G. C. Dousmanis. “Magnetic Hyperfine Effects and Electronic Structure of NO.” In *Physical Review* **97**(4), (1955), 967–970. doi:10.1103/PhysRev.97.967.
- [348] N. J. Stone. “Table of nuclear magnetic dipole and electric quadrupole moments.” In *Atomic Data and Nuclear Data Tables* **90**(1), (2005), 75–176. doi:10.1016/j.adt.2005.04.001.
- [349] P. F. Bernath, P. G. Cummins, and R. W. Field. “Intermodulated fluorescence spectroscopy of CaF $A^2\Pi-X^2\Sigma^+$.” In *Chemical Physics Letters* **70**(3), (1980), 618–620. doi:10.1016/0009-2614(80)80138-2.
- [350] P. F. Bernath, B. Pinchemel, and R. W. Field. “The hyperfine structure of the calcium monohalides.” In *The Journal of Chemical Physics* **74**(10), (1981), 5508–5515. doi:10.1063/1.440957.
- [351] T. Chen, W. Bu, and B. Yan. “Structure, branching ratios, and a laser-cooling scheme for the ^{138}BaF molecule.” In *Physical Review A* **94**(6), (2016), 063415. doi:10.1103/PhysRevA.94.063415.
- [352] L. Xu, B. Wei, Y. Xia, L. Z. Deng, and J. P. Yin. “BaF radical: A promising candidate for laser cooling and magneto-optical trapping.” In *Chinese Physics B* **26**(3), (2017), 033702. doi:10.1088/1674-1056/26/3/033702.
- [353] A. T. Le, H. Wang, and T. C. Steimle. “Hyperfine structure and Zeeman tuning of the $A^2\Pi-X^2\Sigma^+(0,0)$ band system of the odd isotopologue of strontium monofluoride ^{87}SrF .” In *Physical Review A* **80**(6), (2009), 062513. doi:10.1103/PhysRevA.80.062513.
- [354] T. C. Steimle, S. Frey, A. Le, D. DeMille, D. A. Rahlmow, and C. Linton. “Molecular-beam optical Stark and Zeeman study of the $A^2\Pi - X^2\Sigma^+(0,0)$ band system of BaF.” In *Physical Review A* **84**(1), (2011), 012508. doi:10.1103/PhysRevA.84.012508.
- [355] J. H. Van Vleck. “On σ -type doubling and electron spin in the spectra of diatomic molecules.” In *Physical Review* **33**(4), (1929), 467–506. doi:10.1103/PhysRev.33.467.
- [356] R. K. Hinkley, J. A. Hall, T. E. H. Walker, and W. G. Richards. “A doubling in $^2\Pi$ states of diatomic molecules.” In *Journal of Physics B: Atomic and Molecular Physics* **5**(2), (1972), 204–212. doi:10.1088/0022-3700/5/2/016.
- [357] R. S. Mulliken and A. Christy. “A-Type Doubling and Electron Configurations in Diatomic Molecules.” In *Physical Review* **38**(1), (1931), 87–119. doi:10.1103/PhysRev.38.87.

- [358] L. A. Kaledin, J. C. Bloch, M. C. McCarthy, and R. W. Field. “Analysis and Deperturbation of the $A^2\Pi$ and $B^2\Sigma^+$ States of CaF.” In *Journal of Molecular Spectroscopy* **197**(2), (1999), 289–296. doi:10.1006/jmsp.1999.7909.
- [359] T. C. Steimle, D. A. Fletcher, and C. T. Scurlock. “A Molecular Beam Study of the $(0,0)A^2\Pi-X^2\Sigma^+$ Band System of SrF.” In *Journal of molecular spectroscopy* **158**(2), (1993), 487–488. doi:10.1006/jmsp.1993.1094.
- [360] T. C. Steimle, P. J. Domaille, and D. O. Harris. “Rotational analysis of the $B^2\Sigma^+-X^2\Sigma^+$ system of SrF using a cw tunable dye laser.” In *Journal of Molecular Spectroscopy* **68**(1), (1977), 134–145. doi:10.1016/0022-2852(77)90429-5.
- [361] R. F. Barrow, M. W. Bastin, and B. Longborough. “Rotational analysis of some bands of gaseous BaF.” In *Proceedings of the Physical Society* **92**(2), (1967), 518–519. doi:10.1088/0370-1328/92/2/130.
- [362] F. Paschen. “Erweiterung der Spektren Al II, Mg I, Be I und Al I.” In *Annalen der Physik* **404**(4), (1932), 509–527. doi:10.1002/andp.19324040406.
- [363] S. R. Langhoff, C. W. Bauschlicher, H. Partridge, and R. Ahlrichs. “Theoretical study of the dipole moments of selected alkaline-earth halides.” In *The Journal of Chemical Physics* **84**(9), (1986), 5025–5031. doi:10.1063/1.450651.
- [364] P. Fowler and A. Sadlej. “Correlated studies of electric properties of ionic molecules: alkali and alkaline-earth hydrides, halides and chalcogenides.” In *Molecular Physics* **73**(1), (1991), 43–55. doi:10.1080/00268979100101041.
- [365] J. Kobus, D. Moncrieff, and S. Wilson. “Comparison of the electric moments obtained from finite basis set and finite-difference Hartree-Fock calculations for diatomic molecules.” In *Physical Review A* **62**(6), (2000), 062503. doi:10.1103/PhysRevA.62.062503.
- [366] D. L. Wu, B. Tan, J. Y. Qin, H. J. Wan, A. D. Xie, B. Yan, and D. J. Ding. “Ab initio calculations on potential energy curves and radiative lifetimes for the band systems $A^2\Pi-X^2\Sigma^+$ of magnesium monohalides MgX ($X = F, Cl, Br, I$.)” In *Spectrochimica Acta - Part A: Molecular and Biomolecular Spectroscopy* **150**, (2015), 499–503. doi:10.1016/j.saa.2015.05.097.
- [367] S. Hou and P. F. Bernath. “Line list for the MgF ground state.” In *Journal of Quantitative Spectroscopy and Radiative Transfer* **203**, (2017), 511–516. doi:10.1016/j.jqsrt.2017.03.019.
- [368] W. J. Childs, L. S. Goodman, U. Nielsen, and V. Pfeufer. “Electric-dipole moment of CaF ($X^2\Sigma^+$) by molecular beam, laser-rf, double-resonance study of Stark splittings.” In *The Journal of Chemical Physics* **80**(6), (1983), 2283–2287. doi:10.1063/1.447005.

- [369] W. E. Ernst, J. Kändler, S. Kindt, and T. Törring. “Electric dipole moment of SrF $X^2\Sigma^+$ from high-precision stark effect measurements.” In *Chemical Physics Letters* **113**(4), (1985), 351–354. doi:10.1016/0009-2614(85)80379-1.
- [370] W. E. Ernst, J. Kändler, and T. Törring. “Hyperfine structure and electric dipole moment of BaF $X^2\Sigma^+$.” In *The Journal of Chemical Physics* **84**(9), (1986), 4769–4773. doi:10.1063/1.449961.
- [371] W. E. Ernst and J. Kändler. “Different polarization of the $A^2\Pi$ and $C^2\Pi$ state wave functions in CaF observed by visible and uv Stark spectroscopy.” In *Physical Review A* **39**(3), (1989), 1575–1578. doi:10.1103/PhysRevA.39.1575.
- [372] R. N. Zare. *Angular Momentum: Understanding Spatial Aspects in Chemistry and Physics*. New York, Chichester, Brisbane, Toronto, Singapore: John Wiley and Sons, Inc., first edn. (1988). ISBN 978-0-471-85892-8.
- [373] W. Gifford and H. McMahon. “A New Low-Temperature Gas Expansion Cycle. Part I.” In K. D. Timmerhaus, ed., *Advances in Cryogenic Engineering*, pp. 354–367. New York: Springer Science+Business Media, LLC (1960).
- [374] W. Gifford and H. McMahon. “A New Low-Temperature Gas Expansion Cycle. Part II.” In K. D. Timmerhaus, ed., *Advances in Cryogenic Engineering*, pp. 368–372. New York: Springer Science+Business Media, LLC (1960). ISBN 9781475705393. doi:10.1007/978-1-4757-0537-9.44.
- [375] G. Walker. *Cryocoolers, Part 1: Fundamentals*. New York: Springer Science+Business Media, LLC, first edn. (1983). ISBN 9781489952882.
- [376] A. T. A. M. de Waele. “Basic Operation of Cryocoolers and Related Thermal Machines.” In *Journal of Low Temperature Physics* **164**(5-6), (2011), 179–236. doi:10.1007/s10909-011-0373-x.

Research Data Management

This thesis research has been carried out in accordance with the research data management policy of the Institute for Molecules and Materials of Radboud University, the Netherlands.*

Some datasets presented in this thesis have been made available on the online repository Zenodo (<https://zenodo.org>) as part of the respective publications. The datasets in this thesis that have not been published together with their respective publications have been made available under one single link and identifier, again on Zenodo (<https://doi.org/10.5281/zenodo.7158221>).

- **Chapter 2:** All datasets are available at <https://doi.org/10.5281/zenodo.7158221>.
- **Chapter 3:** All datasets are available at <https://doi.org/10.5281/zenodo.7158221>.
- **Chapter 4:** The dataset for the presented optical cycling experiment is available as part of S. Hofsäss, M. Doppelbauer, S. C. Wright, S. Kray, B. G. Sartakov, J. Pérez-Ríos, G. Meijer, S. Truppe. Optical cycling of AlF molecules. *New Journal of Physics* **23**(7), (2021), 075001. <https://doi.org/10.1088/1367-2630/ac06e5/>. Data available on Zenodo, <https://zenodo.org/record/4912554>. The electric dipole interaction Hamiltonian and the dataset associated with the experimental determination of the radiative lifetime of the $a^3\Pi$ state are available at <https://doi.org/10.5281/zenodo.7158221>.
- **Chapter 5:** S. C. Wright, M. Doppelbauer, S. Hofsäss, H. C. Schewe, B. G. Sartakov, G. Meijer, S. Truppe. Cryogenic Buffer Gas beams of AlF, CaF, MgF, YbF, Al, Ca, Yb and NO – a comparison. *Molecular Physics*, (2022), submitted, <https://doi.org/10.48550/arXiv.2209.06564>. Data available on Zenodo, <https://doi.org/10.5281/zenodo.7063976>.
- **Chapter 6:** M. Doppelbauer, S. C. Wright, S. Hofsäss, B. G. Sartakov, G. Meijer, S. Truppe. Hyperfine-resolved optical spectroscopy of the $A^2\Pi \leftarrow X^2\Sigma^+$ transition in MgF. *The Journal of Chemical Physics* **156**(13), (2022), 134301, <https://doi.org/10.1063/5.0081902>. Data available on Zenodo, <https://doi.org/10.5281/zenodo.6110184>.

*<https://www.ru.nl/rdm/vm/policy-documents/policy-imm/>, last accessed 14 October 2022.

Curriculum Vitae

Maximilian Josef Doppelbauer, born June 11th, 1992, in Vienna, Austria

2018 – 2022	Ph.D. student in the Molecular Physics Department Fritz-Haber-Institut der Max-Planck-Gesellschaft, Berlin
2016 – 2017	Graduate researcher École Polytechnique Fédérale de Lausanne, Switzerland
2014 – 2016	M.Sc. , Interdisciplinary Sciences Emphasis on Chemical Physics and Biophysics Eidgenössische Technische Hochschule Zürich, Switzerland Thesis: “Calculating the Rotational Cooling of Ammonia Molecules in a Buffer Gas Cell Using a Direct Simulation Monte Carlo (DSMC) Method” (Prof. T.P. Softley and Dr. B.R. Heazlewood, University of Oxford, United Kingdom)
2011 – 2014	B.Sc. , Interdisciplinary Sciences Eidgenössische Technische Hochschule Zürich, Switzerland Thesis: “Development of a Microfluidic Method for the Formation of Compartmentalised Giant Unilamellar Vesicles” (Prof. P.S. Dittrich)
2010	Matura Gymnasium Kundmannngasse, Vienna, Austria

List of Publications

1. S. C. Wright, M. Doppelbauer, S. Hofsäss, H. C. Schewe, B. G. Sartakov, G. Meijer, S. Truppe. Cryogenic Buffer Gas beams of AlF, CaF, MgF, YbF, Al, Ca, Yb and NO – a comparison. *Molecular Physics*, (2022), submitted. (arXiv:2209.06564)
2. M. Doppelbauer, S. C. Wright, S. Hofsäss, B. G. Sartakov, G. Meijer, S. Truppe. Hyperfine-resolved optical spectroscopy of the $A^2\Pi \leftarrow X^2\Sigma^+$ transition in MgF. *The Journal of Chemical Physics* **156**(13), (2022), 134301.
3. X. Liu, W. Wang, S. C. Wright, M. Doppelbauer, G. Meijer, S. Truppe, J. Pérez-Ríos. The chemistry of AlF and CaF production in buffer gas sources. *The Journal of Chemical Physics* **157**(7), (2022), 074305.
4. N. Walter, M. Doppelbauer, S. Marx, J. Seifert, X. Liu, J. Pérez-Ríos, B. G. Sartakov, S. Truppe, G. Meijer. Spectroscopic characterization of the $a^3\Pi$ state of aluminum monofluoride. *The Journal of Chemical Physics* **156**(12), (2022), 124306.
5. S. Hofsäss, M. Doppelbauer, S. C. Wright, S. Kray, B. G. Sartakov, J. Pérez-Ríos, G. Meijer, S. Truppe. Optical cycling of AlF molecules. *New Journal of Physics* **23**(7), (2021), 075001.
6. M. Doppelbauer, N. Walter, S. Hofsäss, S. Marx, H. C. Schewe, S. Kray, J. Pérez-Ríos, B. G. Sartakov, S. Truppe, G. Meijer. Characterisation of the $b^3\Sigma^+, v = 0$ state and its interaction with the $A^1\Pi$ state in aluminium monofluoride. *Molecular Physics* **119**(1-2), (2021), e1810351.
7. S. Truppe, S. Marx, S. Kray, M. Doppelbauer, S. Hofsäss, H. C. Schewe, N. Walter, J. Pérez-Ríos, B. G. Sartakov, G. Meijer. Spectroscopic characterization of aluminum monofluoride with relevance to laser cooling and trapping. *Physical Review A* **100**(5), (2019), 052513.
8. M. J. Doppelbauer, O. Schullian, J. Loreau, N. Vaeck, A. van der Avoird, C. J. Rennick, T. P. Softley, B. R. Heazlewood. Using a direct simulation Monte Carlo approach to model collisions in a buffer gas cell. *The Journal of Chemical Physics* **146**(4), (2017), 044302.

9. T. F. Segawa, M. Doppelbauer, L. Garbuio, A. Doll, Y. O. Polyhach, G. Jeschke. Water accessibility in a membrane-inserting peptide comparing Overhauser DNP and pulse EPR methods. *The Journal of Chemical Physics* **144**(19), (2016), 194201.
10. A. H. C. West, B. L. Yoder, D. Luckhaus, C.-M. Saak, M. Doppelbauer, R. Signorell. Angle-Resolved Photoemission of Solvated Electrons in Sodium-Doped Clusters. *The Journal of Physical Chemistry Letters* **6**(8), (2015), 1487–1492.

Acknowledgements

Working in the Molecular Physics department at the Fritz Haber Institute was a challenging, inspiring and enjoyable experience during which I grew both as a scientist and as a person. Many people were involved in this process, and I want to thank them for their contributions.

First of all, I want to thank the director of the department, Gerard Meijer, and our group leader, Stefan Truppe, for hiring me as the first PhD student on the AIF project. I learned a lot from Stefan's experimental creativity, hands-on mentality, and determination. He provided the right amount of guidance for a striving lab and made sure that successes would also be celebrated. Gerard gave us almost limitless possibilities to work towards our goals, was a supportive mentor and an invaluable source of wisdom on the spectroscopy of cold small molecules.

The Molecular Physics department is a great group made up of experts in different fields that complement each other and thus achieve great science. Besides the scientists, these experts are engineers, technicians, and administrators.

Silvio Marx was the first postdoc on the AIF project who taught me almost everything I know about pulsed laser spectroscopy. Christian Schewe introduced me to the up- and downsides of ring dye lasers and was always a helpful guide in the following years. Without the support by Sidney Wright during the last two years, this thesis would not exist in this shape; I am always impressed by his knowledge and dedication.

I want to thank my fellow PhD students in the AIF group, Simon, Nicole, Johannes S., and Eduardo for the supportive and productive atmosphere in the lab. Nicole provided valuable parts of the evaluation of the lifetime of the metastable $a^3\Pi$ state of AIF in 4.5.2. Simon performed the experiments that I modelled in 4.4 and introduced me to savvy cabbage humour — it was a pleasure working with him during four years.

I am grateful to Boris Sartakov, who provided the theoretical foundations of all our spectroscopy experiments, calculated Hamiltonians and was always available to explain details as well as trivial notation questions. Jesús Pérez-Ríos introduced me to the optical Bloch equations and the Wigner-Eckart theorem and infected us all with his boundless enthusiasm for science.

The discussions on inorganic chemistry and surface science that I had with André Fielicke and Prof. Hans-Joachim Freund helped me to better understand the processes involved in the production of the diatomic monofluorides presented in this thesis.

Whenever I had technical questions, needed a quick manufacturing job for the experiment, or the data acquisition software had problems, the technical staff of the department — Uwe, Marco, Sandy, Henrik, Thomas, Andreas, Stefan, Klaus-Peter, Sebastian — was exceptionally helpful. I want to expressly thank Klaus-Peter, who often made the impossible possible and without whom building the experiment would have cost me much more time and sweat. Our skilled engineer Sebastian designed our setups, made sure they were manufactured correctly, and was always available for questions and maintenance issues. The electronics and mechanical workshops of the FHI were helpful with any task, no matter the size.

Inga von Dölln, Karin Grassow and Manuela Misch made sure that the department ran smoothly, so that we could focus on science. Karin and Inga were also responsible for two fabulous department excursions.

Many friendly colleagues at the institute made lunch breaks and after-work get-togethers great fun: David, Mallikarjun, Alicia, Mallory, JuHyeon, Jenny, Márkó, Russell, Giacomo, Johannes B., Angelika, Ivana, Marcel, and many more. Maike shared the ups and downs of finishing a PhD thesis with me and was a great co-PhD representative. I appreciate that we are defending our theses on the same day.

Outside of work, several friends helped me enjoy the beauties of Berlin and supported me during more difficult times. Otto and Helene are old friends whom I met again in Berlin — they became like family members for me. Jakob, Robert, Judith, Thomas, Norbert and Pantcho shared my passion for classical music and Jonathan, Jeremie and Hanne shared a lot of other pleasures with me. I am glad that I kept contact with some important old friends from home and university with whom I can share laughs, deep conversations, dinners and annual theatre visits.

My parents are the ones who equipped me with curiosity and who always supported me in my endeavours; for this, I am very grateful. I am also glad to have a brother with a refreshingly different view of the world.

For many years, I have been sharing my life with Eva Lea, whose support and attitude encourage me to give my very best. Thank you.